UC Berkeley
UC Berkeley Electronic Theses and Dissertations

Title

Synthesis and Characterization of Lanthanide Single Molecule Magnets with Unconventional Ligands

Permalink

https://escholarship.org/uc/item/24h4z2vm

Author

Vincent, Alexandre Holland

Publication Date

2024

Peer reviewed|Thesis/dissertation

Synthesis and Characterization of Lanthanide Single Molecule
Magnets with Unconventional Ligands

By

Alexandre H. Vincent

A dissertation submitted in partial satisfaction of the

requirements for the degree of

Doctor of Philosophy

in

Chemistry

in the

Graduate Division

of the

University of California, Berkeley

Committee in Charge:
Professor Jeffrey R. Long Chair
Professor Kwabena Bediako
Professor Alex Zettl

Spring 2024

Abstract

Synthesis and Characterization of Lanthanide Single Molecule
Magnets with Unconventional Ligands

By

Alexandre H. Vincent

Doctor of Philosophy in Chemistry

University of California, Berkeley

Professor Jeffrey R. Long, Chair

The synthesis and characterization of several lanthanide single molecule magnets and a related series of benzene bridged lanthanide compounds are described in this dissertation. Previously overlooked ligand types, namely metalloligands and borole dianions, are shown to improve the operating temperature of lanthanide single molecule magnets by slowing thermally independent relaxation. This dissertation also touches upon a rare example of a highly covalent lanthanide arene interaction in a series of lanthanide benzene inverse sandwich compounds.

Chapter 1 introduces single molecule magnetism and provides relevant background information regarding their electronic structure. The figures of merit used to evaluate the performance of different compounds are defined and important milestones in the field are discussed.

Chapter 2 describes the synthesis and characterization of a series of tetrathiotungstate bridged lanthanide complexes. The magnetic characterization of these compounds and their comparison with isostructural tetrathiomolybdate complexes reveals that relativistic effects impact the magnetic exchange interaction between the bridge electron and the adjacent lanthanides.

Chapter 3 details the synthesis and characterization of a series of cobalt bis-(1,2-diphenyldithiolate) bridged lanthanide complexes as well as their post synthetic reduction. The dysprosium congener of this complex exhibited single molecule magnetism with suppressed temperature independent relaxation.

Chapter 4 describes the synthesis and characterization of a dysprosium bis-borolide single molecule magnet. This compound was found to have an operating temperature of 65 K, which is on par with the best performing dysprosocenium magnets. Computational analysis on the complex showed how substituent modification may be a viable method to increase the blocking temperature of these compounds moving forward.

Chapter 5 describes the synthesis and characterization of a series of lanthanide benzene inverse sandwich compounds. The experimental characterization and computational analysis performed suggests that the central benzene is a tetra-anion stabilized by a rare δ bonding interaction with its adjacent lanthanide ions.

1

Table of Contents

Chapter 5: Lanthanide-Benzene Inverse Sandwich Series Stabilized by a δ-Bonding Interaction

Chapter 6: Closing Remarks

Acknowledgments

Firstly, I'd like to express my gratitude toward my parents. It is unlikely that I'd have survived long enough to write this dissertation had they not spent the time and energy teaching me to pause and reflect prior to touching a hot stove. They have always been a source of guidance and encouragement, and I still turn to them for inspiration on a regular basis. I also should thank my Uncle Dario and Aunt Tracy across the bay. They helped me move and get settled when I first arrived here and have been kind to me ever since. I'd also like to acknowledge my sister for taking the time to administer some memes and entertainment to me in dire moments; these are prophylaxes against despair, as far as I am concerned.

My research career began in the lab of my undergraduate advisor Prof. Jeff Rinehart under the mentorship of Dr. Yijun Xie. I'd like to thank both of them for encouraging me to pursue a PhD, and for sharing their knowledge and experience with me. Their enthusiasm for science was also infectious, and I fear as though I will never fully recover from my initial exposure. They established the necessary foundation for me to grow professionally and I will always remain grateful for that.

I'm also especially grateful to my advisor Prof. Jeff Long. The group he has built is a clear reflection of Jeff's passion for science. It is challenging to put into words, but he has cultivated a particular espirit de corps within the group, one that draws out the best from each individual student. He has routinely gone above and beyond as an advisor, and I'm thankful for the wisdom and support he has shown me over the years.

I was also fortunate enough to overlap with many outstanding mentors within the group. I'd like to express thanks to Dr. Colin Gould for teaching me how to do *everything* in a professional fashion and Dr. Lucy Darago for helping me find a research direction during my first year. A word of thanks also to Dr. Khetpakorn Chakarawet and Dr. Ari Turkiewicz for teaching me everything I know about X-ray crystallography. Many thanks to Dr. Katie Meihaus and Dr. Dave Harris who have generously lent me professional advice and editorial feedback on my manuscripts and proposals. I have also been fortunate to mentor and work with a great undergraduate student David Lu. It was a privilege to work with him and I am eager to see what he will accomplish in the future.

Finally, I would like to acknowledge those that I've had the pleasure of collaborating with, namely Prof. Nicholas Chilton, Prof. Filipp Furche, Prof. Steve Hill, and their students Yasmin Whyatt, Ahmadrezza Rajabi, and Dr. Daphne Lubert-Perquel; all of these individuals made significant contributions to the work presented here, and I consider myself fortunate to have had the opportunity to work alongside them. I would also like to acknowledge Dr. Randall McClain and Dr. Ben Harvey for working closely not only with myself but with many other magnetism students in the group. Finally, I'd like to acknowledge Dr. Simon Teat for working closely with me on the many beamline experiments I've been a part of over the years.

Chapter 1: Introduction to Single Molecule Magnetism

1.1: Key Concepts in Single Molecule Magnetism

Single molecule magnets are discrete coordination compounds which have magnetic bistability and intrinsic slow magnetic relaxation.[1] The behavior of a single molecule magnet is reminiscent that of superparamagnetic nanoparticles, with an important distinction in that they lack the long-range magnetic order typical of most superparamagnetic nanoparticles and bulk magnetic materials more generally. Indeed, many single molecule magnets contain only a single metal ion. Due to their tiny size and novel properties, single molecule magnets are currently being examined for use in data storage, spin-logic, and quantum information processing applications.[2,3]
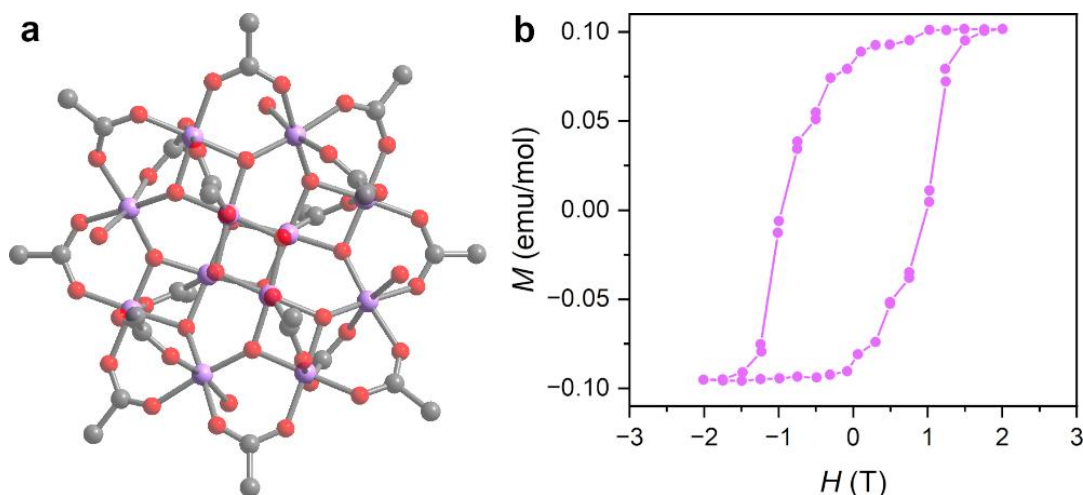
Figure 1.1: a) Crystal structure of the first reported single molecule magnet $Mn_{12}O_{12}(OAc)_{16}(H_2O)_4$. Hydrogen atoms and lattice solvent omitted for clarity.[3] b) Magnetic hysteresis of $Mn_{12}O_{12}(OAc)_{16}(H_2O)_4$ at $T = 2.2$ K.[4]

Broadly speaking, a compound in its ground state must have two features in order to exhibit single molecule magnetism: large magnetic anisotropy, and a bistable ground state.[6] Magnetic anisotropy arises from the orbital angular momentum of the electrons (L) and its interaction with S via the spin-orbit interaction.[7] Where paramagnetic complexes with $L = 0$ have no preferred molecular axis of magnetization, compounds with non-zero L will have a preferred axis defined by the crystal field strength and geometry about the metal. In Kramer's systems with a half integral spin ground state, this anisotropy produces a bistable ground state protected by time-reversal symmetry.[8] The strength of the magnetic anisotropy is experimentally measured as an empirical thermal barrier to depolarization (U_{eff}). The U_{eff} value determines the rate of thermally assisted magnetic relaxation (Orbach relaxation), according to the rate equation $\tau^{-1} = \tau_0^{-1}e^{-U_{eff}/k_BT}$; where τ_0 is the attempt time, k_B is the Boltzmann constant and T is temperature.[9] A high U_{eff} value is a prerequisite to observing a high blocking temperature (T_B), defined here and in the broader literature as the temperature at which the relaxation time τ is equal to 100 seconds.

Single molecule magnetism was first reported in for the transition metal cluster $Mn_{12}O_{12}(OAc)_{16}(H_2O)_4$ (Figure 1.1).[4,5] Magnetization measurements of $Mn_{12}O_{12}(OAc)_{16}(H_2O)_4$ as a function of a swept magnetic field showed open-loop magnetic hysteresis at 2.2 K, which indicated slow magnetic relaxation at zero field. In follow up studies, it was determined by isothermal

ac susceptibility measurements, that a small thermal barrier to magnetic depolarization (U) was responsible for the observed magnetic hysteresis at low temperature.[10] The thermal barrier in $Mn_{12}O_{12}(OAc)_{16}(H_2O)_4$ arises from zero-field splitting of the M_S multiplet of the $S = 10$ coupled ground state. Near 2 K, the resonant phonon population needed to traverse the split Ms states under zero-field is small, which results in slow relaxation and hysteretic behavior. To obtain higher temperature hysteresis, it is therefore necessary to increase the zero-field splitting of the M_S sublevels.

The zero-field splitting in transition metal complexes is directly proportional to the strength of the spin-orbit interaction, through which M_S states are split under zero external field.[11] Due to the strong vibronic coupling in transition metal compounds, the Jahn-Teller effect quenches orbital moment to in the ground state, meaning that all of the orbital moment through which Ms states are split under zero-field arises via their spin orbit interaction with low-lying excited states with unquenched orbital moment. Indeed, the leading strategy in constructing a transition metal based single molecule magnet with a high thermal barrier to depolarization is to build a linear crystal field, where Jahn-Teller distortion is impossible.[12] This fundamental limitation of the transition metals spurred chemists to shift their attention toward lanthanide compounds, as most of their ground-states have unquenched orbital angular momentum regardless of crystal field geometry.

1.2: Lanthanide Single Molecule Magnets

Many of the trivalent lanthanide ions owe their large unquenched orbital angular momentum due to the unique properties of their valence 4f electrons.[13] The 4f valence electrons in are core-like, meaning that they experience minimal perturbation from surrounding crystal field.[14] The orbital degeneracy responsible for producing orbital angular momentum is preserved, as the Jahn-Teller effect is imperceptibly weak among the lanthanides. Additionally, the spin-orbit interaction is much stronger than it is in transition metals due to the high proton counts of the lanthanide ions, which results in well isolated L-S coupled states. The resultant M_J sublevels of the J ground state are what undergo perturbation by the crystal field interaction, the magnitude of which depends on L as well as on the ligand field strength and geometry.[15] An interaction diagram for Dy^{3+} in an axial crystal field is illustrated in Figure 1.2a. As many of the second half of the lanthanide ions compounds have large unquenched L values, the largest U_{eff} values have been observed in lanthanide single molecule magnets.[6]

The first lanthanide single molecule magnet to be reported was the terbium bis-phthalocyanine anion.[15] From inspection of the ac susceptibility measurements as well as electronic structure calculations, it was clear that the U_{eff} value for the terbium bis-phthalocyanine compound was ~215 cm^{-1}, two orders of magnitude higher than those typically observed for transition metal clusters. A qualitative model for the relationship between the charge distribution of lanthanide M_J states and their perturbation under different crystal-field geometries emerged in the years following this initial discovery.[13] As a result of this, single molecule magnets using the Kramer's ion dysprosium routinely reach U_{eff} values $\sim 10^3$ cm^{-1}, a significant improvement over the earlier terbium compounds. An exemplar of this type of compound is the cation $[Dy(OtBu)_2(Py)_5]^+$ (Py = pyridine) which boasts a U_{eff} value of 1220 cm^{-1}.[16] The high U_{eff} value of this cation is the result of the strong axial ligand field exerted by the *tert*-butoxide ligands in concert with a comparatively weak equatorial ligand field consisting of five pyridine solvent molecules.
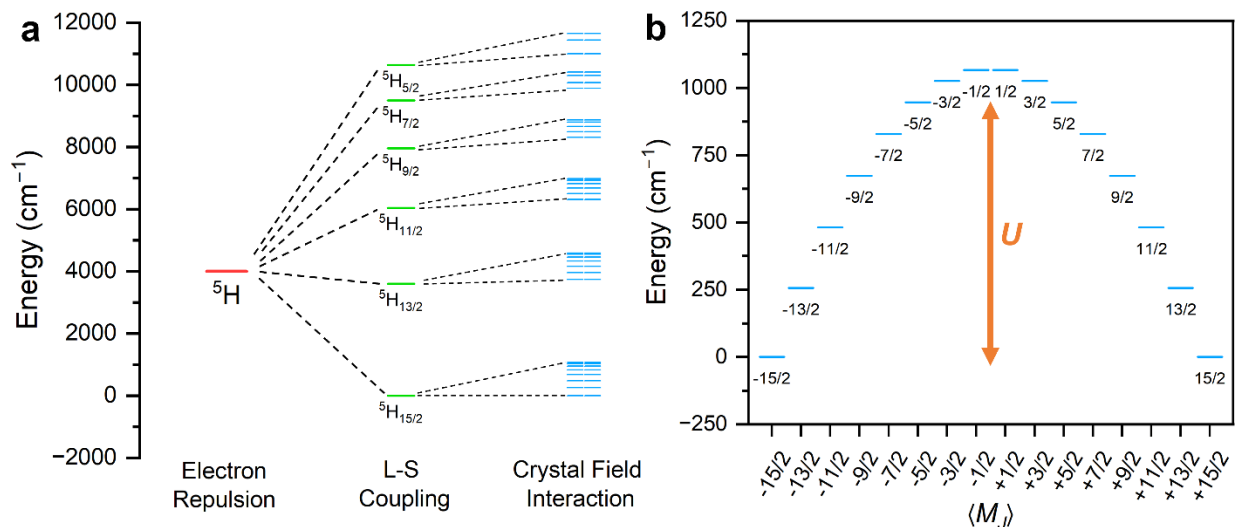
Figure 1.2: a) Electronic structure diagram for a single Dy^{3+} ion with sequential perturbations of electron repulsion, spin-orbit coupling, and an axial crystal field interaction. The blue energy levels are the $2J+1$ M_J microstates of each L-S coupled state. The energy of the electron repulsion parent state was set to 4000 cm^{-1} arbitrarily for the sake of visual clarity. All other energy levels were evaluated in Phi[17] using Hamiltonian given in Equation 1.1. For the L-S coupled states, $B_2^0 = 0$, while for the crystal-field split states, $B_2^0 = 1000$ cm^{-1}. b) Crystal field splitting of the $^5H_{15/2}$ M_J state manifold with the thermal barrier to demagnetization (U) illustrated in orange

$$\hat{H} = \sum_{j=1}^{2S} \lambda_j \left(\vec{L} \cdot \vec{S} \right)^j - \frac{2B_2^0}{135} \left(3\hat{L}_z^{\,2} - \hat{L}^2 \right)$$

(Equation 1.1)

1.3: Through Barrier Relaxation and Methods for its Suppression

In spite of these promising recent developments, room-temperature single molecule magnetism remains elusive. Non-classical relaxation mechanisms, such as quantum tunneling of magnetization and two-phonon Raman spin-relaxation, act to either totally or partially circumvent the thermal barrier. Quantum tunneling of magnetization (QTM) is a significant problem in particular, as it effectively sets the upper bound for relaxation times in each particular compound given its temperature independence.[18–20] Additionally, QTM is often most rapid at zero applied field, which often results in near zero-remanent magnetization and low T_B values. Even in compounds with U_{eff} values above the average thermal energy available at 300 K, high operating temperatures cannot be achieved in the presence of fast QTM. Two dominant strategies have emerged to suppress these non-classical relaxation modes in lanthanide single molecule magnets: building giant-spins through exchange coupling and limiting vibrational degrees of freedom.[20,21]

The first strategy hinges on the use of magnetic exchange to suppress tunneling. In anisotropic multinuclear compounds with a sufficiently stabilized coupled ground state, tunneling at zero field is suppressed. Appreciable magnetic exchange in lanthanide coordination compounds is rare however due to their core-like 4f orbitals. One effective method to facilitate lanthanide exchange has been to use spin-containing bridging ligands.[22] An illustrative example of this can be found in $[(N^*)_2Tb(THF)_2(\mu-\eta^2:\eta^2-N_2)]^-$ (N^* = bis-(trimethylsilyl)amide), which has completely suppressed QTM at zero-field as well as a dc susceptibility profile consistent with a

3

ferrimagnetically coupled giant-spin ground state at low temperature.[23,24] By fitting the dc suscep-tibility of $[(N^*)_2Gd(THF))_2(\mu\text{-}\eta^2\text{:}\eta^2\text{-}N_2)]^-$, it was found that the two lanthanide ions were partici-pating in an unusually strong antiferromagnetic direct exchange interaction with the radical elec-tron on the bridging N_2^{3-} fragment. Due to this, $[(N^*)_2TbTHF)_2(\mu\text{-}\eta^2\text{:}\eta^2\text{-}N_2)]^-$ exhibited a ferri-magnetic coupled ground state at low temperature, which showed exclusively Orbach relaxation and a high T_B of 14 K, in spite of its middling U_{eff} value.

The second strategy shown to slow down quantum tunneling of magnetization was to maxim-ize the axiality of the ligand field in single ion dysprosium systems while limiting the vibrational degrees of freedom. The vibrational flexibility of the equatorial ligand field is correlated to the tunneling rate in axial single ion dysprosium magnets.[21] In a hypothetical dysprosium single-mol-ecule magnet with maximal axial anisotropy (eg. gas-phase DyO^+), there is no equatorial vibration possible, which drives the tunneling rate between Kramer's doublet to zero at zero-field as required under time-reversal symmetry. The first dysprosocenium complex $[Dy(Cp^{ttt})_2]^+$ (Cp^{ttt} = 1,3,5-(tert-butyl)cyclopentadienyl is a good example of this strategy in an isolable compound.[24] While $[Dy(Cp^{ttt})_2]^+$ had a similar U_{eff} value to previously described $[Dy(OtBu)_2(Py)_5]^+$, its tunneling rate was several orders of magnitude slower due to the limited vibrational degrees of freedom in the equatorial plane. As a result of this, $[Dy(Cp^{ttt})_2]^+$ had a T_B of 60 K while $[Dy(OtBu)_2(Py)_5]^+$ had a T_B of 14 K.[16,25]

1.4: Conclusion and Outlook

The work described herein was conducted with the two aforementioned methods of suppress-ing through barrier relaxation in mind. The general aim of this work was to identify new spin containing bridges that are competent at mediating magnetic exchange between lanthanides as well to identify a more nucleophilic alternative to cyclopentadienyl with which to enhance axial anisot-ropy.

Chapter 2 and Chapter 3 focus on lanthanide compounds featuring a spin containing metal-loligand bridge. In chapter 2, the synthesis and magnetic characterization of a series of tetrathio-tunstate bridged lanthanide compounds are reported, followed by a discussion of its properties differ from the earlier reported tetrathiomolybdate structural analogues due to relativistic differ-ences between the two bridges. Chapter 3 is focused on the synthesis and characterization of sev-eral new cobalt 1,2-diphenyldithiolene bridged compounds and their single molecule magnetism. The synthesis and magnetic characterization of a mononuclear dysprosium bis-borolide single molecule magnet with outstanding properties is discussed in Chapter 4. Finally, chapter 5 is fo-cused on the magnetic and electronic properties of a series lanthanide-benzene inverse sandwich compounds which feature an unusually covalent interaction between the lanthanide and benzene. To summarize, this dissertation presents several advances in the synthesis of lanthanide single molecule magnets as well as fundamental insights into the covalent bonding capabilities of the lanthanide ions.

1.5: References and Footnotes

(1) Chilton, N. F. Molecular Magnetism. *Ann. Rev. Mater. Res.* **2022**, *52*, 79–101. DOI: 10.1146/annurev-matsci-081420-042553.

(2) Atzori, M.; Sessoli, R. The Second Quantum Revolution: Role and Challenges of Molecular Chemistry. *J. Am. Chem. Soc.* **2019**, *141* (29), 11339–11352. DOI: 10.1021/jacs.9b00984.

(3)   von Kugelgen, S.; Freedman, D. E. A Chemical Path to Quantum Information. *Science* **2019**, *366* (6469), 1070–1071.

(4)   Lis, T. Preparation, Structure, and Magnetic Properties of a Dodecanuclear Mixed-Valence Manganese Carboxylate. *Acta Crystallogr. Sect. B* **1980**, *36* (9), 2042–2046. DOI: 10.1107/S0567740880007893.

(5)   Sessoli, R.; Gatteschi, D.; Caneschi, A.; Novak, M. A. Magnetic Bistability in a Metal-Ion Cluster. *Nature* **1993**, *365*, 141.

(6)   Woodruff, D. N.; Winpenny, R. E. P.; Layfield, R. A. Lanthanide Single-Molecule Magnets. *Chem. Rev.* **2013**, *113* (7), 5110–5148. DOI: 10.1021/cr400018q.

(7)   Bloch, F.; Gentile, G. Zur Anisotropie der Magnetisierung ferromagnetischer Einkristalle. *Z. Für Phys.* **1931**, *70* (5), 395–408. DOI: 10.1007/BF01339586.

(8)   Kramers, H. A. Théorie Générale de La Rotation Paramagnétique Dans Les Cristaux. *Proc Acad Amst* **1930**, *33* (6).

(9)   Orbach, R. On the Theory of Spin-Lattice Relaxation in Paramagnetic Salts. *Proc. Phys. Soc.* **1961**, *77* (4), 821–826. DOI: 10.1088/0370-1328/77/4/301.

(10)   Sessoli, R.; Tsai, H. L.; Schake, A. R.; Wang, S.; Vincent, J. B.; Folting, K.; Gatteschi, D.; Christou, G.; Hendrickson, D. N. High-Spin Molecules: [Mn12O12(O2CR)16(H2O)4]. *J. Am. Chem. Soc.* **1993**, *115* (5), 1804–1816. DOI: 10.1021/ja00058a027.

(11)   Abragam, A.; Bleaney, B. *Electron Paramagnetic Resonance of Transition Ions | A. Abragam and B. Bleaney | 9780199651528 | Oxford University Press Canada*; OUP Oxford, 1970.

(12)   Bunting, P. C.; Atanasov, M.; Damgaard-Møller, E.; Perfetti, M.; Crassee, I.; Orlita, M.; Overgaard, J.; Slageren, J. van; Neese, F.; Long, J. R. A Linear Cobalt(II) Complex with Maximal Orbital Angular Momentum from a Non-Aufbau Ground State. *Science* **2018**, *362* (6421). DOI: 10.1126/science.aat7319.

(13)   Rinehart, J. D.; Long, J. R. Exploiting Single-Ion Anisotropy in the Design of f-Element Single-Molecule Magnets. *Chem. Sci.* **2011**, *2* (11), 2078–2085. DOI: 10.1039/c1sc00513h.

(14)   Electronic and Magnetic Properties of the Lanthanides. In *Lanthanide and Actinide Chemistry*; John Wiley & Sons, Ltd, 2006; pp 61–87. DOI: 10.1002/0470010088.ch5.

(15)   Ishikawa, N.; Sugita, M.; Ishikawa, T.; Koshihara, S. Y.; Kaizu, Y. Lanthanide Double-Decker Complexes Functioning as Magnets at the Single-Molecular Level. *J. Am. Chem. Soc.* **2003**, *125* (29), 8694–8695. DOI: 10.1021/ja029629n.

(16)   Ding, Y. S.; Chilton, N. F.; Winpenny, R. E. P.; Zheng, Y. Z. On Approaching the Limit of Molecular Magnetic Anisotropy: A Near-Perfect Pentagonal Bipyramidal Dysprosium(III) Single-Molecule Magnet. *Angew. Chem. - Int. Ed.* **2016**, *55* (52), 16071–16074. DOI: 10.1002/anie.201609685.

(17)   Chilton, N. F.; Anderson, R. P.; Turner, L. D.; Soncini, A.; Murray, K. S. PHI: A Powerful New Program for the Analysis of Anisotropic Monomeric and Exchange-Coupled Polynuclear d- and f-Block Complexes. *J. Comput. Chem.* **2013**, *34* (13), 1164–1175. DOI: 10.1002/jcc.23234.

(18)   Gatteschi, D.; Sessoli, R. Quantum Tunneling of Magnetization and Related Phenomena in Molecular Materials. *Angew. Chem. - Int. Ed.* **2003**, *42* (3), 268–297. DOI: 10.1002/anie.200390099.

(19)   Ishikawa, N.; Sugita, M.; Wernsdorfer, W. Quantum Tunneling of Magnetization in Lanthanide Single-Molecule Magnets: Bis(Phthalocyaninato)Terbium and

Bis(Phthalocyaninato)Dysprosium Anions. *Angew. Chem. - Int. Ed.* **2005**, *44* (19), 2931–2935. DOI: 10.1002/anie.200462638.

(20) Swain, A.; Sharma, T.; Rajaraman, G. Strategies to Quench Quantum Tunneling of Magnetization in Lanthanide Single Molecule Magnets. *Chem. Commun.* **2023**, *59* (22), 3206–3228. DOI: 10.1039/D2CC06041H.

(21) Ortu, F.; Reta, D.; Ding, Y.-S.; Goodwin, C. A. P.; Gregson, M. P.; McInnes, E. J. L.; Winpenny, R. E. P.; Zheng, Y.-Z.; Liddle, S. T.; Mills, D. P.; Chilton, N. F. Studies of Hysteresis and Quantum Tunnelling of the Magnetisation in Dysprosium(III) Single Molecule Magnets. *Dalton Trans.* **2019**, *48* (24), 8541–8545. DOI: 10.1039/C9DT01655D.

(22) Demir, S.; Jeon, I.-R.; Long, J. R.; Harris, T. D. Radical Ligand-Containing Single-Molecule Magnets. *Coord. Chem. Rev.* **2015**, *289–290*, 149–176. DOI: 10.1016/j.ccr.2014.10.012.

(23) Rinehart, J. D.; Fang, M.; Evans, W. J.; Long, J. R. A N23–Radical-Bridged Terbium Complex Exhibiting Magnetic Hysteresis at 14 K. *J. Am. Chem. Soc.* **2011**, *133* (36), 14236–14239.

(24) Rinehart, J. D.; Fang, M.; Evans, W. J.; Long, J. R. Strong Exchange and Magnetic Blocking in N 2 3–Radical-Bridged Lanthanide Complexes. *Nat. Chem.* **2011**, *3* (7), 538–542.

(25) Goodwin, C. A. P.; Ortu, F.; Reta, D.; Chilton, N. F.; Mills, D. P. Molecular Magnetic Hysteresis at 60 Kelvin in Dysprosocenium. *Nature* **2017**, *548* (7668), 439–442. DOI: 10.1038/nature23447.

Chapter 2. Synthesis and Magnetic Characterization of Lanthanide-Tetrathiotungstates

Vincent, A. H.[a]; Long, J.R. *In Preparation*. **2023**

2.1 Introduction

Single-molecule magnets are a class of discrete paramagnetic compounds which exhibit intrinsic magnetic bistability.[1,2] Due to this requisite magnetic bistability, single molecule magnets remain polarized at and below a characteristic blocking temperature T_b, following removal of an external applied magnetic field. As this behavior is intrinsic, single molecule magnets have been proposed as candidate materials for use in high-density data storage devices, quantum information processing, as well as nanoscale spintronic devices.[3,4] Previous studies have focused on devising strategies to maximize molecules' thermal barrier to depolarization (U_{eff}) with the overall aim of obtaining higher operating temperatures. Lanthanide complexes were found to yield the highest (U_{eff}) values due to their ground states possessing large unquenched orbital moments.[5] As the number of lanthanide single molecule magnets in the literature has increased, it has become clear that the existence of fast through-barrier magnetic relaxation pathways prevent operating temperatures from increasing in tandem with U_{eff}.[6] In recent years, more emphasis been placed on developing strategies to suppress or entirely eliminate non-classical relaxation pathways.

Establishing a giant-spin ground state by coupling multiple lanthanide ions through magnetic exchange has been shown to suppress quantum tunneling of magnetization.[7,8] Ordinarily, exchange interactions involving lanthanides are vanishingly weak (<1 cm^{-1}) due to the limited radial projection of their magnetic 4f orbitals.[9] As most exchange processes depend on the spatial overlap between spin containing orbitals, the limited overlap between the 4f orbitals and surrounding ligand orbitals yield weak, through-space exchange interactions. Bridging ligands with unpaired electrons and radially diffuse spin containing orbitals have been shown to participate in strong direct exchange with lanthanide ions, leading to well stabilized giant-spin ground states.[8] The best all-round radical bridging ligand which facilitates strong lanthanide exchange coupling is $N_2^{3-\bullet}$. In compound $[\{[(Me_3Si)_2N]_2(THF)Gd\}_2(\mu\text{-}\eta^2{:}\eta^2\text{-}N_2)]^-$, $N_2^{3-\bullet}$ has a coupling constant with Gd ($J_{Gd\text{-}Rad}$) of -27 cm^{-1}.[7,10] The isostructural Tb^{3+} containing complex features only thermally activated Orbach relaxation is observed, indicating through barrier relaxation is suppressed.[7,10]

Paramagnetic metalloligand bridges have also been shown to mediate strong exchange interactions involving lanthanides. It was shown that $[(Cp*_2Gd)_2(\mu\text{-}MoS_4)]^-$ (Cp* = pentamethylcyclopentadienyl), which contains an 4d^1 $S = 1/2$ Mo^{5+} bridge, exhibits a large $J_{Gd\text{-}Mo}$ of +16.1 cm^{-1}, exceeding the coupling constants observed for most organic radical bridged lanthanide species.[11] Unlike $N_2^{3-\bullet}$ however, these thiometallates have multiple chemical handles for further derivatization. The oxidation state of the bridge, the identity of the donor atoms, and the identity of the transition metal could all impact the observed $J_{Ln\text{-}M}$ value with associated lanthanide ions.

In this work, the influence of the transition metal center on the observed exchange interaction in tetrathiometallate bridged lanthanide compounds was examined by synthesizing and characterizing a series of isostructural tetrathiotungstate $(WS_4)^{3-}$ bridged compounds for direct comparison. In $[(Cp*_2Ln)_2(\mu\text{-}MoS_4)]^-$ (**1-Ln**) (Ln = Y, Gd, Tb, Dy) the exchange interaction was found to be a double exchange interaction, in which the unpaired 4d electron of $(MoS_4)^{3-}$ fragment coupled with the lanthanide 4f electrons through the vacant 5d orbitals of the lanthanide ions.[11] We hypothesized initially that switching the metal center to tungsten would relativistically destabilize the frontier d-

---

orbitals, which would improve their energy match with the vacant 5d orbitals of the lanthanide ion, thereby resulting in a stronger double-exchange interaction. The introduction of tungsten was found to decrease the exchange interaction, as revealed by dc susceptibility measurements performed on $[(Cp*_2Gd)_2(\mu\text{-}WS_4)]^-$. Our crystal structure analysis in conjunction with ground state DFT calculations suggest the relativistic stabilization of the proximal 6s orbital and its interaction with the spin containing $5d_z^2$ orbital of tungsten, result in lower spatial overlap between the lanthanide and tungsten orbitals. These results demonstrate that the exchange interaction in tetrathiometallate bridged lanthanide complexes can be modified by changing the identity of the metal center and that even weak effects such as relativistic orbital contraction are handles through which the strength of exchange can be modified in designing molecular magnets.

2.2 Results and Discussion

Synthesis of the target thiotungstate bridged anions required the isolation and subsequent reduction of the overall neutral $(Cp*_2Ln)_2(\mu\text{-}WS_4)$ **2-Ln** (Ln = Y, Gd, Tb, Dy) derivatives as pictured in Scheme 2.1. These neutral species were synthesized using a modified variant of that reported for the preparation of $(Cp*_2Ln)_2(\mu\text{-}MoS_4)$. In this procedure, a THF solution of $Cp*_2Ln(BPh_4)$ is added to a suspension of $(PPh_4)_2WS_4$. The yellow color characteristic of the free tetrathiotungstate dianion changed to red, indicating complexation of the dianion with $Cp*_2Ln^+$. The color change is accompanied by the precipitation of a colorless microcrystalline material, presumed to be $(PPh_4)BPh_4$. The $(PPh_4)BPh_4$ was subsequently separated from suspension by filtration through celite and discarded. Performing the salt metathesis with a two-fold excess of $Cp*_2Ln(BPh_4)$ was necessary to isolate the desired product $(Cp*_2Ln)_2(\mu\text{-}WS_4)$ **2-Ln** (Ln = Y^{3+}, Gd^{3+}, Tb^{3+}, Dy^{3+}), which could be obtained via recrystallization from a concentrated toluene extract of the crude product at −30 °C.
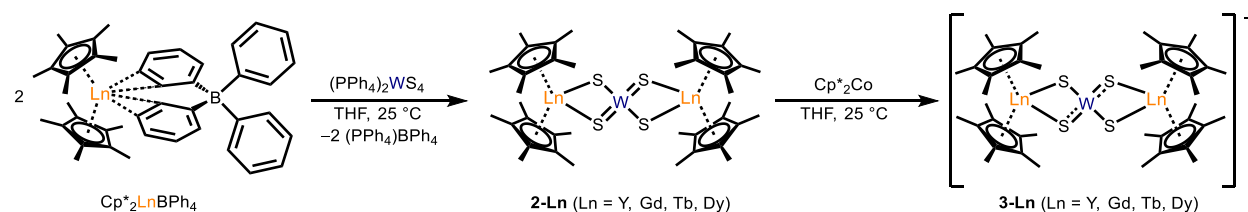
Scheme 2.1. Synthetic route to $[CoCp*_2][(Cp*_2Ln)_2(\mu\text{-}WS_4)]$ **3-Ln** (Ln = Y ,Gd, Tb, Dy) stoichiometry

Cyclic voltammetry of a solution of **2-Gd** in 1,2-difluorobenzene confirmed that the overall neutral $(WS_4)^{2-}$ containing complex could be reversibly reduced by one electron at −1.6 V with respect to ferrocene (Figure 2.1). An unexpected second reversible reduction event located closer to −2 V was also noted. The reduction potential of this second wave is not low enough to ascribe to the Gd^{3+}/Gd^{2+} redox couple, suggesting that a complex featuring a formally tetranionic thiotungstate bridge may be isolable using strong chemical reductants such as potassium graphite or lithium naphthalenide.

To access the desired one electron reduction without the formation of the dianionic product, $CoCp*_2$ was employed as a mild chemical reductant in analogy to the thiomolybdate reduction procedure. Treating an equivalent of **2-Ln** with a THF solution of $CoCp*_2$ rapidly resulted in a color change from red to orange, indicating the formation of the monoanionic compounds of interest. Crystals of $[CoCp*_2][(Cp*_2Y)_2(\mu\text{-}WS_4)]$ **3-Y** were grown by layering a THF concentrate

with diethyl ether. Crystals of [CoCp*$_2$][(Cp*$_2$Ln)$_2$(μ-WS$_4$)] **3-Ln** (Ln = Gd, Tb, Dy) were grown by slowly cooling their respective THF concentrates to −30 °C.

The x-ray crystal structures of **3-Ln** [CoCp*$_2$][(Cp*$_2$Ln)$_2$(μ-WS$_4$)] (Ln = Y, Gd, Tb, Dy) have nearly identical connectivity to those reported for [CoCp*$_2$][(Cp*$_2$Ln)$_2$(μ-MoS$_4$)] (**1-Ln**) (Ln = Y, Gd, Tb, Dy), with the two (Cp*$_2$Ln)$^+$ cations bridged by a thiometalate trianion. The structure of 3-Gd is illustrated in Figure 2.2 and is representative of the three other congeners. In all 3-Ln compounds, the free CoCp*$_2$ had metal-centroid distances close to 1.65 Å, which is consistent with the values for the decamethylcobaltocenium cation in the Cambridge Structural Database.

The average tungsten sulfur bond lengths for **2-Y** and **3-Y** were found to be 2.194(1) Å and 2.232(5) Å respectively. This expansion in the W-S distances is present throughout the series: **2-Gd** and **3-Gd** have average W-S distances of 2.190(2) Å and 2.234(5) Å respectively, **2-Tb** and **3-Tb** have average W-S distances of 2.189(1) and 2.234(6) Å respectively, and **2-Dy** and **3-Dy** have average W-S distances of 2.192(2) Å and 2.233(5) Å respectively. This expansion in the average W-S distance proceeding from **2-Ln** to **3-Ln** (Ln = Y, Gd, Tb, Dy) is consistent with the expected reduction of d^0 (WS$_4$)$^{2-}$ to d^1 (WS$_4$)$^{3-}$, where the d-orbitals of tungsten, which are antibonding with respect to sulfur, would be populated, resulting in a lowering of the overall bond order for the metalloligand.
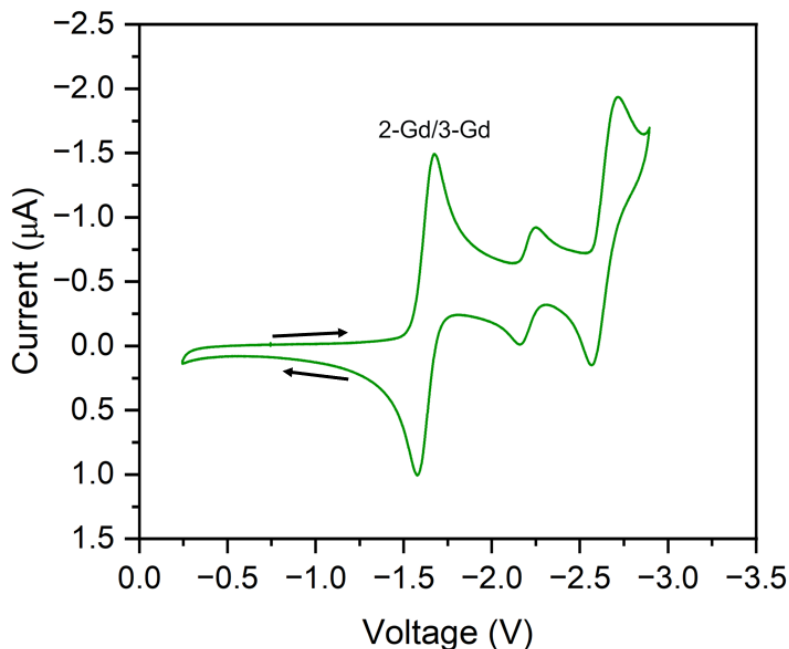
Figure 2.1: Cyclic voltammogram of a 1,2-difluorobenzene solution of **2-Gd**. 0.1 M NBu$_4$PF$_6$ supporting electrolyte. 50 mV/s scan rate. Arrows indicate voltage sweep trajectory. Wave labeled 2-Gd/3-Gd corresponds to the desired one electron reduction.

The average yttrium sulfur distance for **2-Y** and **3-Y** were found to be 2.81(2) Å and 2.75(2) Å respectively. The contraction in the Ln-S distances proceeding from **2-Ln** to **3-Ln** is consistent throughout the series: **2-Gd** and **3-Gd** have average Gd-S distances of 2.84(1) Å and 2.78(1) Å, **2-Tb** and **3-Tb** have average Tb-S distances of 2.82(1) Å and 2.76(1) Å, and **2-Dy** and **3-Dy** have average Dy-S distances of 2.82(1) Å and 2.75(1) Å. This contraction in the average Ln-S distance proceeding from **2-Ln** to **3-Ln** (Ln = Y, Gd, Tb, Dy) is also consistent with the expected reduction of (WS$_4$)$^{2-}$ to (WS$_4$)$^{3-}$, as the trianion would be expected to have a stronger electrostatic interaction

9

with the bound Ln^{3+} ions. The relevant bond lengths for all **2-Ln** compounds are given in Table S2.3, while those for **3-Ln** are given in Table S2.4.

Diffuse reflectance spectra were collected on powders of the **3-Ln** (Ln = Gd, Tb, Dy) compounds for direct comparison with the spectral characteristics of the corresponding thiomolybdate structural analogues from previous studies. A sharp near-infrared band centered around 5500 cm^{-1} was observed for all three of the thiotungstate derivatives (Figure 3). This band shifted in energy and relative intensity as a function of the lanthanide ion, which suggested that lanthanide centered orbitals were involved in the transition. In the **1-Ln** (Ln = Gd, Tb, Dy) thiomolybdates, this feature was also observed and was consistent with a metal-metal charge transfer (MMCT) from the Mo^{5+} 4d orbitals to the vacant 5d orbitals of the connected lanthanide ions.[11]

A broader weak feature in the NIR-Visible region, which was absent in the spectra for **1-Ln** compounds, was observed in the **3-Ln** spectra. This weak feature was also consistent with an MMCT given that its intensity and location also depended on the identity of the lanthanide ion. Low energy visible transitions located at ~11000 cm^{-1} in the **3-Ln** spectra were similar to those identified as transition metal d–d transitions observed in the **1-Ln** compounds, consistent with the d^1 $(WS_4)^{3-}$ assignment obtained in the crystal structure analysis. Finally, the visible region of the spectrum was found to be dominated by two broad absorbances which were both assigned as overlapping ligand to metal charge transfer (LMCT) bands. This spectral assignment is consistent with the available literature spectra of $(WS_4)^{2-}$ containing salts, which exhibited similar broad LMCT transitions within the high-frequency visible region.[12] The full deconvolution of the three spectra for **3-Ln** (Ln = Gd, Tb, Dy) are given in Figure S2.9, Figure S2.10, Figure S2.11 while the fit parameters of each deconvolution are given in Table S2.5, Table S2.6, and Table S2.7 respectively.
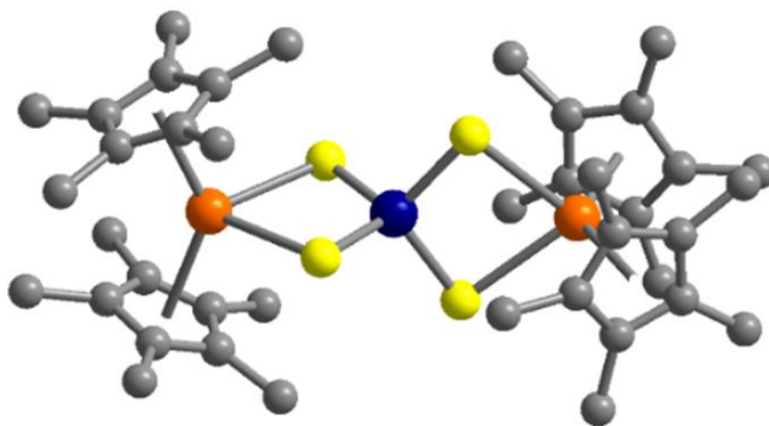
Figure 2.2: X-ray crystal structure of **3-Gd** anion $[(Cp*_2Gd)_2(\mu\text{-}WS_4)]^-$. Hydrogen atoms and proximal $CoCp*_2^+$ have been omitted for clarity. Dark blue, W; orange, Gd; grey, C; yellow, S.

The dc magnetic susceptibility of **2-Gd** was characterized in order in order to obtain a point of comparison with the **3-Gd** results. Indeed, the room temperature susceptibilities of **2-Gd** were consistent with two Gd^{3+} ions with no evidence of a magnetic exchange interaction between the two ions (Figure 2.4a). This was expected, given the internuclear separation of the lanthanide ions and their core like 4f orbitals.

To characterize the exchange interaction between the lanthanides and the thiotungstate trianion in the **3-Ln** (Ln = Gd, Tb, Dy) congeners, dc susceptibility was measured from 2–300 K. The $\chi_M T$ value for **3-Gd** measured at 300 K was 17.2 $cm^3 \cdot K/mol$, which was within the range of expected values for two S = 7/2 centers and one S = ½ center (Figure 2.4b). The experimental value

$17.2 \ \text{cm}^3 \cdot \text{K/mol}$ was slightly higher than the expected value of $16.1 \ \text{cm}^3 \cdot \text{K/mol}$, which indicates a ferromagnetic exchange interaction present between the $S = 7/2$ and $S = 1/2$ centers. The measured temperature dependence of the dc susceptibility of **3-Gd** revealed a gradual increase in $\chi_M T$ with decreasing temperature, which is further indication of a ferromagnetic exchange interaction between the gadolinium sites and the unpaired electron on the bridge.

Fitting the data to the exchange Hamiltonian given in Equation 2.1, a fit consistent with two $S = 7/2$ centers and one $S = 1/2$ center was obtained with a $J_{\text{Gd-W}}$ of $+12.3(9) \ \text{cm}^{-1}$ which is lower than that observed for the **1-Gd** ($J_{\text{Gd-Mo}} = +16.1 \ \text{cm}^{-1}$).[11] This positive exchange interaction along with the observed MMCT bands located in the near IR region of the diffuse reflectance spectra suggest that the magnetic exchange interaction is dominated by an analogous double exchange interaction[13], which proceeds through donation from a singly occupied 5d orbital on the thiotungstate into a vacant low lying 5d orbital of gadolinium.
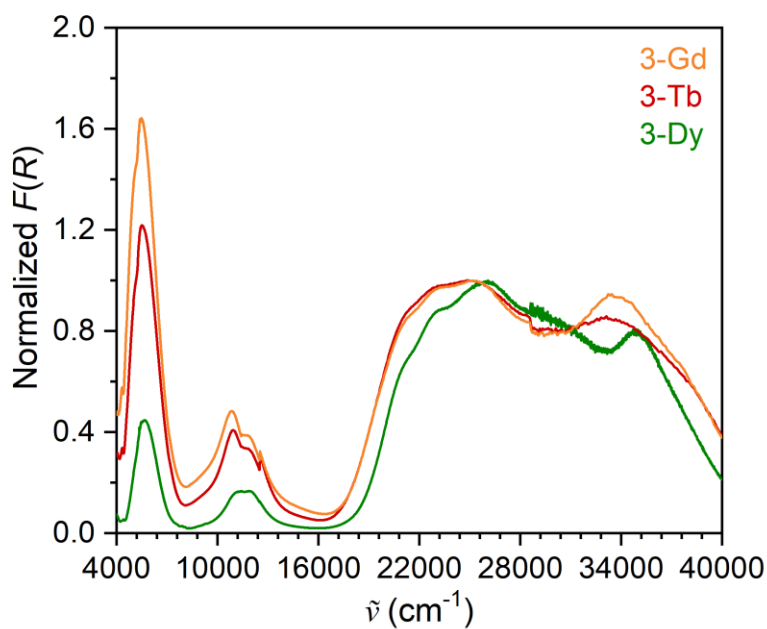
Figure 2.3: Diffuse reflectance spectra of powders of **3-Ln** (Ln = Gd, Tb, Dy). The Kubelka-Munk conversion of reflectance $F(R)$ was measured in place of absorbance. Each spectrum was normalized with respect to the LMCT peak located at $\sim 25600 \ \text{cm}^{-1}$ to aid in direct comparison. BaSO$_4$ was used as background material.

The dc susceptibility at 300 K of **3-Tb** was measured at $24.6 \ \text{cm}^3 \cdot \text{K/mol}$ under an applied field of 0.1 T (Figure S2.14). This room-temperature susceptibility value is consistent with two $J = 6 \ \text{Tb}^{3+}$ ions coupled ferromagnetically with a single unpaired electron. The temperature dependence of the $\chi_M T$ plot is also indicative of ferromagnetic exchange, as the $\chi_M T$ value increases as temperature decreases from 300 K. For **3-Dy**, the 300 K value of $\chi_M T$ was found to be $23.8 \ \text{cm}^3 \cdot \text{K/mol}$, consistent with two $J = 15/2 \ \text{Dy}^{3+}$ ions coupled ferromagnetically with an unpaired electron (Figure S2.18). The $\chi_M T$ value of **3-Dy** also monotonic increases in as temperature decreases from 300 K, which is further indication of a ferromagnetic exchange interaction.

The magnetization of **3-Ln** (Ln = Tb^{3+}, Dy^{3+}) were measured with respect to a swept applied field in an effort to observe magnetic hysteresis. Consistent with observations of the **1-Ln**

structural analogues, we observed weakly hysteretic behavior for **3-Tb** at 2 K (Figure 2.5a) and no hysteresis for **3-Dy** at 2 K (Figure 2.5b). To evaluate the rapid relaxation at low temperature, the zero-field ac susceptibility for **3-Tb** (Figures S2.16 and S2.17) was measured. The out of phase ac susceptibility was dominated by a broad distribution of relaxation processes. Relaxation times were extracted using CCFit2[14] with the generalized Debye model and are ploted as a function of inverse temperature in Figure 2.6a. The temperature dependence of the relaxation times was fit to Equation S2.2. The temperature dependence of the resulting ensemble of relaxation times was characterized as Raman relaxation for the majority of the temperature window. Onset of Orbach relaxation was only observed near the high-frequency limit of the instrument at zero field, however, it is uncertain that these points truly represent Orbach relaxation or a secondary Raman process. This is reflected in the quality of the fit parameters, as the U_{eff} value of 70 cm^{-1} is within error of zero.
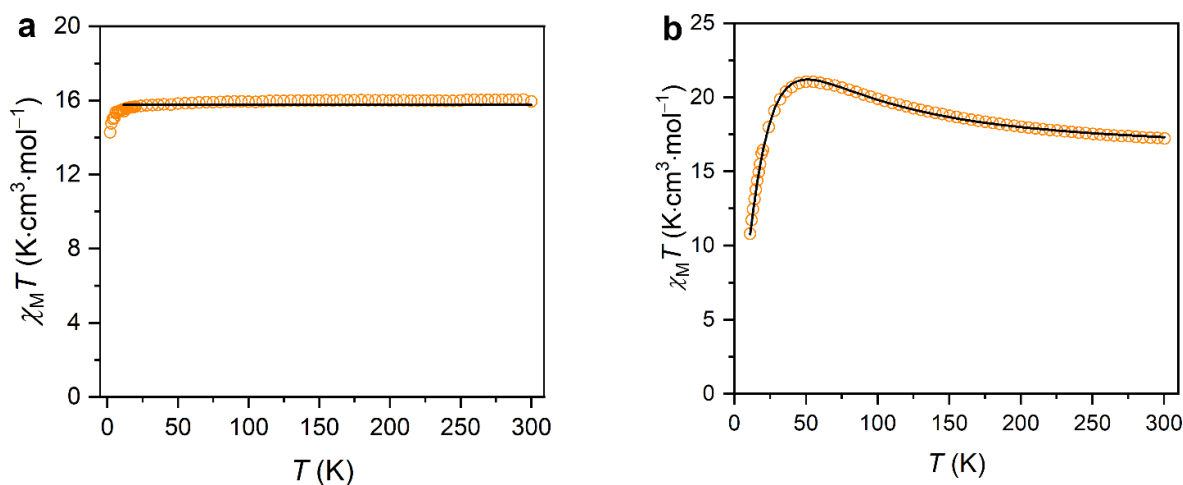
Figure 2.4: a) dc magnetic susceptibility of **2-Gd** measured under a 0.1 T applied field. Solid line corresponds to expected 300 K $\chi_M T$ value for two $S = 7/2$ ions. b) dc magnetic susceptibility of **3-Gd** measured under a 7 T applied field. Open Circles correspond to experimental data. Solid line corresponds to fit to an exchange Hamiltonian. (Equation 2.1) with $J_{\text{Gd-W}} = +12.3(9)$ cm^{-1}. A 7 T applied field was necessary as the low field data was affected by strong temperature independent paramagnetism (Figure S2.13).

$$\hat{H} = -2J_{Gd-W}\left(\vec{S}_W \cdot \left(\vec{S}_{Gd1} + \vec{S}_{Gd2}\right)\right) + \mu_B g\left(\vec{S}_{Gd1} + \vec{S}_{Gd2} + \vec{S}_W\right) \cdot \vec{B} \qquad \text{(Equation 2.1)}$$

The zero-field ac susceptibility for **3-Dy** was found to have a major relaxation process and a minor process with a broad distribution of relaxation times. This necessitated the use of a dual process Debye model. The minor process, given its large α values could not yield meaningful fit parameters however the major process was found to fit to a similar Orbach/Raman scheme (Equation S2.2) to that of **3-Tb,** with somewhat longer relaxation times across the temperature window (Figure 2.6b). The lack of hysteresis for **3-Dy** can therefore be ascribed to this fast minor relaxation channel. Again, the Orbach region occupies a small high temperature region, and the observed U_{eff} value of 100 cm^{-1} is within error of zero.
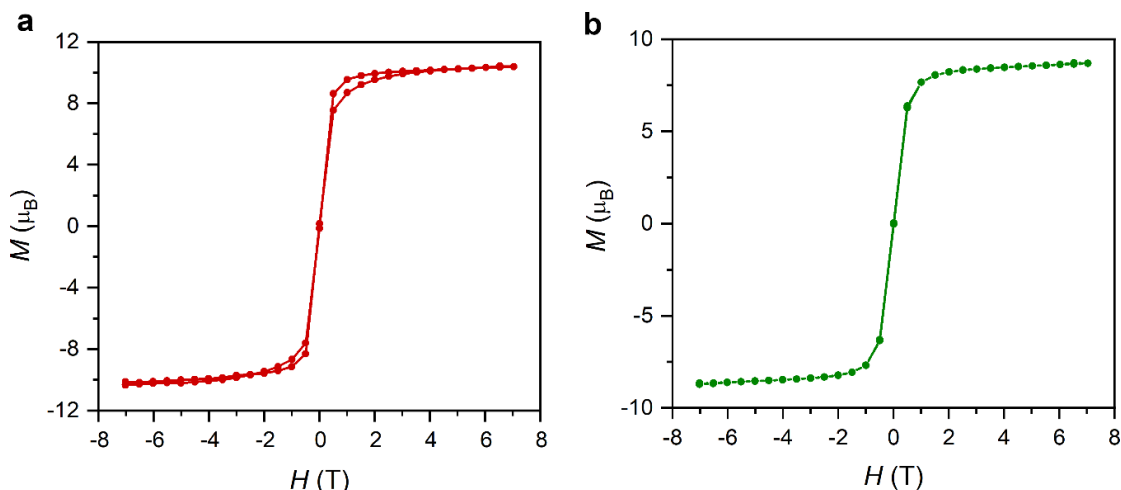
Figure 2.5: a) Variable field magnetic hysteresis for **3-Tb** with average field sweep rate of 8(1) mT/s. b) Variable field magnetic hysteresis for **3-Dy** with average field sweep rate of 9(2) mT/s. Both measurements carried out at 2 K.
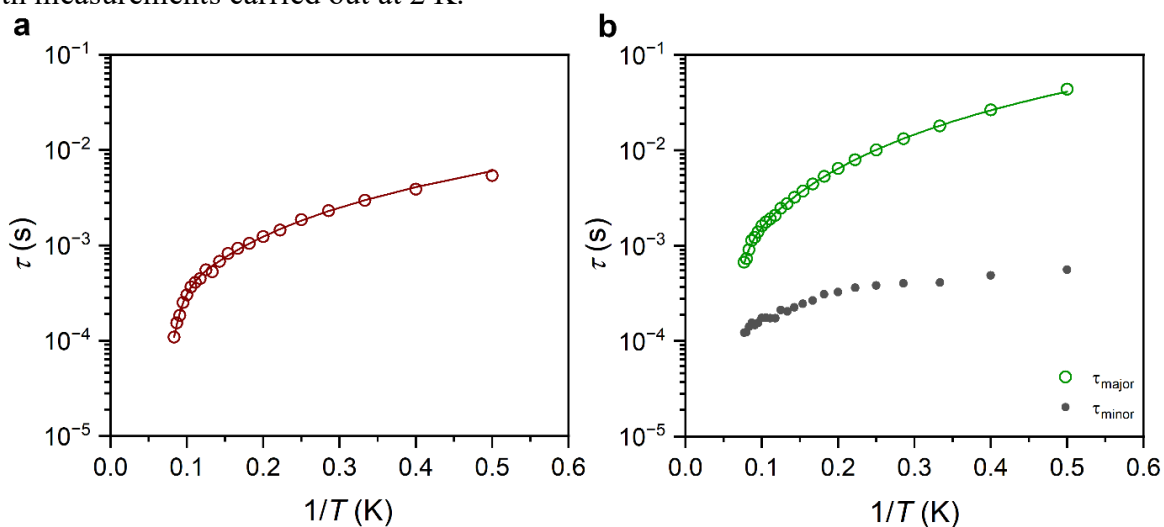
Figure 2.6: a) Arrhenius plot for **3-Tb**. Solid line corresponds to fit to Equation S2.2. Fit parameters: $U_{eff} = 70(100)$ cm^{-1}, $\tau_0 = 10^{-9(7)}$, $C = 10^{1.7(7)}$, $n = 1.7(9)$. b) Arrhenius plot for **3-Dy**. Solid line corresponds to fit to Equation S2.2. Fit parameters: $U_{eff} = 100(300)$ cm^{-1}, $\tau_0 = 10^{-10(10)}$, $C = 10^{0.8(5)}$, $n = 2.0(6)$.

The lack of observed hysteresis and rapid ac timescale relaxation was expected for **3-Tb** and **3-Dy** based on the previous measurements on **1-Tb** and **1-Dy**.[11] The local quantization axes of each lanthanide fragment are fixed at approximately 90° to one another by the tetrahedral bridge. The formation of an anisotropic giant spin ground state requires for both coupled fragments to either share a quantization axis or have parallel quantization axes. In the orthogonal arrangement, if both centers are coupled in a giant spin configuration, one of the lanthanide fragments must necessarily be magnetized about its local 'hard' axis, as dictated by the local crystal field established by the Cp* ligands. This leads to the mixture of excited M_J states into the coupled ground state, which facilitates fast through barrier relaxation. To better utilize magnetic exchange, a single ion magnet fragment which possesses a local easy axis collinear to the metal containing axis of the molecule should be synthesized moving forward.

The tungsten containing **3-Gd** exhibited a weaker exchange interaction than that observed in molybdenum containing **1-Gd**. The tetrathiometallates in both the **1-Ln** and **3-Ln** series are Jahn-Teller unstable and undergo a decent in symmetry from T_d to D_{2d} point group symmetry (Figure 2.7a). This results in the formation of an a_1 orbital in the crystal field region which can mix with the vacant 5s or 6s orbitals, lowering its energy. The relativistically stabilized 6s orbital of WS_4^{3-} was hypothesized to have greater mixing with the singly occupied a_1 orbital of the crystal field region, lowering its energy with respect to the lanthanide $5d_{z^2}$ and increasing the energy separation between the thiometallate donor orbital and lanthanide 5d acceptor orbitals. This would explain the decrease in the magnitude of J going from Mo to W, as in the case of double-exchange, J has an inverse relationship with the energy separation of the participating donor and acceptor orbitals.[15] To substantiate this picture, a DFT optimization using the ORCA[16] software package was performed on **3-Y** to determine the s orbital character of the ground state SOMO as well as the amount of spin delocalization throughout the complex. As the diffuse reflectance spectroscopy demonstrated, the frontier orbitals of **3-Ln** are all $(WS_4)^{3-}$ centered, meaning that the simplified electronic structure of **3-Y** should be representative of the electronic structure for the whole series.
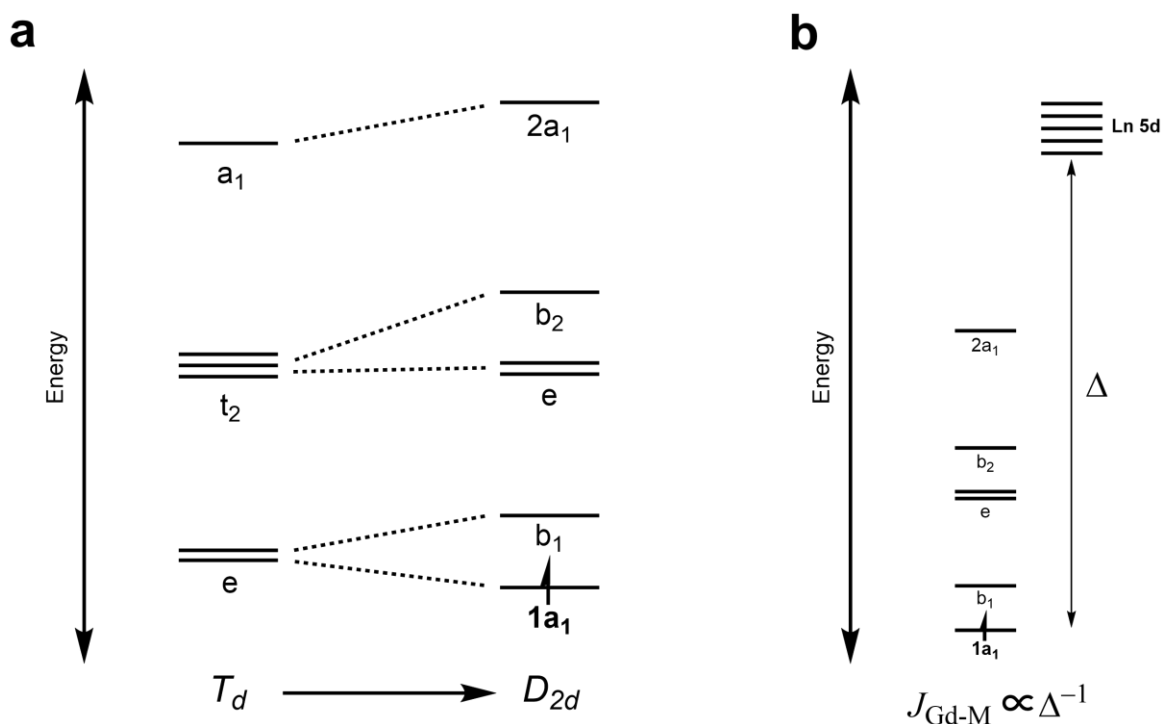
Figure 2.7: a) Decent in symmetry from T_d to D_{2d} for the $(MS_4)^{3-}$ (M = Mo, W) crystal field region in **1-Ln** and **3-Ln**. High energy a_1 orbital corresponds to 5s for Mo or 6s for W. b) Illustration of the inverse relationship between the donor acceptor orbital energy separation (Δ) and $J_{\text{Gd-M}}$.

After first optimizing the solid-state geometry of **3-Y** using effective core potentials to model the core electron density of the yttrium atoms and tungsten, the all-electron ground-state calculation was performed using the ZORA[17] Hamiltonian and associated basis sets (see Computational Methods for details).[18] A simplified scheme was used for the decamethylcobaltocenium cation in these calculations in order to address SCF convergence difficulties while still roughly simulating

the polarizing influence of the $[CoCp*_2]^+$ cation on the geometry of the anion. Additionally, this approximation served to eliminate the possibility of the unpaired electron delocalizing onto $[CoCp*_2]^+$ within the calculated ground state. The atoms of the $[CoCp*_2]^+$ were optimized independently starting from its solid-state coordinates, and Mulliken analysis[19] was subsequently performed on the optimized wavefunction. The optimized geometry and the Mulliken charges calculated for each atom are given in Table S2.8. The bridged thiotungstate anion was then subsequently optimized with point charges corresponding to the charge values taken from Mulliken population analysis located at each of the optimized coordinates of the cation.
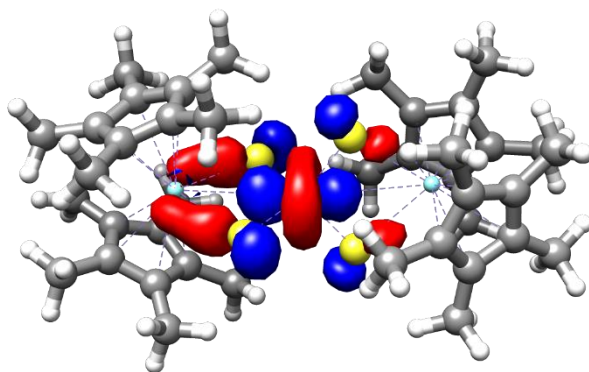
Figure 2.8: Contour plot of the singly occupied Kohn-Sham molecular orbital of gas phase optimized geometry for **3-Y**. Contour value of 0.04 used. Proximal $CoCp*_2^+$ omitted for clarity.

The reduced Mullkien spin population values of **3-Y** (Table S2.9), suggest that the unpaired electron is mostly localized on the thiotungstate fragment and that it occupies an orbital with more tungsten 6s character than **1-Y** has Mo-5s character (Table S2.10). The tungsten s spin population value in **3-Y** was 0.44 whereas that for molybdenum in **1-Y** was 0.25. This suggests that the degree of transition metal s orbital mixing into the SOMO (pictured in Figure 2.8) had increased as a result of exchanging molybdenum for tungsten, which supports the earlier hypothesis that the relativistic contraction of the 6s orbtials on tungsten may impact the magnetic properties.

2.3 Conclusion and Outlook

The synthesis and subsequent comparison of the magnetic properties of 3-Ln (Ln = Y, Gd, Tb, Dy) with those of $[(Cp*_2Ln)_2(MoS_4)]^-$ (Ln = Y, Gd, Tb, Dy) revealed that the strength of the exchange interaction can be controlled by changing the metal center of the thiometallate fragment. We showed that even subtle changes in the electronic structure and spin distribution derived from relativistic perturbations on the electronic structure of the bridging moiety can measurably impact the exchange interaction. The transition metal in tetrathiometallate bridges can therefore serve as a tuning handle for magnetic exchange. We expect that changing the oxidation state of the bridge as well as switching to transition metal centers with different d-electron counts should produce pronounced changes in the exchange interaction for this reason.

2.4 Experimental Methods

Geneal Details

All manipulations were performed under either N_2 or Ar with rigorous exclusion of air and water using standard Schlenk techniques or glovebox techniques. THF, Toluene, Et_2O, and benzene were dried and saturated with Argon on a JC Meyer solvent system and were subsequently stored over activated 4 Å molecular sieves prior to use. Celite was dried 150 °C for a minimum of 48 hr under vacuum prior to use. $Cp*_2Ln(BPh_4)$ (Ln = Y, Gd, Tb, Dy) starting materials described were prepared as detailed in the literature.[20] $(PPh_4)_2WS_4$ preparation on reported literature proceedure.[21] $CoCp*_2$ was purchased from Millipore-Sigma. Prior to use, $CoCp*_2$ was extracted into ether, filtered through celite, and isolated under vacuum. Air-free elemental analyses were performed at the UC Berkeley Microanalytical facility. H^1 NMR spectra were collected at the UC Berkeley NMR facility on an AVB-400 MHz spectrometer. Diffuse Reflectance measurements were performed on ground powders loosely packed on a bed of $BaSO_4$ under an N_2 atmosphere on a Varian Cary 5000 spectrometer. Spectral deconvolution was performed by least-squares fitting the spectra as a sum of Gaussian line shapes. The Gaussian function used is given in Equation S2.1, where $F(R)_0$ is the baseline, $\tilde{v}_c$ is the peak maximum, w is the peak width at half max, and A is an intensity scaling coefficient. Cyclic voltammograms were collected under Ar using a jacketed platinum working electrode, platinum counter electrode, and a silver reference electrode. NBu_4PF_6 was used as a supporting electrolyte. Voltages were measured with respect to ferrocene as an internal standard.

$$F(R)_{norm} = F(R)_0 + \left(\frac{A}{w\sqrt{\pi/2}}\right) e^{-2\left(\frac{\tilde{v}-\tilde{v}_c}{w}\right)^2} \hspace{2cm} \text{(Equation S2.1)}$$

Synthetic Methods

2-Y $(Cp*_2Y)_2(\mu\text{-}WS_4)$: 196 mg (0.289 mmol) of $Cp*_2Y(BPh_4)$ were suspended in 10 mL of THF. This suspension was quickly added to 72 mg (0.073 mmol) of $(PPh_4)_2WS_4$. The resulting suspension quickly took on a red color with concomitant formation of colorless precipitate. The mixture was allowed to stir at ambient temperature for 12 hours. The suspension was then centrifuged to remove solids then was pumped to dryness under vacuum. The resulting dark orange solids were then dissolved with a minimal amount of benzene. This solution was filtered through celite then dried under vacuum. The solids were extracted with warm toluene (80 °C). The extract was passed through celite to remove undissolved material then moved to a freezer at −30 °C to recrystallize. Yield: 31.4 mg (0.0305 mmol), 42% based on $(PPh_4)_2WS_4$. Calcd. $C_{68}H_{80}Y_2WS_4$ (%): C, 64.7; H, 6.39. Found (%): C, 64.5; H, 6.35. Crystals grown were of suitable quality for x-ray diffraction measurements.

2-Gd $(Cp*_2Gd)_2(WS_4)$: Synthesized using analogous procedure to **2-Y** using 217 mg (0.290 mmol) $Cp*_2GdBPh_4$ and 71 mg (0.072 mmol) $(PPh_4)_2WS_4$. Yield: 25 mg (0.021 mmol), 29% based on $(PPh_4)_2WS_4$. Calcd. for $C_{40}H_{60}Gd_2WS_4$ (%) C, 41.15; H, 5.18; S, 10.98. Found (%): C, 40.77; H, 4.84; S, 11.15.

2-Tb $(Cp*_2Tb)_2(WS_4)$: Synthesized using analogous procedure to **2-Y** using 248.8 mg (0.332 mmol) $Cp*_2TbBPh_4$ and 80.8 mg (0.082 mmol) $(PPh_4)_2WS_4$. Yield: 38 mg (0.032 mmol), 39% based on $(PPh_4)_2WS_4$. Calcd. for $C_{68}H_{80}Tb_2CoS_4$ (%) 41.03 5.17 10.95 Found: C, 41.30; H, 5.08 10.65.

2-Dy $(Cp*_2Dy)_2(WS_4)$: Synthesized using analogous procedure to **2-Y** using 257 mg (0.342 mmol) $Cp*_2DyBPh_4$ and 85 mg (0.086 mmol) $(PPh_4)_2WS_4$. Yield: 30.4 mg (0.0258 mmol), 30%

based on $(PPh_4)_2WS_4$. Calcd. for $C_{40}H_{60}Dy_2WS_4$ (%): C, 41.15; H, 5.18; S, 10.98. Found (%): C, 40.77; H, 4.84; S, 11.15.

3-Y $[CoCp*_2][(Cp*_2Y)_2(\mu\text{-}WS_4)]$: 32 mg (0.031 mmol) of **2-Y** was suspended in 2 mL of THF. A solution of 12 mg (0.036 mmol) of $CoCp*_2$ in 2 mL THF was added to this solution dropwise. The addition was followed by a rapid color change from red to bright orange. The mixture was allowed to stir at ambient temperature for 12 hours. The solution was pumped to dryness under vacuum. The resulting orange solids were then washed with small volumes of ether to remove excess $CoCp*_2$. Crystals suitable for X-ray diffraction experiments could be grown by layering a THF concentrate with two volume equivalents of Et_2O. Yield: 20 mg (0.015 mmol), 47% based on **2-Y**. Calc. for $C_{68}H_{80}Y_2CoWS_4$ (%): C, 64.7; H, 6.39. Found: C, 64.5; 6.35 H.

3-Gd $[CoCp*_2][(Cp*_2Gd)_2(WS_4)]$: Synthesized using analogous procedure to **3-Y** using 35.0 mg (0.0300) mmol) **2-Gd** and 9.6 mg (0.029 mmol) $CoCp*_2$. Yield: 24.4 mg (0.163 mmol), 54.3% based on **2-Gd**. Calcd. for $C_{60}H_{90}CoGd_2WS_4$ (%): C, 48.14; H, 6.06; S, 8.57. Found (%): C, 48.64; H, 5.75; S, 7.71. Diffraction quality crystals of **3-Gd** were grown by the slow cooling of a THF concentrate at −30 °C.

3-Tb $[CoCp*_2][(Cp*_2Tb)_2(WS_4)]$: Synthesized using analogous procedure to **3-Y** using 33.0 mg (0.0281 mmol) **2-Tb** and 9.1 mg (0.028 mmol) $CoCp*_2$. Yield: 14.3 mg (0.0095 mmol), 33.9% based on **2-Tb**. Calcd. for $C_{68}H_{80}Tb_2CoS_4$ (%): C, 48.04; H, 6.05. Found: C, 48.29; H, 6.21. Crystals for diffraction were grown by slow cooling a THF concentrate at −30 °C.

3-Dy $[CoCp*_2][(Cp*_2Dy)_2(WS_4)]$: Synthesized using analogous procedure to **3-Y** using 30.4 mg (0.0258 mmol) **2-Dy** and 8.3 mg (0.025 mmol) $CoCp*_2$. Yield: 25 mg (0.023 mmol), 64% based on **2-Dy**. Calcd. for $C_{60}H_{90}CoDy_2WS_4$ (%): C, 47.81; H, 6.02; S, 8.51. Found (%): C, 47.96; H, 6.00; S, 8.39. Crystals for diffraction were grown by slow cooling a THF concentrate at −30 °C.

X-Ray Crystallography

Prior to measurement, single crystal samples were first removed from mother liquor, and stored under Paratone-N oil at −78 °C beneath an atmosphere of N_2. For compounds **2-Gd** and **2-Tb** samples were mounted on Kapton loops and moved under a nitrogen cyrostream manufactured by Oxford Cryosystems. The diffraction patterns were collected using a Rigaku Dectris diffractometer operating with an Mo rotating anode radiation source. Unit cell determination and spot integration was performed using CrysAlis software. Absorption corrections were applied using the SADABS package.[22] Structural solutions were obtained using Intrinsic Phasing as implemented in ShelXT.[23] Least Squares refinement as implemented in ShelXL was used to refine the structural model.[24] Olex2 was used as a graphical frontend to the aforementioned packages.[25]

For **3-Dy** sample was mounted on a Kapton loop and moved under a nitrogen cyrostream manufactured by Oxford Cryosystems. The diffraction patterns were collected using a using a Bruker QUAZAR diffractometer equipped with a microfocus sealed X-ray source and a Bruker APEX-II detector. Unit cell determination and spot integration was performed using SMART and SAINT respectively as implemented in the Bruker APEX II suite.[26–28] Absorption corrections were applied using the SADABS package.[22] Structural solutions were obtained using Intrinsic Phasing as implemented in ShelXT.[23] Least Squares refinement as implemented in ShelXL was used to

refine the structural model.[24] Olex2 was used as a graphical frontend to the aforementioned packages.[25]

For all other samples crystals were mounted onto MiTeGen 10 μm loops and moved under a nitrogen cryostream supplied by Oxford Cryosystems. The diffraction patterns were collected using synchrotron radiation at beamline 12.2.1 of the Advanced Light Source at the Lawrence-Berkeley National Lab. Unit cell determination and spot integration was performed using SMART and SAINT respectively as implemented in the Bruker APEX III suite.[26–28] Absorption corrections were applied to raw data using the SADABS package.[22] Structural solutions were obtained using Intrinsic Phasing as implemented in ShelXT.[23] Least Squares refinement as implemented in ShelXL was used in model refinement.[24] Olex2 was used as a graphical frontend to the aforementioned packages. Solvent masks were applied using the SQUEEZE tool in Olex2 to model disordered lattice THF equivalents in all **3-Ln** structures.

CheckCIF Report A and B level alerts:
2-Y
PLAT220_ALERT_2_B NonSolvent Resd 1 C Ueq(max)/Ueq(min) Range 6.8 Ratio
> Alert is indicative of incorrect atom assignment for carbon in non-solvent residue. None of the carbon atoms in the structure were incorrectly identified. The alternative formulations including N or O are chemically unreasonable.

Reflection (0,1,0) Omitted as it was obscured by the beamstop.

2-Gd
PLAT213_ALERT_2_B Atom C7A has ADP max/min Ratio ..... 4.2 Prolat
> Cp* Methyl carbon found to have large ADP ratio. A second disordered position had already been modeled. As there was no third disordered position that could be clearly resolved and none of the other methyl carbons had disorder, the problematic C7A was left alone.

PLAT220_ALERT_2_B NonSolvent Resd 1 C Ueq(max)/Ueq(min) Range 6.6 Ratio
> Alert is indicative of incorrect atom assignment for carbon in non-solvent residue. None of the carbon atoms in the structure were incorrectly identified. The alternative formulations including N or O are chemically unreasonable.

PLAT910_ALERT_3_B Missing # of FCF Reflection(s) Below Theta(Min). 17 Note
> Low angle reflections in several frames were occluded by incoherent scattering from the copper pin supporting the Kapton loop. The frames in which this incoherent scattering was visible had low angle reflections masked for this reason.

2-Tb
PLAT220_ALERT_2_B NonSolvent Resd 1 C Ueq(max)/Ueq(min) Range 6.4 Ratio
> Alert is indicative of incorrect atom assignment for carbon in non-solvent residue.. None of the carbon atoms in the structure were incorrectly identified. The alternative formulations including N or O are chemically unreasonable.

PLAT250_ALERT_2_B Large U3/U1 Ratio for Average U(i,j) Tensor .... 4.1 Note

18

It is unclear what is giving rise to this alert. The elipsoids are not all pointing in the same direction as suggested in the alert reference.

PLAT910_ALERT_3_B Missing # of FCF Reflection(s) Below Theta(Min).   14 Note
Low angle reflections in several frames were occluded by incoherent scattering from the copper pin supporting the Kapton loop. The frames in which this incoherent scattering was visible had low angle reflections masked for this reason.

2-Dy

PLAT220_ALERT_2_B NonSolvent   Resd 1 C   Ueq(max)/Ueq(min) Range   7.3 Ratio
Alert is indicative of incorrect atom assignment for carbon in non-solvent residue. None of the carbon atoms in the structure were incorrectly identified. The alternative formulations including N or O are chemically unreasonable.

PLAT972_ALERT_2_B Check Calcd Resid. Dens. 0.85Ang From W001   -3.47 eA-3
Residual electron density around tungsten position can be ascribed as a Fourier artifact. These artifacts are common in diffraction patterns involving heavy atoms such as tungsten.

PLAT972_ALERT_2_B Check Calcd Resid. Dens. 0.84Ang From W001   -2.89 eA-3
Residual electron density around tungsten position can be ascribed as a Fourier artifact. These artifacts are common in diffraction patterns involving heavy nuclei such as tungsten.

Reflection (0,1,0) Omitted as it was obscured by the beamstop.

3-Gd
No A or B Alerts in report
All omitted reflections were low angle reflections obscured by the beamstop.

3-Tb
No A or B Alerts in report
All omitted reflections were low angle reflections obscured by the beamstop.

3-Dy
PLAT213_ALERT_2_B Atom C1B   has ADP max/min Ratio .....   4.5 prolat
Atom C1B is one part of a rotationally disordered Cp*. Attempts were made to model a third Cp* site however the refinements were unstable. The two position model was used in spite of this warning in order to arrive at a stable solution. Given the high temperature of the measurement (250 K), it is dubious that a third position can be resolved.

3-Y
PLAT971_ALERT_2_A Check Calcd Resid. Dens. 1.27Ang From C01C   4.95 eA-3
PLAT972_ALERT_2_A Check Calcd Resid. Dens. 0.75Ang From C01C   -5.57 eA-3
PLAT972_ALERT_2_A Check Calcd Resid. Dens. 1.76Ang From C00X   -3.99 eA-3
PLAT972_ALERT_2_A Check Calcd Resid. Dens. 0.75Ang From C00W   -3.89 eA-3
PLAT971_ALERT_2_B Check Calcd Resid. Dens. 0.47Ang From C01C   3.02 eA-3

PLAT972_ALERT_2_B Check Calcd Resid. Dens. 0.81Ang From C01R   -2.93 eA-3
PLAT972_ALERT_2_B Check Calcd Resid. Dens. 0.84Ang From C00C   -2.78 eA-3
PLAT972_ALERT_2_B Check Calcd Resid. Dens. 1.27Ang From C00Y   -2.75 eA-3
PLAT972_ALERT_2_B Check Calcd Resid. Dens. 1.52Ang From C01L   -2.55 eA-3

     All of these A and B residual density alerts were due to the presence of a weakly diffracting twin component in the data set given their chemically unrealistic locations with respect to the other components of the model. Attempts to integrate the dataset as a twinned dataset failed as the number and intensity of twin reflections were too limited to obtain a unit cell transformation. CELL_NOW was able to fit nearly all peaks of I>5σ to a single unit cell. The peaks and holes responsible for these alerts equate to 2-3 carbon atoms worth of electron density and the solution/refinement process were otherwise tractable, with the application of restraints. For these reasons, the residual twin density was left unmodeled.

Reflections (1,0,0),(0,2,0),(0,1,1),(0,2,1),(0,0,2),(0,1,2) omitted as they were obscured by beamstop.

SQUID Magnetometry

     All magnetic measurements were carried out on a Quantum Design MPMS-XL SQUID magnetometer. Solid samples were mechanically ground, and flame sealed in evacuated quartz tubes (inner diameter 10 mm) below a layer of eicosane. (Sample Masses: **2-Gd** 11.2 mg, 23.3 mg eicosane; **3-Gd** 9.7 mg, 14.9 mg eicosane; **3-Tb** 8.3 mg, 16.1 mg eicosane; **3-Dy** 9.3 mg, 14.7 mg eicosane). The eicosane was subsequently melted at 40 °C in order to immobilize the sample and to improve thermal conductivity between the sample and the walls of the tube. Diamagnetic corrections were calculated using Pascal's constants.[29] Magnetic dc susceptibility data of 3-Gd was fit using PHI with the spin Hamiltonian given in Equation 2.1.[30] Ac susceptibility data of **3-Tb** was fit using the generalized Debye model as implemented in CCFit2 while the ac susceptibility data of **3-Dy** was fit using the dual process Debye model.[31] The resulting relaxation times were fit as a function of temperature using CCFit2[31] using Equation S2.2.

$$\tau^{-1} = CT^n + \tau_0^{-1}e^{\frac{-U_{eff}}{K_BT}} \qquad \text{(Equation S2.2)}$$

2.5: Computational Methods

     The ORCA computational chemistry package version 4.2.0 was used to carry out all reported DFT calculations.[16] The TPPSh functional[32] was used in all calculations to aid in direct comparison with the results of the tetrathiomolybdate calculations. Reported analyses were carried out on geometry optimized wavefunctions starting from crystallographic positions. The Becke-Johnson damping scheme (D3BJ) was used to aid in correctly modeling non-covalent interactions.[33] CPCM implicit solvation with THF was employed as THF molecules were present in the voids separating ion pairs within the crystal lattice which serve to screen some of the charge associated with the ion pair. Following geometry optimization, a final single point energy calculation was carried out on the optimized geometry using a zeroth-order regular approximation (ZORA) Hamiltonian in order to model the impact of relativistic effects on the final electronic structure.[17] The reported Mulliken population analysis[19] comes from this final single point calculation. For tungsten, basis set SARC-

ZORA-TZVP was used.[34] All yttrium and sulfur atoms were modeled using ZORA-TZP[35], all other atoms were modeled with ZORA-SVP.[18] Auxiliary basis sets for use with the resolution of identity approximations were generated using the AutoAux generation procedure.[36] The decamethylcobaltocenium cation was modeled as a collection of point charges in order to speed up optimization convergence significantly and to prevent SOMO delocalization over the non-covalently bound decamethylcobaltocenium ion. The locations for each point charge were collected from an independently optimized cation geometry in its singlet ground state. This decamethylcobaltocenium geometry was obtained using a TPPSh functional, def2-mSVP[18] basis. The charge sign and magnitudes used in the optimization of **3-Y** were taken from the Mulliken charge population analysis of the final wavefunction from this calculation (Table S2.8). During all geometry optimizations, the resolution of identity approximation was used on coulomb integrals with COSX numerical integration for HF exchange (RIJCOSX)[37]. For the final, all electron single point energy calculation, the resolution of identity approximation was applied to coulomb integrals.

The effective core potential schemes used during the geometry optimizations are as follows: W [Def2-ECP] and Y [Def2-ECP]: Ce-Yb(ecp-28),[38] Y-Cd(ecp-28), Hf-Hg(ecp-46),[39] In-Sb(ecp-28), Tl-Bi(ecp-46),[40] Te-Xe(ecp-28), Po-Rn(ecp-46),[41] Rb(ecp-28), Cs(ecp-46),[42] Sr(ecp-28), Ba(ecp-46),[43] La(ecp-46),[44] Lu(ecp-28).[45]

2.6: Acknowledgments

2.7: References and Footnotes

(1) Gatteschi, D.; Sessoli, R.; Villain, J. *Molecular Nanomagnets*; Oxford University Press, 2007; Vol. 1. DOI: 10.1093/acprof:oso/9780198567530.001.0001.

(2) Chilton, N. F. Molecular Magnetism. *Annu. Rev. Mater. Res.* **2022**, *52* (1), 79–101. DOI: 10.1146/annurev-matsci-081420-042553.

(3) Bogani, L.; Wernsdorfer, W. Molecular Spintronics Using Single-Molecule Magnets. *Nat. Mater.* **2008**, *7* (3), 179–186. DOI: 10.1038/nmat2133.

(4) Atzori, M.; Sessoli, R. The Second Quantum Revolution: Role and Challenges of Molecular Chemistry. *J. Am. Chem. Soc.* **2019**, *141* (29), 11339–11352. DOI: 10.1021/jacs.9b00984.

(5) Woodruff, D. N.; Winpenny, R. E. P.; Layfield, R. A. Lanthanide Single-Molecule Magnets. *Chem. Rev.* **2013**, *113* (7), 5110–5148. DOI: 10.1021/cr400018q.

(6) Swain, A.; Sharma, T.; Rajaraman, G. Strategies to Quench Quantum Tunneling of Magnetization in Lanthanide Single Molecule Magnets. *Chem. Commun.* **2023**, *59* (22), 3206–3228. DOI: 10.1039/D2CC06041H.

(7) Rinehart, J. D.; Fang, M.; Evans, W. J.; Long, J. R. A N23–Radical-Bridged Terbium Complex Exhibiting Magnetic Hysteresis at 14 K. *J. Am. Chem. Soc.* **2011**, *133* (36), 14236–14239.

(8) Demir, S.; Gonzalez, M. I.; Darago, L. E.; Evans, W. J.; Long, J. R. Giant Coercivity and High Magnetic Blocking Temperatures for N2 3− Radical-Bridged Dilanthanide Complexes upon Ligand Dissociation. *Nat. Commun.* **2017**, *8* (1), 2144. DOI: 10.1038/s41467-017-01553-w.

(9) Demir, S.; Jeon, I.-R.; Long, J. R.; Harris, T. D. Radical Ligand-Containing Single-Molecule Magnets. *Coord. Chem. Rev.* **2015**, *289–290*, 149–176. DOI: 10.1016/j.ccr.2014.10.012.

(10) Rinehart, J. D.; Fang, M.; Evans, W. J.; Long, J. R. Strong Exchange and Magnetic Blocking in N 2 3–Radical-Bridged Lanthanide Complexes. *Nat. Chem.* **2011**, *3* (7), 538–542.

(11) Darago, L. E.; Boshart, M. D.; Nguyen, B. D.; Perlt, E.; Ziller, J. W.; Lukens, W. W.; Furche, F.; Evans, W. J.; Long, J. R. Strong Ferromagnetic Exchange Coupling and Single-Molecule Magnetism in MoS43–-Bridged Dilanthanide Complexes. *J. Am. Chem. Soc.* **2021**, *143* (22), 8465–8475. DOI: 10.1021/jacs.1c03098.

(12) McDonald, J. W.; Friesen, G. D.; Rosenhein, L. D.; Newton, W. E. Syntheses and Characterization of Ammonium and Tetraalkylammonium Thiomolybdates and Thiotungstates. *Inorganica Chim. Acta* **1983**, *72*, 205–210. DOI: 10.1016/S0020-1693(00)81720-X.

(13) Anderson, P. W.; Hasegawa, H. Considerations on Double Exchange. *Phys. Rev.* **1955**, *100* (2), 675–681. DOI: 10.1103/PhysRev.100.675.

(14) Reta, D.; Chilton, N. F. Uncertainty Estimates for Magnetic Relaxation Times and Magnetic Relaxation Parameters. *Phys. Chem. Chem. Phys.* **2019**, *21* (42), 23567–23575. DOI: 10.1039/C9CP04301B.

(15) Goodenough, J. B. *Magnetism and the Chemical Bond*; Interscience Publishers New York: New York, 1963.

(16) Neese, F. The ORCA Program System. *Wiley Interdiscip. Rev. Comput. Mol. Sci.* **2012**, *2* (1), 73–78.

(17) Wolff, S.; Ziegler, T.; Van Lenthe, E.; Baerends, E. Density Functional Calculations of Nuclear Magnetic Shieldings Using the Zeroth-Order Regular Approximation (ZORA) for

Relativistic Effects: ZORA Nuclear Magnetic Resonance. *J. Chem. Phys.* **1999**, *110* (16), 7689–7698.

(18) Weigend, F.; Ahlrichs, R. Balanced Basis Sets of Split Valence, Triple Zeta Valence and Quadruple Zeta Valence Quality for H to Rn: Design and Assessment of Accuracy. *Phys Chem Chem Phys* **2005**, *7* (18), 3297–3305. DOI: 10.1039/B508541A.

(19) Mulliken, R. S. Electronic Population Analysis on LCAO–MO Molecular Wave Functions. I. *J. Chem. Phys.* **1955**, *23* (10), 1833–1840. DOI: 10.1063/1.1740588.

(20) Demir, S.; Zadrozny, J. M.; Nippe, M.; Long, J. R. Exchange Coupling and Magnetic Blocking in Bipyrimidyl Radical- Bridged Dilanthanide Complexes. *J Am Chem Soc* **2012**, *134* (2), 18546–18549. DOI: 10.1021/ja308945d.

(21) Letko, C. S.; Panetier, J. A.; Head-Gordon, M.; Tilley, T. D. Mechanism of the Electrocatalytic Reduction of Protons with Diaryldithiolene Cobalt Complexes. *J. Am. Chem. Soc.* **2014**, *136* (26), 9364–9376. DOI: 10.1021/ja5019755.

(22) Sheldrick, G. SADABS, 1996.

(23) Sheldrick, G. M. SHELXT - Integrated Space-Group and Crystal-Structure Determination. *Acta Crystallographica Section A: Foundations of Crystallography*. January 2015, pp 3–8. DOI: 10.1107/S2053273314026370.

(24) Sheldrick, G. M. Crystal Structure Refinement with SHELXL. *Acta Crystallographica Section C: Structural Chemistry*. January 2015, pp 3–8. DOI: 10.1107/S2053229614024218.

(25) Dolomanov, O. V.; Bourhis, L. J.; Gildea, R. J.; Howard, J. a. K.; Puschmann, H. OLEX2: A Complete Structure Solution, Refinement and Analysis Program. *J. Appl. Crystallogr.* **2009**, *42* (2), 339–341. DOI: 10.1107/S0021889808042726.

(26) Bruker. SMART, 2012.

(27) Bruker. SAINT, 2012.

(28) Bruker. APEX III, 2012.

(29) Bain, G. A.; Berry, J. F. Diamagnetic Corrections and Pascal ' s Constants. **2008**, *85* (4), 1–5.

(30) Schrauzer, G. N.; Mayweg, V.-P. Preparation, Reactions, and Structure of Bisdithio-$α$-Diketone Complexes of Nickel, Palladium, and Platinum1, 2. *J. Am. Chem. Soc.* **1965**, *87* (7), 1483–1489.

(31) Reta, D.; Chilton, N. Uncertainty Estimates for Magnetic Relaxation Times and Magnetic Relaxation Parameters. *ChemRXiv* **2019**. DOI: 10.26434/chemrxiv.8863904.v1.

(32) Staroverov, V. N.; Scuseria, G. E.; Tao, J.; Perdew, J. P. Comparative Assessment of a New Nonempirical Density Functional: Molecules and Hydrogen-Bonded Complexes. *J. Chem. Phys.* **2003**, *119* (23), 12129–12137. DOI: 10.1063/1.1626543.

(33) Grimme, S.; Antony, J.; Ehrlich, S.; Krieg, H. A Consistent and Accurate Ab Initio Parametrization of Density Functional Dispersion Correction (DFT-D) for the 94 Elements H-Pu. *J. Chem. Phys.* **2010**, *132* (15), 154104.

(34) Pantazis, D. A.; Chen, X.-Y.; Landis, C. R.; Neese, F. All-Electron Scalar Relativistic Basis Sets for Third-Row Transition Metal Atoms. *J. Chem. Theory Comput.* **2008**, *4* (6), 908–919. DOI: 10.1021/ct800047t.

(35) Canal Neto, A.; Ferreira, I. B.; Jorge, F. E.; de Oliveira, A. Z. All-Electron Triple Zeta Basis Sets for ZORA Calculations: Application in Studies of Atoms and Molecules. *Chem. Phys. Lett.* **2021**, *771*, 138548. DOI: 10.1016/j.cplett.2021.138548.

(36) Stoychev, G. L.; Auer, A. A.; Neese, F. Automatic Generation of Auxiliary Basis Sets. *J. Chem. Theory Comput.* **2017**, *13* (2), 554–562.

(37) Neese, F.; Wennmohs, F.; Hansen, A.; Becker, U. Efficient, Approximate and Parallel Hartree–Fock and Hybrid DFT Calculations. A 'Chain-of-Spheres' Algorithm for the Hartree–Fock Exchange. *Chem. Phys.* **2009**, *356* (1–3), 98–109.

(38) Dolg, M.; Stoll, H.; Preuss, H. Energy-Adjusted Abinitio Pseudopotentials for the Rare Earth Elements. *J. Chem. Phys.* **1989**, *90* (3), 1730–1734.

(39) Andrae, D.; Haeussermann, U.; Dolg, M.; Stoll, H.; Preuss, H. Energy-Adjustedab Initio Pseudopotentials for the Second and Third Row Transition Elements. *Theor. Chim. Acta* **1990**, *77* (2), 123–141.

(40) Metz, B.; Stoll, H.; Dolg, M. Small-Core Multiconfiguration-Dirac--Hartree--Fock-Adjusted Pseudopotentials for Post-d Main Group Elements: Application to PbH and PbO. *J. Chem. Phys.* **2000**, *113* (7), 2563–2569.

(41) Peterson, K. A.; Figgen, D.; Goll, E.; Stoll, H.; Dolg, M. Systematically Convergent Basis Sets with Relativistic Pseudopotentials. II. Small-Core Pseudopotentials and Correlation Consistent Basis Sets for the Post-d Group 16--18 Elements. *J. Chem. Phys.* **2003**, *119* (21), 11113–11123.

(42) Leininger, T.; Nicklass, A.; Küchle, W.; Stoll, H.; Dolg, M.; Bergner, A. The Accuracy of the Pseudopotential Approximation: Non-Frozen-Core Effects for Spectroscopic Constants of Alkali Fluorides XF (X= K, Rb, Cs). *Chem. Phys. Lett.* **1996**, *255* (4–6), 274–280.

(43) Kaupp, M.; Schleyer, P. v R.; Stoll, H.; Preuss, H. Pseudopotential Approaches to Ca, Sr, and Ba Hydrides. Why Are Some Alkaline Earth MX2 Compounds Bent? *J. Chem. Phys.* **1991**, *94* (2), 1360–1366.

(44) Dolg, M.; Stoll, H. A. Savin and H. Preuss. *Theor Chim Acta* **1989**, *75*, 173–194.

(45) Cao, X.; Dolg, M. Valence Basis Sets for Relativistic Energy-Consistent Small-Core Lanthanide Pseudopotentials. *J. Chem. Phys.* **2001**, *115* (16), 7348–7355.

2.8 Supporting Information

Figure S2.1: X-ray crystal structure of 2-Y. Ellipsoids plotted at 50% probability. Free toluene position and H atoms positions omitted for clarity.

Figure S2.2: X-ray Crystal structure of 2-Gd. Ellipsoids plotted at 50% probability. Free toluene position and H atoms positions omitted for clarity.

Figure S2.3: X-ray Crystal structure of 2-Tb. Ellipsoids plotted at 50% probability. Free toluene position and H atoms positions omitted for clarity. Color code: Tb, red; W, dark blue; C, grey; S, yellow

Figure S2.4: X-ray Crystal structure of 2-Dy. Ellipsoids plotted at 50% probability. Free toluene position and H atoms positions omitted for clarity. Color code: Dy, green; W, dark blue; C, grey; S, yellow
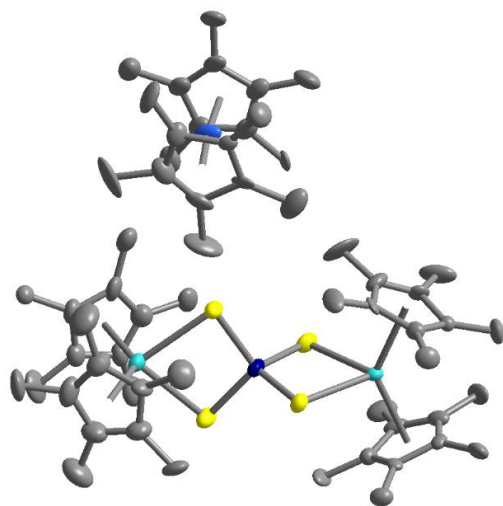
Figure S2.5: X-ray Crystal structure of **3-Y**. Ellipsoids plotted at 50% probability. Free toluene position and H atoms positions omitted for clarity. Y, cyan; W, dark blue; C, grey; S, yellow; Co, light blue
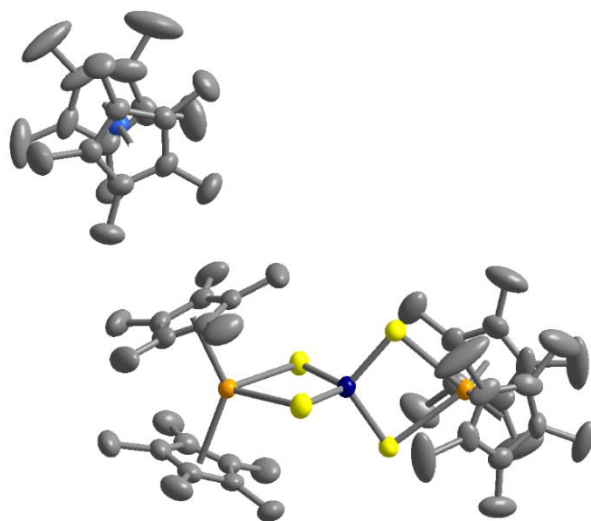
Figure S2.6: X-ray Crystal structure of **3-Gd**. Ellipsoids plotted at 50% probability. H-Atom positions omitted for clarity. Color code: Gd, orange; W, dark blue; C, grey; S, yellow; Co, light blue
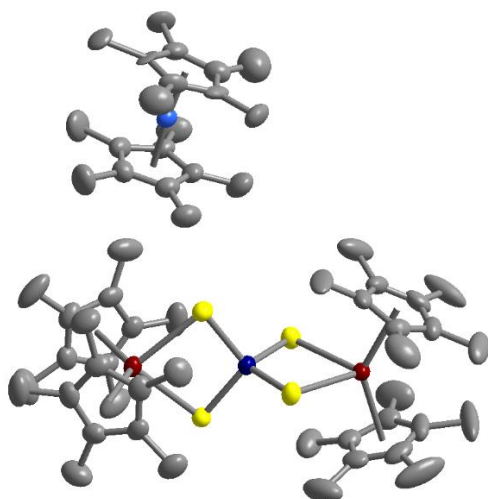
Figure S2.7: X-ray Crystal structure of 3-Tb. Ellipsoids plotted at 50% probability. H-Atom positions omitted for clarity. Color code: Tb, red; W, dark blue; C, grey; S, yellow; Co, light blue
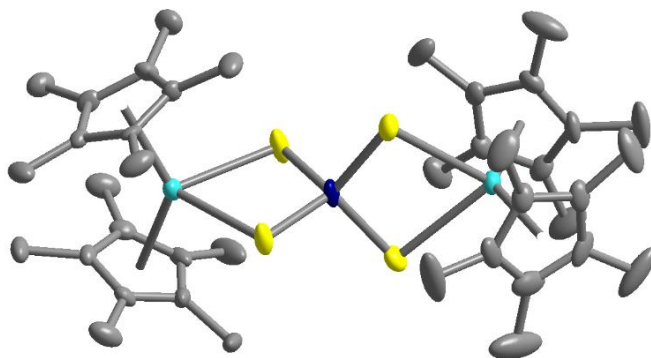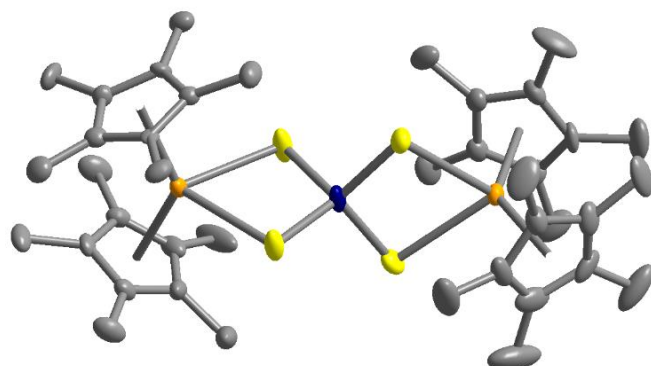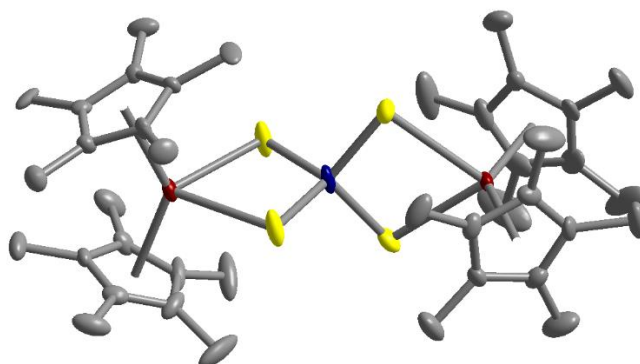

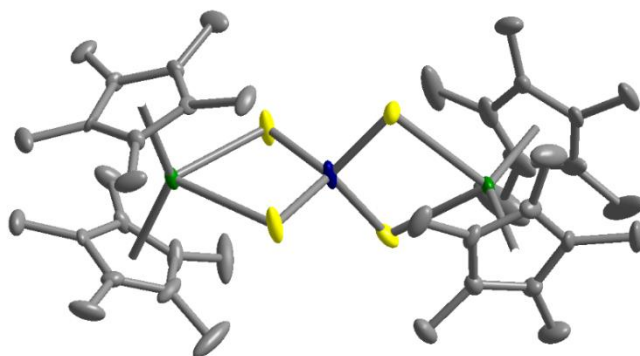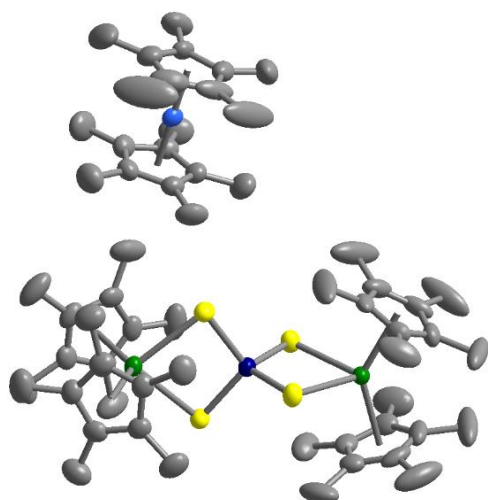**Figure S2.8**: X-ray Crystal structure of 3-Dy. Ellipsoids plotted at 50% probability. H-Atom positions omitted for clarity. Color code: Dy, green; W, dark blue; C, grey; S, yellow; Co, light blue

Table S2.1: Unit cell and refinement parameters for **2-Ln** (Ln = Y, Gd, Tb, Dy)

Sample Identifier	**2-Y**	**2-Gd**	**2-Tb**	**2-Dy**
Empirical formula	$C_{87}H_{128}S_8W_2Y_4$	$C_{87}H_{128}Gd_4S_8W_2$	$C_{87}H_{128}S_8Tb_4W_2$	$C_{87}H_{128}Dy_4S_8W_2$
Formula weight	2153.71	2427.07	2433.75	2448.07
Temperature/K	100	100	100	100
Crystal system	triclinic	triclinic	triclinic	triclinic
Space group	P-1	P-1	P-1	P-1
a/Å	10.604(10)	10.5990(3)	10.5976(2)	10.611(3)
b/Å	13.716(13)	13.7884(5)	13.7360(2)	13.725(3)
c/Å	17.211(16)	17.2607(5)	17.2069(3)	17.194(4)
α/°	108.871(7)	109.193(3)	108.955(2)	109.193(4)
β/°	106.330(10)	106.651(3)	106.431(2)	106.469(3)
γ/°	94.620(8)	94.428(3)	94.5410(10)	94.601(3)
Volume/Å^3	2232(4)	2241.10(13)	2231.45(7)	2225.9(9)
Z	1	1	1	1
ρ_{calc}g/cm^3	1.602	1.798	1.811	1.826
μ/mm^{-1}	3.403	5.7	5.922	6.487
F(000)	1082	1182	1186	1190
Crystal size/mm^3	$0.01 \times 0.005 \times 0.005$	$0.05 \times 0.025 \times 0.025$	$0.05 \times 0.05 \times 0.01$	$0.043 \times 0.021 \times 0.021$
Radiation	synchrotron (λ = 0.7288)	Mo Kα (λ = 0.71073)	Mo Kα (λ = 0.71073)	synchrotron (λ = 0.7288)
2Θ range for data collection/°	2.712 to 54.074	6.372 to 57.868	5.636 to 52.744	2.724 to 64.686
Index ranges	$-13 \leq h \leq 13$, $-17 \leq k \leq 17$, $-21 \leq l \leq 21$	$-14 \leq h \leq 14$, $-18 \leq k \leq 18$, $-23 \leq l \leq 23$	$-13 \leq h \leq 13$, $-17 \leq k \leq 17$, $-21 \leq l \leq 21$	$-15 \leq h \leq 15$, $-20 \leq k \leq 20$, $-25 \leq l \leq 25$
Reflections collected	37554	19597	46992	47640
Independent reflections	9064 [R_{int} = 0.0642, R_{sigma} = 0.0500]	19597 [R_{int} = ?, R_{sigma} = 0.0451]	9102 [R_{int} = 0.0565, R_{sigma} = 0.0409]	14747 [R_{int} = 0.0539, R_{sigma} = 0.0548]
Data/restraints/parameters	9064/141/613	19597/155/613	9102/162/613	14747/155/610
Goodness-of-fit on F^2	1.043	1.026	1.028	1.064
Final R indexes [I>=2σ (I)]	R_1 = 0.0355, wR_2 = 0.0721	R_1 = 0.0519, wR_2 = 0.1473	R_1 = 0.0309, wR_2 = 0.0678	R_1 = 0.0382, wR_2 = 0.0731
Final R indexes [all data]	R_1 = 0.0502, wR_2 = 0.0772	R_1 = 0.0683, wR_2 = 0.1636	R_1 = 0.0381, wR_2 = 0.0704	R_1 = 0.0527, wR_2 = 0.0807
Largest diff. peak/hole / e Å^{-3}	1.08/-0.94	2.29/-1.53	1.76/-1.25	2.79/-3.48

Table S2.2: Unit cell and refinement parameters for 3-Ln (Ln = Y, Gd, Tb, Dy)

	3-Y	**3-Gd**	**3-Tb**	**3-Dy**
Sample Identifier				
Empirical formula	$C_{72}H_{116}CoO_3S_4WY_2$	$C_{76}H_{122}CoGd_2O_4S_4W$	$C_{76}H_{122}CoO_4S_4Tb_2W$	$C_{72}H_{114}CoDy_2O_3S_4W$
Formula weight	1578.48	1785.25	1788.59	1723.65
Temperature/K	100.15	250	250	250.01
Crystal system	monoclinic	triclinic	triclinic	triclinic
Space group	$P2_1/c$	P-1	P-1	P-1
a/Å	10.363(2)	13.529(2)	13.513(3)	13.4899(7)
b/Å	26.642(5)	15.655(3)	15.646(4)	15.6468(8)
c/Å	25.344(5)	18.068(3)	18.053(3)	18.0398(9)
α/°	90	96.237(2)	96.144(3)	96.044(2)
β/°	98.986(2)	97.482(4)	97.479(3)	97.491(2)
γ/°	90	92.950(2)	92.994(3)	93.015(2)
Volume/Å^3	6911(2)	3763.5(10)	3754.1(14)	3745.7(3)
Z	4	2	2	2
ρ_{calc}g/cm^3	1.517	1.575	1.582	1.528
μ/mm^{-1}	2.632	3.856	3.991	3.873
F(000)	3260	1806	1810	1734
Crystal size/mm^3	$0.01 \times 0.01 \times 0.005$	$0.07 \times 0.05 \times 0.035$	$0.086 \times 0.07 \times 0.07$	$0.07 \times 0.07 \times 0.05$
Radiation	synchrotron (λ = 0.6199)	synchrotron (λ = 0.7288)	synchrotron (λ = 0.7288)	MoKα (λ = 0.71073)
2Θ range for data collection/°	3.718 to 44.42	2.348 to 63.756	3.362 to 54.146	2.624 to 52.822
Index ranges	-12 ≤ h ≤ 12, -32 ≤ k ≤ 32, -30 ≤ l ≤ 30	-19 ≤ h ≤ 19, -22 ≤ k ≤ 19, -26 ≤ l ≤ 26	-16 ≤ h ≤ 16, -19 ≤ k ≤ 19, -22 ≤ l ≤ 22	-16 ≤ h ≤ 16, -19 ≤ k ≤ 19, -22 ≤ l ≤ 19
Reflections collected	120593	87790	64840	80315
Independent reflections	13121 [R_{int} = 0.0946, R_{sigma} = 0.0477]	23783 [R_{int} = 0.0632, R_{sigma} = 0.0511]	15269 [R_{int} = 0.0594, R_{sigma} = 0.0493]	15289 [R_{int} = 0.0408, R_{sigma} = 0.0400]
Data/restraints/parameters	13121/579/883	23783/192/739	15269/804/880	15289/85/739
Goodness-of-fit on F^2	1.234	0.962	1.027	1.026
Final R indexes [I>=2σ (I)]	R_1 = 0.1113, wR_2 = 0.2694	R_1 = 0.0338, wR_2 = 0.0803	R_1 = 0.0400, wR_2 = 0.1052	R_1 = 0.0292, wR_2 = 0.0535
Final R indexes [all data]	R_1 = 0.1203, wR_2 = 0.2730	R_1 = 0.0543, wR_2 = 0.0915	R_1 = 0.0608, wR_2 = 0.1160	R_1 = 0.0489, wR_2 = 0.0596
Largest diff. peak/hole / e Å^{-3}	4.81/-4.55	0.64/-0.73	1.13/-1.28	1.35/-0.76

Table S2.3: Relevant Bond Lengths for 2-Ln (Ln=Y,Gd,Tb,Dy) with parenthesized standard uncertainties. All quantities are in Å.

	2-Y	2-Gd	2-Tb	2-Dy
W-S1	2.194(2)	2.191(2)	2.189(1)	2.193(1)
W-S2	2.194(2)	2.188(3)	2.190(1)	2.189(1)
W-S3	2.193(2)	2.188(3)	2.190(1)	2.195(1)
W-S4	2.196(2)	2.194(2)	2.187(1)	2.189(1)
Ln1-S1	2.812(2)	2.839(2)	2.823(1)	2.816(1)
Ln1-S2	2.822(3)	2.845(2)	2.827(1)	2.820(1)
Ln2-S3	2.834(2)	2.850(2)	2.803(1)	2.797(1)
Ln2-S4	2.787(2)	2.819(2)	2.840(1)	2.831(1)
Ln1-Cp1	2.348(2)	2.3805(4)	2.3603(2)	2.3488(5)
Ln1-Cp2	2.343(2)	2.3807(3)	2.3680(2)	2.3507(5)
Ln2-Cp3	2.344(2)	2.3759(4)	2.3600(3)	2.3495(4)
Ln2-Cp4	2.410(2)	2.4532(5)	2.4307(3)	2.4322(5)
Average W-S	2.194(1)	2.190(2)	2.189(1)	2.192(2)
Average Ln-S	2.81(2)	2.84(1)	2.82(1)	2.82(1)
Average Ln-Cp*	2.36(3)	2.40(3)	2.38(3)	2.37(4)

Table S2.4: Relevant Bond Lengths for 3-Ln (Ln=Y,Gd,Tb,Dy) with parenthesized standard uncertainties. All quantities are in Å.

	3-Y	3-Gd	3-Tb	3-Dy
W-S1	2.235(4)	2.237(1)	2.240(2)	2.238(1)
W-S2	2.236(5)	2.2400(9)	2.241(2)	2.238(1)
W-S3	2.223(5)	2.230(1)	2.227(2)	2.2292(9)
W-S4	2.235(5)	2.229(1)	2.230(2)	2.228(1)
Ln1-S1	2.731(4)	2.757(1)	2.746(2)	2.730(1)
Ln1-S2	2.735(4)	2.7680(9)	2.759(2)	2.740(1)
Ln2-S3	2.743(5)	2.784(1)	2.773(2)	2.7556(9)
Ln2-S4	2.776(5)	2.7927(9)	2.779(2)	2.763(1)
Ln1-Cp1	2.386(1)	2.4387(4)	2.4170(4)	2.4039(2)
Ln1-Cp2	2.390(1)	2.4270(3)	2.4103(4)	2.3899(1)
Ln2-Cp3	2.366(2)	2.4149(5)	2.4050(7)	2.3862(2)
Ln2-Cp4	2.393(2)	2.3875(4)	2.4083(6)	2.3765(2)
Co-Cp1	1.652(2)	1.6546(6)	1.6538(9)	1.6485(5)
Co-Cp2	1.652(2)	1.6462(6)	1.6117(9)	1.6515(5)
Average W-S	2.232(5)	2.234(5)	2.234(6)	2.233(5)
Average Ln-S	2.75(2)	2.78(1)	2.76(1)	2.75(1)
Average Ln-Cp*	2.38(1)	2.41(2)	2.410(4)	2.39(1)
Average Co-Cp*	1.652(2)	1.650(4)	1.63(2)	1.650(1)

Figure S2.9. **3-Gd** deconvolved diffused reflectance spectrum. Spectrum was fit as a sum of Gaussian line shapes (Equation S2.1). Fit parameters given in Table S2.3.
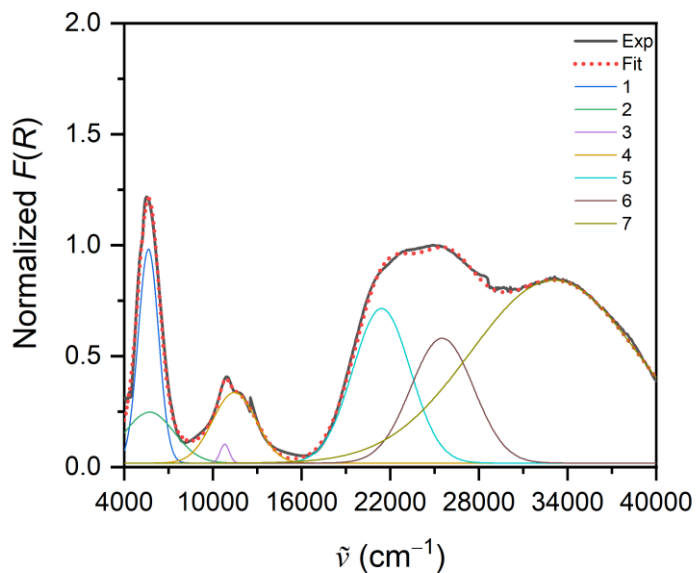
Figure S2.10. **3-Tb** deconvolved diffused reflectance spectrum. Spectrum was fit as a sum of Gaussian line shapes (Equation S2.1). Fit parameters given in Table S2.4.
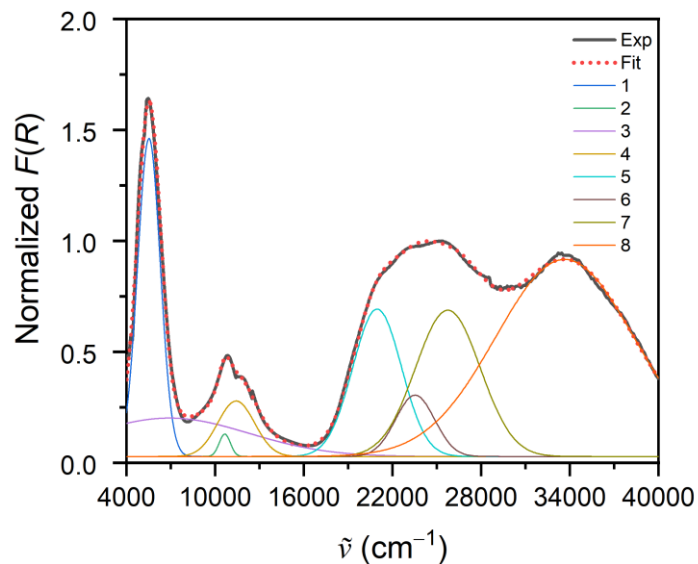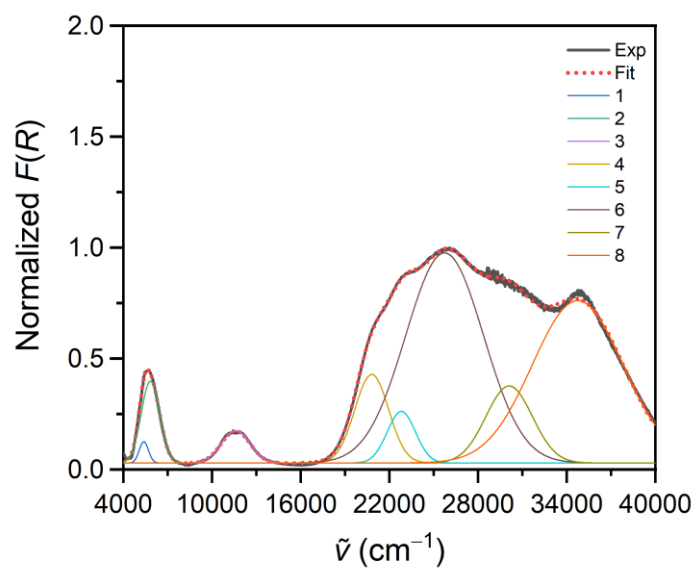
Figure S2.11. **3-Dy** deconvolved diffused reflectance spectrum. Spectrum was fit as a sum of Gaussian line shapes (Equation S2.1). Fit parameters given in Table S2.5.

Table S2.5. **3-Gd** deconvolution fit parameters with parenthesized uncertainties. Fit parameters correspond to Equation S2.1. $R^2 = 0.994$. $\tilde{v}_c$ and w are given in wavenumbers.

Peak Index	1	2	3	4	5	6	7	8
$F(R)_0$	0.03(6)	0.03(6)	0.03(6)	0.03(6)	0.03(6)	0.03(6)	0.03(6)	0.03(6)
$\tilde{v}_c$	5526(2)	10650(30)	6900(400)	11420(40)	21000(400)	23500(400)	25700(800)	33700(100)
w	1533(6)	760(70)	11000(3000)	2500(100)	3300(300)	2600(800)	4400(800)	9300(500)
A	2750(18)	96(10)	2000(1000)	780(60)	2700(700)	1000(1000)	4000(1000)	10000(1000)

Table S2.6. **3-Tb** deconvolution fit parameters with parenthesized uncertainties. Fit parameters correspond to Equation S2.1. $R^2 = 0.995$. $\tilde{v}_c$ and w are given in wavenumbers.

Peak Index	1	2	3	4	5	6	7
$F(R)_0$	0.018(6)	0.018(6)	0.018(6)	0.018(6)	0.018(6)	0.018(6)	0.018(6)
$\tilde{v}_c$	5631(2)	5700(20)	10790(20)	11440(20)	21400(100)	25500(200)	33100(100)
w	1370(10)	3400(200)	620(60)	2930(70)	3900(100)	4200(300)	11300(400)
A	1660(50)	960(50)	66(8)	1170(40)	3400(300)	3000(400)	11600(400)

Table S2.7. **3-Dy** deconvolution fit parameters with parenthesized uncertainties. Fit parameters correspond to Equation S2.1. $R^2 = 0.999$. $\tilde{v}_c$ and w are given in wavenumbers.

Peak Index	1	2	3	4	5	6	7	8
$F(R)_0$	0.0281(5)	0.0281(5)	0.0281(5)	0.0281(5)	0.0281(5)	0.0281(5)	0.0281(5)	0.0281(5)
$\tilde{v}_c$	5383(9)	5829(8)	11596(7)	20800(40)	22810(40)	25740(20)	30110(30)	34750(20)
w	620(30)	1245(7)	1940(2)	2290(5)	1910(50)	5300(100)	3150(50)	6140(20)
A	75(7)	576(8)	354(3)	1140(60)	560(40)	6300(200)	1370(90)	5630(30)
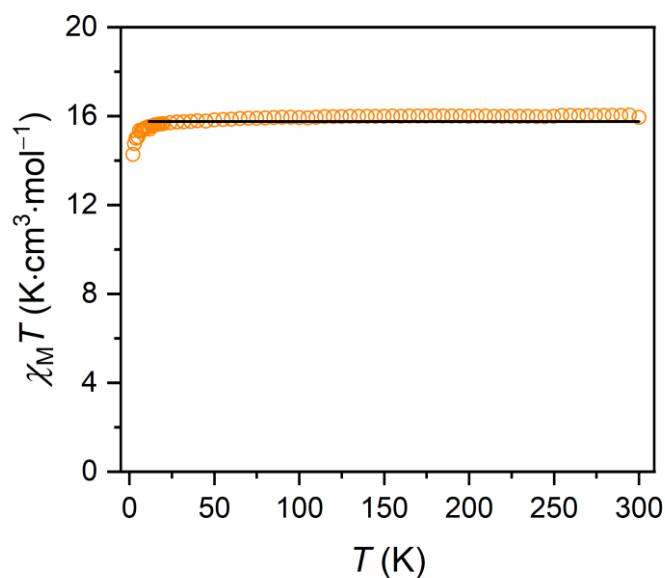
Figure S2.12. Dc susceptibility of **2-Gd** measured under a 0.1 T applied field. Solid line represents calculated $\chi_M T$ product for two $S = 7/2$ Gd^{3+} ions using Equation S2.3.

$$\hat{H} = g\mu_B \left(\vec{S}_{Gd1} + \vec{S}_{Gd2} \right) \cdot \vec{B} \qquad \text{Equation S2.3}$$
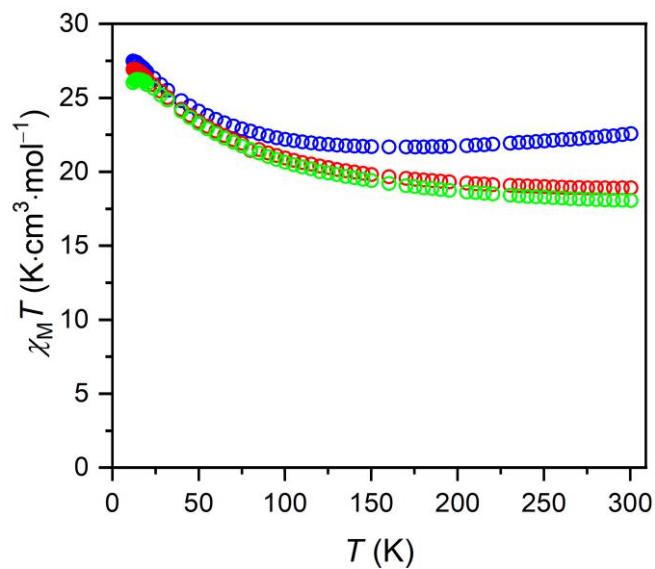
Figure S2.13. Dc susceptibility of **3-Gd** measured under applied fields of 0.1 T(Blue), 0.5 T(red), and 1 T(green)

Figure S2.14. Dc susceptibility of 3-Tb measured under 0.1 T applied field.
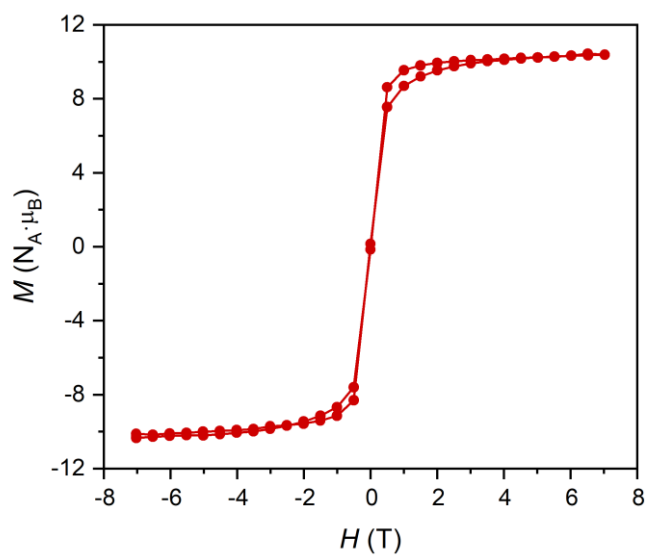
Figure S2.15. Hysteresis loop of 3-Tb measured at $T = 2$ K. Field swept at ---- mT/s
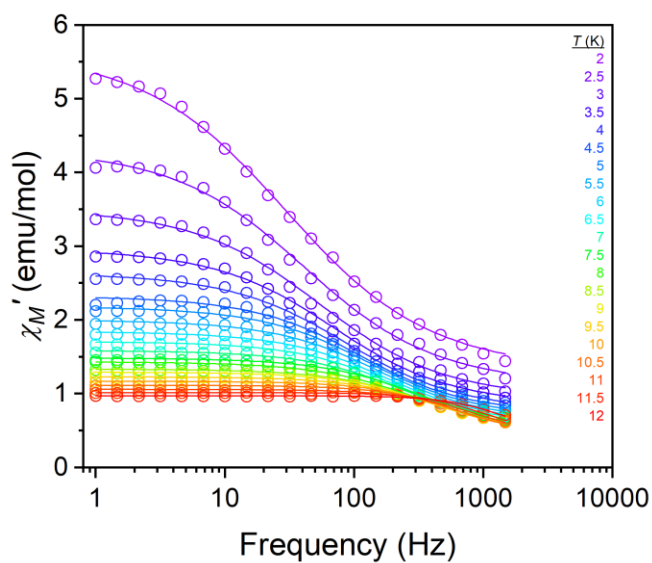
Figure S2.16. Zero-field in-phase ac susceptibility of **3-Tb**. Solid lines correspond to generalized Debye model fits as implemented in CCFit2. Fit parameters are given in Table S2.5.
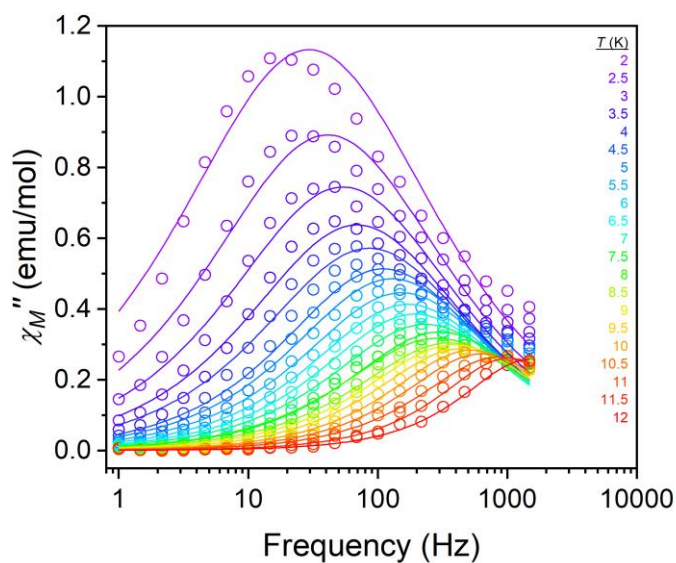
Figure S2.17. Zero-Field out-of-phase ac susceptibility of **3-Tb**. Solid lines correspond to generalized Debye model fits as implemented in CCFit2. Fit parameters are given in Table S2.5.

Table S2.8. Generalized Debye model fit parameters for 3-Tb.

T (K)	τ (s)	τ_{Err} (s)	χ_S (emu/mol)	$\chi_{S\ Err}$ (emu/mol)	χ_T (emu/mol)	$\chi_{T\ Err}$ (emu/mol)	α	α_{err}
1.99986	0.0054	0.0003	1.29	0.05	5.68	0.06	0.39	0.02
2.50025	0.0039	0.0002	1.10	0.05	4.33	0.04	0.36	0.02
2.99988	0.0030	0.0001	0.92	0.04	3.52	0.03	0.34	0.02
3.49944	0.0023	0.0001	0.83	0.03	2.97	0.03	0.31	0.02
3.99907	0.00186	0.00009	0.75	0.03	2.64	0.02	0.31	0.02
4.49905	0.00144	0.00008	0.72	0.03	2.32	0.02	0.28	0.02
4.99869	0.00123	0.00006	0.67	0.03	2.18	0.02	0.27	0.02
5.49859	0.00104	0.00005	0.63	0.03	2.00	0.01	0.27	0.02
5.99832	0.00093	0.00004	0.61	0.02	1.84	0.01	0.25	0.02
6.49855	0.00082	0.00004	0.58	0.02	1.705	0.009	0.23	0.02
6.99789	0.00068	0.00003	0.54	0.02	1.584	0.008	0.24	0.02
7.49791	0.00053	0.00003	0.52	0.02	1.481	0.008	0.22	0.02
7.99833	0.00055	0.00003	0.50	0.02	1.430	0.006	0.24	0.02
8.49772	0.00045	0.00002	0.46	0.02	1.331	0.006	0.22	0.02
8.99779	0.00041	0.00002	0.46	0.02	1.290	0.005	0.20	0.02
9.49814	0.00036	0.00001	0.46	0.02	1.226	0.004	0.18	0.02
9.99863	0.00030	0.00001	0.45	0.02	1.166	0.004	0.15	0.02
10.49709	0.000251	0.000009	0.44	0.01	1.111	0.003	0.13	0.01
10.99394	0.000184	0.000006	0.40	0.01	1.056	0.002	0.13	0.01
11.49125	0.000153	0.000007	0.44	0.02	1.012	0.002	0.06	0.02
11.99994	0.000109	0.000006	0.42	0.02	0.969	0.002	0.04	0.02
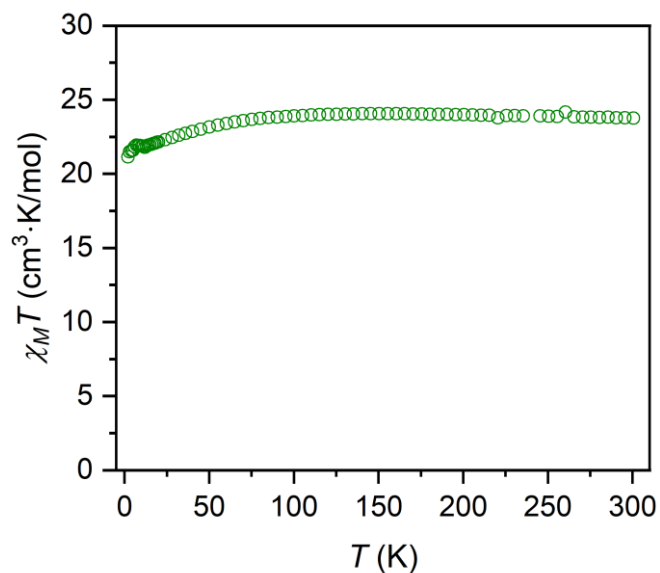
Figure S2.18. Dc susceptibility of **3-Dy** measured under 0.1 T appled field.
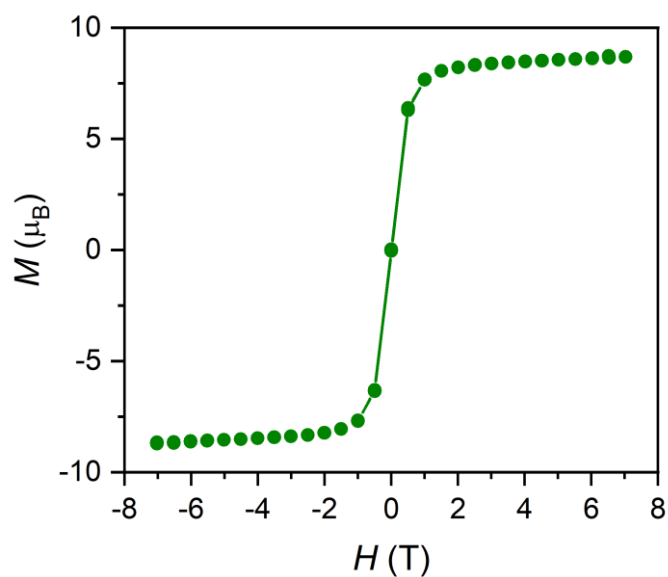
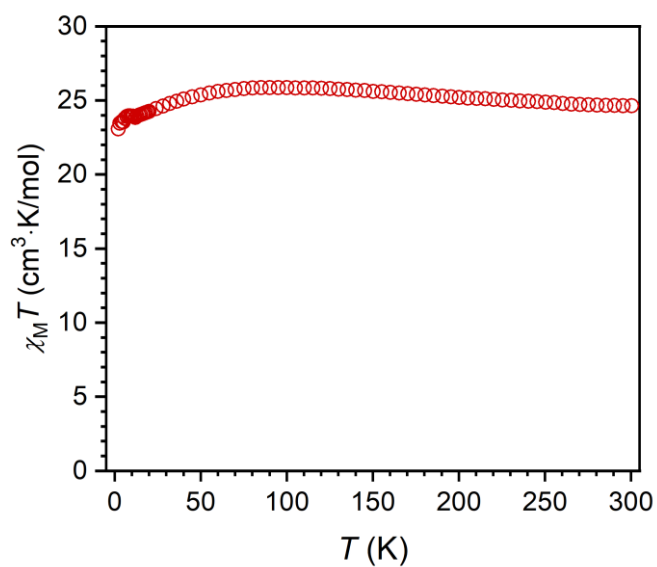**Figure S2.19**. Hysteresis loop of 3-Dy measured at $T = 2$ K. Average field sweep rate ---- mT/s. Solid line is a guide for the eye.
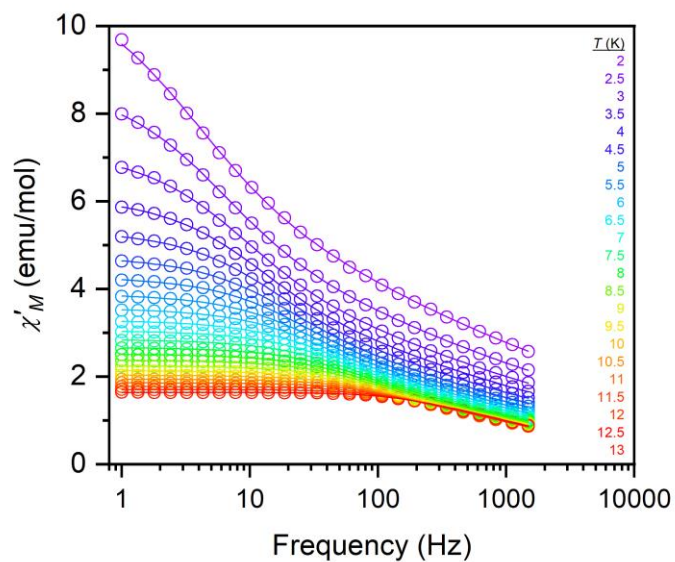
Figure S2.20. Zero-field in-phase ac susceptibility of **3-Dy**. Solid lines correspond to dual-process Debye model fits as implemented in CCFit2.
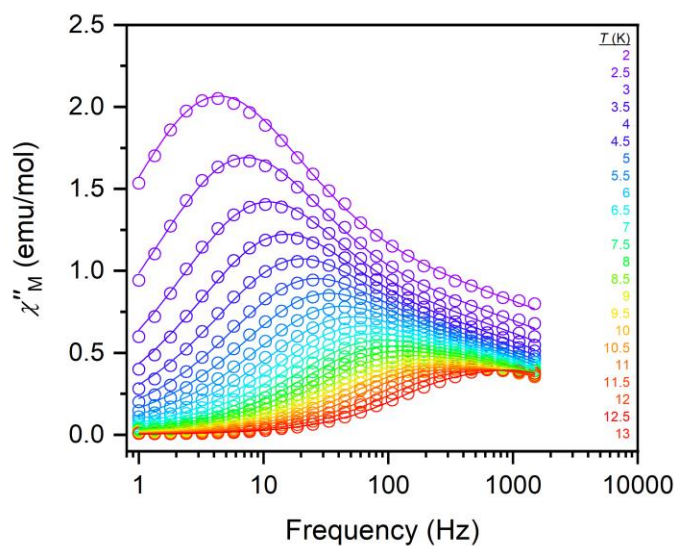
Figure S2.21. Zero-Field out-of-phase ac susceptibility of **3-Dy**. Solid lines correspond to the dual-process Debye model as implemented in CCFit2.

Table S2.9. Ac fit parameters for **3-Dy**. τ_1 corresponds to the observed minor process whereas τ_2 corresponds to the major process.

| T (K)	τ_1 (s)	τ_{1_err} (s)	$\Delta_{\chi 1}$ (emu/mol)	$\Delta_{\chi 1\_err}$ (emu/mol)	α_1	α_{1_err}	τ_2 (s)	τ_{2_err} (s)	$\Delta_{\chi 2}$ (emu/mol)	$\Delta_{\chi 2\_err}$ (emu/mol)	α_2	α_{2_err}	χ_{total} (emu/mol)	χ_{total_err} (emu/mol)
2.00024	0.0006	0.0006	5	3	0.7	0.1	0.0437	0.0009	5	1	0.31	0.05	0.6	0.6
2.49992	0.0005	0.0003	4	1	0.61	0.09	0.0266	0.0005	4.1	0.8	0.27	0.04	0.7	0.3
2.99979	0.0004	0.0002	3.1	0.9	0.56	0.08	0.0180	0.0006	3.4	0.6	0.25	0.03	0.8	0.2
3.49961	0.0004	0.0002	2.6	0.7	0.52	0.08	0.0132	0.0005	2.8	0.5	0.23	0.03	0.8	0.2
3.99935	0.0004	0.0002	2.3	0.6	0.49	0.07	0.0101	0.0005	2.4	0.4	0.22	0.03	0.8	0.1
4.49946	0.0004	0.0001	2.0	0.5	0.46	0.07	0.0080	0.0005	2.0	0.4	0.21	0.03	0.8	0.1
4.99899	0.0003	0.0001	1.8	0.5	0.43	0.08	0.0064	0.0004	1.8	0.4	0.20	0.04	0.72	0.10
5.49909	0.0003	0.0001	1.7	0.4	0.42	0.08	0.0053	0.0004	1.6	0.4	0.19	0.04	0.68	0.09
5.99878	0.00027	0.00009	1.5	0.4	0.40	0.08	0.0044	0.0003	1.4	0.3	0.19	0.04	0.63	0.08
6.49848	0.00025	0.00008	1.4	0.4	0.38	0.08	0.0037	0.0003	1.3	0.3	0.18	0.04	0.61	0.08
6.9987	0.00023	0.00007	1.3	0.4	0.36	0.08	0.0032	0.0003	1.1	0.3	0.17	0.04	0.59	0.08
7.49843	0.00020	0.00006	1.2	0.3	0.34	0.09	0.0028	0.0003	1.1	0.3	0.17	0.04	0.57	0.08
7.99846	0.00021	0.00007	1.2	0.3	0.33	0.09	0.0025	0.0003	0.9	0.3	0.16	0.05	0.57	0.07
8.4984	0.00017	0.00004	1.1	0.3	0.31	0.09	0.0021	0.0002	0.9	0.2	0.16	0.04	0.54	0.07
8.9986	0.00017	0.00005	1.0	0.3	0.30	0.09	0.0019	0.0002	0.8	0.2	0.15	0.04	0.53	0.07
9.49776	0.00018	0.00004	1.0	0.3	0.29	0.08	0.0018	0.0002	0.7	0.2	0.13	0.04	0.52	0.05
9.99791	0.00017	0.00004	1.0	0.2	0.27	0.08	0.0016	0.0002	0.6	0.2	0.12	0.05	0.52	0.05
10.49678	0.00016	0.00003	0.9	0.2	0.26	0.08	0.0014	0.0002	0.6	0.2	0.11	0.05	0.49	0.05
10.99385	0.00015	0.00003	0.9	0.2	0.24	0.08	0.0012	0.0001	0.6	0.2	0.10	0.04	0.49	0.05
11.49108	0.00015	0.00003	0.9	0.2	0.22	0.08	0.0011	0.0002	0.5	0.2	0.06	0.06	0.49	0.05
11.99929	0.00014	0.00003	0.8	0.2	0.19	0.08	0.0009	0.0001	0.4	0.2	0.06	0.05	0.50	0.04
12.49917	0.00012	0.00003	0.8	0.3	0.16	0.10	0.0007	0.0001	0.4	0.2	0.06	0.06	0.49	0.05
12.99942	0.00012	0.00002	0.8	0.2	0.14	0.08	0.0007	0.0001	0.3	0.2	0.03	0.07	0.49	0.04

Table S2.10: TPPSh Optimized coordinates of **3-Y** anion given in Å

Atom	x	y	z
W	9.28413	8.86077	17.28322
Y	10.63	6.047759	15.92367
Y	8.401429	11.77791	18.92699
S	10.96432	7.610615	18.12066
S	7.64913	9.096857	18.80494
S	10.03326	10.92815	16.82258
S	8.541537	7.799449	15.40301
C	10.70258	3.454006	16.58187
C	13.2027	6.204706	15.26198
C	12.74391	7.556005	15.19648
C	14.24774	5.702459	16.22347
H	14.02998	6.011506	17.25338
H	15.24137	6.09613	15.97118
H	14.31645	4.610854	16.21153
C	8.994934	4.688305	17.53173
C	13.27848	8.700362	16.01434
H	12.50402	9.437654	16.24499
H	14.08763	9.211121	15.47248
H	13.68565	8.349452	16.96636
C	12.96985	4.097875	13.72575
H	13.49754	3.535869	14.49824
H	13.64686	4.174624	12.86326
H	12.10876	3.502838	13.40824
C	10.29597	4.152326	17.75783
C	11.9132	2.560743	16.51321
H	12.03969	2.120621	15.52171
H	11.81185	1.734687	17.22923
H	12.83884	3.088113	16.76676
C	11.70314	6.364789	13.51813
C	8.605335	4.34209	16.207
C	9.657578	3.579926	15.61427
C	10.26553	12.96877	20.3458
C	11.82042	7.655108	14.12137
C	10.70882	11.61511	20.2287
C	5.556603	13.8091	20.21394
H	4.504446	14.05037	20.01316
H	6.03217	14.71136	20.59989
H	5.565925	13.05821	21.01248
C	7.188668	14.02786	18.16336
C	6.584799	12.11359	17.02113
C	7.408131	13.27629	16.97091
C	8.146429	5.406022	18.54188
H	8.761055	5.950324	19.26365

H	7.513003	4.699866	19.09806
H	7.491352	6.141321	18.06407
C	11.05592	4.180449	19.05773
H	12.13833	4.16454	18.89048
H	10.80707	3.30683	19.67695
H	10.82061	5.078358	19.63718
C	6.232627	13.32193	18.95793
C	9.555613	2.878396	14.28355
H	9.38887	3.576288	13.45184
H	8.720802	2.163738	14.28163
H	10.46362	2.312554	14.06007
C	10.93842	6.051601	12.25869
H	10.66787	4.990534	12.20888
H	11.54662	6.278086	11.36721
H	10.01582	6.638213	12.18838
C	5.866299	12.13672	18.25232
C	11.19731	8.928562	13.61834
H	10.2153	8.735181	13.17034
H	11.8421	9.40771	12.86516
H	11.04079	9.644263	14.43143
C	9.805623	10.79271	20.95958
C	6.452337	11.08464	15.93494
H	7.410786	10.92912	15.42674
H	5.707465	11.39105	15.18355
H	6.147777	10.11669	16.34505
C	7.729367	15.41295	18.40387
H	7.52433	15.75536	19.42009
H	7.260843	16.13131	17.71869
H	8.810908	15.47273	18.24135
C	8.25756	13.72055	15.80968
H	9.153095	14.25474	16.14575
H	7.700562	14.40366	15.15202
H	8.591263	12.86641	15.21166
C	8.796236	11.63381	21.5205
C	9.103285	12.98556	21.17678
C	11.99937	11.18377	19.58548
H	11.94249	10.15798	19.20913
H	12.82415	11.24095	20.31009
H	12.25639	11.82965	18.74011
C	11.00323	14.17392	19.82051
H	11.29635	14.05305	18.7703
H	11.92386	14.3523	20.39074
H	10.39101	15.07654	19.89644
C	7.668597	11.1463	22.39417
H	7.154416	10.28744	21.94351
H	6.923839	11.92946	22.5636

H	8.034475	10.81999	23.3764
C	8.505771	14.21342	21.80909
H	8.440597	15.05528	21.11626
H	9.135416	14.5353	22.64907
H	7.507728	14.02247	22.20799
C	9.967966	9.331766	21.27373
H	9.000542	8.849472	21.44332
H	10.5686	9.207389	22.18623
H	10.46776	8.791257	20.46582
C	7.253051	4.585718	15.5934
H	6.804809	5.500274	15.99429
H	6.567579	3.750808	15.80231
H	7.325631	4.690057	14.50228
C	4.808976	11.16151	18.69498
H	4.962015	10.17507	18.24724
H	3.806338	11.5133	18.41188
H	4.810988	11.03292	19.78305
C	12.58306	5.472575	14.20423

Table S2.9: TPPSh Optimized CoCp*$_2^+$ coordinates given in Å with Mulliken charges

Atom	x	y	z	Charge
Co	6.353237	7.580417	10.28499	0.063758
C	5.441306	9.137105	9.34117	0.080059
C	5.608456	10.60474	9.573678	-0.6865
H	4.967849	11.15972	8.878891	0.247052
H	6.638337	10.92615	9.400976	0.226034
H	5.319861	10.88973	10.58788	0.22734
C	7.27015	8.854626	7.501928	-0.67875
H	6.820502	9.272093	6.593403	0.244037
H	7.955273	8.058536	7.202333	0.224832
H	7.849699	9.648147	7.97967	0.225489
C	4.470156	8.284268	9.971488	0.078729
C	3.457995	8.718619	10.98516	-0.67941
H	3.848577	9.51482	11.62466	0.225384
H	3.143249	7.888524	11.62181	0.227228
H	2.569304	9.106828	10.47334	0.244259
C	4.617177	6.963277	9.421462	0.074564
C	6.190034	8.344187	8.404188	0.077325
C	6.128515	5.846664	7.61121	-0.68605
H	7.152189	5.981419	7.25536	0.228095
H	5.477159	5.756418	6.734512	0.246239
H	6.073104	4.904417	8.163042	0.225399
C	3.781503	5.764647	9.747479	-0.68839
H	4.352538	4.839124	9.639582	0.227779
H	2.931187	5.712272	9.058477	0.247407
H	3.383532	5.811609	10.76365	0.227996
C	5.679756	7.000727	8.45253	0.081387
C	5.430139	6.385044	13.10117	-0.68074
H	4.822277	5.602993	12.63913	0.225499
H	4.772006	7.204035	13.39917	0.227462
H	5.877639	5.964546	14.00939	0.243956
C	6.514234	6.854058	12.18153	0.080221
C	7.238354	6.025943	11.25552	0.07719
C	7.037256	4.557579	11.05729	-0.68562
H	7.670249	4.00403	11.76052	0.246219
H	7.312854	4.244211	10.0475	0.226616
H	6.001412	4.264234	11.24374	0.227291
C	8.223441	6.843648	10.6007	0.080672
C	9.217985	6.367012	9.58876	-0.67834
H	10.10473	5.975144	10.10091	0.244034
H	9.540323	7.176174	8.929717	0.225896
H	8.807768	5.56316	8.971912	0.225437
C	8.108352	8.178956	11.1236	0.07495
C	8.966283	9.352198	10.76546	-0.68973
H	9.377834	9.260085	9.757889	0.229236

45

H	9.807466	9.418757	11.46513	0.247885
H	8.407777	10.28988	10.82929	0.226493
C	7.052439	8.18503	12.10055	0.079156
C	6.634359	9.365432	12.92104	-0.68451
H	5.59812	9.27847	13.25517	0.228406
H	6.743278	10.29851	12.36245	0.225408
H	7.26891	9.435801	13.81153	0.24563

Table S2.11: Selected Mulliken reduced spin population values for optimized **3-Y** geometry.

3-Y	s	p	d	Total
W	0.044	0.004	0.610	0.662
Y1	0.026	0.029	0.089	0.144
Y2	0.016	0.012	0.024	0.053
S1 & S2	<0.001	0.079	0.026	0.099
S3 & S4	<0.001	0.044	0.014	0.054

Table S2.12: Mulliken reduced spin population values for Optimized **1-Y**.

1-Y	s	p	d	Total
Mo	0.025	0.006	0.750	0.780
Y1	0.027	0.002	0.031	0.060
Y2	0.014	0.006	0.030	0.051
S1 & S2	0.001	0.099	0.009	0.109
S3 & S4	0.001	0.087	0.009	0.097

Chapter 3. Magnetic Exchange and Hysteresis in A Series of Lanthanide-Cobalt Dithiolenes

Vincent, A.H.[a]; Lubert-Perquel, D.[b]; Hill, S.[b]; Long, J.R. *In Preparation.* **2023.**

3.1 Introduction

Single-molecule magnets have been the subject of intense study over the past several decades for their unique physical properties and potential applications in sensing devices, information storage, and data processing.[1–3] The lanthanide ions have since overtaken transition metals in the design of single-molecule magnets as due to their unquenched orbital angular momentum and magnetocrystalline anisotropy, their compounds routinely exhibit large relaxation barriers and high-temperature magnetic hysteresis.[4,5] However, unlike in transition metal compounds, lanthanide compounds typically lack significant magnetic exchange interactions in multinuclear clusters as a result of their radially contracted valence 4f orbitals.[6]

Harnessing strong magnetic exchange to achieve large-moment ground states with high magnetic anisotropy can eliminate fast magnetic tunneling that typically plagues single-molecule magnets.[6] This motivated early efforts to develop 3d−4f single-molecule magnets.[7] Magnetic exchange in these clusters is weak (<1 cm^{-1}), and therefore slow magnetic relaxation of the exchange-coupled system typically occurs at very low temperatures, where most of the thermal population lies within the coupled ground state. The discovery of the N_2^{3-} radical-bridged compounds $[\{[(Me_3Si)_2N]_2(THF)Ln\}_2(\mu\text{-}\eta^2\text{:}\eta^2\text{-}N_2)]^-$ (Ln = Gd, Tb, Dy)[8,9] verified that lanthanides could engage in strong magnetic exchange and that building such coupled molecule was a viable strategy for achieving high-performance single-molecule magnets. In these types of compounds, the diffuse nature of the N_2^{3-} radical spin orbital enables it to engage in antiferromagnetic direct exchange with the core-like lanthanide 4f orbitals. The antiferromagnetic exchange interaction yields a well isolated ferrimagnetically coupled ground state, which was able to persist to higher temperatures.[10]

Previous studies on transition-metal lanthanide exchange were focused on complexes featuring bridging atoms with limited polarizability, which failed to produce any substantial exchange interactions due to their miniscule orbital overlap with the lanthanide 4f and 5d orbitals.[11,12] The recent synthesis and characterization of $[(Cp^*_2Ln)_2(\mu\text{-}MoS_4)]^-$ (Ln = Y, Gd, Tb, Dy)[13] as well as of $[(Cp^*_2Ln)_2(\mu\text{-}WS_4)]^-$ (Ln = Y, Gd, Tb, Dy) discussed in Chapter 1, has demonstrated that metalloligands can support exchange interactions of similar magnitude to those observed for organic radical systems when softer, polarizable donor atoms like sulfur are employed.

While $[(Cp^*_2Gd)_2(\mu\text{-}MoS_4)]^-$ and $[(Cp^*_2Gd)_2(\mu\text{-}WS_4)]^-$ were found to have considerable ferromagnetic exchange between gadolinium and the unpaired electron of the transition metal fragment, it was found that the terbium and dysprosium structural analogues of these compounds only showed minimal butterfly hysteresis at 2 K. This was hypothesized to be a consequence of the bridge geometry, as the tetrahedral metalloligand forced the local quantization axes of each lanthanide ion into an orthogonal arrangement, thus precluding the formation of a coupled ground state with any meaningful magnetic anisotropy. For this reason, square-planar metalloligands with were examined for use as bridging ligands, as these would enforce a parallel arrangement of the quantization axes for bound $[LnCp^*_2]^+$ subunits, thereby preserving single-ion anisotropy in the coupled ground state.

---

[a] Vincent, A. H. carried out all syntheses, crystallographic characterization, magnetometry, and NIR/UV/Vis spectroscopy presented in this chapter.
[b] Lubert-Perquel, D and Hill, S. carried out all of the EPR spectroscopy and analysis presented in this chapter.

Herein, the square-planar, $S = 1/2$ cobalt dithiolene anion $[Co(pdt)_2]^{2-}$ (pdt^{2-} = 1,2-diphenylethylenedithiolate) is shown to bridge two $[LnCp^*_2]^+$ fragments, resulting in a compound which shows open-loop hysteresis. Additionally, a hitherto unobserved pseudo-tetrahedral $S = 1$ $[Co(pdt)_2]^{3-}$ bridging species was isolated and characterized, presumably stabilized by the highly electrophilic environment between the two lanthanocenium cations. Both bridge oxidation states exhibited appreciable Ln–Co ferromagnetic exchange interactions between the lanthanide centers and cobalt, with the interaction strength decreasing only slightly proceeding from $[Co(pdt)_2]^{2-}$ to $[Co(pdt)_2]^{3-}$.

3.2 Results and Discussion

Initial synthetic efforts towards a square planar metalloligand-bridged species were focused on square planar transition metal 1,2-benzenedithiolates, specifically $[Fe(bdt)_2]^{2-}$ and $[Co(bdt)_2]^{2-}$ (bdt^{2-} = 1,2-benzenedithiolate). Iron benzenedithiolate had already been characterized as a free square planar complex anion with tetraphenylarsenate counter cations.[39] A cyanide substituted variant of $[Co(bdt)_2]^{2-}$ which was square planar had been previously reported as well, and so it seemed reasonable that the unsubstituted variant would be an accessible target.[40] Aside from their potential square planar geometry and paramagnetic ground states, these complexes were targeted due to their soft sulfur donors which were hypothesized to facilitate strong magnetic exchange with the bound lanthanides. Compounds of the formula $(Cp^*_2Gd)_2(\mu\text{-}Fe(bdt)_2)$ and $(Cp^*_2Gd)_2(\mu\text{-}Co(bdt)_2)$ were successfully synthesized under mild conditions from the salt metathesis reaction between two equivalents of $Cp^*_2Gd(BPh_4)$ and one equivalent of either $(PPh_4)_2[Fe(bdt)_2]$ or $(PPh_4)_2[Co(bdt)_2]$ respectively (see Experimental for details). Crystallization from layered toluene and hexamethyldisiloxane yielded large, diffraction quality crystals of each compound. Crystallographic characterization of both compounds immediately revealed, however, that the metalloligand had adopted a pseudo-tetrahedral geometry upon metalation with gadolinium (Figures S3.27 and S3.28). As the focus of this effort was to identify square planar metalloligands, the transition metal 1,2-benzenedithiolates were abandoned and a more geometrically stable square planar complex anion was sought. The complex anion $[Co(pdt)_2]^{2-}$ (pdt^{2-} = 1,2-diphenylethenedithiolate) was subsequently identified as a candidate.
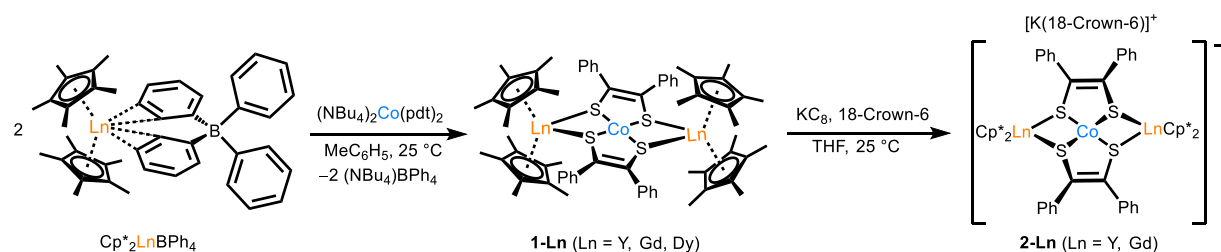
Scheme 3.1. Synthetic route to $(Cp^*_2Ln)_2(\mu\text{-}Co(pdt)_2)$ **1-Ln** (Ln = Y, Gd, Tb, Dy) and [K(18-Crown-6)][$(Cp^*_2Ln)_2(\mu\text{-}Co(pdt)_2)$] **2-Ln** (Ln = Y, Gd).

The $[Co(pdt)_2]^{2-}$-bridged complexes $(Cp^*_2Ln)_2(\mu\text{-}Co(pdt)_2)$ (**1-Ln**) (Ln = Y, Gd, Dy) were synthesized via salt metathesis between $Cp^*_2Ln(BPh_4)$ (Ln = Y, Gd, Dy) and $(NBu_4)_2[Co(pdt)_2]$ (Scheme 3.1). Slightly less than an equivalent of $(NBu_4)_2[Co(pdt)_2]$ was used in the reaction in order to drive the formation of the desired dilanthanide compounds. Crystallization from layered benzene/hexamethyldisiloxane yielded red **1-Y**, **1-Gd**, and **1-Dy** as analytically pure crystalline solids in moderate yields. Single-crystal x-ray diffraction analysis of each **1-Ln** congener revealed

that the compounds are isostructural, with the lanthanide subunits related by a crystallographic inversion center at the central cobalt atom. Additionally, the bridging $[Co(pdt)_2]^{2-}$ retains the square-planar geometry of its unmetalated precursor compound $(NBu_4)_2[Co(pdt)_2]$ (Figure S3.6). As a result, the two lanthanide ions and four bridging sulfur atoms constitute a six-membered ring with a chair-like conformation (Figure 3.1a). The Co–S and alkene C–C distances are consistent with literature values for the $[Co(X-pdt)_2]^{2-}$ dianion as well as with the observed distance in $(NBu_4)_2[Co(pdt)_2]$.[14] The Cp*–Ln distances of **1-Ln** (see Table S3.3) lie within the range of values reported for structurally comparable compounds featuring $[MoS_4]^{2-}$, $[WS_4]^{2-}$, and PhS^- bridges (2.35−2.40 Å).[13,15] This result, together with the 2− oxidation state assignment for the bridging cobalt unit, suggests a negligible degree of charge transfer from the bridge to the lanthanide subunits.

Given literature precedent for square planar $S=1$ $[Co(bdt)_2]^{1-}$,[16] dinuclear compounds featuring the corresponding $[Co(pdt)_2]^-$ bridge were also targeted. Cyclic voltammetry data collected for **1-Gd** (Figure S3.6) in 1,2-difluorobenzene revealed the first oxidation event to be irreversible, suggesting that **1-Gd** dissociates upon oxidation of the $[Co(pdt)_2]^{2-}$ bridge. Unexpectedly, a quasi-reversible feature at approximately −1.68 V vs $[Cp_2Fe]^{+/0}$, with a peak separation consistent with a one-electron process was observed, suggesting that the $[Co(pdt)_2]^{2-}$ subunit in **1-Gd** could undergo one-electron reduction. Indeed, the reaction of **1-Ln** (Ln = Y^{3+}, Gd^{3+}) with KC_8 in THF prompted an immediate color change from red to dark green, and following subsequent complexation with 18-crown-6, yielded the $[Co(pdt)_2]^{3-}$-bridged compounds [K(18-Crown-6)][$(Cp*_2Ln)_2(Co(pdt)_2)$] (**2-Ln**, Ln = Y, Gd). Crystallization from a THF solution layered with diethyl ether at room temperature resulted in the formation of dark green single crystals of **2-Y** and **2-Gd** in 22% and 42% yield, respectively.
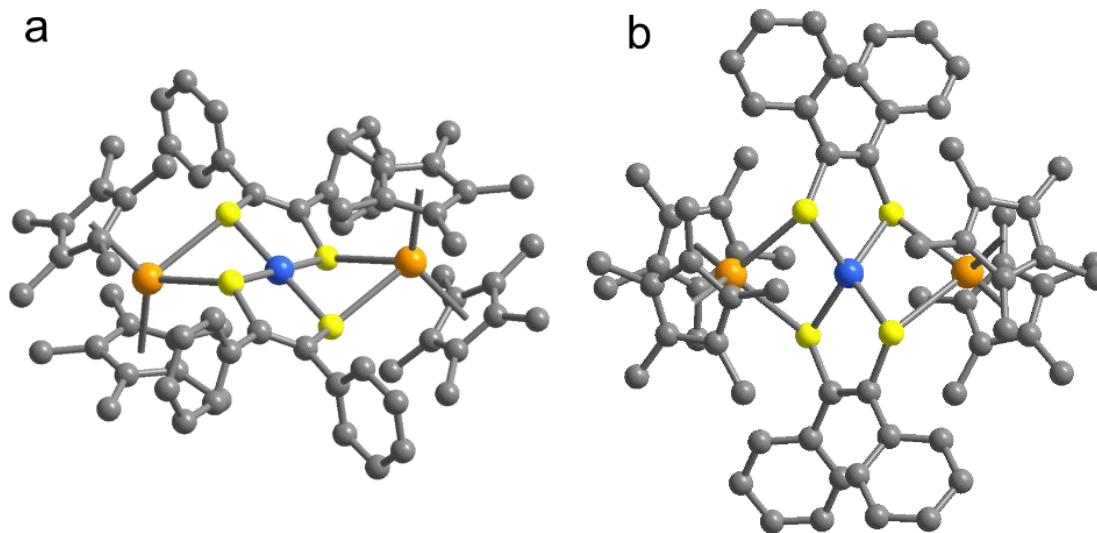
Figure 3.1: a) X-ray crystal structure of **1-Gd**. Hydrogen atom positions and lattice solvent are omitted for visual clarity. b) X-ray crystal structure of **2-Gd**. Hydrogen atom positions, [K(18-Crown-6)]$^+$ cation, and lattice solvent are omitted for visual clarity

We initially anticipated that the bridge in **2-Ln** would be isoelectronic and isostructural to known $S = 0$ d^8 square-planar nickel dithiolene complexes reported in the literature.[17] Indeed, $[Co(mnt)_2]^{3-}$ (mnt^{2-} = maleonitrile-2,3-dithiolate) was assigned an $S = 0$ ground state based on the absence of an EPR signal in solution samples.[18] However, single-crystal x-ray diffraction analysis

49

revealed that the bridging trianion in **2-Ln** adopts a pseudo-tetrahedral geometry with approximate D_{2d} symmetry (Figure 3.1b). We hypothesize that, rather than pairing with the electron in the singly occupied d_{xz}-derived molecular orbital in the parent compound, the added electron initially populates the highest σ^* orbital of $d_{x^2-y^2}$ character; reorganization to a tetrahedral geometry would then serve to minimize the antibonding character of the metal–ligand interactions. Regardless of the nature of the electron transfer, the geometric rearrangement about cobalt must be quite facile in solution at ambient temperature, given the quasi-reversible profile of the cyclic voltammogram collected for **1-Gd**. The change in local geometry at Co is associated with a significant shortening of the lanthanide–cobalt distance by ~0.37 Å. This shortening is accompanied by lengthening of the Gd–Cp*$_{centroid}$ distances by ~0.04 Å, indicating some degree of charge transfer from the bridge to each of the Cp*$_2$Gd subunits (Table S3.4).
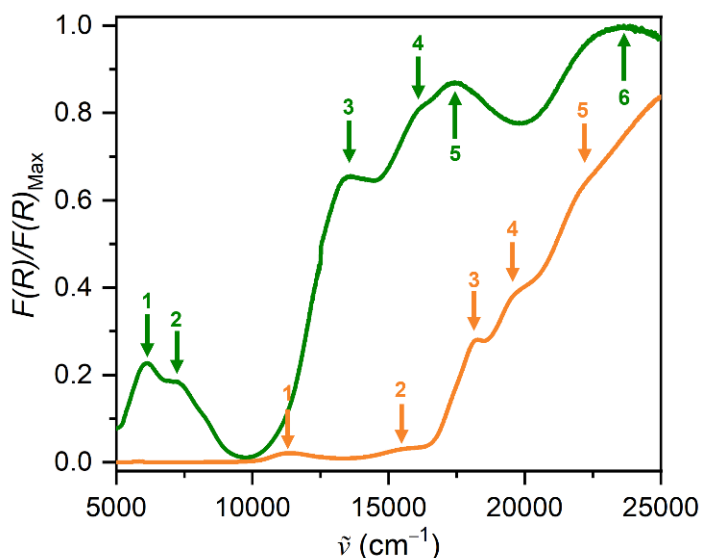

Figure 3.2: Normalized diffuse reflectance spectra of **1-Gd**(orange) and **2-Gd**(green).

Diffuse reflectance spectra were collected on powders of **1-Gd** and **2-Gd** in order to interrogate the electronic structure of the bridging subunit in each compound. The spectrum obtained for **1-Gd** exhibits features at high frequency in the visible region of the spectrum. The two transitions of low intensity at 11570 and 15564 cm^{-1} are consistent with Laporte-forbidden d–d transitions. The subsequent transitions at 18324, 18867, 22054, and 25420 cm^{-1} have higher intensity and are consistent with ligand-to-metal charge transfer (LMCT) bands. These observations are consistent with the expected spectral profile of [Co(pdt)$_2$]$^{2-}$, which should consist of high-energy LMCT and low-intensity d–d transitions.[19] In the spectrum for **2-Gd**, transitions associated with LMCT appear between 17980 and 25000 cm^{-1}, while the d–d transitions between 13103 and 15720 cm^{-1} dramatically increase in intensity, which we ascribe to the relaxation of the Laporte selection rule for the cobalt centered transitions.[20] Crucially, two features of moderate intensity are also present in the NIR region of the spectrum for **2-Gd** at 5896 and 7220 cm^{-1}, consistent with metal-to-metal charge transfer transitions.[13]

Given the precedent for substantial *g*-factor anisotropy in square-planar low-spin cobalt compounds,[18,21] EPR spectra for powdered samples of **1-Y** were collected with the aim of determining the *g*-values for the [Co(pdt)$_2$]$^{2-}$ spin unambiguously. With these values in hand, extracting the

exchange constant $J_{\text{Gd–Co}}$ from subsequent fitting of dc magnetic susceptibility data for **1-Gd** can be done with a much higher degree of confidence. The variable-field EPR spectra of finely powdered **1-Y** (Figure 3.3) show a dominant $S = 1/2$ species with pronounced g-factor anisotropy (g_x = 3.42, g_y = 3.03, g_z = 1.8). Moreover, the anisotropic hyperfine interaction of $A_x = 620$ MHz and hyperfine patterns are consistent with D_{2h} square-planar Co^{2+}, accounting for 90% of the observed signal. The remaining 10% of the observed signal was attributed to a minor decomposition product, suspected to be $Co(pdt)_2$.
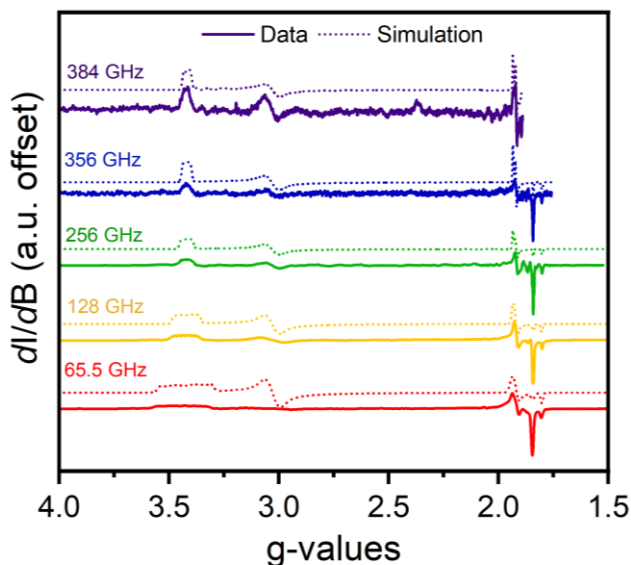

Figure 3.3: Continuous-wave variable-frequency, high-field EPR spectra for a solid-state sample of **1-Y**. Each simulation corresponds to a linear combination of a dominant species α and minor species β, as detailed in Figure S3.21.

Variable-temperature dc magnetic susceptibility data were collected for **1-Ln** (Ln = Gd, Dy) and **2-Gd** from 2 to 300 K under an applied field of 0.1 T (Figure 3.4a). The $\chi_M T$ product for **1-Gd** at 300 K is 19.5 emu K/mol, slightly larger than that of 16.6 emu·K/mol predicted for two non-interacting $S = 7/2$ Gd^{3+} centers and an $S = 1/2$ $[Co(pdt)_2]^{2-}$ with g-values assigned from EPR analysis. With decreasing temperature, $\chi_M T$ increases monotonically, which is consistent with the thermal population of a spin ground state arising from intramolecular ferromagnetic exchange. The magnetic data were fit in PHI[22] using a Heisenberg-exchange Hamiltonian (Equation S3.1), giving a coupling constant of $J_{\text{Gd–Co}} = +11.48(8)$ cm^{-1}. The ferromagnetic nature of this interaction is in accord with those of other 3d–4f heterobimetallic systems in the literature. For instance, Gd–Cu compounds are known to exhibit ferromagnetic exchange interactions on the order of ~6–8 cm^{-1} with little apparent electron transfer between the Cu and Gd ions. The exchange interactions in these compounds are often ascribed to a strong configuration interaction between the charge-localized ground state and charge transfer excited states.[23] The notably higher exchange interaction strength noted in **1-Gd** compared to those of typical 4f–3d compounds suggests that the sulfur bridging atoms improve the strength of this configuration interaction.[24]

At T = 300 K, dc susceptibility data obtained for **2-Gd** (Figure 3.4b) show $\chi_M T = 18.4$ emu K/mol, consistent with an $S = 1$ Co^+ and two isolated $S = 7/2$ Gd^{3+} ions. The monotonic rise in $\chi_M T$ with decreasing temperature is indicative of ferromagnetic coupling between the Gd and Co. The data were fit to a single-exchange Hamiltonian (Equation S3.2), which yielded $J_{\text{Gd–Co}} = +7.33(4)$

cm^{-1}. Simultaneous fitting of reduced magnetization (Figure S3.17) and $\chi_M T$ data for **2-Gd** yielded zero-field splitting values of $D = 60(1)$ cm^{-1} and $E/D = 0.30(9)$ for the bridging $[Co(pdt)_2]^{3-}$ unit. These values are consistent with an $S = 1$ Co$^+$ center in with local D_{2d} symmetry. High-field EPR measurements were also carried out on **2-Y** to better quantify D and E parameters, however no signal could be resolved. This result may suggest that the zero-field splitting is quite pronounced, as the expected signals would lie beyond of the measurable field and frequency ranges. Indeed, assuming the zero-field splitting parameters from fitting reduced magnetization data are correct, the field required to observe an $S = 1$ resonance at the maximum frequency available of 384 GHz with $D = 60$ cm^{-1} was calculated to be nearly 50 T, which is outside of the available field range.
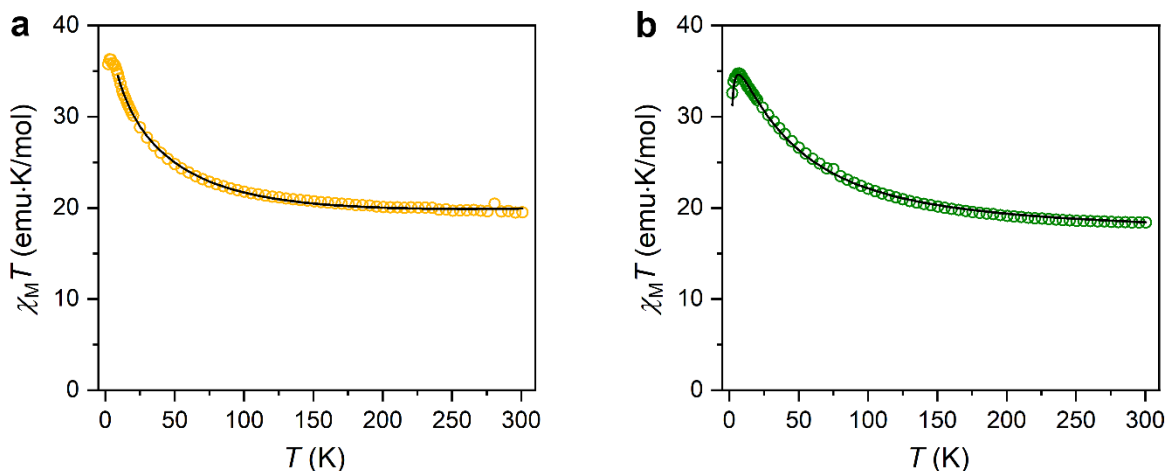
Figure 3.4: a) Variable temperature dc susceptibility of **1-Gd**. Orange open circles are experimental data b) Variable temperature dc susceptibility of **2-Gd**. Green open circles are experimental data. Black traces represent simulated curves using the following parameters: **1-Gd**: $J_{Gd-Co} = +11.48(8)$ cm^{-1}, g$_x = 3.42$, g$_y = 3.03$, g$_z = 1.803$, Equation S3.1; **2-Gd**: $J_{Gd-Co} = +7.33(4)$ cm^{-1}, $|D| = 60(1)$, $|E/D| = 0.30(9)$, Equation S3.2
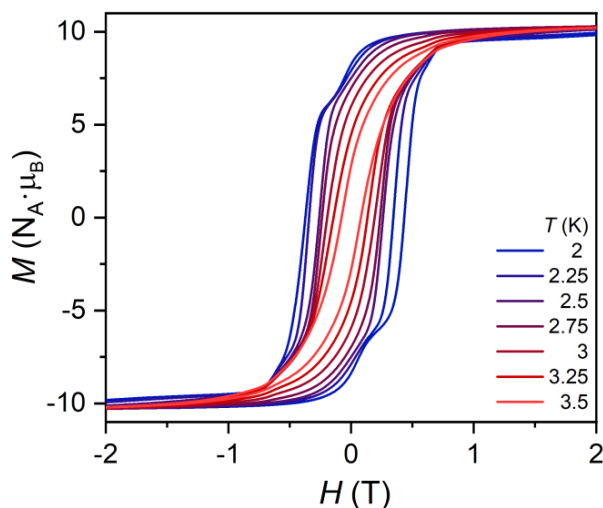
Figure 3.5: Variable field magnetic hysteresis loops of **1-Dy** measured from 2 – 3.5 K. Average field sweep rate = 0.005 T/s

As an initial probe of slow magnetic relaxation in **1-Dy**, we collected variable-field magnetization data for a microcrystalline powder sample (Figure 3.5), which revealed open magnetic hysteresis as high as 3.5 K and a coercive field of 0.6 T at 2 K. While $[\mu\text{-MoS}_4]^{3-}$ engages in stronger magnetic exchange than does $[\mu\text{-Co(pdt)}_2]^{2-}$, the magnetic hysteresis loops of $[(\text{Cp*}_2\text{Dy})_2(\mu\text{-MoS}_4)]^-$ featured limited butterfly hysteresis at 2 K, where the remanent magnetization is close to zero at zero-field. We ascribe this behavior in **1-Dy** to the geometry of the bridge. Specifically, due to the inversion center Co, the local quantization axes of the coupled lanthanide ions are pinned in parallel with one another (Figure S3.19). This geometry maximizes the magnetic anisotropy of the exchange-coupled ground state. Tn the structure of $[(\text{Cp*}_2\text{Dy})_2(\mu\text{-MoS}_4)]^-$, the local quantization axes of $[\text{DyCp*}_2]^+$ subunits are positioned in an orthogonal orientation with respect to one another, which limits the magnetic anisotropy of the resulting coupled ground state (Figure S3.18).
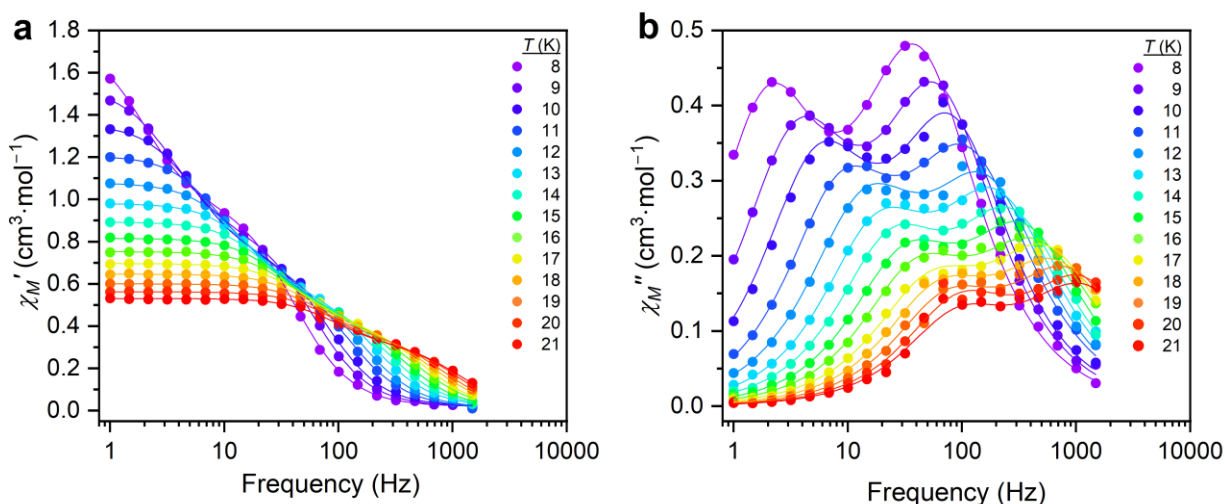
Figure 3.4: a) Isothermal in-phase ac susceptibility of **1-Dy**. b) Isothermal out-of-phase ac susceptibility of **1-Dy**. Circles are experimental data; solid lines are fits to the dual-process Debye model as implemented in Phi[22] with fit parameters given in Table S3.7.
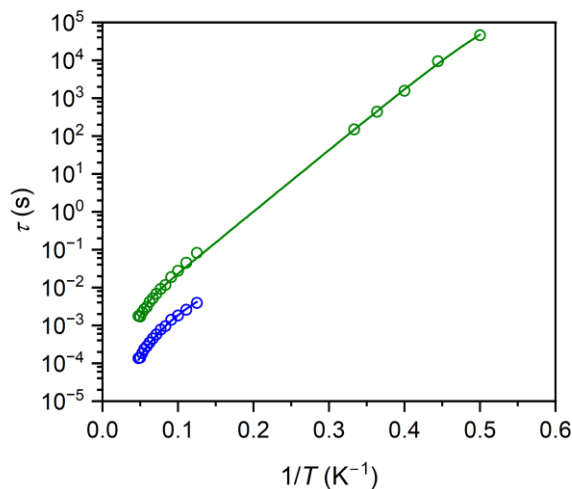
Figure 3.5: Arrhenius plot of **1-Dy**. Experimental data is represented by open circles. Fit to Equation S3.4 represented by solid blue trace. Fit to Equation S3.5 represented by solid green trace. Process A (blue) fit parameters: $C = 10^{-0.9(4)}$ s$^{-1} \cdot$K^{-n}, $n = 3.6(3)$. Process B (green) fit parameters: $U_{\text{eff}} = 26.05(4)$ cm^{-1}, $\tau_0 = 10^{-3.25(1)}$ s. $C = 10^{-7.37(2)}$ s$^{-1} \cdot$K^{-n} $n = 7.57(2)$.

Magnetization decay experiments were also carried out on **1-Dy** in the temperature range 2–3 K to verify that temperature-independent relaxation is fully suppressed at low temperature. Fits to an exponential decay function (Equation S3.3) showed that the relaxation times remained strongly temperature-dependent from 2–3 K (Figure 3.7.13), with the highest measured relaxation times being on the order of 10^4 s. Moreover, ac magnetic susceptibility data collected under zero dc field and temperatures ranging from 6 to 20 K revealed a frequency-dependent signal in the out-of-phase susceptibility, χ_M'', with two distinct, partially overlapping relaxation modes (Figure 3.4b). These data were fit using the dual-process Debye model implemented in CCFIT2[25,26] to extract two sets of relaxation times (τ) at each temperature (Figure 3.5). The faster of the two processes, denoted process A, could be adequately fit to a Raman relaxation process (Equation S3.4).[27] For the slower of the two relaxation processes (process B), the profile could be fit using an Orbach and Raman model (Equation S3.5). Of note, temperature-independent relaxation is not evident at the ac or dc timescales measured here, suggesting that magnetic exchange in **1-Dy** mitigates tunneling of the magnetization that is observed at low temperatures for $[(Cp^*_2Dy)_2(\mu\text{-}MoS_4)]^-$.[13]

3.3 Conclusion and Outlook

The foregoing results describe the synthesis and characterization of **1-Ln** $(Cp^*_2Ln)_2(\mu\text{-}Co(pdt)_2)$ (Ln = Y, Gd, Dy) and **2-Ln** $[K(18\text{-}Crown\text{-}6)][(Cp^*_2Ln)_2(\mu\text{-}Co(pdt)_2)]$ (Ln = Y, Gd). A spectroscopic comparison between **1-Gd** and **2-Gd** was carried out to understand the differences in electronic structure between these species. In addition, the magnetic ground states and relaxation properties of **1-Gd**, **1-Dy**, and **2-Gd** have also been determined through SQUID magnetometry and variable-field EPR spectroscopic analysis of **1-Y**. The magnetic exchange coupling between cobalt and gadolinium in **1-Gd** is large and ferromagnetic, suggesting a dipolar exchange pathway which gives way to a double exchange pathway upon reduction to **2-Gd**, which is indicated by the formation of two new MMCT bands upon reduction. These results demonstrate the utility of metal-loligands in facilitating magnetic exchange between lanthanide ions as well as the importance of bridge geometry in obtaining an anisotropic coupled ground state.

3.4 Experimental

Geneal Details

Unless otherwise stated, all manipulations were performed under an atmosphere of dinitrogen or argon with rigorous exclusion of air and water using standard Schlenk and glovebox techniques. Tetrahydrofuran (THF), toluene, diethyl ether, and benzene were dried over alumina columns in a JC Meyer solvent system and were stored over 4 Å molecular sieves prior to use. Water and 1,4-dioxane were degassed by sparging with argon for 30 min immediately prior to use in the synthesis of $[Co(pdt)_2]_2$. Acetonitrile was dried over alumina columns in a JC Meyer solvent system and were stored over 3 Å molecular sieves prior to use. Methanol was degassed using three freeze-pump-thaw cycles and subsequently dried over 3 Å molecular sieves prior to use. Unless otherwise noted, other solvents used were degassed with three freeze pump thaw cycles and were dried over 4 Å molecular sieves for a minimum of 48 h prior to use. The precursor compounds $Cp^*_2LnBPh_4$ (Ln = Y, Gd, Tb, or Dy) were prepared as described previously.[28] Air-free elemental analyses were performed at the UC Berkeley Microanalytical facility. Proton NMR spectra were collected on a Bruker Avance AVB-400 MHz spectrometer at ambient temperature. Ultraviolet-visible-NIR

diffuse reflectance spectra were collected on ground powders loosely packed on a bed of dry $BaSO_4$ under an N_2 atmosphere using a Varian Cary 5000 spectrometer. Infrared spectra were collected on neat samples using a Shimadzu IRSpirit FTIR operating in ATR mode.

Synthetic Methods

1-Y $(Cp*_2Y)_2(Co(pdt)_2)$. Solid $Cp*_2Y(BPh_4)$ (271.3 mg, 0.3998 mmol) was suspended in toluene (15 mL) in a 20 mL scintillation vial. This suspension was quickly added with stirring to solid $(NBu_4)_2[Co(pdt)_2]$ (157.3 mg, 0.1529 mmol) in a separate 20 mL vial. Within seconds, the reaction mixture turned a red-orange color with concomitant formation of a colorless precipitate, presumed to be $(NBu_4)BPh_4$. The mixture was allowed to stir at ambient temperature for 12 h. The suspension was then centrifuged to separate the solids from solution and the toluene was decanted off into a separate vial. The toluene was then removed under vacuum to yield a dark red solid, which was dissolved with a minimal amount of benzene. The resulting red solution was filtered through diatomaceous earth, and hexamethyldisiloxane was slowly added to the resulting filtrate to precipitate a crystalline red-orange solid of analytical purity. Crystals suitable for single-crystal x-ray diffraction analysis were grown by layering concentrated solutions of benzene with hexamethyldisiloxane at room temperature. Yield: 83.4 mg, 43.3% based on $(NBu_4)_2[Co(pdt)_2]$. Calcd. for $C_{68}H_{80}Y_2CoS_4$ (%): C, 64.7; H, 6.39. Found (%): C, 64.5; H, 6.35. ^{1}H NMR (400 MHz, benzene-d[6]) δ 8.41 (s, 4H), 4.51 (s, 8H), 3.29 (s, 10H), 1.29 (s, 60H).

1-Gd $(Cp*_2Gd)_2(Co(pdt)_2)$. The compound was synthesized using a procedure analogous to that described for 1-Y, using $Cp*_2GdBPh_4$ (97.0 mg, 0.130 mmol) and $(NBu_4)_2[Co(pdt)_2]$ (51.1 mg, 0.0499 mmol). Yield: 24.4 mg, 35.1% based on $(NBu_4)_2[Co(pdt)_2]$ Calcd for $C_{68}H_{80}Gd_2CoS_4$ (%): C, 58.38; H, 5.76. Found (%): C, 57.24; H, 6.01.

1-Dy $(Cp*_2Dy)_2(Co(pdt)_2)$. The compound was synthesized using a procedure analogous to that described for **1-Y**, using $Cp*_2Dy(BPh_4)$ (147.3 mg, 0.1958 mmol) and $(NBu_4)_2[Co(pdt)_2]$ (76.6 mg, 0.0745 mmol). Yield: 45.0 mg, 42.8% based on $(NBu_4)_2[Co(pdt)_2]$. Calcd. for $C_{68}H_{80}Dy_2CoS_4$ (%): C, 57.94; H, 5.72. Found (%): C, 57.81; H, 5.96.

2-Y $[K(18\text{-}Crown\text{-}6)][(Cp*_2Y)_2(Co(pdt)_2)]$. Solid $(Cp*_2Y)_2(Co(pdt)_2)$ (**1-Y**; 60.0 mg, 0.0475 mmol) was dis-solved in THF (5 mL). With stirring, 18-Crown-6 (14.9 mg, 0.0564 mmol) was added to the solution, followed by KC_8 (6.80 mg, 0.0504 mmol). Upon addition of KC_8, the solution changed from red-orange to a dark green color. The solution was then stirred at room temperature for 1 h to give a heterogeneous mixture. The mixture was centrifuged to separate the suspended graphite, and the THF solution was subsequently decanted. The THF was then removed under reduced pressure, leaving an oily dark green residue. The dark green residue was washed once with 5 mL of toluene to remove any unreacted starting material and excess 18-Crown-6. The resulting green solid was dissolved in a minimal amount of THF (~1 mL), and the ensuing solution was then layered with diethyl ether and left to stand at room temperature. Block-shaped crystals suitable for single-crystal x-ray diffraction analysis formed after 24 hrs. Yield: 34 mg, 22% based on $(Cp*_2Y)_2(\mu\text{-}Co(pdt)_2)$. Calcd. for $C_{80}H_{104}CoKO_6S_4Y_2$ (%): C, 61.37; H, 6.70. Found (%): C, 60.88; H, 6.93.

2-Gd $[K(18\text{-}Crown\text{-}6)][(Cp*_2Gd)_2(Co(pdt)_2)]$. Solid $(Cp*_2Gd)_2(Co(pdt)_2)$ (1-Gd, 49.6 mg, 0.0354 mmol) was dissolved in 5 mL of THF. With stirring, 18-Crown-6 (18.2 mg, 0.0689 mmol) was added to the solution, followed by KC_8 (7.0 mg, 0.052 mmol). Upon addition of KC_8, the

solution changed from red-orange to a dark green color. The solution was then stirred at room temperature for 1 h to give a heterogeneous mixture. The mixture was centrifuged to separate the suspended graphite, and the THF solution was subsequently decanted. The THF was then removed under reduced pressure, leaving an oily dark green residue. The dark green residue was washed once with 5 mL of toluene to remove any unreacted starting material and excess 18-Crown-6. The resulting green solid was dissolved in a minimal amount of THF (~1 mL), and the ensuing solution was then layered with diethyl ether and left to stand at room temperature. Block-shaped crystals suitable for single-crystal x-ray diffraction analysis formed after 24 hrs. Yield: 25.4 mg, 42.1% based on $(Cp*_2Gd)_2(\mu\text{-}Co(pdt)_2)$. Calcd. for $C_{80}H_{104}CoKO_6S_4Gd_2$ (%): C, 56.44; H, 6.16. Found (%): C, 56.80 C; H, 6.44.

[Co(pdt)$_2$]$_2$. Adapted from method described by Letko et. al. for the preparation of [Co(F-pdt)$_2$]$_2$.[14] Caution: Large quantities of H_2S are released over the course of this preparation. N_2 was blown over reaction mixture into a reservoir of bleach to sequester H_2S vapors. A 250 mL Schlenk was charged with 5.02 g (23.9 mmol) of benzil and 12.8 g (57.6 mmol) of P_2S_5. Approximately 100 mL of degassed undried 1,4-dioxane was poured over the solid mixture. The resulting suspension was brought to reflux under an atmosphere of N_2 with strong stirring for 2 hours over which time the color changed from light yellow to a darker brown. This mixture was then canula filtered while hot into a degassed solution of 2.84 g (11.9 mmol) of $CoCl_2 \cdot 6H_2O$ in 50 mL of water. This cloudy mixture was then brought to 90 °C under strong stirring for 2 hours. During this time, a dark blue material precipitated from solution. After cooling the mixture to room temperature, the solids were isolated by decanting the solvent mixture away. 50 mL MeOH was then added to the solids and brought to reflux for 30 minutes to wash the material. The MeOH was then cooled to room temperature and decanted away. The solids were then washed with 50 mL water, followed by 50 mL of MeOH. The damp solids were subsequently dried under dynamic vacuum for several hours. The resulting dark blue powder was used directly without further purification. 3.94 g yield (3.63 mmol), 60.9% based on $CoCl_2 \cdot 6H_2O$.

(NBu$_4$)$_2$[Co(pdt)$_2$]. The cobalt(II) dithiolene precursor was prepared using a method slightly modified from the procedure reported by Letko et al. for the preparation of $(NBu_4)_2[Co(F\text{-}pdt)_2]$.[14] In a N_2 glovebox, dark blue [Co(pdt)$_2$]$_2$ (0.9986 g, 0.9184 mmol) was added to a suspension of KC_8 (500.0 mg, 3.6982 mmol) in THF (20 mL) at room temperature. The suspension quickly turned dark red/orange with the slow concomitant precipitation of yellow microcrystalline material presumed to be $K_2Co(pdt)_2$. The suspension was allowed to stir at room temperature for 4 h. At this stage, NBu$_4$I (1.3624 g, 3.6883 mmol) was added to the reaction mixture. The yellow precipitate quickly dissolved into solution with concomitant formation of a colorless precipitate presumed to be KI. The mixture was then stirred for 1 h at 60 °C, cooled to room temperature, and stirred for an additional 1 h before being centrifuged. The THF was removed under vacuum, and the resulting dark red residue washed with diethyl ether. Dark red microcrystalline (NBu$_4$)$_2$[Co(pdt)$_2$] was isolated by decanting away the solution and drying the resulting solid under vacuum. The red solid was used in subsequent synthesis steps without further purification. Isolated yield: 309 mg, 65% based on [Co(pdt)$_2$]$_2$. Crystals suitable for single crystal x-ray diffraction studies were be grown from a concentrated THF solution layered with diethyl ether. ^{1}H NMR (400 MHz, acetonitrile-d[3]) δ 8.69 (bs, 4H), 7.13 (s, 10H), 6.56 (s, 8H), 3.00 (bs, 16H), 1.51 (bs, 18H), 1.27 (bs, 18H), 0.97 (bs, 26H).

(Cp*$_2$Gd)$_2$(μ-Fe(bdt)$_2$). 47.7 mg (0.0639 mmol) of Cp*$_2$Gd(BPh$_4$) was suspended in 5 mL of toluene with 30 mg (0.030 mmol) of (PPh$_4$)$_2$[Fe(bdt)$_2$]. The solution was stirred under ambient conditions for 24 hours yielding a brownish orange solution. The suspension was centrifuged, and

colorless solids separated from the supernatant. After discarding the solids, the now clear solution was evacuated to dryness. The residue was redissolved in 1 mL of toluene and layered with 3 mL of hexamethyldisiloxane for recrystallization. 21 mg of red crystals were isolated (0.018 mmol; 61 % yield based on $(PPh_4)_2[Fe(bdt)_2]$). Calcd. for $C_{52}H_{68}Gd_2FeS_4$ (%): C, 52.3; H, 5.74. Found (%): C, 52.6; H, 5.6.

$(Cp*_2Gd)_2(\mu-Co(bdt)_2)$. 96.0 mg (0.128 mmol) of $Cp*_2Gd(BPh_4)$ was suspended together with 65.3 mg (0.0642 mmol) of putative $(PPh_4)_2[Co(bdt)_2]$ in 10 mL of toluene. The mixture was stirred at ambient temperature for 2 days. Colorless solids were removed from suspension via centrifugation and discarded. The resultant dark brown solution was then concentrated to incipient precipitation and layered with hexamethyldisiloxane to recrystallize at room temperature. 31.2 mg of dark blue crystals isolated (0.0261 mmol; 40.7% based on $(PPh_4)_2[Co(bdt)_2]$). Calcd. for $C_{52}H_{68}Gd_2CoS_4$ (%): C, 52.3; H, 5.74. Found (%): C, 52.5; H, 5.7.

$(PPh_4)_2[Fe(bdt)_2]$. Synthesis was carried out using a modified form of a literature preparation of $(AsPh_4)_2[Fe(bdt)_2]$, using $(PPh_4)^+$ instead of $(AsPh_4)^+$.[39] 51.3 mg (0.405 mmol) of anhydrous $FeCl_2$ was stirred in 10 mL of THF at 60 °C overnight. This suspension was allowed to cool to room temperature before a solution of 126 mg (0.818 mmol) of Li_2bdt in 5 mL of THF was added slowly. The solution was allowed to stir under ambient conditions for 2 hours. The suspended solids were removed by filtration and the filtrate was then added to a solution of 340 mg (0.811 mmol) of PPh_4Br dissolved in 8 mL of dry and degassed MeOH. This resulted in the immediate formation of a dark colored precipitate. The suspension was stirred for 2 hours and then the solids were isolated by filtration. The solids were washed with three 5 mL aliquots of acetonitrile followed by a single 10 mL THF aliquot. After drying the solid under reduced pressure, the isolated yield was 40 mg (0.039 mmol; 9.6% yield based on $FeCl_2$) of a brown powder. The crude product was used in subsequent steps without further purification.

$(PPh_4)_2[Co(bdt)_2]$. Synthesis was carried out using a modified form of the $(PPh_4)_2[Fe(bdt)_2]$ preparation, using anhydrous $CoCl_2$ instead of anhydrous $FeCl_2$. 208 mg (1.60 mmol) of anhydrous $CoCl_2$ was solvated in 15 mL of THF. This solution was subsequently added to 493 mg (3.20 mmol) of Li_2bdt. The now dark brown colored solution was stirred for 3 hours under ambient conditions. The suspended solids were subsequently removed by filtration and discarded. A solution of 1.345 g (3.208 mmol) of PPh_4Br in 15 mL of dry degassed MeOH was added slowly to the filtrate with gentle stirring. A dark colored precipitate formed immediately following the addition. These dark colored solids were collected by filtration and washed with acetonitrile followed by THF. The dark brown microcrystalline solid was then dried under reduced pressure. 120 mg yield dark powder (0.118 mmol; 7.4 % yield based on $CoCl_2$). Used in subsequent steps without further purification.

Li_2bdt. 429.0 mg (3.02 mmol) of freshly distilled 1,2-benzenedithiol was dissolved in 25 mL of THF. The solution was subsequently cooled to -78 °C and 3.75 mL of 1.6 M n-BuLi in n-hexane (6.00 mmol) was added with stirring. The solution was then allowed to warm to room temperature slowly over the course of 3 hours with stirring. The room temperature solution was then vacuum distilled to dryness and the resulting solid material isolated as an off-white powder. 431 mg (93.2% based on n-BuLi) isolated yield of crude powder. Crude material was stored at -30 C and used in subsequent steps without further purification.

X-Ray Crystallography

Prior to analysis, all single crystal samples were first removed from their mother liquor, and briefly stored under Paratone-N oil at −78 °C beneath an atmosphere of N_2 for transport from the glovebox to the diffractometer. X-ray diffraction data for **1-Gd**, $(Cp*_2Gd)_2(\mu\text{-Fe(bdt)}_2)$, and $(Cp*_2Gd)_2(\mu\text{-Co(bdt)}_2)$. were collected at the UC Berkeley College of Chemistry X-ray crystallography facility on a Rigaku XtalLab P200 diffractometer equipped with a MicroMax 007HF MoK source. A crystal was mounted on a Kapton loop and moved under a nitrogen cryostat supplied by Oxford Cryosystems. Unit cell determination and spot integration was performed using the CrysAlis software suite.[29] Absorption corrections were applied using the SADABS package with angle of incidence corrections applied.[30] Structural solutions were obtained using Intrinsic Phasing as implemented in ShelXT.[35] Least Squares refinement as implemented in ShelXL was used in model refinement.[36] Olex2 was used as a graphical frontend to the aforementioned packages.[31]

Diffraction data for all other compounds were collected using synchrotron radiation at Beamline 12.2.1 at the Advanced Light Source, Lawrence Berkeley National Laboratory. Crystals were mounted onto MiTeGen 10 μm loops and moved under an Oxford Cryosystems nitrogen cryostat. Unit cell determination and spot integration were performed using SMART and SAINT algorithms as implemented in the Bruker APEX III software suite.[32–34] Absorption corrections were applied to spot intensities using the SADABS package.[30] Structural solutions were obtained using Intrinsic Phasing as implemented in ShelXT.[35] Least Squares refinement as implemented in ShelXL was used to refine structural models against F^2.[36] Olex2 was used as a graphical front-end for structural solution and refinement.[31] A solvent mask was applied using the SQUEEZE tool in Olex2 to model a total of three disordered THF equivalents per unit cell in $[NBu_4]_2[Co(pdt)_2]$.

IUCr CheckCIF Structure Validation Alerts and Reflection Omissions:

1-Gd

PLAT910_ALERT_3_B Missing # of FCF Reflection(s) Below Theta(Min).   11 Note
> Low angle reflections in several frames were affected by scattering from the copper pin on which the Kapton loop was supported. The low angle data contained in the pathological frames was masked to remove the copper scattering from the data, resulting in the 11 missing FCF reflections noted in CheckCIF.

1-Dy

PLAT971_ALERT_2_B Check Calcd Resid. Dens. 0.82Ang From Dy01   2.58 eA-3
> The q-peak in proximity to the Dy position is likely a Fourier artifact, meaning it would be inappropriate to model it as positional disorder.

2-Gd

PLAT250_ALERT_2_B Large U3/U1 Ratio for Average U(i,j) Tensor ....   4.1 Note
> Upon visual inspection, the thermal ellipsoids were found to be fairly isotropic on the two unique complex anions. The large U3/U1 ratio must therefore be due to the [K(18-Crown-

6)]+ cation and its atoms' thermal displacement orthogonal to the plane of the ring. Attempts were made to model the crown ether as disordered alongside the potassium cation, however these attempts yielded numerous atomic positions with negative thermal displacement parameters. It therefore seemed appropriate to leave the disorder unmodeled and accept the large U3/U1 ratio in the displacement parameters.

PLAT601_ALERT_2_B Unit Cell Contains Solvent Accessible VOIDS of .   183 Ang**3
    The void in question likely contains some extremely disordered solvent position with small chemical occupation, as the q peaks present in this space are all <2 electrons in intensity. Attempts to generate a solvent mask for this region of the unit cell failed as the mask generated always failed to include the void in question regardless of the solvent radius or truncation values used. As the unmodeled electron density was a small fraction of the total modeled electron density, we opted to leave the region unmodeled.

PLAT934_ALERT_3_B Number of (Iobs-Icalc)/Sigma(W) > 10 Outliers ..   10 Check
    These outliers (-1,1,5); (-2,1,4); (-5,0,3); (-3,2,1); (-4,1,2); (1,3,1); (2,2,0); (4,0,0); (-1,1,3); (5,0,1) were all located between 6.6 and 3.8 Å. Inspecting the fast phi run, all of these reflections were found to have zero or near-zero intensity. These disagreeable reflections are ascribed to the poorly resolved solvent peaks, which appear above and below the plane of the [K(18-Crown-6)]+ cation, and which could not be explicitly modeled or masked in the structure.

(h,k,l) omissions with justification:
    (0,0,2); (-1,1,1); (2,0,0); (1,0,1); (0,1,0); (-1,0,3) All of these reflections were found to be obscured by the beamstop.

2-Y
PLAT601_ALERT_2_B Unit Cell Contains Solvent Accessible VOIDS of .   188 Ang**3
    The void in question likely contains some extremely disordered solvent with small population, as the q peaks present in this space are all <2 electrons in intensity. Attempts to map a solvent mask to this region of the unit cell failed. As the unmodeled electron density was so insignificant, we opted not to continue our efforts to model this region.

PLAT934_ALERT_3_B Number of (Iobs-Icalc)/Sigma(W) > 10 Outliers ..   8 Check
    These outliers (-3,2,1); (4,1,0); (2,2,2); (-1,1,5); (5,0,1); (4,2,0); (5,2,1); (5,1,1) were all located between 6.4 and 3.7 Å. Inspecting the fast phi run, all of these reflections were found to have zero or near-zero intensity. These disagreeable reflections are ascribed to the poorly resolved solvent peaks, which appear above and below the plane of the [K(18-Crown-6)]+ cation, and which could not be explicitly modeled or masked in the structure.

h,k,l omissions with justification:
    (1,1,1); (0,0,2); (-1,1,1); (2,0,0); (1,1,0); (-3,1,1); All of these reflections were found to be obscured by the beamstop.

Magnetometry

Direct current (dc) and alternating current (ac) magnetic susceptibility data were collected using a Quantum Design MPMS-XL magnetometer. Magnetic samples were prepared by first grinding crystalline samples to a microcrystalline powder. The crystalline powder was then loaded into 7 mm o.d./5 mm i.d. quartz sample tubes with a raised quartz platform (14.2 mg of 1-Gd; 15.4 mg of 1-Dy; 11.0 mg of 2-Gd). Solid eicosane was added on top of each sample (32.0 mg, 31.9 mg, and 26.1 mg, respectively). The sample tubes were placed under static vacuum, removed from the glove box, and flame sealed. The eicosane was then melted at 40 °C to restrain the samples for measurement. Diamagnetic corrections were applied using Pascal's constants.[37]

Dc susceptibility of **1-Gd** was fit in Phi using the Hamiltonian given in Equation S3.1 while that of **2-Gd** used the Hamiltonian given in Equation S3.2 and was simultaneously fit with reduced magnetization data given in Figure S3.17.

$$\hat{H} = -2J_{Gd-Co}\hat{S}_{Co}(\hat{S}_{Gd1} + \hat{S}_{Gd2}) + \mu_B[\bar{\bar{g}}_{Co}\hat{S}_{Co} + g(\hat{S}_{Gd1} + \hat{S}_{Gd2})] \cdot \vec{B} \qquad \text{(Equation S3.1)}$$

$$\hat{H} = D\hat{S}_{z-Co}^2 + \frac{D\hat{S}_{Co}(\hat{S}_{Co}+1)}{3} + E(\hat{S}_{x-Co}^2 - \hat{S}_{y-Co}^2) - 2J_{Gd-Co}\hat{S}_{Co}(\hat{S}_{Gd1} + \hat{S}_{Gd2}) + \mu_B g(\hat{S}_{Co} + \hat{S}_{Gd1} + \hat{S}_{Gd2}) \cdot \vec{B} \qquad \text{(Equation S3.2)}$$

Magnetization decay data was fit in OriginLab to an exponential decay function given in Equation 2.4.4.3. Ac susceptibility data was fit using a dual process generalized Debye model as implemented in CCFit2 unless otherwise noted.[25] The resulting average relaxation times for Process A were fit to a Raman function in CCFit2 (Equation S3.4). The ac relaxation times for Process B along with the average relaxation times derived from the magnetization decay experiments were fit in CCFit2 using Equation S3.5.

$$M = M_0 e^{-\frac{t}{\tau}} \qquad \text{(Equation S3.3)}$$

$$\tau^{-1} = CT^n \qquad \text{(Equation S3.4)}$$

$$\tau^{-1} = \tau_0^{-1} e^{(-\frac{U_{eff}}{k_B T})} + CT^n \qquad \text{(Equation S3.5)}$$

2.5 Acknowledgments

2.6 References and Footnotes

(1)   Atzori, M.; Sessoli, R. The Second Quantum Revolution: Role and Challenges of Molecular Chemistry. *J. Am. Chem. Soc.* **2019**, *141* (29), 11339–11352. DOI: 10.1021/jacs.9b00984.

(2)   Bogani, L.; Wernsdorfer, W. Molecular Spintronics Using Single-Molecule Magnets. *Nat. Mater.* **2008**, *7* (3), 179–186. DOI: 10.1038/nmat2133.

(3)   Gatteschi, D.; Sessoli, R.; Villain, J. *Molecular Nanomagnets*; Oxford University Press, 2006. DOI: 10.1093/acprof:oso/9780198567530.001.0001.

(4)   Goodwin, C. A. P.; Ortu, F.; Reta, D.; Chilton, N. F.; Mills, D. P. Molecular Magnetic Hysteresis at 60 Kelvin in Dysprosocenium. *Nature* **2017**, *548* (7668), 439–442. DOI: 10.1038/nature23447.

(5)   Woodruff, D. N.; Winpenny, R. E. P.; Layfield, R. A. Lanthanide Single-Molecule Magnets. *Chem. Rev.* **2013**, *113* (7), 5110–5148. DOI: 10.1021/cr400018q.

(6)   Demir, S.; Jeon, I.-R.; Long, J. R.; Harris, T. D. Radical Ligand-Containing Single-Molecule Magnets. *Coord. Chem. Rev.* **2015**, *289–290*, 149–176. DOI: 10.1016/j.ccr.2014.10.012.

(7)   Liu, K.; Shi, W.; Cheng, P. Toward Heterometallic Single-Molecule Magnets: Synthetic Strategy, Structures and Properties of 3d–4f Discrete Complexes. *Coord. Chem. Rev.* **2015**, *289–290*, 74–122. DOI: 10.1016/j.ccr.2014.10.004.

(8)   Rinehart, J. D.; Fang, M.; Evans, W. J.; Long, J. R. Strong Exchange and Magnetic Blocking in N 2 3–Radical-Bridged Lanthanide Complexes. *Nat. Chem.* **2011**, *3* (7), 538–542.

(9)   Rinehart, J. D.; Fang, M.; Evans, W. J.; Long, J. R. A N23–Radical-Bridged Terbium Complex Exhibiting Magnetic Hysteresis at 14 K. *J. Am. Chem. Soc.* **2011**, *133* (36), 14236–14239.

(10)   Demir, S.; Gonzalez, M. I.; Darago, L. E.; Evans, W. J.; Long, J. R. Giant Coercivity and High Magnetic Blocking Temperatures for N2 3− Radical-Bridged Dilanthanide Complexes upon Ligand Dissociation. *Nat. Commun.* **2017**, *8* (1), 2144. DOI: 10.1038/s41467-017-01553-w.

(11)   Huang, Y.-G.; Jiang, F.-L.; Hong, M.-C. Magnetic Lanthanide–Transition-Metal Organic–Inorganic Hybrid Materials: From Discrete Clusters to Extended Frameworks. *Coord. Chem. Rev.* **2009**, *253* (23), 2814–2834. DOI: 10.1016/j.ccr.2009.05.007.

(12)   Piquer, L. R.; Sañudo, E. C. Heterometallic 3d–4f Single-Molecule Magnets. *Dalton Trans.* **2015**, *44* (19), 8771–8780. DOI: 10.1039/C5DT00549C.

(13)   Darago, L. E.; Boshart, M. D.; Nguyen, B. D.; Perlt, E.; Ziller, J. W.; Lukens, W. W.; Furche, F.; Evans, W. J.; Long, J. R. Strong Ferromagnetic Exchange Coupling and Single-Molecule Magnetism in MoS43−-Bridged Dilanthanide Complexes. *J. Am. Chem. Soc.* **2021**, *143* (22), 8465–8475. DOI: 10.1021/jacs.1c03098.

(14)   Letko, C. S.; Panetier, J. A.; Head-Gordon, M.; Tilley, T. D. Mechanism of the Electrocatalytic Reduction of Protons with Diaryldithiolene Cobalt Complexes. *J. Am. Chem. Soc.* **2014**, *136* (26), 9364–9376. DOI: 10.1021/ja5019755.

(15)   Evans, W. J.; Davis, B. L.; Champagne, T. M.; Ziller, J. W. C–H Bond Activation through Steric Crowding of Normally Inert Ligands in the Sterically Crowded Gadolinium and Yttrium (C5Me5)3M Complexes. *Proc. Natl. Acad. Sci.* **2006**, *103* (34), 12678–12683. DOI: 10.1073/pnas.0602672103.

(16)   Mrkvová, K.; Kameníček, J.; Šindelář, Z.; Kvítek, L.; Mrozinski, J.; Nahorska, M.; Žák, Z. Synthesis, Properties and Crystal Structures of R[MIII(Bdt)2] Complexes (M = Ni, Co, Cu). *Transit. Met. Chem.* **2004**, *29* (3), 238–244. DOI: 10.1023/B:TMCH.0000020349.69302.37.

(17)   Lim, B. S.; Fomitchev, D. V.; Holm, R. H. Nickel Dithiolenes Revisited: Structures and Electron Distribution from Density Functional Theory for the Three-Member Electron-

Transfer Series [Ni(S2C2Me2)2]0,1-,2-. *Inorg. Chem.* **2001**, *40* (17), 4257–4262. DOI: 10.1021/ic010138y.

(18) Maki, A. H.; Edelstein, N.; Davison, A.; Holm, R. H. Electron Paramagnetic Resonance Studies of the Electronic Structures of Bis(Maleonitriledithiolato)Copper(II), -Nickel(III), -Cobalt(II), and -Rhodium(II) Complexes. *J. Am. Chem. Soc.* **1964**, *86* (21), 4580–4587. DOI: 10.1021/ja01075a013.

(19) Selby-Karney, T.; Grossie, D. A.; Arumugam, K.; Wright, E.; Chandrasekaran, P. Structural and Spectroscopic Characterization of Five Coordinate Iron and Cobalt Bis(Dithiolene)-Tri-methylphosphine Complexes. *J. Mol. Struct.* **2017**, *1141*, 477–483. DOI: 10.1016/j.mol-struc.2017.03.119.

(20) Miessler, G. L.; Fischer, P. J.; Tarr, D. a. *Inorganic Chemistry*; 2013.

(21) Sandman, D. J.; Allen, G. W.; Acampora, L. A.; Stark, J. C.; Jansen, S.; Jones, M. T.; Ashwell, G. J.; Foxman, B. M. Nickel, Cobalt, and Copper Complexes of o-Benzenedise-lenolate: Synthesis and Structural and Magnetic Properties. *Inorg. Chem.* **1987**, *26* (11), 1664–1669. DOI: 10.1021/ic00258a007.

(22) Chilton, N. F.; Anderson, R. P.; Turner, L. D.; Soncini, A.; Murray, K. S. PHI: A Powerful New Program for the Analysis of Anisotropic Monomeric and Exchange-Coupled Polynu-clear d- and f-Block Complexes. *J. Comput. Chem.* **2013**, *34* (13), 1164–1175. DOI: 10.1002/jcc.23234.

(23) Willett, R. D.; Gatteschi, D.; Kahn, O. *Magneto-Structural Correlations in Exchange Cou-pled Systems*; D Reidel Publishing Co, 1985.

(24) Paulovič, J.; Cimpoesu, F.; Ferbinteanu, M.; Hirao, K. Mechanism of Ferromagnetic Cou-pling in Copper(II)-Gadolinium(III) Complexes. *J. Am. Chem. Soc.* **2004**, *126* (10), 3321–3331. DOI: 10.1021/ja030628k.

(25) Reta, D.; Chilton, N. F. Uncertainty Estimates for Magnetic Relaxation Times and Magnetic Relaxation Parameters. *Phys. Chem. Chem. Phys.* **2019**, *21* (42), 23567–23575. DOI: 10.1039/C9CP04301B.

(26) Blackmore, W. J. A.; Gransbury, G. K.; Evans, P.; Kragskow, J. G. C.; Mills, D. P.; Chilton, N. F. Characterisation of Magnetic Relaxation on Extremely Long Timescales. *Phys. Chem. Chem. Phys.* **2023**, *25* (25), 16735–16744. DOI: 10.1039/D3CP01278F.

(27) Liddle, S. T.; Slageren, J. V. Improving F-Element Single Molecule Magnets. *Chem. Soc. Rev.* **2015**, *44* (19), 6655–6669. DOI: 10.1039/c5cs00222b.

(28) Demir, S.; Zadrozny, J. M.; Nippe, M.; Long, J. R. Exchange Coupling and Magnetic Blocking in Bipyrimidyl Radical-Bridged Dilanthanide Complexes. *J. Am. Chem. Soc.* **2012**, *134* (45), 18546–18549. DOI: 10.1021/ja308945d.

(29) CrysAlis, P. Agilent Technologies Ltd, 2014.

(30) Sheldrick, G. SADABS, 1996.

(31) Dolomanov, O. V.; Bourhis, L. J.; Gildea, R. J.; Howard, J. a. K.; Puschmann, H. OLEX2: A Complete Structure Solution, Refinement and Analysis Program. *J. Appl. Crystallogr.* **2009**, *42* (2), 339–341. DOI: 10.1107/S0021889808042726.

(32) Bruker. APEX III, 2012.

(33) Bruker. SAINT, 2012.

(34) Bruker. SMART, 2012.

(35) Sheldrick, G. M. SHELXT – Integrated Space-Group and Crystal-Structure Determination. *Acta Crystallogr. Sect. Found. Adv.* **2015**, *71* (1), 3–8. DOI: 10.1107/S2053273314026370.

(36) Müller, P.; Herbst-Irmer, R.; Spek, A. L.; Schneider, T. R.; Sawaya, M. R. *Crystal Structure Refinement: A Crystallographer's Guide to SHELXL*; Oxford University Press, 2006. DOI: 10.1093/acprof:oso/9780198570769.001.0001.

(37) Bain, G. A.; Berry, J. F. Diamagnetic Corrections and Pascal's Constants. *J. Chem. Educ.* **2008**, *85* (4), 532. DOI: 10.1021/ed085p532.

(38) Chilton, N. F.; Collison, D.; McInnes, E. J. L.; Winpenny, R. E. P.; Soncini, A. An Electrostatic Model for the Determination of Magnetic Anisotropy in Dysprosium Complexes. *Nat. Commun.* **2013**, *4* (1), 2551. DOI: 10.1038/ncomms3551.

(39) Sellmann, D.; Kleine-Kleffmann, U.; Zapf, L.; Huttner, G.; Zsolnai, L. Übergangsmetall-Komplexe Mit Schwefelliganden: VII. Synthese Und Struktur Der Benzoldithiolato-Eisen-Komplexe [AsPh4]2[Fe(S2C6H4)2] Und [Fe(S2C6H4)(PMe3)3]. *J. Organomet. Chem.* **1984**, *263* (3), 321–331. DOI: 10.1016/0022-328X(84)85035-4.

(40) Cerdeira, A. C.; Afonso, M. L.; Santos, I. C.; Pereira, L. C. J.; Coutinho, J. T.; Rabaça, S.; Simão, D.; Henriques, R. T.; Almeida, M. Synthesis, Structure and Physical Properties of Transition Metal Bis 4-Cyanobenzene-1,2-Dithiolate Complexes [M(Cbdt)2]Z− (M=Zn, Co, Cu, Au, Ni, Pd, Z=0, 1, 2). *Polyhedron* **2012**, *44* (1), 228–237. DOI: 10.1016/j.poly.2012.07.010.

3.7 Supporting information
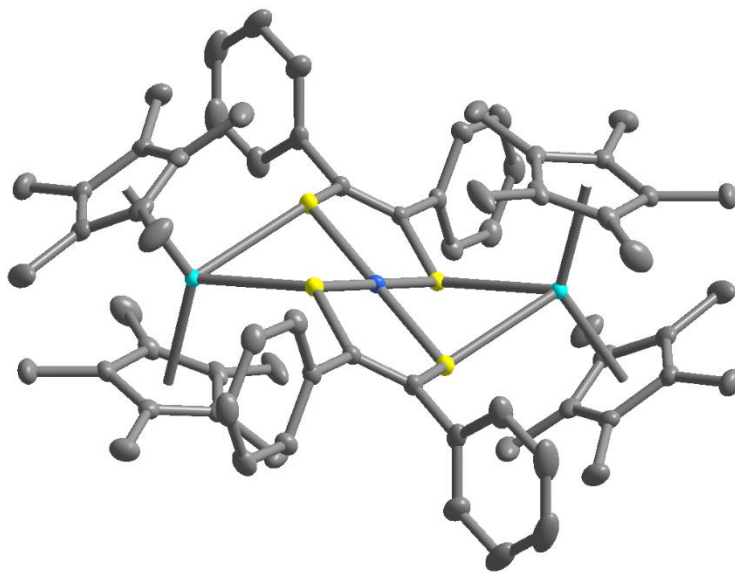
Figure S3.1: Crystal Structure of 1-Y. Ellipsoids drawn at 50% probability. Y, Cyan; Co, blue; C, gray; S, yellow. One lattice benzene and hydrogen atoms have been omitted for clarity.
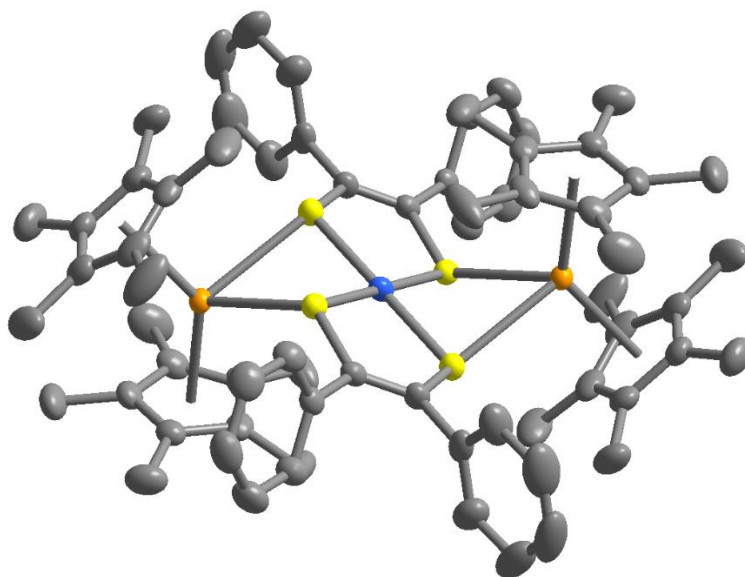
Figure S3.2. Crystal Structure of **1-Gd**. Thermal ellipsoids drawn at 50% probability. Gd, orange; Co, blue; C, gray; S, yellow. One lattice benzene and hydrogen atoms have been omitted for clarity
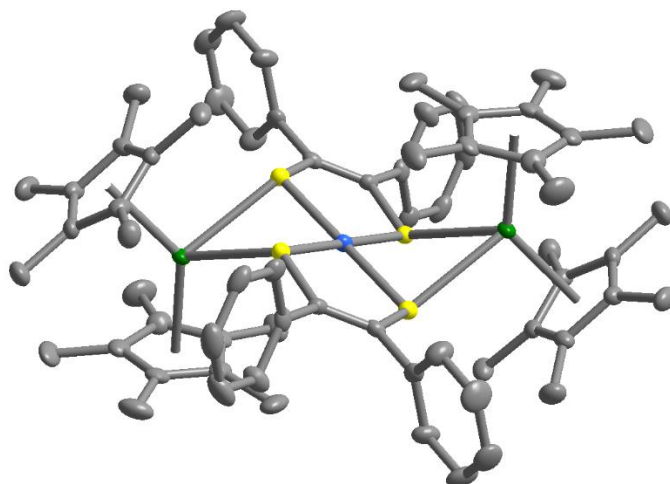
Figure S3.3. Crystal structure of 1-Dy. Thermal ellipsoids drawn at 50% probability. Dy, green; Co, blue; C, gray; S, yellow. One lattice benzene and hydrogen atoms have been omitted for clarity
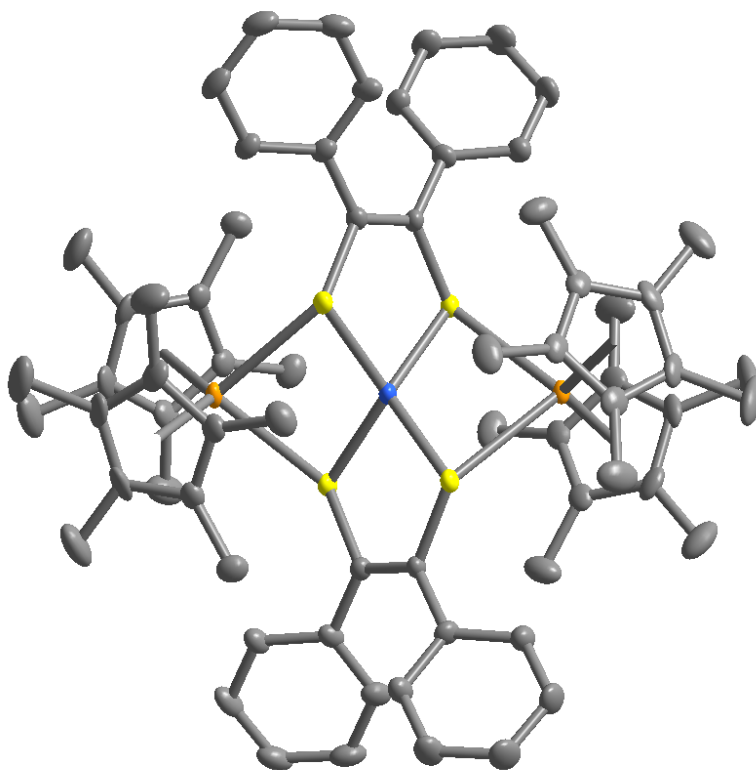
Figure S3.4. Crystal structure of 2-Gd. Thermal ellipsoids drawn at 50% probability. Gd, orange; Co, blue; C, gray; S, yellow. [K(18-crown-6)]⁺, hydrogen atom positions, and two outer sphere THF molecules omitted for clarity
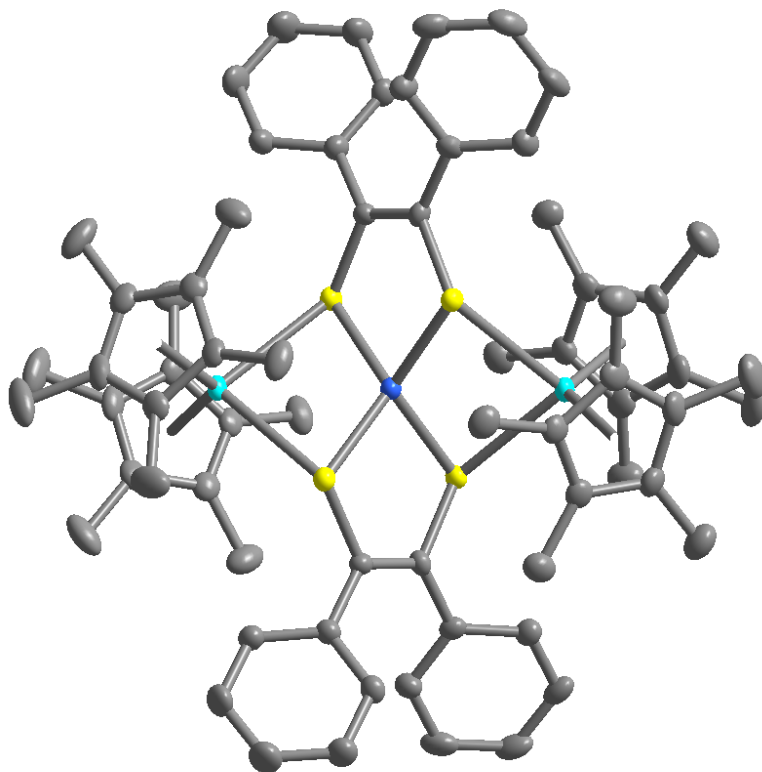
Figure S3.5. Crystal structure of 2-Y. Thermal ellipsoids drawn at 50% probability. Y, cyan; Co, blue; C, gray; S, yellow. [K(18-crown-6)]$^+$, hydrogen atom positions, and two outer sphere THF molecules omitted for clarity
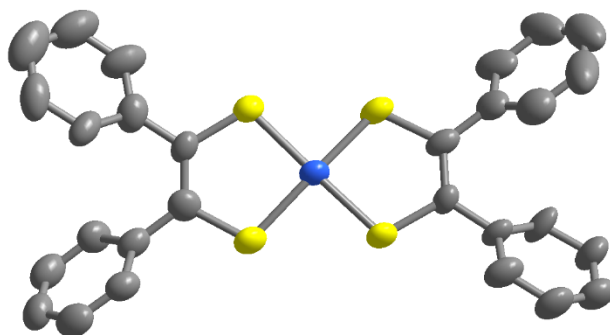
Figure S3.6. Crystal structure of [NBu₄]₂[Co(pdt)₂]. One of the two equally occupied and roughly equivalent disordered positions shown. Two symmetry equivalent [NBu₄]⁺ cations located above and below the square plane were omitted for clarity. Hydrogen atoms were assigned using a riding model. Hydrogen atom positions were also omitted for clarity. Thermal ellipsoids drawn at 50% probability. Co, light blue; C, gray; S, yellow.

Table S3.1. Crystal Data and Structural Refinement Parameters for **1-Ln** (Ln = Y, Gd, or Dy)

Identifier	1-Y	1-Gd	1-Dy
Empirical formula	$C_{80}H_{92}CoS_4Y_2$	$C_{80}H_{92}CoGd_2S_4$	$C_{74}H_{86}CoDy_2S_4$
Formula weight	1418.52	1555.2	1487.59
Temperature/K	100	250	100
Crystal system	monoclinic	monoclinic	monoclinic
Space group	C2/c	C2/c	C2/c
a/Å	25.6512(9)	25.9379(10)	28.7455(8)
b/Å	16.5239(6)	16.6026(5)	12.5826(4)
c/Å	18.7617(7)	19.0936(8)	19.5261(5)
α/°	90	90	90
β/°	117.766(2)	118.069(5)	107.859(2)
γ/°	90	90	90
Volume/Å^3	7036.6(5)	7255.3(6)	6722.1(3)
Z	4	4	4
ρ_{calc}g/cm^3	1.339	1.424	1.47
μ/mm^{-1}	1.444	2.19	2.767
F(000)	2964	3164	3012
Crystal size/mm^3	0.021 × 0.015 × 0.01	0.383 × 0.153 × 0.086	0.012 × 0.01 × 0.007
Radiation	synchrotron (λ = 0.6199)	Mo Kα (λ = 0.71073)	synchrotron (λ = 0.7288)
2Θ range for data collection/°	3.844 to 70.056	5.874 to 59.242	3.654 to 51.418
Index ranges	-47 ≤ h ≤ 47, -30 ≤ k ≤ 30, -34 ≤ l ≤ 34	-35 ≤ h ≤ 35, -22 ≤ k ≤ 21, -25 ≤ l ≤ 24	-34 ≤ h ≤ 34, -14 ≤ k ≤ 14, -23 ≤ l ≤ 23
Reflections collected	148784	64497	51220
Independent reflections	23407 [R_{int} = 0.0861, R_{sigma} = 0.0551]	9031 [R_{int} = 0.0746, R_{sigma} = 0.0447]	5930 [R_{int} = 0.0841, R_{sigma} = 0.0446]
Data/restraints/parameters	23407/0/404	9031/36/459	5930/1/377
Goodness-of-fit on F^2	1.008	1.048	1.058
Final R indexes [I>=2σ (I)]	R_1 = 0.0352, wR_2 = 0.0860	R_1 = 0.0282, wR_2 = 0.0617	R_1 = 0.0336, wR_2 = 0.0633
Final R indexes [all data]	R_1 = 0.0565, wR_2 = 0.0955	R_1 = 0.0393, wR_2 = 0.0645	R_1 = 0.0485, wR_2 = 0.0692
Largest diff. peak/hole / e Å^{-3}	0.60/-0.72	0.71/-0.42	1.94/-1.25

Table S3.2. Crystal Data and Structural Refinement Parameters for 2-Ln (Ln = Y or Gd) and [NBu$_4$]$_2$[Co(pdt)$_2$]

Identifier	**2-Gd**	**2-Y**	[NBu$_4$]$_2$[Co(pdt)$_2$]
Empirical formula	C$_{88}$CoGd$_2$KO$_8$S$_4$H$_{120}$	C$_{88}$H$_{120}$CoKO$_8$S$_4$Y$_2$	C$_{61.33}$H$_{90.67}$CoN$_2$O$_{0.33}$S$_4$
Formula weight	1846.60	1709.92	1048.43
Temperature/K	100	100	100
Crystal system	monoclinic	monoclinic	trigonal
Space group	P2/n	P2/n	R-3
a/Å	21.3826(8)	21.281(13)	28.7391(10)
b/Å	16.6097(6)	16.655(18)	28.7391(10)
c/Å	25.4404(9)	25.505(14)	18.6157(7)
α/°	90	90	90
β/°	91.086(2)	91.103(13)	90
γ/°	90	90	120
Volume/Å^3	9033.8(6)	9038(12)	13315.5(11)
Z	4	4	9
ρ_{calc}g/cm^3	1.358	1.257	1.177
μ/mm^{-1}	1.931	1.168	0.499
F(000)	3800.0	3600	5097
Crystal size/mm^3	0.016 × 0.01 × 0.007	0.07 × 0.01 × 0.01	0.02 × 0.02 × 0.01
Radiation	synchrotron (λ = 0.7288)	synchrotron (λ = 0.6199)	synchrotron (λ = 0.7288)
2Θ range for data collection/°	2.514 to 56.49	2.548 to 43.206	4.792 to 50.746
Index ranges	-27 ≤ h ≤ 27, -21 ≤ k ≤ 21, -33 ≤ l ≤ 33	-25 ≤ h ≤ 25, -19 ≤ k ≤ 19, -30 ≤ l ≤ 30	-33 ≤ h ≤ 33, -33 ≤ k ≤ 33, -21 ≤ l ≤ 21
Reflections collected	168184	145343	83588
Independent reflections	20740 [R$_{int}$ = 0.0928, R$_{sigma}$ = 0.0520]	15826 [R$_{int}$ = 0.1123, R$_{sigma}$ = 0.0593]	5048 [R$_{int}$ = 0.0641, R$_{sigma}$ = 0.0271]
Data/restraints/parameters	20740/57/1006	15826/9/1006	5048/126/595
Goodness-of-fit on F^2	1.102	1.077	1.055
Final R indexes [I>=2σ(I)]	R$_1$ = 0.0437, wR$_2$ = 0.1284	R$_1$ = 0.0556, wR$_2$ = 0.1642	R$_1$ = 0.0515, wR$_2$ = 0.1403
Final R indexes [all data]	R$_1$ = 0.0584, wR$_2$ = 0.1479	R$_1$ = 0.0839, wR$_2$ = 0.1838	R$_1$ = 0.0592, wR$_2$ = 0.1484
Largest diff. peak/hole / e Å^{-3}	2.08/-1.52	1.54/-0.68	0.32/-0.27

Table S3.3. 1-Ln (Ln = Y, Gd, Dy) selected distances. All distances are given in Å. LnCp$^{*}_{2}$ subunits are related by an inversion center at cobalt.

Type		1-Y	1-Gd	1-Dy
Co-S	Co01-S01	2.1745(3)	2.1771(5)	2.181(3)
Co-S	Co01-S02	2.1717(2)	2.1768(5)	2.173(2)
C-S (thiolate)	C01-S01	1.762(1)	1.766(2)	1.768(5)
C-S (thiolate)	C02-S02	1.764(1)	1.767(2)	1.771(5)
C-C (alkene)	C01-C02	1.345(1)	1.338(3)	1.336(6)
Ln-Cp*	Ln-Cp*1 (centroid)	2.34589(9)	2.3947(2)	3.352(3)
Ln-Cp*	Ln-Cp*2 (centroid)	2.35867(6)	2.4057(2)	3.369(2)
Ln-S	Ln-S01	2.8030(3)	2.8320(5)	2.826(3)
Ln-S	Ln-S02	2.8235(3)	2.8505(5)	2.849(3)

Table S3.4. Selected distances for **2-Ln** (Ln = Y or Gd). All distances are given in Å. Two unique molecules were observed in the unit cell for both 2-Y and 2-Gd, The first unique anion contained a C_2 axis along the Ln-Co-Ln axis, the other unique anion contained a C_2 axis which passes through the center of each pdt^{2-} alkene and cobalt. Subscripts are used to denote the unique ion under measurement. The structural differences between each molecule in the unit cell are within error of each other.

Type	2-Y$_1$	Distance (Å)	2-Y$_2$	Distance (Å)	2-Gd$_1$	Distance (Å)	2-Gd$_2$	Distance (Å)
Co-S	Co01-S01	2.248(2)	Co02-S03	2.240(2)	Co01-S01	2.242(1)	Co02-S03	2.235(1)
Co-S	Co01-S02	2.249(2)	Co02-S04	2.247(2)	Co01-S02	2.243(1)	Co02-S04	2.237(1)
C-S (thiolate)	C01-S01	1.774(5)	C03-S03	1.777(5)	C01-S01	1.771(5)	C03-S03	1.774(4)
C-S (thiolate)	C02-S02	1.771(5)	C04-S04	1.778(5)	C02-S02	1.774(4)	C04-S04	1.770(5)
C-C (alkene)	C01-C02	1.364(7)	C03-C04	1.348(7)	C01-C02	1.362(6)	C03-C04	1.351(6)
Ln-Cp*	Y01-Cp*1	2.394(1)	Y03-Cp*3	2.403(2)	Gd01-Cp*1	2.4312(2)	Y03-Cp*3	2.4362(2)
Ln-Cp*	Y02-Cp*2	2.399(1)	Y03-Cp*4	2.402(2)	Gd02-Cp*2	2.4313(2)	Y03-Cp*4	2.4316(2)
Ln-S	Y01-S01	2.779(2)	Y03-S03	2.786(2)	Gd01-S01	2.801(1)	Y03-S03	2.803(1)
Ln-S	Y02-S02	2.788(2)	Y03-S04	2.785(2)	Gd02-S02	2.793(1)	Y03-S04	2.799(2)

73

Table S3.5. [NBu$_4$]$_2$[Co(pdt)$_2$] selected distances. All distances are given in Å.

Type		Distance (Å)
Co-S	Co-S1	2.202(3)
Co-S	Co-S0	2.163(4)
Co-S	Co-S002	2.176(4)
Co-S	Co-S003	2.134(3)
C-S (thiolate)	S1-C1	1.760(9)
C-S (thiolate)	S0-C0	1.758(8)
C-S (thiolate)	S003-C007	1.739(9)
C-S (thiolate)	S002-C005	1.748(9)
C-C (alkene)	C007-C005	1.359(9)
C-C (alkene)	C1-C0	1.37(1)
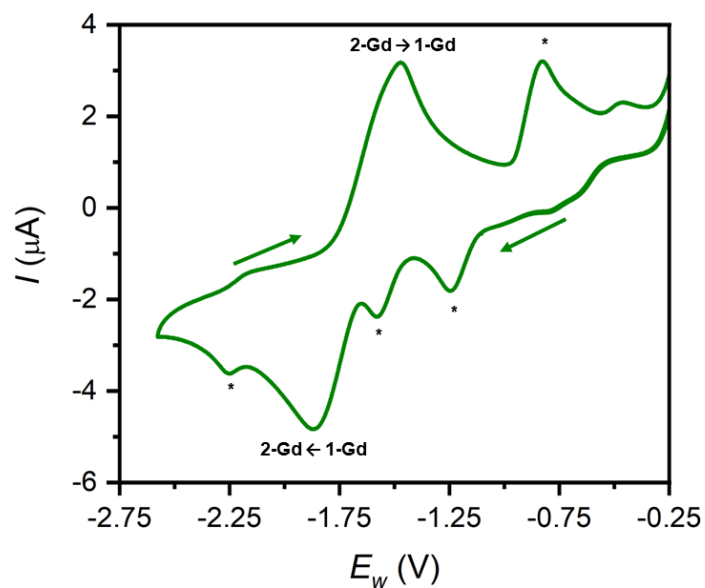
Figure S3. Cyclic voltammogram of 1.5 mM solution of **1-Gd** in 1,2-DFB with 0.1 M [nBu$_4$N][PF$_6$] supporting electrolyte. E_w= working electrode potential. I= current. Scan rate maintained at 50 mV/s. Arrows indicate scan trajectory. One electron reduction of 1-Gd was quasi-reversible. Cathodic asterisk represents irreversible oxidation of 1-Gd. Anodic asterisks represent irreversible reduction of irreversible oxidation products.

Table S3.6. Transition energies of 1-Gd and 2-Gd collected from their diffuse reflectance spectra. Values are reported in wavenumbers

Peak Index	1-Gd	2-Gd[a]
1	11570	5896
2	15564	7220
3	18324	13103
4	18867	15720
5	22054	17980
6	25420[b]	23621
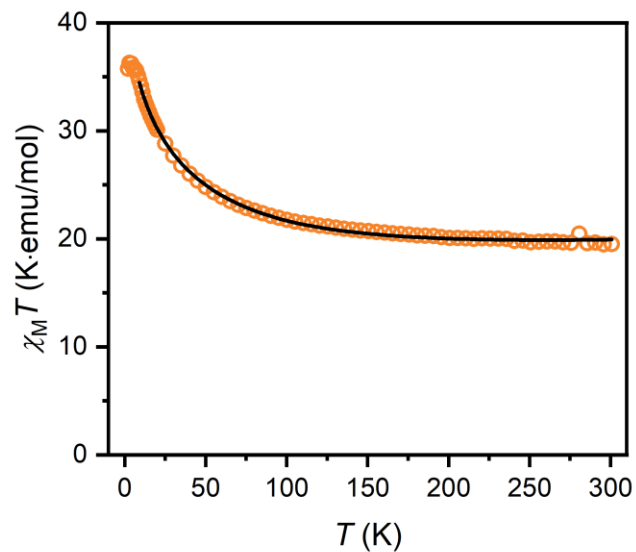
Figure S3.8. 1-Gd dc magnetic susceptibility measured under an applied field of 0.1 T. Solid line corresponds to fit to Equation S2 with fitted parameters: $J_{Gd\text{-}Co}$ = +11.48(8) cm^{-1}, zJ = 0.0045(1), TIP = 0.0068(1) cm$^3 \cdot$K/mol. zJ and TIP are corrections for intermolecular interactions and temperature independent paramagnetism respectively, as implemented in Phi.[22]
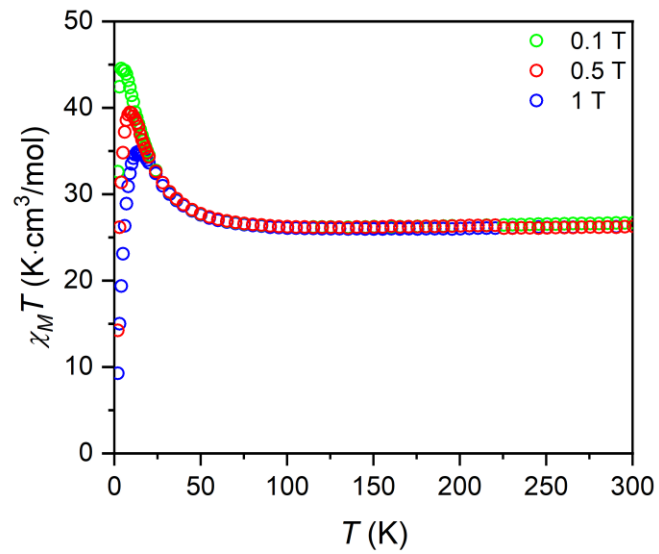
Figure S3.9. 1-Dy dc magnetic susceptibility measured under applied fields of 0.1 T (green circle), 0.5 T (red circles) and 1 T (blue circles)
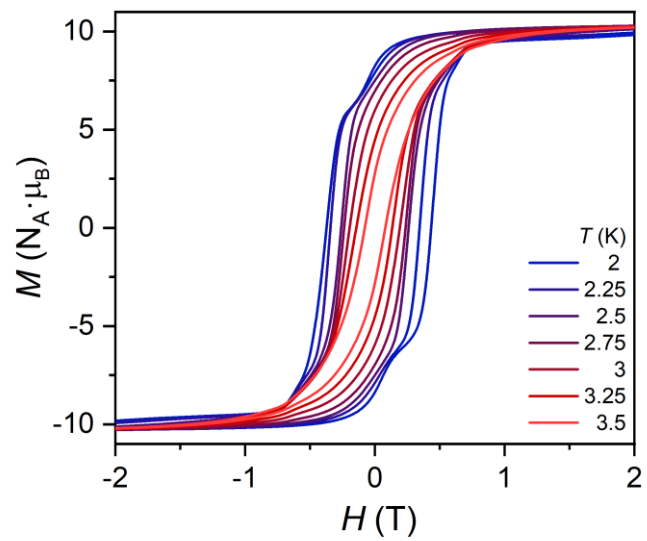
Figure S3.10. Variable field magnetic hysteresis loops of 1-Dy measured from 2 – 3.5 K
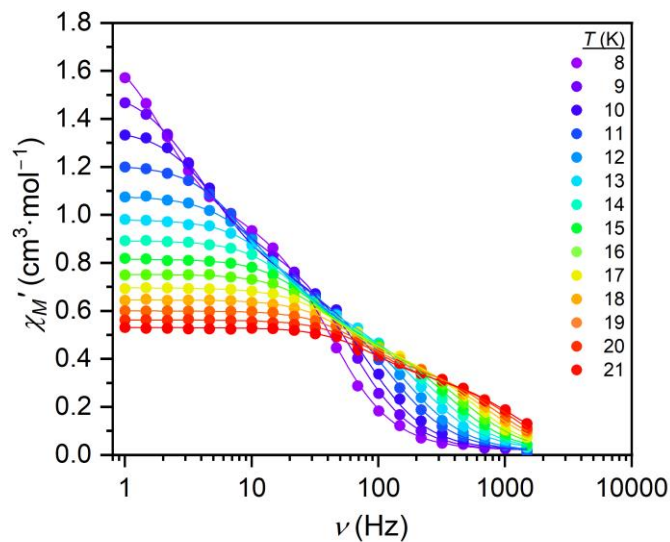
Figure S3.11. Variable frequency in-phase ac magnetic susceptibility of **1-Dy** measured from 8 – 21 K. Solid lines are fits to a dual-process generalized Debye model.
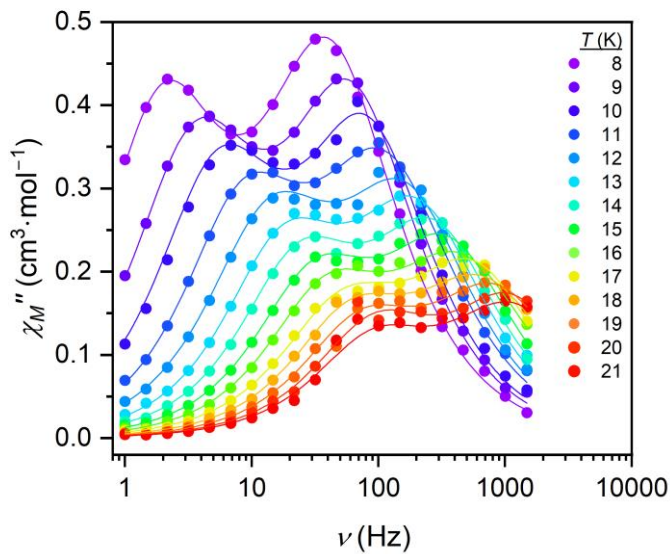
Figure S3.12. Variable frequency out of phase ac magnetic susceptibility of **1-Dy** measured from 6 – 20 K. Solid lines are fits to a dual-process generalized Debye model.

Table S3.7. Dual-mode Debye model fit parameters for **1-Dy**. Uncertainty values are given in parentheses.

T (K)	τ_1 (s)	$\Delta_{\chi 1}$ (cm^3/mol)	α_1	τ_2 (s)	$\Delta_{\chi 2}$ (cm^3/mol)	α_2	χ_{Total} (cm^3/mol)
8.00	0.00390(6)	0.97(1)	0.059(7)	0.081(1)	0.74(2)	0.00(2)	0.017(3)
9.00	0.00260(3)	0.84(1)	0.051(6)	0.0450(6)	0.67(1)	0.02(1)	0.016(2)
10.00	0.00181(4)	0.74(2)	0.04(1)	0.0274(7)	0.60(2)	0.01(2)	0.019(4)
11.00	0.00141(3)	0.70(2)	0.09(1)	0.0187(5)	0.50(2)	0.00(1)	0.006(3)
12.00	0.00096(3)	0.57(2)	0.05(2)	0.0116(4)	0.49(2)	0.03(2)	0.011(5)
13.00	0.00077(2)	0.56(2)	0.06(1)	0.0090(3)	0.41(2)	0.00(1)	0.015(4)
14.00	0.00057(2)	0.50(2)	0.05(2)	0.0068(2)	0.38(2)	0.00(2)	0.016(5)
15.00	0.00045(1)	0.47(3)	0.06(2)	0.0052(2)	0.34(1)	0.00(1)	0.007(5)
16.00	0.00035(2)	0.45(3)	0.08(3)	0.0041(2)	0.30(3)	0.00(3)	0.00(1)
17.00	0.00028(1)	0.39(3)	0.04(3)	0.0031(2)	0.29(2)	0.03(2)	0.008(9)
18.00	0.000234(9)	0.39(2)	0.08(3)	0.0026(1)	0.25(2)	0.00(2)	0.000(9)
19.00	0.00018(1)	0.36(4)	0.05(6)	0.0022(2)	0.24(3)	0.00(3)	0.00(2)
20.00	0.000140(8)	0.31(4)	0.01(7)	0.0017(1)	0.25(2)	0.01(3)	0.00(2)
21.00	0.00014(1)	0.32(6)	0.1(1)	0.0018(2)	0.21(3)	0.00(5)	0.00(3)
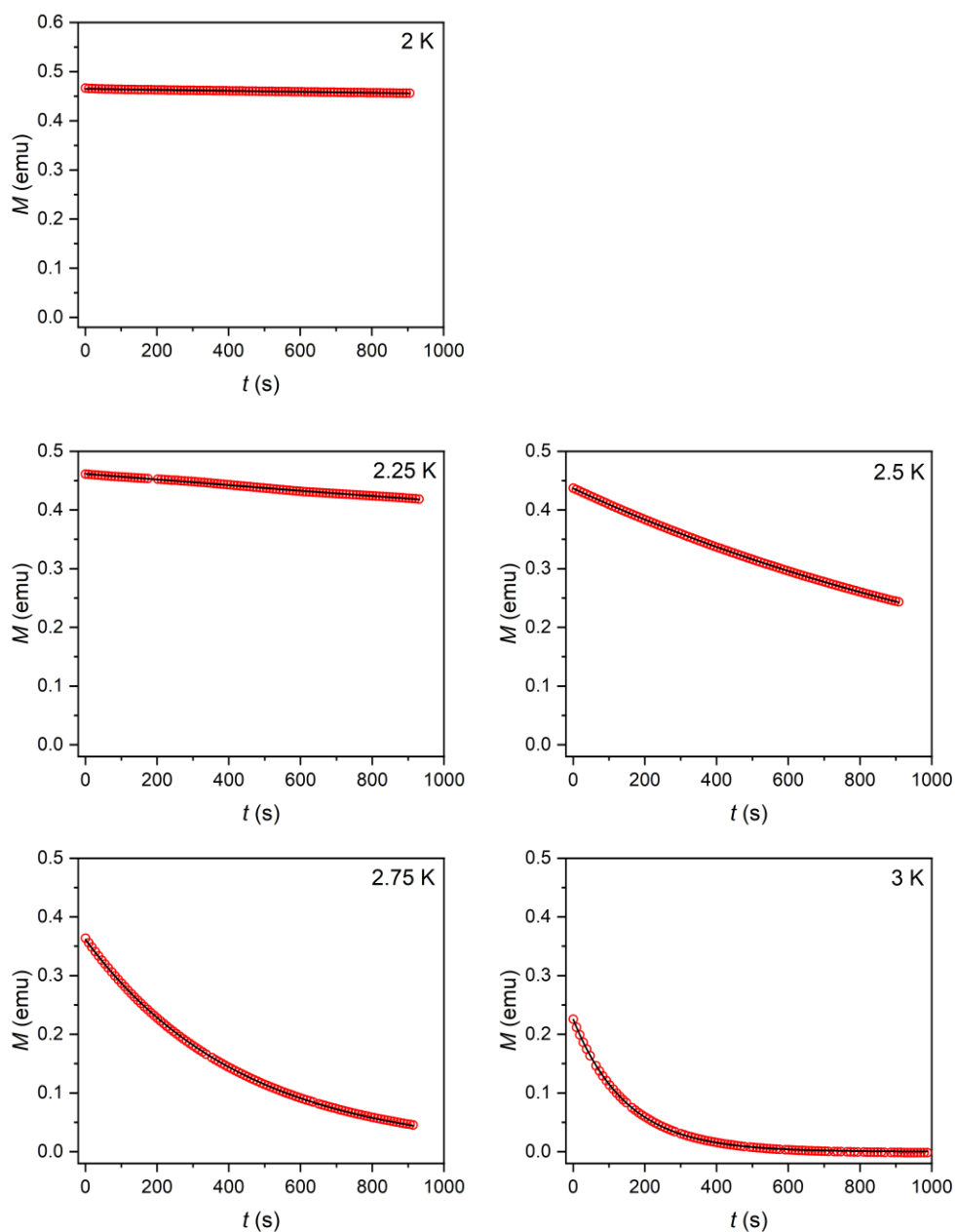
Figure S3.13. Isothermal magnetization decay measured from 2 – 3 K. Fit parameters τ and M_0 with parenthesized uncertainties: $T = 2.00$ K, $\tau = 45400(400)$ s, $M_0 = 0.46495(5)$ emu; $T = 2.25$ K, $\tau = 9350(60)$ s, $M_0 = 0.4617(2)$ emu; $T = 2.50$ K, $\tau = 1543(7)$ s, $M_0 = 0.43680(6)$ emu. $T = 2.75$ K, $\tau = 435.3(4)$ s, $M_0 = 0.3615(2)$ emu; $T = 3.00$ K, $\tau = 148.8(5)$ s, $M_0 = 0.2255(5)$ emu
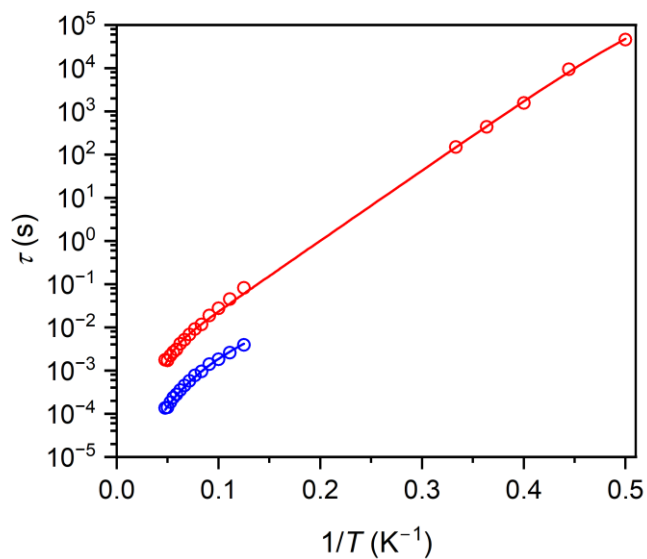
Figure S3.14. Arrhenius plot of **1-Dy**. Open circles correspond to average relaxation times derived from the dual-process model implemented in CCFIT2. Process A is colored blue, process B is colored red. Process A was fit in CCFIT2 using Equation S4. Process 2 was fit in CCFIT2 using Equation S5. Process A (blue) fit parameters: $C = 10^{-0.9(4)}\,\text{s}^{-1}\cdot\text{K}^{-n}$, $n = 3.6(3)$. Process B (red) fit parameters: $U_{\text{eff}} = 26.05(4)\,\text{cm}^{-1}$, $\tau_0 = 10^{-3.25(1)}$ s. $C = 10^{-7.37(2)}\,\text{s}^{-1}\cdot\text{K}^{-n}$ $n = 7.57(2)$.
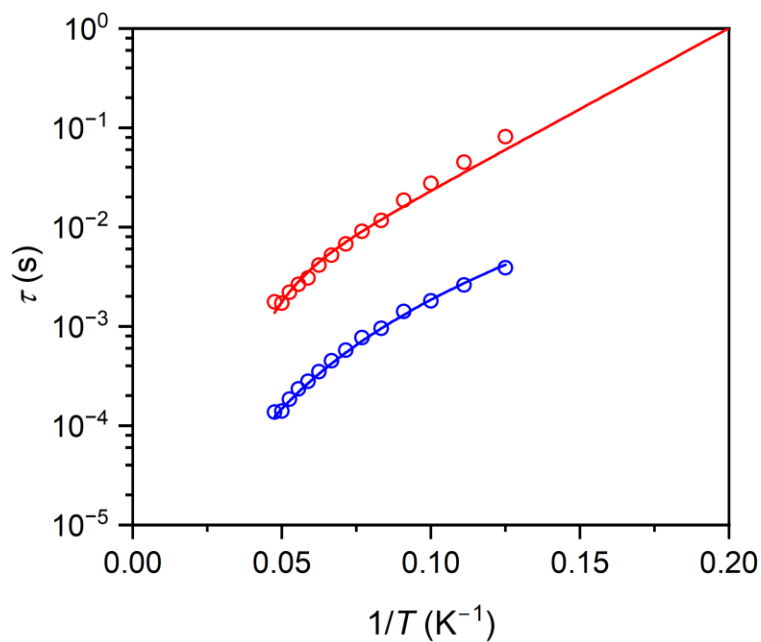
Figure S2.7.15. Arrhenius plot of 1-Dy within the ac susceptometry timescale. Open circles correspond to average relaxation times derived from the dual-process model implemented in CCFIT2. Process A was fit in CCFIT2 using Equation S4. Process 2 was fit in CCFIT2 using Equation S5. Process A (blue) fit parameters: $C = 10^{-0.9(4)}$ s$^{-1}\cdot$K^{-n}, $n = 3.6(3)$. Process B (red) fit parameters: $U_{eff} = 26.05(4)$ cm^{-1}, $\tau_0 = 10^{-3.25(1)}$ s. $C = 10^{-7.37(2)}$ s$^{-1}\cdot$K^{-n} $n = 7.57(2)$.
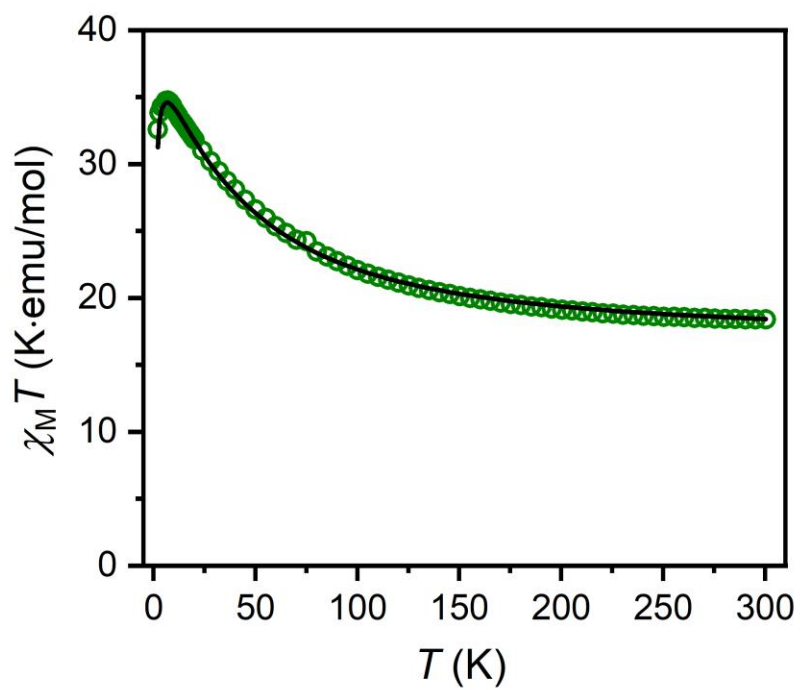
Figure S3.16. 2-Gd dc magnetic susceptibility measured under an applied field of 0.1 T. Solid line corresponds to fit to Equation S2 with fitted parameters: $D = 60(1)$ cm^{-1}, $|E/D| = 0.30(9)$ $J_{Gd-Co} = 7.33(4)$ cm^{-1}
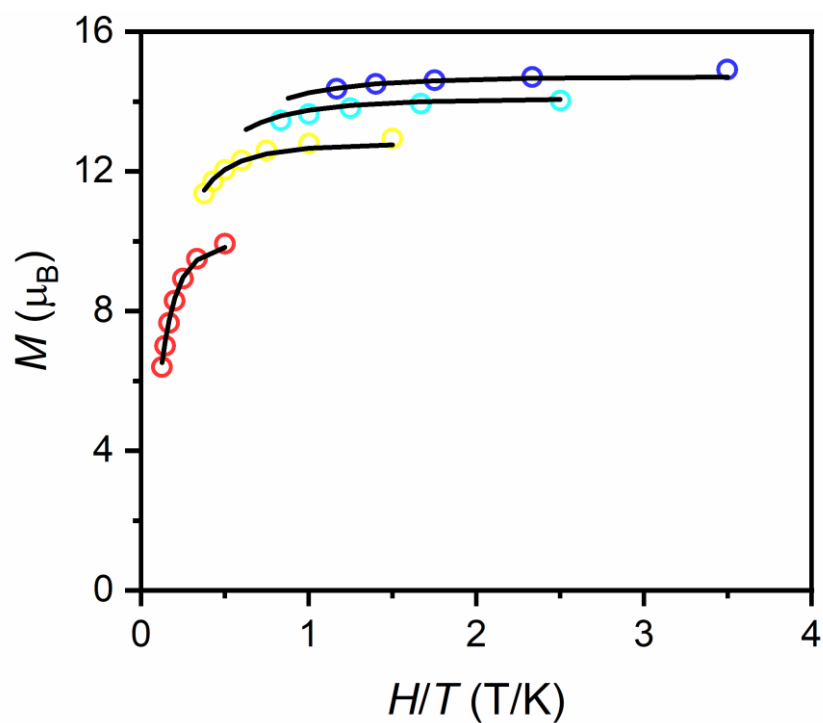
Figure S3.17. 2-Gd reduced magnetization measured under 1 T(red) 3 T(yellow) 5 T(cyan) and 7 T(blue) applied field. Solids lines represents fits to Equation S2 with fitted parameters: $D = 60(1)$ cm^{-1}, $|E/D| = 0.30(9)$ $J = 7.33(4)$ cm^{-1}
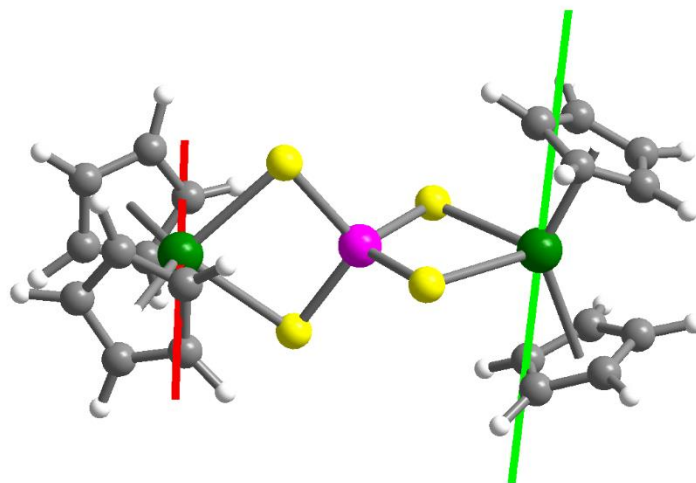
Figure S3.18. Calculated local quantization axes for simplified $[(Cp_2Dy)_2(MoS_4)]^{1-}$ structural model.[13] Calculations were carried out using Magellan.[38] Peripheral methyl substituents were removed and substituted with H atoms to simplify the process of assigning atomic charges. All C atoms were assigned a charge of -0.2. All S atoms were assigned a charge of -0.75. Dy was assigned a charge of +3, Mo and H were assumed to have no charge.
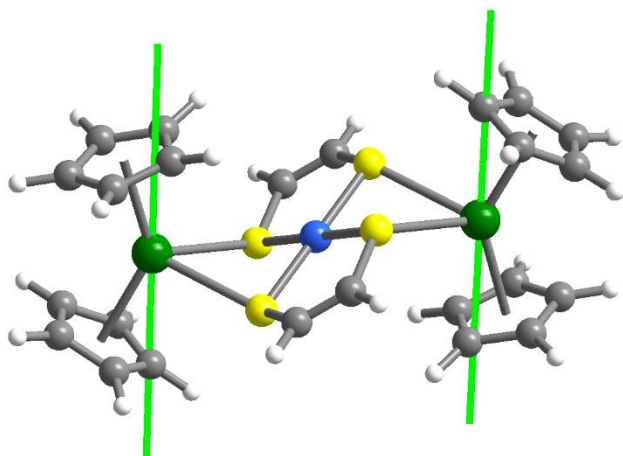
Figure S3.19. Calculated local quantization axes for simplified $(Cp_2Dy)_2(Co(pdt)_2)$ structural model. Calculations were carried out using Magellan.[38] Peripheral methyl substituents were removed and substituted with H atoms to simplify the process of assigning atomic charges. All Cp carbon atoms were assigned a charge of -0.2. All S atoms were assigned a charge of -0.4. Dy was assigned a charge of +3. Co assumed to carry no charge.
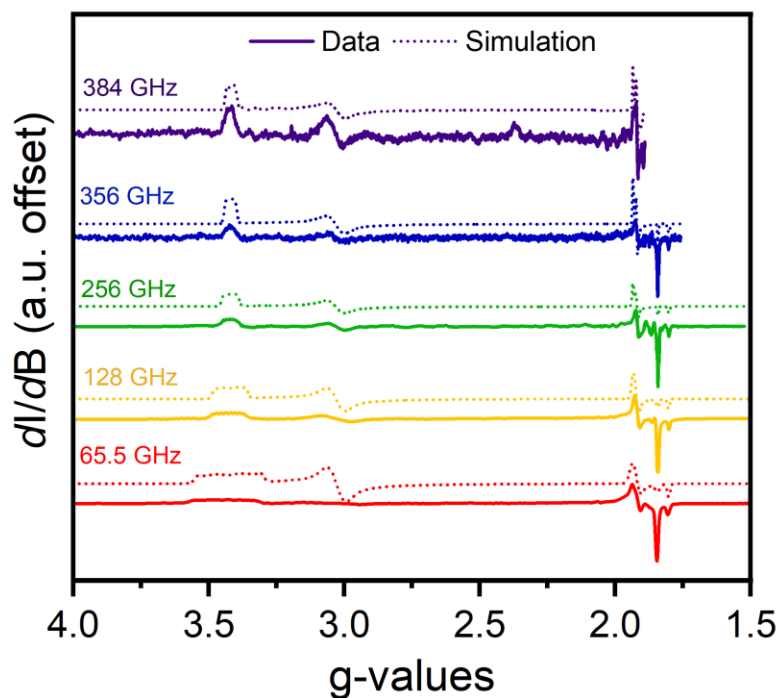
Figure S3.20. The HFEPR frequency dependence of **1-Y** with experimental traces (solid lines) and simulated traces (dotted lines). Two species are present, the **1-Y** anisotropic contribution with $g_x = 3.42$, $g_y = 3.03$ and $g_z \approx 1.8$. Hyperfine splitting is seen on the $g_x = 3.42$ peak, leading to the assignment of a purely Ax component in the simulation. An second isotropic contribution with $g \approx 1.8$-1.9 is assigned to an impurity, as it also appears in spectra of a degraded sample of **1-Y** and in the **2-Y** sample (not shown here).
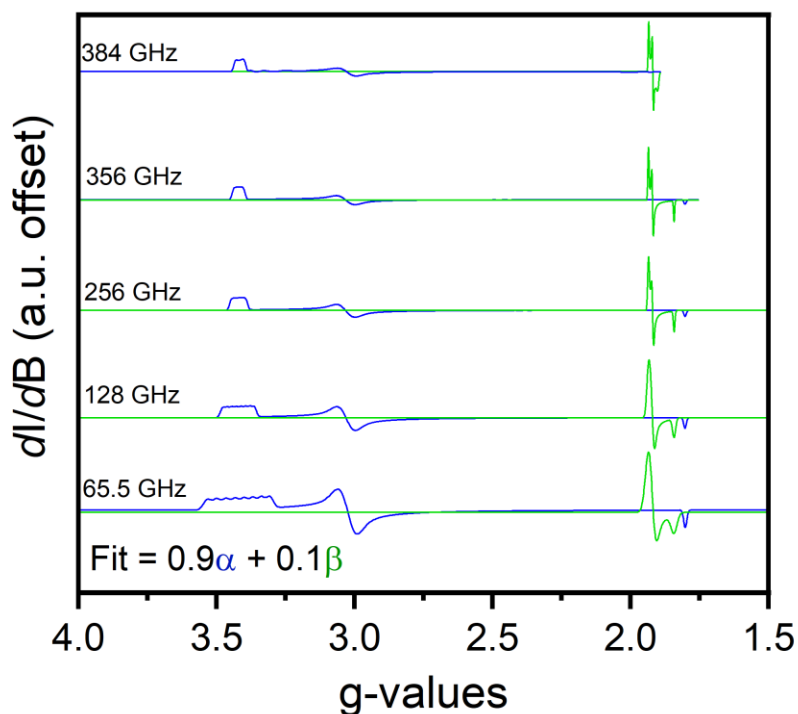
Figure S3.21. Deconvoluted Simulation of **1-Y** EPR Spectra. The frequency dependence enabled the identification of 2 species labelled α and β, individually simulated in blue and red respectively. The α component is an anisotropic low spin ($S=1/2$) cobalt species with $g_x = 3.42$, $g_y = 3.03$ and $g_z \approx 1.8$. Hyperfine splitting can be observed, with the pattern invariant in field as is characteristic of this zero-field interaction. This feature is only apparent on the $g_x = 3.42$ peak, leading to the assignment of a purely Ax component. The β component is more isotropic with all g-values around 1.8-1.9 and is assigned to an impurity. This feature is also observed in degraded samples (not shown here) suggesting the impurity is a form of the compound, namely free mono-nuclear Co(pdt)$_2$
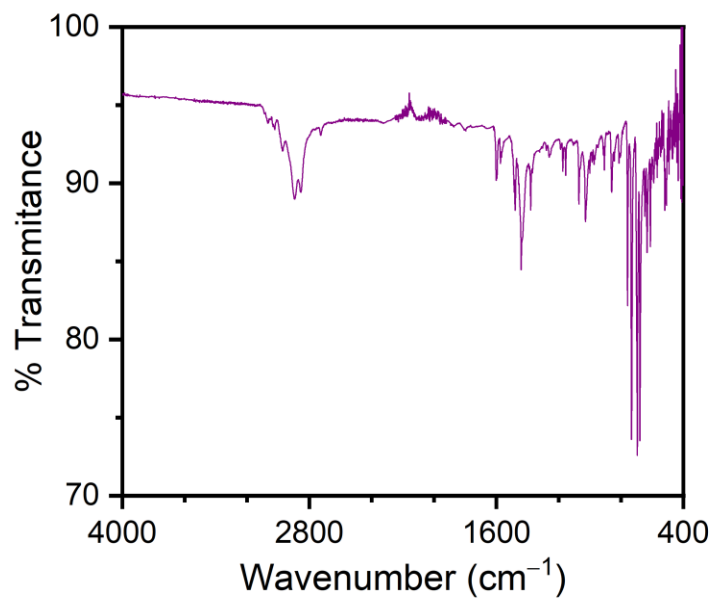
Figure S3.22. Fourier transform infrared spectrum of 1-Y
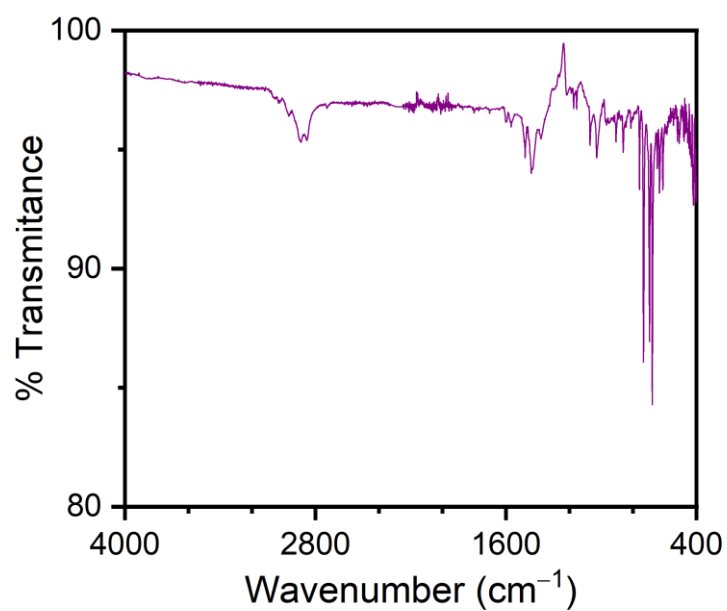
Figure S3.23. Fourier transform infrared spectrum of 1-Gd
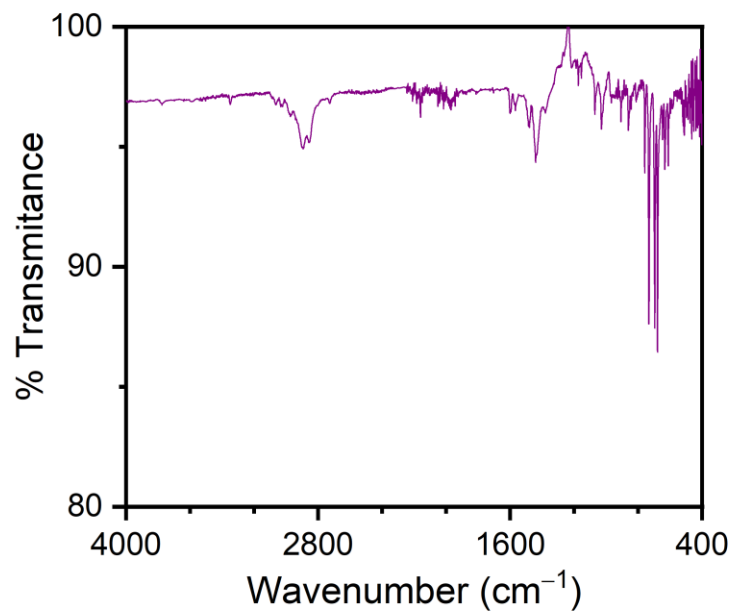
Figure S3.24. Fourier transform infrared spectrum of 1-Dy
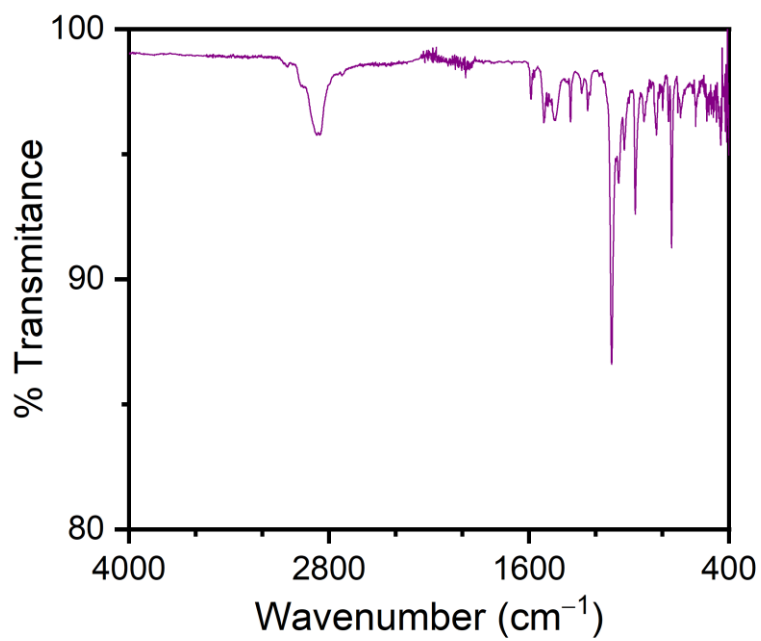
Figure S3.25. Fourier transform infrared spectrum of 2-Gd
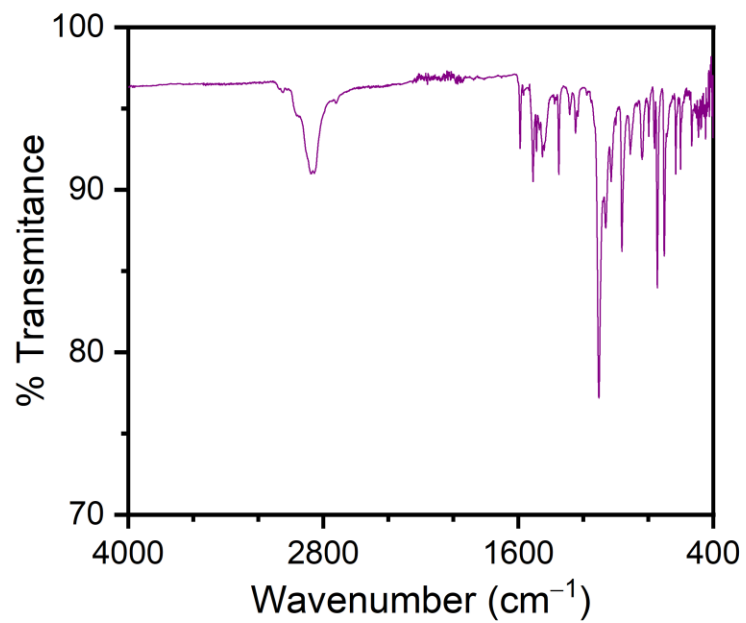
Figure S3.26. Fourier transform infrared spectrum of 2-Y
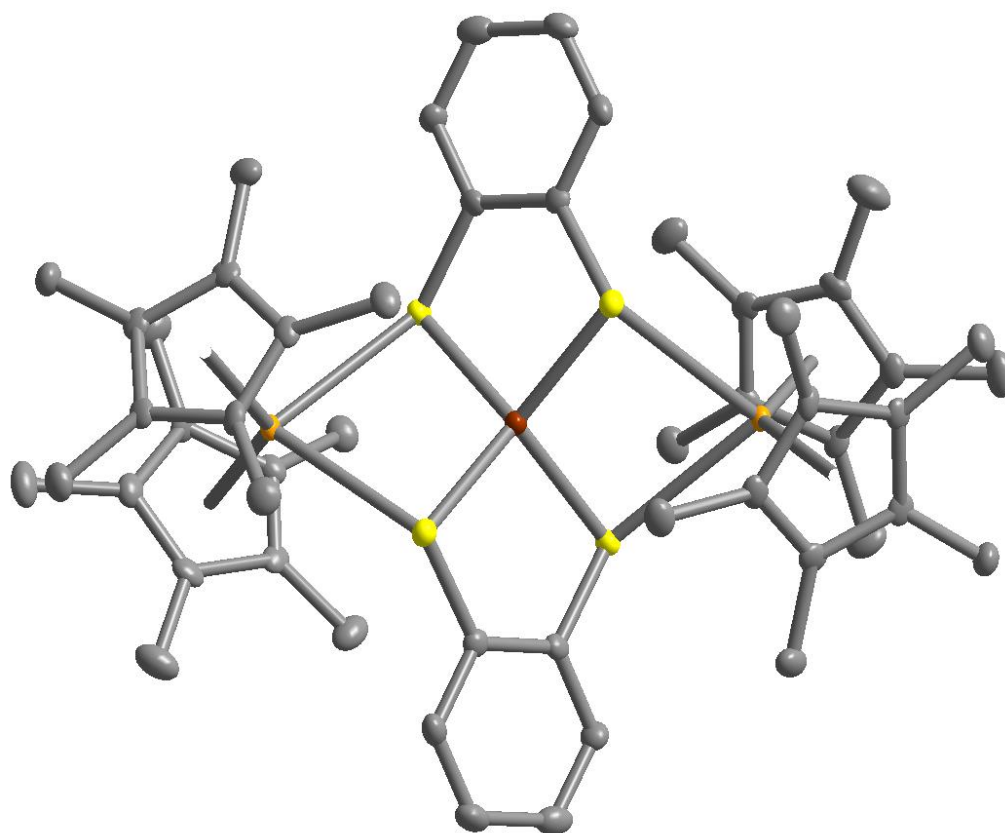
Figure S3.27. X-ray crystal structure of (Cp*₂Gd)₂(Fe(bdt)₂). Thermal ellipsoids are plotted at 50 % probability. Gd, Orange; Fe, red-orange; S, yellow; C, gray. Hydrogen atom positions were omitted for clarity
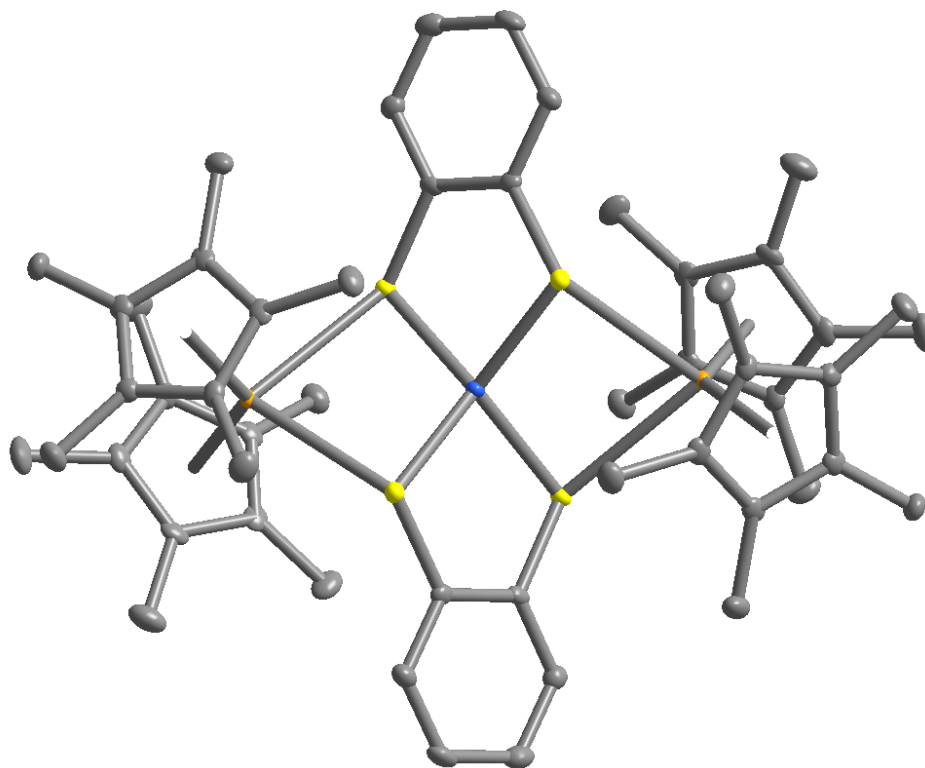
Figure S3.28. X-ray crystal structure of (Cp*$_2$Gd)$_2$(Co(bdt)$_2$). Thermal ellipsoids are plotted at 50 % probability. Gd, Orange; Co, blue; S, yellow; C, gray. Hydrogen atom positions were omitted for clarity

Table S3.8. Crystal Data and Structural Refinement Parameters for (Cp*$_2$Gd)$_2$(Fe(bdt)$_2$) and (Cp*$_2$Gd)$_2$(Co(bdt)$_2$)

Empirical formula	C$_{52}$H$_{68}$FeGd$_2$S$_4$	C$_{52}$H$_{68}$CoGd$_2$S$_4$
Formula weight	1191.65	1194.73
Temperature/K	100	100(2)
Crystal system	monoclinic	monoclinic
Space group	C2/c	C2/c
a/Å	13.1476(4)	13.1756(3)
b/Å	14.7191(5)	14.6666(3)
c/Å	26.1477(8)	26.2000(5)
α/°	90	90
β/°	101.470(3)	101.628(2)
γ/°	90	90
Volume/Å^3	4959.1(3)	4959.01(18)
Z	4	4
ρ_{calc}g/cm^3	1.596	1.6
μ/mm^{-1}	3.134	3.176
F(000)	2392	2396
Crystal size/mm^3	0.1 × 0.1 × 0.05	0.26 × 0.08 × 0.06
Radiation	Mo Kα (λ = 0.71073)	Mo Kα (λ = 0.71073)
2Θ range for data collection/°	5.636 to 46.508	5.556 to 52.738
Index ranges	-14 ≤ h ≤ 14, -13 ≤ k ≤ 16, -28 ≤ l ≤ 28	-16 ≤ h ≤ 16, -18 ≤ k ≤ 18, -32 ≤ l ≤ 32
Reflections collected	18182	32103
Independent reflections	3552 [R$_{int}$ = 0.0638, R$_{sigma}$ = 0.0402]	5086 [R$_{int}$ = 0.0464, R$_{sigma}$ = 0.0300]
Data/restraints/parameters	3552/0/277	5086/0/277
Goodness-of-fit on F^2	1.034	1.077
Final R indexes [I>=2σ (I)]	R$_1$ = 0.0251, wR$_2$ = 0.0595	R$_1$ = 0.0217, wR$_2$ = 0.0520
Final R indexes [all data]	R$_1$ = 0.0288, wR$_2$ = 0.0611	R$_1$ = 0.0245, wR$_2$ = 0.0529
Largest diff. peak/hole / e Å^{-3}	0.76/-0.74	0.69/-0.60

Chapter 4. Synthesis and Magnetic Characterization of a Dysprosium(III) Bis(borolide) Single Molecule Magnet

Vincent, A. H.[a]; Whyatt, Y. L.[b]; Chilton, N. F.[b]; Long, J. R. *J. Am. Chem. Soc.* **2023**, *145* (3), 1572–1579.

4.1: Introduction

Slow magnetic relaxation of molecular origin can be observed in paramagnetic complexes possessing a bistable magnetic ground state. Known as single-molecule magnets, such compounds can exhibit magnetic memory effects at the single molecule level.[1,2] A characteristic of single-molecule magnets is an intrinsic energy barrier to magnetization reversal, similar to that occurring in superparamagnetic nanoparticles,[2] which can be overcome by sequential spin-phonon excitations. Relaxation via this mechanism is known as the Orbach process, and the experimentally determined barrier is denoted U_{eff}.[1] Some of the most promising single-molecule magnets discovered to date are based on trivalent lanthanide ions, where the electronic states that define the U_{eff} barrier are the M_J levels of the ground Russel-Saunders spin-orbit term.[3] The splitting and mixing of these M_J states, and hence the nature of the magnetic anisotropy, can been manipulated using coordination chemistry.[4] As such, single-molecule magnets have attracted considerable attention for their potential use as a bit-patterned information storage medium, as well as their potential utility in the nascent field of quantum information science.[5–7]

While lanthanide single-molecule magnets have been the subject of intense study for nearly two decades, only recently was it discovered that mononuclear compounds containing dysprosocenium cations can exhibit open magnetic hysteresis near liquid nitrogen temperatures,[8–10] with 100-s blocking temperatures as high as $T_b = 65$ K in the case of $[Cp^{iPr5}DyCp^*][B(C_6F_5)_4]$ (Cp^{iPr5} = pentaisopropylcyclopentadienyl; Cp^* = pentamethylcyclopentadienyl).[8] These studies validated the notion that molecular magnets could retain magnetic memory at practical temperatures and have also contributed to the body of evidence showing that high-temperature hysteresis is not obtained solely through maximization of U_{eff}.[11,12] This general observation is illustrated through a comparison of the dysprosocenium compound $[Dy(Cp^{ttt})_2][B(C_6F_5)_4]$ (Cp^{ttt} = 1,2,4-tri(tert-butyl)cyclopentadienyl)[13] and the pentagonal bipyramidal complex salt $[Dy(O^tBu)_2(py)_5][B(C_6H_5)_4]$ (py = pyridine).[14] Although the experimental relaxation barrier of the former is comparable to that of the latter compound (1223(28) versus 1251(14) cm^{-1}, respectively),[15] the dysprosocenium compound exhibits open magnetic hysteresis at much higher temperatures (up to 60 versus 14 K). In the case of $[Dy(O^tBu)_2(py)_5][B(C_6H_5)_4]$, additional magnetization reversal pathways, namely two-phonon (Raman) and quantum tunneling of magnetization processes,[1] supersede Orbach relaxation at temperatures below 70 K and occur on faster timescales than in $[Dy(Cp^{ttt})_2][B(C_6F_5)_4]$. It has been shown that the remarkable performance of dysprosocenium-based compounds arises due to their strong axial ligand field, high-energy intramolecular vibrations, and low-energy intermolecular vibrations. The latter have the effect of suppressing the Raman relaxation mechanism,[16] while

---

[a] Vincent, A. H. carried out the synthesis, crystallographic characterization, and magnetometry presented in this chapter.

[b] Whyatt, Y. L. and Chilton, N. F. carried out the ab-initio electronic structure calculations as well as the ab-inito spin-dynamics calculations presented in this chapter.

it is speculated that the high-energy intramolecular vibrations also play a role in suppressing the quantum tunneling of magnetization.[17]

Recently, *ab initio* methods to understand the factors contributing to the very slow magnetic relaxation observed for dysprosocenium cations have been developed.[10,18–20] These studies revealed that both a large crystal field splitting (with appropriate uniaxial magnetic anisotropy) and a low density of vibrational modes near electronic excitation energies are important characteristics. However, these computations also suggest that the upper limit of the relaxation barrier in biscyclopentadienyl dysprosium compounds may have already been achieved, and as such, enhancements in blocking temperatures within that family should focus on structural modifications to minimize the vibrational modes that are on resonance with electronic excitations.[19] An alternative strategy is to target complexes analogous to the dysprosocenium compounds but possessing even stronger ligand fields in order to enhance the crystal field splitting, such as via heteroatom substitution in the cyclopentadienyl ring. To date, there is only one example of a dysprosium sandwich complex featuring a five-membered heterocycle, namely $[Dy(P(C^tBuCMe)_2)_2][B(C_6F_5)_4]$,[19] which features substituted phospholyl ligands and exhibits similar performance to some dysprosocenium single-molecule magnets[10] with a $U_{eff} = 1220(50)$ cm^{-1} and a 100-s blocking temperature of 23 K.[20]

In considering alternatives to the substituted dysprosocenium archetype, we sought to identify heterocycles that could provide structural rigidity and a stronger ligand field. Inspired by the linear divalent lanthanide metallocenes $Ln(Cp^{Ph5})_2$ (Ln = Eu, Yb; Cp^{Ph5} = pentaphenylcyclopentadienyl),[21,22] we hypothesized that a dysprosium sandwich complex featuring the dianionic pentaphenylborolide $(BC_4Ph_5)^{2-}$ ligand[23] might exhibit an even larger crystal field splitting—and hence a larger barrier to magnetic relaxation—than members of the dysprosocenium family, as a result of the larger negative charge on the ligands. Further, the phenyl substituents might lead to higher-energy intramolecular C–C vibrational modes than characterized for dysprosocenium compounds with alkyl substituents. Here, we present the synthesis and characterization of [K(18-crown-6)][Dy(BC_4Ph_5)_2] (**1**), featuring such an anionic Dy^{III} sandwich complex. Of note, while the present work was under review, a related study was published on the magnetic properties of the compound $[K(2.2.2-cryptand)][Dy(BC_4Ph_4Pip)_2]$ $((BC_4Ph_4Pip)^{2-} = 1$-(piperidino)-2,3,4,5-tetraphenylborolide),[24] which features a similar anionic Dy^{III} bis(borolide) sandwich complex. We find that our compound **1** exhibits a large relaxation barrier of $U_{eff} = 1500(100)$ cm^{-1} and a 100-s blocking temperature of $T_b = 65$ K that are among the highest reported to date among dysprosium single-molecule magnets and comparable with the magnitudes of U_{eff} and T_b reported for [K(2.2.2-cryptand)][Dy(BC_4Ph_4Pip)_2].[8,24,25]

4.2: Results and Discussion

The compound [K(18-crown-6)][Dy(BC_4Ph_5)_2] (**1**) was synthesized via salt metathesis of anhydrous DyCl$_3$ with K$_2$BC$_4$Ph$_5$ in tetrahydrofuran (THF) followed by the addition of a small stoichiometric excess of 18-crown-6 (Scheme 4.1; see the Experimental methods section for details). Dark red parallelepiped crystals were grown by layering a concentrated THF solution of the crude compound with diethyl ether. Single crystal x-ray diffraction analysis revealed these crystals to be the solvated compound [K(18-crown-6)(THF)_2][Dy(BC_4Ph_5)_2] (**1·2THF**; Figure 4.1), in which two THF molecules are axially bound to the [K(18-crown-6)]$^+$ countercation.
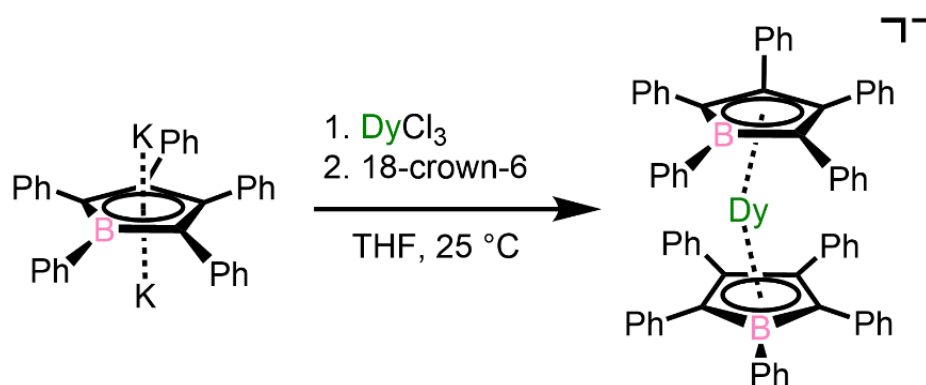
Scheme 4.1. Synthesis of **1**·2THF from potassium pentaphenylborolide and DyCl$_3$. The [K(18-crown-6)(THF)$_2$]$^+$ countercation in the product is not shown
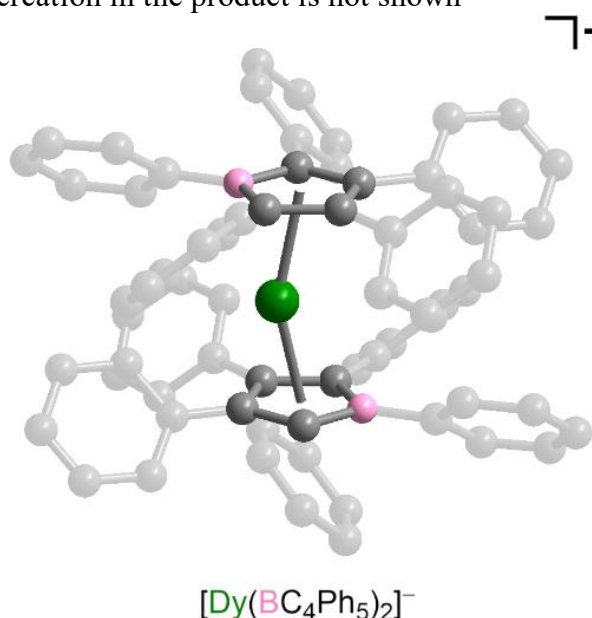
$[Dy(BC_4Ph_5)_2]^-$

Figure 4.1. Structure of one of the unique [Dy(BC$_4$Ph$_5$)$_2$]$^-$ anions in the structure of **1**·2THF as determined via single-crystal x-ray diffraction. Green, grey, and pink spheres represent Dy, C, and B atoms, respectively. Hydrogen atoms, the lower occupancy dysprosium site, inversion-related dysprosium sites, and the [K(18-crown-6)(THF)$_2$]$^+$ cation are omitted for clarity. Selected interatomic distances and angles are provided in Table S4.2.

The compound **1**·2THF crystallizes in the space group P–1 with two unique complex ions in the unit cell, each having identical connectivity but with slightly different bond lengths and angles (see Table S4.2). The Dy^{III} center in each unique anionic complex is disordered about a crystallographic inversion center located at the center of the molecule. For each unique anion, two partially occupied dysprosium sites were identified with variable occupancies totaling to 0.5. Applying the inversion operation yielded two more symmetry equivalent positions for each anion, affording a total Dy occupancy across all disordered positions of ~1. The average Dy–centroid distance is 2.326 Å, and the average centroid–Dy–centroid bend angle is 156.5°, within the range of reported values (2.273(7)–2.358(6) Å and 146.4(5)–162.50(12)°, respectively) for substituted

dysprosocenium cations.[8,9,13] In the structure of [K(2.2.2-cryptand)][Dy(BC₄Ph₄Pip)₂], the dysprosium(III) was modeled as disordered over two sites with average Dy–centroid distances and centroid–Dy–centroid bend angles of 2.259 Å and 161.4(3)° and 2.269 Å and 158.6(3)°, respectively, which are slightly larger than those determined for **1**·2THF.[24] We ascribe these differences to the greater electron donating ability of piperidyl over phenyl and the greater overall steric bulk of $(BC_4Ph_4Pip)^{2-}$ relative to $(BC_4Ph_5)^{2-}$. Non-covalent edge-to-face interactions between phenyl groups of the individual $(BC_4Ph_5)^{2-}$ ligands in **1**·2THF are also apparent from close edge-to-face distances. These interactions, in concert with the steric bulk of the ligands, stabilize the desired axial coordination geometry. We note that all magnetic characterization data described below were collected for a sample of **1**·2THF dried under reduced pressure for a minimum of 30 min to remove bound solvent. This was done to avoid any uncertainty in the bulk composition (molecular mass) of the sample being measured and therefore the quantitative magnetic results (see Magnetometry section in Section 4.4 for details). Inductively coupled plasma optical emission spectrometry analysis of a sample prepared in this way revealed Dy, K, and B content consistent with the fully-desolvated formula $[K(18\text{-crown-}6)][Dy(BC_4Ph_5)_2]$ (**1**). The local coordination environment around the Dy^{III} centers is not expected to change substantially with loss of the two outer-sphere THF molecules, and therefore we expect there to be limited impact on the magnetic properties (see the discussion of the magnetic properties below for additional details).
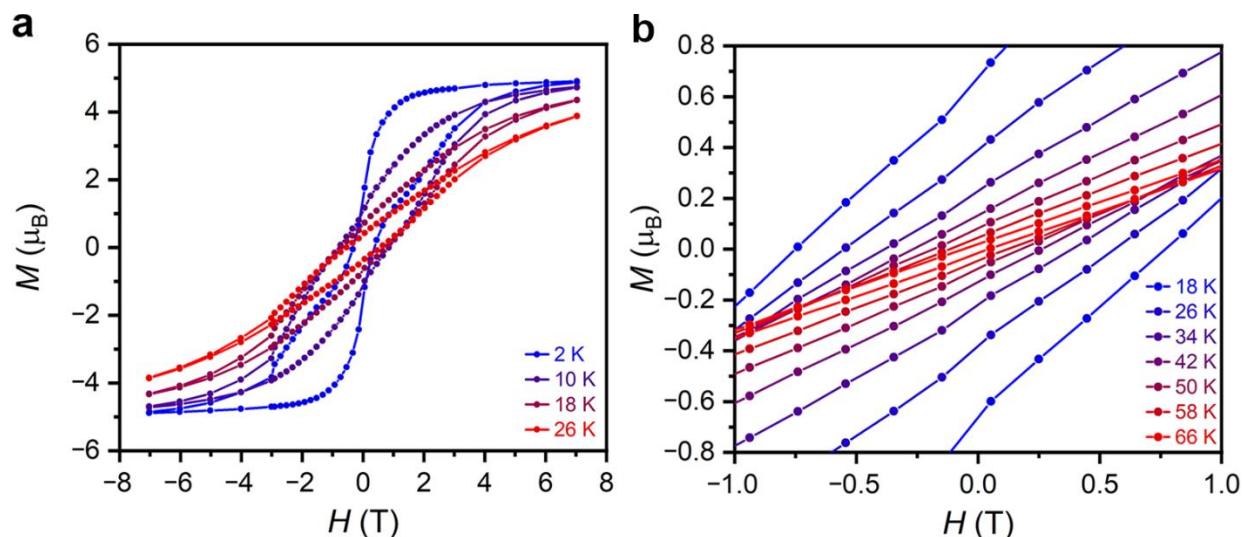
Figure 4.2. (a) Variable-field magnetization curves for **1** at select temperatures. A sweep rate of 84 Oe/s was used for data collected below 3 T, whereas a sweep rate of 165 Oe/s was used for data collected above 3 T. (b) Expanded view of the variable-field magnetization curves for **1** between ±1 T at the indicated temperatures.

State-average complete active space self-consistent field spin-orbit (CASSCF-SO) calculations were performed in OpenMolcas[26] using the single-crystal structure of one of the $[Dy(BC_4Ph_5)_2]^-$ anions in **1**·2THF; the active space comprised nine electrons in seven 4f orbitals of Dy^{III}. These calculations predict that the crystal field splitting of the $^6H_{15/2}$ ground state is approximately 1800 cm⁻¹, which is comparable with that predicted for the two disordered components in $[K(2.2.2\text{-cryptand})][Dy(BC_4Ph_4Pip)_2]^{24}$ (1713 and 1638 cm⁻¹) and slightly smaller than

the total crystal field splitting of 2104 cm^{-1} calculated for [Cp^{iPr5}DyCp*][B(C$_6$F$_5$)$_4$].[8] Projecting the spin-orbit states onto a crystal field Hamiltonian with SINGLE_ANISO,[27] the calculations predict a pure $M_J = \pm^{15}/_2$ ground state (easy-axis magnetic anisotropy; see Tables S4.11 and S4.12), and the first four excited state terms (well-approximated by $M_J = \pm^{13}/_2, \pm^{11}/_2$, and $\pm^9/_2$, respectively) are also highly axial; however, the effective g-values of the remaining Kramers doublets are significantly non-axial. Based on the calculated energies of the sixth Kramers doublet from two different levels of theory, U_{eff} is predicted to be between 1420 and 1480 cm^{-1}.
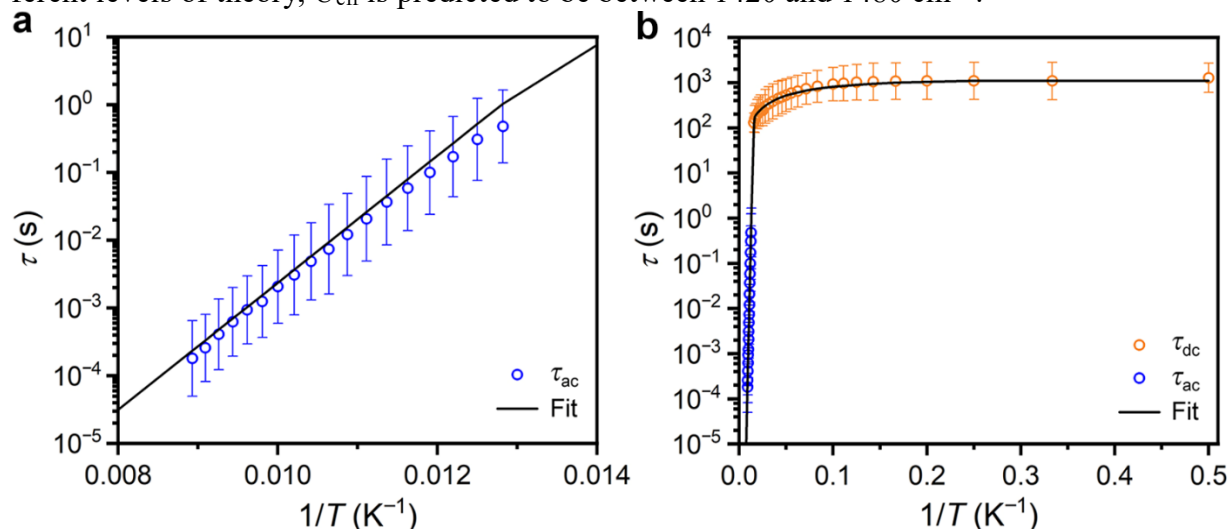
Figure 4.3. (a) Plot of the magnetic relaxation times (τ, log scale) versus $1/T$ determined for **1** from ac susceptibility data (blue symbols) and corresponding fit using eq 1 as described in the text. Estimated standard deviations at the 1σ level from the generalized Debye model are indicated with error bars.[15] (b) Plot of the magnetic relaxation times (τ, log scale) versus $1/T$ determined for **1** from dc relaxation data (orange symbols) and ac susceptibility data (blue symbols) and corresponding fit using equation 4.1 as described in the text. Estimated standard deviations at the 1σ level for the ac data are from the generalized Debye model and indicated with error bars.[15] Estimated standard deviations at the 1σ level for the dc data were calculated according to the empirical formula given in Table S4.3.[20]

$$\log_{10}[\tau^{-1}] = \log_{10}[10^{-Q} + 10^R T^n + 10^{-A} e^{-U_{eff}/k_B T}] \qquad \text{(Equation 4.1)}$$

Variable-field magnetization data were collected for 1 between ±7 T as an initial probe of slow magnetic relaxation. Open-loop magnetic hysteresis was apparent at temperatures as high as 66 K (Figure 2), comparable to the highest hysteresis temperature of 70 K reported for [K(2.2.2-cryptand)][Dy(BC$_4$Ph$_4$Pip)$_2$] (determined using a sweep rate of 9 Oe/s).[24] At 2 K, the slightly waist-restricted hysteresis may arise due to quantum tunneling of the magnetization. The magnetic remanence and coercive field at this temperature are 1.77 μ_B and 0.34 T, respectively. Frequency-dependent ac magnetic susceptibility data were collected for **1** to investigate the mechanism(s) of magnetic relaxation at higher temperatures (see the Supporting Information for details). Under zero dc field, peaks were apparent in the out-of-phase magnetic susceptibility at temperatures ranging from 78 to 112 K. Plots of the molar in-phase (χ_M') and out-of-phase (χ_M'') components of the

ac susceptibility versus frequency (Figures S4.18 and S4.19) were fit to the generalized Debye model[15] to extract temperature-dependent relaxation times (τ). As shown in Figure 3a, the resulting plot of τ (natural log scale) versus T (inverse scale) is approximately linear, indicating relaxation via an Orbach mechanism.[28]

Temperature-dependent dc magnetic relaxation measurements were also carried out to determine relaxation times at lower temperatures from 2 to 64 K. These data could be adequately fit using a stretched exponential function (see Figures S4.12–S4.14, Table S4.3, and the Supporting Information for details), which is frequently employed to extract relaxation times from magnetization decay data.[2,28] The τ values derived from the dc relaxation measurements (log scale) are plotted versus $1/T$ in Figure 3b along with the corresponding data from the ac relaxation measurements. Below ~10 K the data are nearly temperature-independent, consistent with relaxation via quantum tunneling of the magnetization. Between 10 and 64 K, the relaxation times for each process exhibit a weak temperature dependence consistent with a two-phonon Raman process.

The combined relaxation times obtained from the ac susceptibility and dc magnetic relaxation data were fit with CCFIT2[15] using Equation 4.1 (where A and Q are the negative logarithms of the attempt time (τ_0) and tunneling time (τ_{tun}), respectively, and C and n are the Raman prefactor exponent and temperature exponent, respectively) to give $U_{eff} = 1500(100)$ cm^{-1}, $\tau_0 = 10^A = 10^{-12.0(9)}$ s, $C = 10^R = 10^{-5(1)}$ s^{-1} K^{-n}, $n = 1.3(8)$ and $\tau_{tun} = 10^Q = 10^{3.1(3)}$ s (Figure 3, black curve). Importantly, the fitted value of U_{eff} is in very good agreement with that predicted from CASSCF-SO calculations using the optimized structure of $\mathbf{1}\cdot$2THF, supporting our assertion that desolvation should not significantly impact the magnetic properties. We also attempted to prepare a magnetic sample of the pristine solvated compound, $\mathbf{1}\cdot$2THF, immediately following recrystallization and after only brief (a few seconds) exposure to dynamic vacuum to remove crystallization solvent. However, dc magnetic susceptibility data collected for this sample (see Figures S4.10 and S4.11) suggest that the sample readily desolvates (see Magnetometry Section of Experimental methods for details). Even still, a suite of magnetic data collected for this second sample (see Tables S4.4, S4.6, and S4.7; Figures S4.10, S4.11, S4.15–S4.17, and S4.21–S4.24) support the reproducibility of the data collected for compound $\mathbf{1}$. Indeed, the fit parameters ($U_{eff} = 1600(100)$ cm^{-1}, $\tau_0 = 10^A = 10^{-12.6(8)}$ s, $C = 10^R = 10^{-5(2)}$ s^{-1} K^{-n}, $n = 1(1)$ and $\tau_{tun} = 10^Q = 10^{3.1(3)}$ s) are within error of those determined for $\mathbf{1}$.

The estimated $U_{eff} = 1500(100)$ cm^{-1} for $\mathbf{1}$ is among the highest values reported to date for dysprosium-containing single-molecule magnets,[8–10,19] and comparable to the magnitudes of the two U_{eff} values reported for [K(2.2.2-cryptand)][Dy(BC$_4$Ph$_4$Pip)$_2$] (1600(100) and 1300(300) cm^{-1}), which were ascribed to the two disordered components in the structure.[24] Interestingly, quantum tunneling in $\mathbf{1}$ is at least an order of magnitude faster than in [Cp^{iPr5}DyCp*][B(C$_6$F$_5$)$_4$] ($\tau_{tun} \sim 10^4$ s), as suggested by the narrowed hysteresis loops observed for compound $\mathbf{1}$ (Figure 4.2a). The Raman exponent is quite small but similar in magnitude to those determined for dysprosocenium cations and [K(2.2.2-cryptand)][Dy(BC$_4$Ph$_4$Pip)$_2$].[10,16,24] Such low values arise in the so-called "high-temperature" limit of traditional approximations to the Raman mechanism, where the Debye frequency of the lattice acoustic phonons is larger than $k_B T/\hbar$.[16,29]

In addition to U_{eff}, another metric often used to compare single-molecule magnets is the so-called magnetic blocking temperature (T_b), which has been defined as the temperature at which the magnetic relaxation time is equal to 100 s.[2] From the fit of the ac and dc relaxation data for $\mathbf{1}$, we

can estimate $T_b = 65$ K, which is among the highest values reported to date for a dysprosium single-molecule magnet. The same blocking temperature was reported for [Cp^{iPr5}DyCp*][B(C$_6$F$_5$)$_4$] (T_b = 65 K),[8] while a 100-s blocking temperature of 66 K was determined for [K(2.2.2-cryptand)][Dy(BC$_4$Ph$_4$Pip)$_2$].[24] To our knowledge, the only compound to exhibit a higher 100-s blocking temperature is the mixed-valent dinuclear complex (Cp^{iPr5})$_2$Dy$_2$I$_3$, with T_b = 72 K.[25]
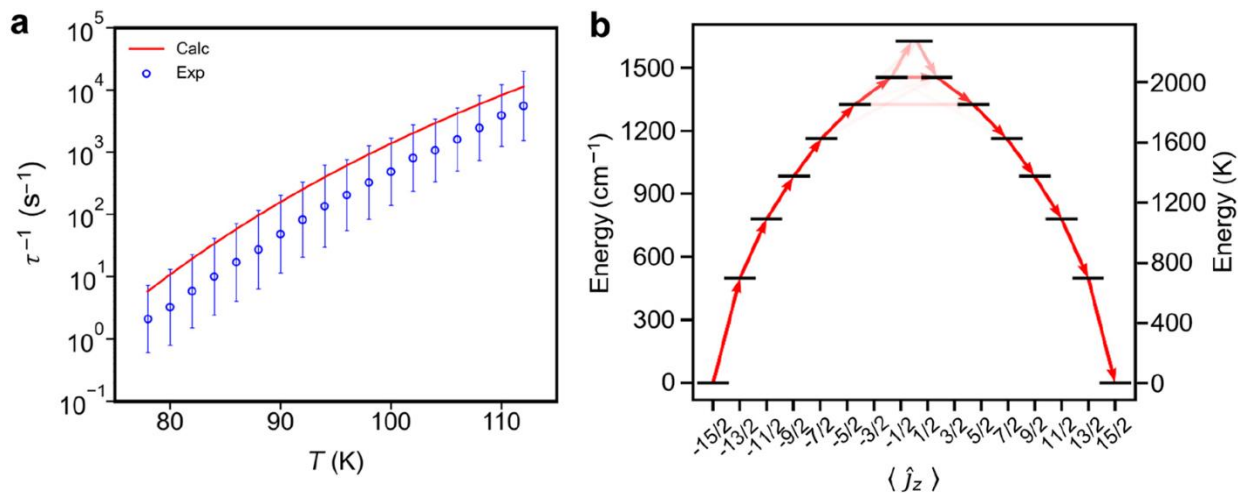
Figure 4.4. (a) Temperature dependence of calculated (red line, FWHM = 10 cm^{-1}, **1-PBE**) and experimental (blue symbols) relaxation rates. Error bars are 1σ estimated standard deviations determined from the generalized Debye model.[15] (b) Electronic states of the eight Kramers doublets of the ground ^{6}H$_{15/2}$ multiplet of **1-PBE**. Red arrows represent relaxation pathways, where the opacity of each arrow is proportional to the normalized spin-phonon transition probability.

To gain insight into the molecular origin of the high-temperature relaxation in **1**, we performed spin-dynamics calculations using a method previously described by some of us.[19] Gas-phase geometry optimizations and vibrational normal mode calculations were performed on one of the [Dy(BC$_4$Ph$_5$)$_2$]$^-$ anions in **1·2THF** using Gaussian 09d,[30] where the PBE (leading to structure 1-PBE) and PBE0 (leading to structure 1-PBE0) density functionals and Grimme's empirical dispersion correction were employed.[31–33] The root-mean-square deviations between the optimized [Dy(BC$_4$Ph$_5$)$_2$]$^-$ structures and the experimental structure were found to be only 0.245 and 0.236 Å for 1-PBE and 1-PBE0, respectively. We then used OpenMolcas[26] to perform state-average CASSCF-SO calculations on the optimized equilibrium structures of the anion (active space: nine electrons in seven 4f orbitals) and projected the spin-orbit states onto a crystal field Hamiltonian.[27] The spin-phonon coupling coefficients of each vibrational mode were determined by distorting the equilibrium geometry of 1-PBE and 1-PBE0 along their normal mode coordinates in positive and negative directions, and performing CASSCF-SO calculations to obtain the derivatives of the crystal field parameters via finite differences.

With the spin-phonon coupling coefficients in hand, we calculated magnetic relaxation times using Fermi's Golden Rule.[19] Here, the only free parameter is the full-width-at-half-maximum (FWHM) vibrational linewidth, and we considered values of 5, 10, and 20 cm^{-1}. The relaxation rate was generally found to increase with increasing linewidth (Figure S4.27), due to more modes coming into resonance with the relevant electronic transitions. The calculated relaxation rates are

in good agreement with experimental data (Figures 4.4a and Figure S4.27). In particular, at a fixed linewidth of 10 cm^{-1}, the results for 1-PBE0 are in excellent agreement with experiment (Figure S4.28). The results for 1-PBE would only require a slight decrease in the FWHM linewidth in order to bring them to the same level of agreement (Figure 4.4a), but we do not perform such an optimization here. Instead, to be consistent with our previous work, we will here focus on results using the PBE density functional and a FWHM linewidth of 10 cm^{-1}.[19] Based on the results of our *ab initio* spin phonon coupling calculations, relaxation via the Orbach mechanism likely proceeds via the fifth or sixth excited Kramers doublets, as illustrated in the diagram in Figure 4.4b.

In order to facilitate a more direct comparison of factors dictating Orbach relaxation in 1 and dysprosocenium complexes, we selected $[Cp^{iPr5}DyCp^*][B(C_6F_5)_4]$[8] and $[Dy(Cp^{iPr4})_2][B(C_6F_5)_4]$,[9] which exhibit the slowest and fastest relaxation rates in the Orbach region for this family of compounds. A comparison of the experimental temperature-dependent relaxation times revealed that compound 1 exhibits faster relaxation than the former but slower relaxation than the latter compound (Figure S4.29a), and this ordering is also borne out by our *ab initio* calculations (Figure S4.29b). To gain insight into this result, we performed a mode-weighted analysis comparing 1 with these two dysprosocenium compounds (see Computational methods section for additional details). Briefly, in this approach, we decompose the relaxation rate matrix of a compound into its components (spin-phonon coupling $\langle \bar{\bar{H}}_{SP} \rangle$, phonon occupation $\langle \bar{\bar{Q}} \rangle$, phonon density of states $\langle \bar{\rho} \rangle$, and average number of phonon modes $\langle \bar{\bar{n}} \rangle$), substitute one of these components for the equivalent component from another compound, solve the master equation by diagonalizing the rate matrix, and assesses how this changes the relaxation rate. However, as the rates are eigenvalues of the rate matrix, substitution of components does not always result in exact reciprocity. For example, substituting the spin-phonon coupling $\langle \bar{\bar{H}}_{SP} \rangle$ from molecule X into the rate matrix for molecule Y may increase the relaxation rate by an order of magnitude, but one may not observe the reciprocal numerical decrease in the relaxation rate if the $\langle \bar{\bar{H}}_{SP} \rangle$ from molecule Y is used for molecule X. Hence, the safest analysis is made by looking at the largest changes, and for consistency in the direction of changes under reciprocal swaps.

The largest change for any swap between 1 and $[Cp^{iPr5}DyCp^*][B(C_6F_5)_4]$ occurs when $\langle \bar{\bar{H}}_{SP} \rangle$ from 1 is used for $[Cp^{iPr5}DyCp^*][B(C_6F_5)_4]$, rendering relaxation in $[Cp^{iPr5}DyCp^*][B(C_6F_5)_4]$ approximately five times faster; the reciprocal swap ($\langle \bar{\bar{H}}_{SP} \rangle$ from $[Cp^{iPr5}DyCp^*][B(C_6F_5)_4]$ into 1) results in a decrease in the relaxation rate of 1 by a factor of ~2 (Table S4.17). These changes are consistent in their direction and with the overall difference in relaxation rates between the two compounds (Figure S4.29); swapping other components has a smaller effect, and also shows non-reciprocity. Hence, this analysis suggests that compound 1 exhibits faster relaxation than $[Cp^{iPr5}DyCp^*][B(C_6F_5)_4]$ due to overall stronger spin-phonon coupling. Comparing 1 with $[Dy(Cp^{iPr4})_2][B(C_6F_5)_4]$, the largest change is observed when the phonon occupation $\langle \bar{\bar{Q}} \rangle$ from 1 is substituted into $[Dy(Cp^{iPr4})_2][B(C_6F_5)_4]$, which renders relaxation in $[Dy(Cp^{iPr4})_2][B(C_6F_5)_4]$ 14 times slower; the reciprocal swap (when $\langle \bar{\bar{Q}} \rangle$ is swapped from $[Dy(Cp^{iPr4})_2][B(C_6F_5)_4]$ into 1) results in nearly an order of magnitude increase in the relaxation of 1; all other swaps have a far less significant effect (Table S4.18). Hence, this analysis suggests that 1 is a higher-performance single-molecule magnet than $[Dy(Cp^{iPr4})_2][B(C_6F_5)_4]$ because of its larger crystal field splitting.[19]

While our original hypothesis was that the formally dianionic borolide ligands could engender a larger crystal field splitting in the ground state of dysprosium(III)—and therefore give rise to a larger U_{eff}—than monoanionic cyclopentadienide ligands, the performance of **1** is similar to its dysprosocenium relatives. Given the similar structural metrics between the dysprosocenate anion in **1** and known dysprosocenium cations, this suggests that the effective charges on the ligands are also similar. To explore this possibility, we performed DFT calculations on the isolated ligands $(BC_4Ph_5)^{2-}$, $(Cp^{ttt})^-$, $(Cp^{iPr5})^-$, $(Cp^*)^-$ and $[P(C^tBuCMe)_2]^-$ in the gas phase and used Löwdin population analysis to infer effective atomic charges (see the Computational Metods section for details). These calculations give aggregate charges on the five-membered rings of −0.71, −0.90, −0.60, −0.68 and −0.78, respectively (Tables S4.19 and S4.20). It is clear from these data that the BC_4 ring in $(BC_4Ph_5)^{2-}$ does not hold double the anionic charge compared to its monoanionic counterparts, and that the phenyl rings withdraw significant charge (approximately −0.2 to −0.3, Table S4.19). Hence, along with the structural similarities described above, these data serve to explain the similar performance of **1** compared to dysprosocenium-based single-molecule magnets. Our results also suggest that the design of dysprosium bis(borolide) complexes featuring ligands with electron-donating substituents is a worthwhile pursuit.

4.3: Conclusions and Outlook

We have detailed the synthesis and characterization of a new dysprosium(III) compound featuring dianionic borolide ligands, $[K(18\text{-crown-}6)][Dy(BC_4Ph_5)_2]$ (**1**), which is a single-molecule magnet with performance comparable to the state-of-the art dysprosocenium compounds and the recently discovered dysprosium(III) bis(borolide) complex $[Dy(BC_4Ph_4Pip)_2]^-$.[24] In particular, compound **1** displays magnetic hysteresis with a 100-s magnetic blocking temperature of 65 K, and analysis of ac magnetic susceptibility data showed it to exhibit a single Orbach relaxation process with $U_{eff} = 1500(100)$ cm^{-1} and $\tau_0 = 10^{-A} = 10^{-12.0(9)}$ s. *Ab initio* calculations of the spin dynamics of **1** predicted relaxation rates in the Orbach regime in excellent agreement with the experimentally determined rates. Further, our mode-weighted analysis suggests that although the crystal field splitting of **1** is slightly smaller than that of the top-performing dysprosocenium single-molecule magnet $[Cp^{iPr5}DyCp^*][B(C_6F_5)_4]$,[8] stronger spin-phonon coupling in **1** is the more important factor influencing its faster relaxation dynamics. As such, an exciting area of future investigation will be the synthesis and study of other substituted dysprosocenate complexes with the goal of identifying substituents that will minimize spin-phonon coupling in this system. Further, our DFT calculations suggest that enhancement of the crystal field splitting in dysprosium bis(borolide) complexes may also be achieved through judicious choice of electron-donating functional groups. Notably, there are a large number of reported substituted boroles,[34,35] which could conceivably undergo reduction and subsequent metalation with Dy^{III}. As a result of the more diverse substitution chemistry of the borole heterocycle relative to cyclopentadiene, a potentially large and diverse family of new dysprosocenate compounds featuring strongly axial borolide ligands is accessible.

4.4: Experimental Methods

Material Preparation

All manipulations were carried out under an atmosphere of argon with rigorous exclusion of air and water using either standard Schlenk line techniques or a glovebox. Commercial reagents were used directly without further treatment unless otherwise noted. Anhydrous $DyCl_3$ was purchased from Strem Chemicals. The ligand $K_2BC_4Ph_5$ was synthesized from $PhBC_4Ph_4$ and potassium metal strips following literature procedure.[23] The ligand precursor $PhBC_4Ph_4$ was synthesized according to the literature method[36] from $(LiC_2Ph_2)_2$ and dichlorophenylborane (synthesized according to the literature method[37] from 1M BCl_3 in heptane (Millipore-Sigma) and tetraphenyltin (Alfa-Aesar)). The reagent $(LiC_2Ph_2)_2$ was synthesized from diphenylacetylene (Alfa-Aesar) and lithium metal strips according to the literature method.[38] Lithium and potassium metal pieces were flattened and cut into strips ($\sim 20 \times 5 \times 2$ mm) prior to their addition to reaction mixtures. Tetrahydofuran (THF), benzene, toluene, and diethyl ether were dried and degassed using a JC Meyer solvent purification system and stored under Argon over 4 Å molecular sieves prior to use. A diethyl ether solution of 18-crown-6 was dried over 4 Å sieves for three days prior to use. The diethyl ether was then removed under reduced pressure to furnish solid, anhydrous 18-crown-6.

Synthesis of [K(18-crown-6)][Dy(BC$_4$Ph$_5$)$_2$] (1). In the glovebox, colorless anhydrous $DyCl_3$ (30.5 mg, 0.113 mmol) and THF (10 mL) were added to a 20 mL scintillation vial equipped with a stir bar, and the slurry was stirred for several minutes. The resulting suspension was then added quickly to a 20 mL scintillation vial containing red $K_2BC_4Ph_5$ powder (118 mg, 0.226 mmol, 2.00 equiv). The mixture was allowed to stir for 18 h at ambient temperature. Following the reaction, the mixture was centrifuged to separate the insoluble colorless solid, presumed to be mostly KCl with possible traces of unreacted $DyCl_3$. The solution was decanted into a separate scintillation vial. The solvent was removed from this solution under vacuum to yield a red solid residue and the residue was washed once with diethyl ether. A solution of 18-crown-6 (37 mg, 0.140 mmol) in THF (5 mL) was then added to the solid. The mixture was agitated until complete dissolution was achieved. The red color of the solution became more intense than it had been following centrifugation. The THF solvent was then removed under vacuum, and the resulting solid dark red residue was washed with diethyl ether (1 mL), and the resulting powder redissolved in THF (1 mL). This solution was layered beneath two volume equivalents of diethyl ether and left to recrystallize at room temperature. After standing for one day, dark red crystals of **1**·2THF had formed, which were suitable for single-crystal diffraction. Dry yield of **1**: 32.0 mg (21%). All attempts to obtain CHN analysis on both **1** and **1**·2THF failed. ICP-OES was used to establish compositional purity of **1**. Dy, K, B ICP-OES. Expected for $C_{80}H_{74}B_2DyKO_6$: 12.0% Dy, 2.89% K, 1.60% B; Found: 11.52% Dy, 3.05% K, 1.34% B.

Single Crystal X-Ray Diffraction Analysis

Crystals coated in Paratone-N oil were mounted onto MiTeGen 10 µm loops and moved under an Oxford Cryosystems nitrogen cryostat. Crystals were found to be very sensitive to oxygen, even under Paratone-N oil, decomposing into colorless material after only a few minutes of sitting in oil under the microscope. The diffraction patterns were produced using synchrotron radiation at

the Advanced Light Source; Beamline 12.2.1. Unit cell determination and spot integration was performed using Bruker AXS and SAINT.[39] Absorption corrections were applied to spot intensities using the SADABS package.[40] Structural solutions were obtained using the Intrinsic Phasing method as implemented in ShelXT.[41] Least Squares refinement as implemented in ShelXL was used to refine structural models against F^2.[42] Olex2 was used as a graphical front-end for structural solution and refinement.[43] Boron positions were initially assigned by assigning all five ring atoms as carbon, allowing chemical occupancies of the five-membered ring atoms to vary, and then selecting the position with the lowest chemical occupancy value to assign as boron. During preliminary CIF validation, the Hirshfeld rigid-bond test[44] detected incorrectly modeled boron atoms, producing a B-level alert. This alert was no longer present when the B atoms were assigned correctly.

Two other level B alerts arose during final cif validation as follows.

PLAT230_ALERT_2_B Hirshfeld Test Diff for   C025   --C029   .   7.4 s.u.
>C025 and C029 correspond to meta and para carbon atoms on one of the phenyl rings of $BC_4Ph_5^{2-}$. These two atoms are likely disordered across two positions. Attempts to model this disorder using SPLIT+SAME commands resulted in an unstable refinement with wildly variable thermal displacement parameters and low chemical occupancy values for one of the disordered phenyl positions. This instability was unresponsive to restraints, and so the second disordered position was ultimately not modeled, given its apparent low chemical occupancy and the instability of its thermal displacement parameters.

PLAT230_ALERT_2_B Hirshfeld Test Diff for   C02A   --C02J   .   11.6 s.u.
>C02A and C02J correspond to meta and para carbon atoms on another one of the phenyl rings of $BC_4Ph_5^{2-}$. These two atoms are probably disordered across two positions. Attempts to model this disorder also resulted in an unstable refinement with wildly variable thermal displacement parameters and small chemical occupancy values for one of the disordered phenyl positions. Again, this instability was unresponsive to restraints. The second disordered position was not modeled, given its low chemical occupancy and the instability of its thermal displacement parameters.

Inductively Coupled Plasma–Optical Emission Spectrometry

Inductively coupled plasma–optical emission spectrometry was performed on a Perkin Elmer ICP Optima 7000. Commercial standard solutions (1000 ppm in 5% nitric acid) were purchased from Inorganic Ventures. Calibration curves were constructed using five standard solutions, each containing Dy, B and K. The Dy, B, and K concentrations for each of the five standard solutions are as follows: 0.1 ppm, 1 ppm, 5 ppm, 10 ppm and 15 ppm. Each standard also contained 0.1 ppm Y as an internal standard. A blank solution only containing 0.1 ppm Y was also prepared to set the zero-point of the calibration curve. Samples were fully digested overnight with 2 mL of piranha solution prepared from analytical grade 30% H_2O_2 (Millipore-Sigma) and reagent grade sulfuric acid (Fisher). It was found that digesting in acid without an oxidant failed to fully dissolve the boron containing organic material, leading to consistently low boron values. After adding the

internal standard to the acid digest, the solution was diluted with 5% nitric acid to a nominal concentration of ~10 ppm prior to analysis. Calibration curves for all analytes had $R^2 > 0.999$.

Fourier Transform Infrared Spectroscopy

The Fourier-transform infrared (FTIR) spectrum of **1** was collected inside of an N_2 glovebox using neat crystalline powder and a Shimadzu IRSpirit FTIR spectrometer operating in ATR mode. Peaks were identified using the multiple peak fitting routine as implemented in Origin 2022.

Magnetometry

All magnetic measurements were carried out on a Quantum Design MPMS-XL SQUID magnetometer. Under the conditions used for magnetic sample preparation (described below), at least partial desolvation of the potassium cation is likely. Thus, in order to avoid ambiguity regarding the bulk composition of the sample and the quantitative magnetic results, a sample of **1**·2THF was fully desolvated before sample preparation. A crystalline sample of **1**·2THF was dried under vacuum for a minimum of 30 min, mechanically ground, and 21.4 mg loaded into a quartz tube (inner diameter 5 mm outer diameter 7 mm), covered with a solid layer of eicosane (56.8 mg), and flame sealed under vacuum. The eicosane was subsequently melted at 40 °C in order to restrain the sample (prevent crystallite torquing) and to improve thermal conductivity between the sample and the environment. A second magnetic sample was prepared using a freshly prepared (and recrystallized) sample of **1**·2THF held under dynamic vacuum for only a few seconds, with the goal of removing surface crystallization solvent while retaining coordinated THF. The crystals were then crushed to form a microcrystalline powder (sample mass was 12.6 mg) and the sample prepared as described above (eicosane mass used was 47.0 mg). Work up of dc susceptibility data collected for this sample assuming the molecular weight for **1**·2THF (see Figures S4.10 and S4.11) revealed that the magnitude of the $\chi_M T$ product at 300 K is 17.7 emu·K/mol, larger than that determined for **1** (15.0 emu·K/mol) and predicted for a free Dy^{3+} (14.17 emu·K/mol), which suggests overestimation of the sample mass and likely desolvation of the sample. Even still, a full suite of ac and dc relaxation data collected for this second sample are consistent with those obtained for **1** and serve to validate the data for the desolvated compound. Diamagnetic corrections were calculated using Pascal's constants,[45] and were applied to all reported magnetic susceptibility values unless otherwise noted.

To collect isothermal magnetization decay data, the samples were initially magnetized under an applied magnetic field of 7 T for 5 minutes and then the field set to zero, and magnetization measured for ca. 1600 s. However, we found there was a trapped field in the superconducting magnet, and magnetization decay curves at 64, 68 and 72 K fully equilibrated during the measurement time to a negative magnetization value. These negative equilibrium magnetization values were used to fit a Curie law $M(T) = C/T$ with $C = -0.00232$ emu K; this corresponds to a field of approximately -12 Oe. Decay data for 64 K and below were fit using Equation S4.1,[46] where M_{eq} was fixed to $M_{eq} = -0.00232/T$, M_0 is the first measured data point (set as time zero), t is the time after the first measured point M_0, τ is the characteristic relaxation time, and β is a stretching parameter $(0 < \beta \leq 1)$.

$$M = M_{\text{eq}} + \left(M_0 - M_{\text{eq}}\right)e^{-\left(\frac{t}{\tau}\right)^{\beta}}$$ (Equation S4.1)

Frequency dependent in-phase (χ') and out-of-phase (χ'') magnetic susceptibility data were collected between 72 and 112 K. The relaxation time for each temperature increment was extracted using the generalized Debye model (Equations S4.2 and S4.3) as implemented in CC-FIT2.[47] The relaxation times were then tabulated with those from the magnetization decay experiments and fit using CC-FIT2.[47]

$$\chi'(\omega) = \chi_S + (\chi_T - \chi_S)\frac{1 + (\omega\tau)^{1-\alpha}\sin(\pi\alpha/2)}{1 + 2(\omega\tau)^{1-\alpha}\sin(\pi\alpha/2) + (\omega\tau)^{2-2\alpha}}$$ (Equation S4.2)

$$\chi''(\omega) = (\chi_T - \chi_S)\frac{(\omega\tau)^{1-\alpha}\cos(\pi\alpha/2)}{1 + 2(\omega\tau)^{1-\alpha}\sin(\pi\alpha/2) + (\omega\tau)^{2-2\alpha}}$$ (Equation S4.3)

Nuclear Magnetic Resonance Spectroscopy

Proton NMR spectra and proton decoupled ^{13}C NMR spectra were collected at the UC Berkeley College of Chemistry NMR Facility on a Bruker Advance 400 MHz spectrometer operating at 9.4 T under ambient temperature. Samples were sealed under an atmosphere of Ar prior to measurement. Tetrahydrofuran-d8 (99.8%) was purchased from Sigma-Adrich, saturated with argon using three freeze-pump-thaw cycles, and dried for 72 hrs over 3 Å molecular sieves prior to use.

Powder X-Ray Diffraction

A microcrystalline powder sample of **1** was loaded into a 1.0-mm borosilicate capillary inside a glovebox under an argon atmosphere. The capillary was subsequently flame sealed under Ar prior to measurement. High-resolution synchrotron X-ray powder diffraction data was collected at Beamline 17-BM at the Advanced Photon Source at Argonne National Laboratory. The temperature of the capillary samples was maintained at 298 K during measurement using an Oxford Cryosystems Cryostream 800. Scattered intensity was measured by a PerkinElmer a-Si flat panel detector. The average wavelength of all measurements was 0.45236 Å.

4.5. Computational Methods

Density Functional Theory (DFT) Calculations

Geometry optimization of the crystal structure and normal mode calculations were performed in the gas-phase on the anion in **1**·2THF using the Gaussian 09d software,[30] with both PBE and PBE0 density functionals and Grimme's empirical dispersion correction. Dysprosium was substituted for yttrium with an isotopic mass of 162.5 to aid self-consistent field (SCF) convergence, for which the Stuttgart RSC 1997 effective core potential (ECP) basis set was used for the 28 core electrons, with the remaining valence electrons being described by the corresponding valence basis

set. The cc-pVTZ basis set was used for boron and carbon atoms, whilst the cc-pVDZ was applied for hydrogen atoms.[48] Geometry optimization and Löwdin population analysis[49] was also performed on the free ligands, as described in the main text, using the Gaussian 09d software employing the 6-31G* basis set on all atoms.[50]

CASSCF-SO Calculations

The OpenMolcas[26] package was used to perform state-averaged complete active space self-consistent field spin-orbit (CASSCF-SO) calculations on the crystallographic and optimized structures of the anion, where the active space comprised nine 4f electrons in seven 4f orbitals of Dy^{III}. Basis sets were taken from the ANO-RCC library,[51] where the Dy atom had VTZP quality, the five-membered heterocycle was modelled with VDZP quality, with all other atoms in VDZ quality. After CASSCF optimization, the states were mixed by spin-orbit coupling using the RASSI module and the electronic structures projected onto a crystal field Hamiltonian using SINGLE_AN-ISO.[27]

Spin Dynamics Calculations

To reduce computational demand for spin dynamics calculations, we limited our CASSCF-SO calculations to the lowest 18 states of sextet multiplicity and used the atomic compact Cholesky decomposition (acCD) approach to fit the two-electron integrals. To check the validity of this approximation, we also calculated the electronic structure of **1-PBE** and **1-PBE0** at a higher level considering 21 sextets along with 244 quartets and 490 doublets in the CASSCF step, and 128 quartets and 130 doublets in the spin-orbit coupling step; we found only a trivial difference between the results (Tables S4.10–S4.14). Assuming the harmonic approximation, the maximum displacement along each mode at 100 K was calculated, and the optimized structure was then distorted along the normal mode coordinates. The CASSCF-SO calculations were then performed at four evenly spaced points in the positive and negative direction from the equilibrium position and crystal field parameters extracted. Following the most recently defined method,[19] we employed Bose-Einstein statistics and expanded the crystal field parameters in a Taylor series. Our approach herein differs only in the definition of zero-point displacement (ZPD), herein we define the ZPD as specified in ref. [52] by equation S4.4, where $\hbar$ is the reduced Planck constant, ω_j is the angular frequency, and μ_j is the reduced mass of mode j.

$$Q_{j,0} = \sqrt{\frac{\hbar}{\omega_j \mu_j}}$$

(Equation S4.4)

Mode-Weighted Analysis

We use the same methodology described in ref. [19] to decompose total gamma matrices into their mode-weighted components, where $\langle \bar{\bar{H}}_{SP} \rangle$ is the spin-phonon coupling, $\langle \bar{\bar{Q}} \rangle$ is the vibrational occupancy, $\langle \bar{\rho} \rangle$ is the vibrational density of states and $\langle \bar{n} \rangle$ is the effective number of modes. This enabled the switching of components between **1**, $[Cp^{iPr5}Dy^{III}Cp^*][B(C_6F_5)_4]$,[53] and $[Dy(Cp^{iPr4})_2][B(C_6F_5)_4]$[54] to form fictitious total rate matrices which were diagonalized to give fictitious relaxation times. By comparing the fictitious relaxation times to the experimental

110

relaxation times, we were able to elucidate the factors that most substantially contribute to the differences in the relaxation between **1** and $[Cp^{iPr5}Dy^{III}Cp^*][B(C_6F_5)_4]$ or $[Dy(Cp^{iPr4})_2][B(C_6F_5)_4]$.

4.6. Acknowledgments

4.7. References and Footnotes

(1) Chilton, N. F. Molecular Magnetism. *Annu. Rev. Mater. Res.* **2022**, *52*, 79–101. DOI: 10.1146/annurev-matsci-081420-042553.

(2) Gatteschi, D.; Sessoli, R.; Villain, J. *Molecular Nanomagnets*; 2007; Vol. 1. DOI: 10.1093/acprof:oso/9780198567530.001.0001.

(3) Woodruff, D. N.; Winpenny, R. E. P.; Layfield, R. A. Lanthanide Single-Molecule Magnets. *Chem. Rev.* **2013**, *113* (7), 5110–5148. DOI: 10.1021/cr400018q.

(4) Rinehart, J. D.; Long, J. R. Exploiting Single-Ion Anisotropy in the Design of f-Element Single-Molecule Magnets. *Chem. Sci.* **2011**, *2* (11), 2078–2085. DOI: 10.1039/c1sc00513h.

(5) McAdams, S. G.; Ariciu, A. M.; Kostopoulos, A. K.; Walsh, J. P. S.; Tuna, F. Molecular Single-Ion Magnets Based on Lanthanides and Actinides: Design Considerations and New Advances in the Context of Quantum Technologies. *Coord. Chem. Rev.* **2017**, *346*, 216–239. DOI: 10.1016/j.ccr.2017.03.015.

(6) Troiani, F.; Affronte, M. Molecular Spins for Quantum Information Technologies. *Chem. Soc. Rev.* **2011**, *40* (6), 3119–3129. DOI: 10.1039/c0cs00158a.

(7) Gaita-Ariño, A.; Luis, F.; Hill, S.; Coronado, E. Molecular Spins for Quantum Computation. *Nat. Chem.* **2019**, *11* (4), 301–309. DOI: 10.1038/s41557-019-0232-y.

(8) Layfield, R. A.; Tong, M.-L.; Day, B. M.; Chen, Y.-C.; Guo, F.-S.; Mansikkamäki, A. Magnetic Hysteresis up to 80 Kelvin in a Dysprosium Metallocene Single-Molecule Magnet. *Science* **2018**, *362* (6421), 1400–1403. DOI: 10.1126/science.aav0652.

(9) Randall McClain, K.; Gould, C. A.; Chakarawet, K.; Teat, S. J.; Groshens, T. J.; Long, J. R.; Harvey, B. G. High-Temperature Magnetic Blocking and Magneto-Structural Correlations in a Series of Dysprosium(Iii) Metallocenium Single-Molecule Magnets. *Chem. Sci.* **2018**, *9* (45), 8492–8503. DOI: 10.1039/c8sc03907k.

(10) Goodwin, C. A. P.; Ortu, F.; Reta, D.; Chilton, N. F.; Mills, D. P. Molecular Magnetic Hysteresis at 60 Kelvin in Dysprosocenium. *Nature* **2017**, *548* (7668), 439–442. DOI: 10.1038/nature23447.

(11) Blagg, R. J.; Ungur, L.; Tuna, F.; Speak, J.; Comar, P.; Collison, D.; Wernsdorfer, W.; McInnes, E. J. L.; Chibotaru, L. F.; Winpenny, R. E. P. Magnetic Relaxation Pathways in Lanthanide Single-Molecule Magnets. *Nat. Chem.* **2013**, *5* (8), 673–678. DOI: 10.1038/nchem.1707.

(12) Giansiracusa, M. J.; Al-Badran, S.; Kostopoulos, A. K.; Whitehead, G. F. S.; Collison, D.; Tuna, F.; Winpenny, R. E. P.; Chilton, N. F. A Large Barrier Single-Molecule Magnet without Magnetic Memory. *Dalton Trans.* **2019**, *48* (29), 10795–10798. DOI: 10.1039/C9DT01791G.

(13) Goodwin, C. A. P.; Ortu, F.; Reta, D.; Chilton, N. F.; Mills, D. P. Molecular Magnetic Hysteresis at 60 Kelvin in Dysprosocenium. *Nature* **2017**, *548* (7668), 439–442. DOI: 10.1038/nature23447.

(14) Ding, Y. S.; Chilton, N. F.; Winpenny, R. E. P.; Zheng, Y. Z. On Approaching the Limit of Molecular Magnetic Anisotropy: A Near-Perfect Pentagonal Bipyramidal Dysprosium(III) Single-Molecule Magnet. *Angew. Chem. - Int. Ed.* **2016**, *55* (52), 16071–16074. DOI: 10.1002/anie.201609685.

(15) Reta, D.; Chilton, N. F. Uncertainty Estimates for Magnetic Relaxation Times and Magnetic Relaxation Parameters. *Phys. Chem. Chem. Phys.* **2019**, *21* (42), 23567–23575. DOI: 10.1039/C9CP04301B.

(16) Chiesa, A.; Cugini, F.; Hussain, R.; Macaluso, E.; Allodi, G.; Garlatti, E.; Giansiracusa, M.; Goodwin, C. A. P.; Ortu, F.; Reta, D.; Skelton, J. M.; Guidi, T.; Santini, P.; Solzi, M.; Renzi, R. D.; Mills, D. P.; Chilton, N. F.; Carretta, S. Understanding Magnetic Relaxation in Single-Ion Magnets with High Blocking Temperature. *Phys. Rev. B* **2020**, *101* (17), 174402. DOI: 10.1103/PhysRevB.101.174402.

(17) Ortu, F.; Reta, D.; Ding, Y.-S.; Goodwin, C. A. P.; Gregson, M. P.; McInnes, E. J. L.; Winpenny, R. E. P.; Zheng, Y.-Z.; Liddle, S. T.; Mills, D. P.; Chilton, N. F. Studies of Hysteresis and Quantum Tunnelling of the Magnetisation in Dysprosium(III) Single Molecule Magnets. *Dalton Trans.* **2019**, *48* (24), 8541–8545. DOI: 10.1039/C9DT01655D.

(18) Briganti, M.; Santanni, F.; Tesi, L.; Totti, F.; Sessoli, R.; Lunghi, A. A Complete *Ab Initio* View of Orbach and Raman Spin–Lattice Relaxation in a Dysprosium Coordination Compound. *J. Am. Chem. Soc.* **2021**, *143* (34), 13633–13645. DOI: 10.1021/jacs.1c05068.

(19) Reta, D.; Kragskow, J. G. C.; Chilton, N. F. Ab Initio Prediction of High-Temperature Magnetic Relaxation Rates in Single-Molecule Magnets. *J. Am. Chem. Soc.* **2021**, *143* (15), 5943–5950. DOI: 10.1021/jacs.1c01410.

(20) Evans, P.; Reta, D.; Whitehead, G. F. S.; Chilton, N. F.; Mills, D. P. Bis-Monophospholyl Dysprosium Cation Showing Magnetic Hysteresis at 48 K. *J. Am. Chem. Soc.* **2019**, *141* (50), 19935–19940. DOI: 10.1021/jacs.9b11515.

(21) Kelly, R. P.; Bell, T. D. M.; Cox, R. P.; Daniels, D. P.; Deacon, G. B.; Jaroschik, F.; Junk, P. C.; Le Goff, X. F.; Lemercier, G.; Martinez, A.; Wang, J.; Werner, D. Divalent Tetra- and Penta-Phenylcyclopentadienyl Europium and Samarium Sandwich and Half-Sandwich Complexes: Synthesis, Characterization, and Remarkable Luminescence Properties. *Organometallics* **2015**, *34* (23), 5624–5636. DOI: 10.1021/acs.organomet.5b00842.

(22) Deacon, G. B.; Forsyth, C. M.; Jaroschik, F.; Junk, P. C.; Kay, D. L.; Maschmeyer, T.; Masters, A. F.; Wang, J.; Field, L. D. Accessing Decaphenylmetallocenes of Ytterbium, Calcium, and Barium by Desolvation of Solvent-Separated Ion Pairs: Overcoming Adverse Solubility Properties. *Organometallics* **2008**, *27* (18), 4772–4778. DOI: 10.1021/om800501z.

(23) Herberich, G. E.; Buller, B.; Hessner, B.; Oschmann, W. Derivative Des Borols: II. Penta-phenylborol: Synthese, Reduktion Zum Dianion Und Komplexe von Kobalt Und Platin. *J. Organomet. Chem.* **1980**, *195* (3), 253–259. DOI: 10.1016/S0022-328X(00)93308-4.

(24) Vanjak, J. C.; Wilkins, B. O.; Vieru, V.; Bhuvanesh, N. S.; Reibenspies, J. H.; Martin, C. D.; Chibotaru, L. F.; Nippe, M. A High-Performance Single-Molecule Magnet Utilizing Dianionic Aminoborolide Ligands. *J. Am. Chem. Soc.* **2022**, *144* (39), 17743–17747. DOI: 10.1021/jacs.2c06698.

(25) Gould, C. A.; McClain, K. R.; Reta, D.; Kragskow, J. G. C.; Marchiori, D. A.; Lachman, E.; Choi, E.-S.; Analytis, J. G.; Britt, R. D.; Chilton, N. F.; Harvey, B. G.; Long, J. R. Ultrahard Magnetism from Mixed-Valence Dilanthanide Complexes with Metal-Metal Bonding. *Science* **2022**, *375* (6577), 198–202. DOI: 10.1126/science.abl5470.

(26) Fdez. Galván, I.; Vacher, M.; Alavi, A.; Angeli, C.; Aquilante, F.; Autschbach, J.; Bao, J. J.; Bokarev, S. I.; Bogdanov, N. A.; Carlson, R. K.; Chibotaru, L. F.; Creutzberg, J.; Dattani, N.; Delcey, M. G.; Dong, S. S.; Dreuw, A.; Freitag, L.; Frutos, L. M.; Gagliardi, L.; Gendron, F.; Giussani, A.; González, L.; Grell, G.; Guo, M.; Hoyer, C. E.; Johansson, M.; Keller, S.; Knecht, S.; Kovačević, G.; Källman, E.; Li Manni, G.; Lundberg, M.; Ma, Y.; Mai, S.; Malhado, J. P.; Malmqvist, P. Å.; Marquetand, P.; Mewes, S. A.; Norell, J.; Olivucci, M.; Oppel, M.; Phung, Q. M.; Pierloot, K.; Plasser, F.; Reiher, M.; Sand, A. M.; Schapiro, I.; Sharma, P.; Stein, C. J.; Sørensen, L. K.; Truhlar, D. G.; Ugandi, M.; Ungur, L.; Valentini, A.; Vancoillie, S.; Veryazov, V.; Weser, O.; Wesołowski, T. A.; Widmark, P.-O.; Wouters, S.; Zech, A.; Zobel, J. P.; Lindh, R. OpenMolcas: From Source Code to Insight. *J. Chem. Theory Comput.* **2019**, *15* (11), 5925–5964. DOI: 10.1021/acs.jctc.9b00532.

(27) Ungur, L.; Chibotaru, L. F. Ab Initio Crystal Field for Lanthanides. *Chem. – Eur. J.* **2017**, *23* (15), 3708–3718. DOI: 10.1002/chem.201605102.

(28) Orbach, R. On the Theory of Spin-Lattice Relaxation in Paramagnetic Salts. *Proc. Phys. Soc.* **1961**, *77* (4), 821–826. DOI: 10.1088/0370-1328/77/4/301.

(29) Gu, L.; Wu, R. Origin of the Anomalously Low Raman Exponents in Single Molecule Magnets. *Phys Rev B* **2021**, *103* (1), 14401. DOI: 10.1103/PhysRevB.103.014401.

(30) Frisch, M. J.; Trucks, G. W.; Schlegel, H. B.; Scuseria, G. E.; Robb, M. A.; Cheeseman, J. R.; Scalmani, G.; Barone, V.; Mennucci, B.; Petersson, G. A.; Nakatsuji, H.; Caricato, M.; Li, X.; Hratchian, H. P.; Izmaylov, A. F.; Bloino, J.; Zheng, G.; Sonnenberg, J. L.; Hada, M.; Ehara, M.; Toyota, K.; Fukuda, R.; Hasegawa, J.; Ishida, M.; Nakajima, T.; Honda, Y.; Kitao, O.; Nakai, H.; Vreven, T.; Montgomery, J. A., Jr.; Peralta, J. E.; Ogliaro, F.; Bearpark, M.; Heyd, J. J.; Brothers, E.; Kudin, K. N.; Staroverov, V. N.; Kobayashi, R.; Normand, J.; Raghavachari, K.; Rendell, A.; Burant, J. C.; Iyengar, S. S.; Tomasi, J.; Cossi, M.; Rega, N.; Millam, J. M.; Klene, M.; Knox, J. E.; Cross, J. B.; Bakken, V.; Adamo, C.; Jaramillo, J.; Gomperts, R.; Stratmann, R. E.; Yazyev, O.; Austin, A. J.; Cammi, R.; Pomelli, C.; Ochterski, J. W.; Martin, R. L.; Morokuma, K.; Zakrzewski, V. G.; Voth, G. A.; Salvador, P.; Dannenberg, J. J.; Dapprich, S.; Daniels, A. D.; Farkas, Ö.; Foresman, J. B.; Ortiz, J. V.; Cioslowski, J.; Fox, D. J. Gaussian09d.

(31) Perdew, J.; Burke, K.; Ernzerhof, M. Generalized Gradient Approximation Made Simple. *Phys. Rev. Lett.* **1996**, *77* (18), 3865–3868. DOI: 10.1103/PhysRevLett.77.3865.

(32) Adamo, C.; Barone, V. Toward Reliable Density Functional Methods without Adjustable Parameters: The PBE0 Model. *J. Chem. Phys.* **1999**, *110* (13), 6158–6170. DOI: 10.1063/1.478522.

(33) Grimme, S.; Antony, J.; Ehrlich, S.; Krieg, H. A Consistent and Accurate Ab Initio Parametrization of Density Functional Dispersion Correction (DFT-D) for the 94 Elements H-Pu. *J. Chem. Phys.* **2010**, *132* (15), 154104.

(34) Heitkemper, T.; Sindlinger, C. P. Electronic Push-Pull Modulation by Peripheral Substituents in Pentaaryl Boroles. *Chem. - Eur. J.* **2019**, *25* (26), 6628–6637. DOI: 10.1002/chem.201900826 CO - CEUJED.

(35) Braunschweig, H.; Dyakonov, V.; Jimenez-Halla, J. O. C.; Kraft, K.; Krummenacher, I.; Radacki, K.; Sperlich, A.; Wahler, J. An Isolable Radical Anion Based on the Borole Framework. *Angew. Chem. Int. Ed.* **2012**, *51* (12), 2977. DOI: 10.1002/anie.201108632 CO - ACIEF5.

(36) Eisch, J. J.; Galle, J. E.; Kozima, S. The Physical and Chemical Consequences of Cyclic Conjugation in Boracyclopolyenes. The Antiaromatic Character of Pentaarylboroles1. *J. Am. Chem. Soc.* **1986**, *108* (3), 379–385. DOI: 10.1021/ja00263a006.

(37) Niedenzu, K.; Dawson, J. W. Boron-Nitrogen Compounds. III.1,2 Aminoboranes, Part 2: The B-N Bond Character in Substituted Aminoboranes. *J. Am. Chem. Soc.* **1960**, *82* (16), 4223–4228. DOI: 10.1021/ja01501a028.

(38) Eisch, J. J.; Galle, J. E.; Kozima, S. The Physical and Chemical Consequences of Cyclic Conjugation in Boracyclopolyenes. The Antiaromatic Character of Pentaarylboroles1. *J. Am. Chem. Soc.* **1986**, *108* (3), 379–385. DOI: 10.1021/ja00263a006.

(39) AXS, B. SAINT and APEX 2 Software for CCD Diffractometers. *SAINT and APEX 2 software for CCD diffractometers.* 2006.

(40) Sheldrick, G. M. Sadabs. *University of Göttingen, Germany*. 1996.

(41) Sheldrick, G. M. SHELXT - Integrated Space-Group and Crystal-Structure Determination. *Acta Crystallographica Section A: Foundations of Crystallography*. January 2015, pp 3–8. DOI: 10.1107/S2053273314026370.

(42) Sheldrick, G. M. Crystal Structure Refinement with SHELXL. *Acta Crystallographica Section C: Structural Chemistry*. January 2015, pp 3–8. DOI: 10.1107/S2053229614024218.

(43) Dolomanov, O. V; Bourhis, L. J.; Gildea, R. J.; Howard, J. A. K.; Puschmann, H. OLEX2: A Complete Structure Solution, Refinement and Analysis Program. *J. Appl. Crystallogr.* **2009**, *42* (2), 339–341. DOI: 10.1107/S0021889808042726.

(44) Hirshfeld, F. L. Can X-Ray Data Distinguish Bonding Effects from Vibrational Smearing? *Acta Crystallogr. Sect. A* **1976**, *32* (2), 239–244. DOI: 10.1107/S0567739476000533.

(45) Bain, G. A.; Berry, J. F. Diamagnetic Corrections and Pascal's Constants. **2008**, *85* (4), 1–5.

(46) Hilgar, J. D.; Butts, A. K.; Rinehart, J. D. A Method for Extending AC Susceptometry to Long-Timescale Magnetic Relaxation. *Phys Chem Chem Phys* **2019**, *21* (40), 22302–22307. DOI: 10.1039/C9CP03936H.

(47) Reta, D.; Chilton, N. Uncertainty Estimates for Magnetic Relaxation Times and Magnetic Relaxation Parameters. *ChemRXiv* **2019**. DOI: 10.26434/chemrxiv.8863904.v1.

(48) Dunning, T. H. Gaussian Basis Sets for Use in Correlated Molecular Calculations. I. The Atoms Boron through Neon and Hydrogen. *J. Chem. Phys.* **1989**, *90* (2), 1007–1023. DOI: 10.1063/1.456153.

(49) Löwdin, P. On the Non-Orthogonality Problem Connected with the Use of Atomic Wave Functions in the Theory of Molecules and Crystals. *J. Chem. Phys.* **1950**, *18* (3), 365–375. DOI: 10.1063/1.1747632.

(50) Rassolov, V. A.; Pople, J. A.; Ratner, M. A.; Windus, T. L. 6-31G* Basis Set for Atoms K through Zn. *J. Chem. Phys.* **1998**, *109* (4), 1223–1229. DOI: 10.1063/1.476673.

(51) Roos, B. O.; Lindh, R.; Malmqvist, P.-Å.; Veryazov, V.; Widmark, P.-O. Main Group Atoms and Dimers Studied with a New Relativistic ANO Basis Set. *J. Phys. Chem. A* **2004**, *108* (15), 2851–2858. DOI: 10.1021/jp031064+.

(52) Kragskow, J. G. C.; Marbey, J.; Buch, C. D.; Nehrkorn, J.; Ozerov, M.; Piligkos, S.; Hill, S.; Chilton, N. F. Analysis of Vibronic Coupling in a 4f Molecular Magnet with FIRMS. *Nat. Commun.* **2022**, *13* (1), 825. DOI: 10.1038/s41467-022-28352-2.

(53) Layfield, R. A.; Tong, M.-L.; Day, B. M.; Chen, Y.-C.; Guo, F.-S.; Mansikkamäki, A. Magnetic Hysteresis up to 80 Kelvin in a Dysprosium Metallocene Single-Molecule Magnet. *Science* **2018**, *362* (6421), 1400–1403. DOI: 10.1126/science.aav0652.

(54) McClain, K. R.; Gould, C. A.; Chakarawet, K.; Teat, S. J.; Groshens, T. J.; Long, J. R.; Harvey, B. G. High-Temperature Magnetic Blocking and Magneto-Structural Correlations in a Series of Dysprosium(Iii) Metallocenium Single-Molecule Magnets. *Chem. Sci.* **2018**, *9* (45), 8492–8503. DOI: 10.1039/c8sc03907k.

(55) So, C.-W.; Watanabe, D.; Wakamiya, A.; Yamaguchi, S. Synthesis and Structural Characterization of Pentaarylboroles and Their Dianions. *Organometallics* **2008**, *27* (14), 3496–3501. DOI: 10.1021/om8002812.

4.8: Supporting Information
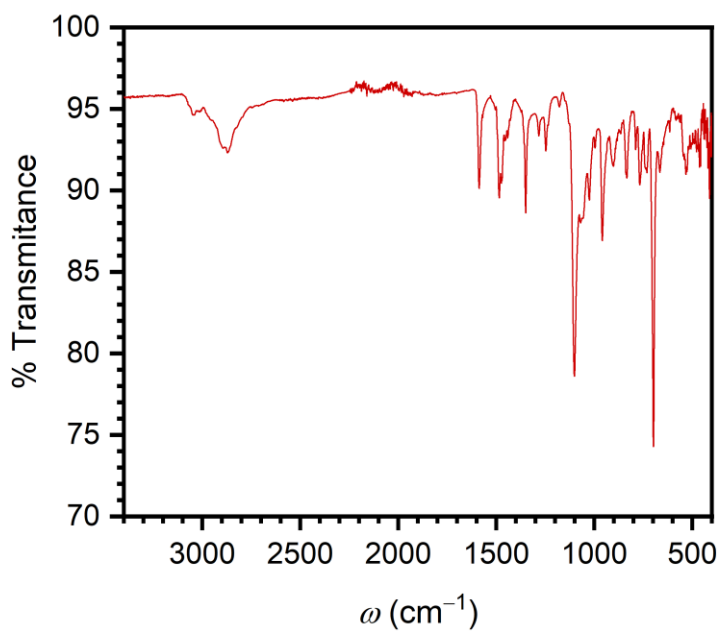
Figure S4.1: Fourier-transform infrared spectrum of **1**.
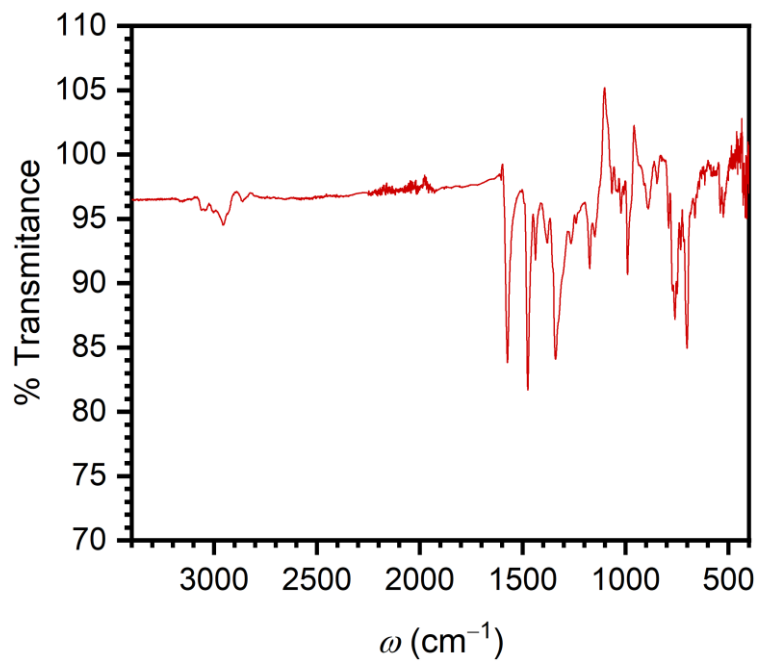
Figure S4.2: Fourier transform infrared spectrum of putative **1·2THF**
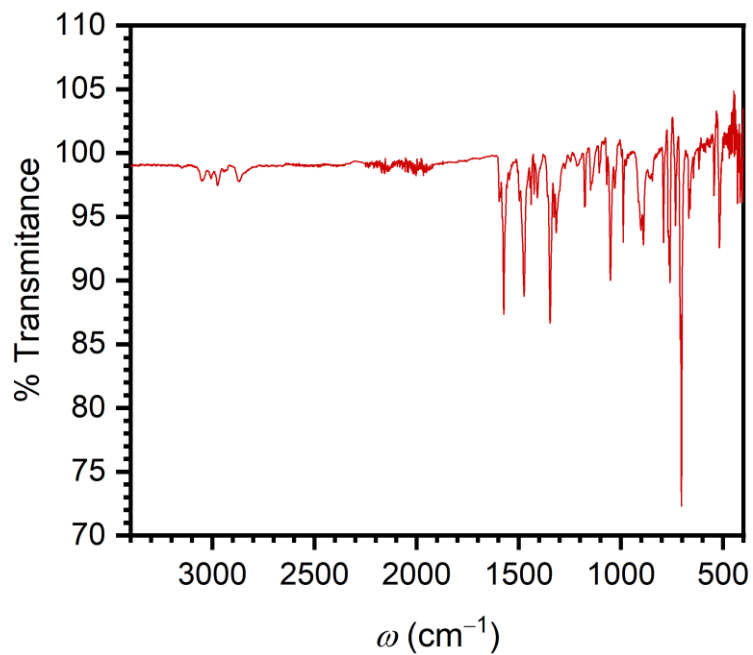
Figure S4.3. Fourier-transform infrared spectrum of $K_2BC_4Ph_5$.
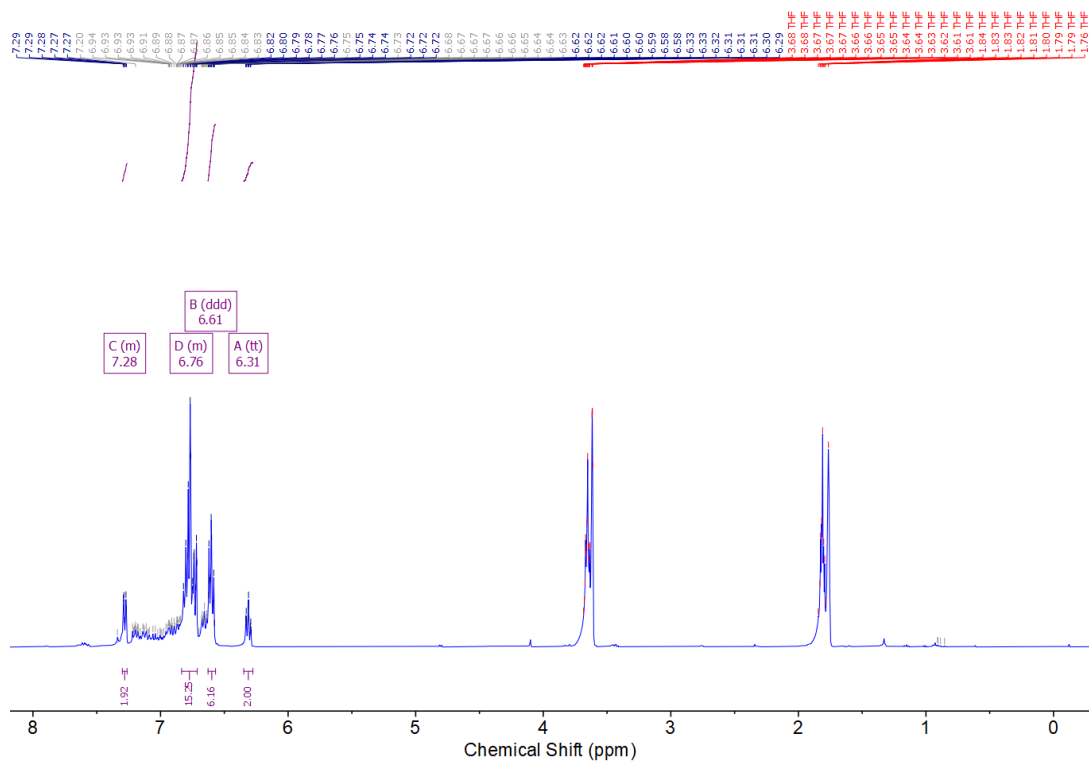
Figure S4.4. ^{1}H NMR Spectrum of $K_2BC_4Ph_5$. ^{1}H NMR (400 MHz, THF) δ 7.30 – 7.26 (m, 2H), 6.83 – 6.71 (m, 15H), 6.61 (ddd, J = 10.2, 5.4, 2.0 Hz, 6H), 6.31 (tt, J = 7.1, 1.4 Hz, 2H).
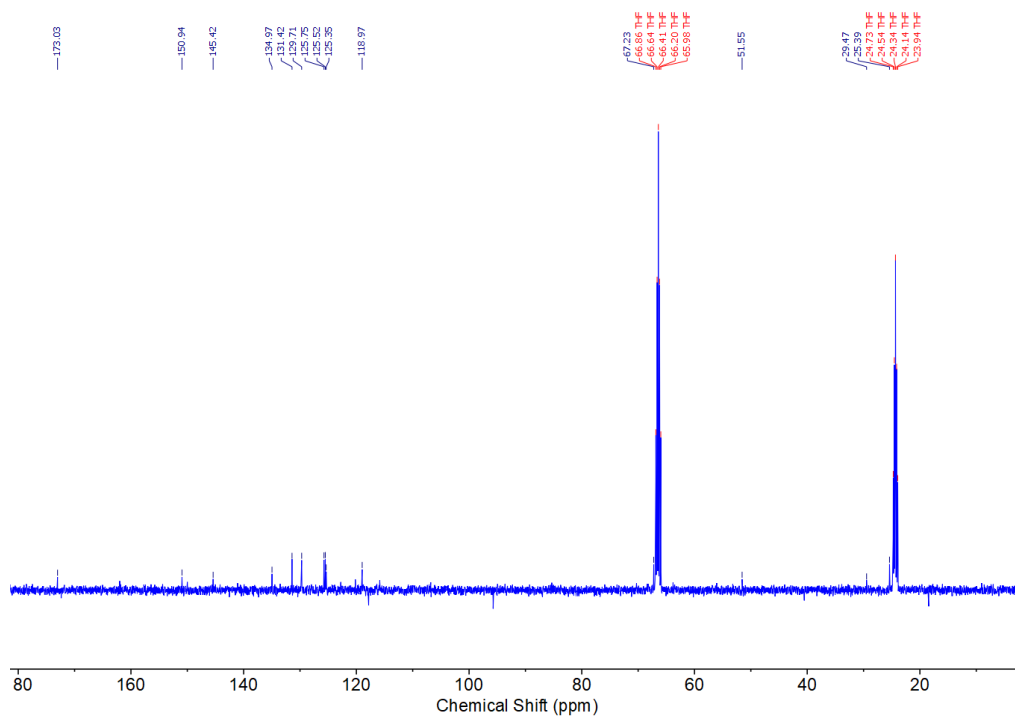
Figure S4.5. ^{13}C NMR spectrum of $K_2BC_4Ph_5$. ^{13}C NMR (101 MHz, THF) δ 173.03, 150.94, 145.42, 134.97, 131.42, 129.71, 125.75, 125.52, 125.35, 118.97, 67.23, 51.55, 29.47, 25.39.
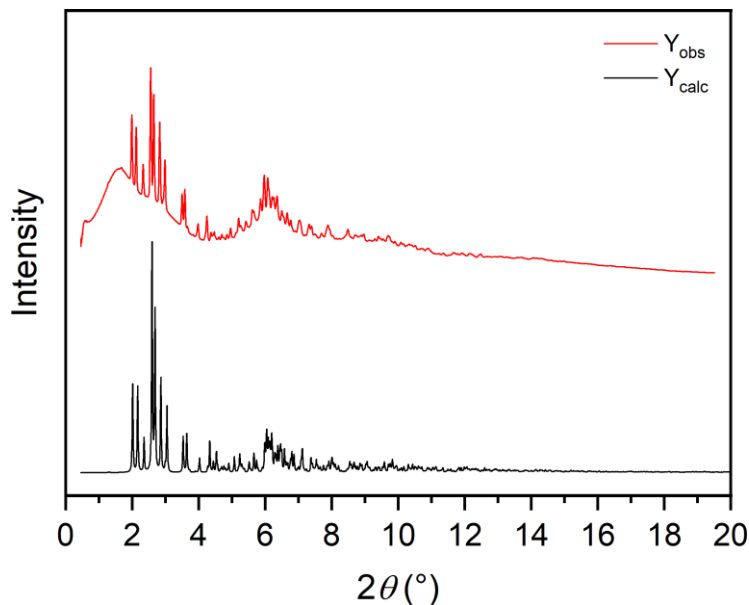
Figure S4.6. Comparison of powder x-ray diffraction pattern obtained for mechanically crushed crystals of **1** (red trace) with the simulated diffraction pattern based on the single-crystal structure of **1**·2THF (black trace). The sharp peaks in both patterns overlap, suggesting that the bulk structure of desolvated **1** and **1**·2THF are the same. The broadness, particularly at low angles, in the experimental pattern for **1** is likely background scattering from the borosilicate sample capillary.
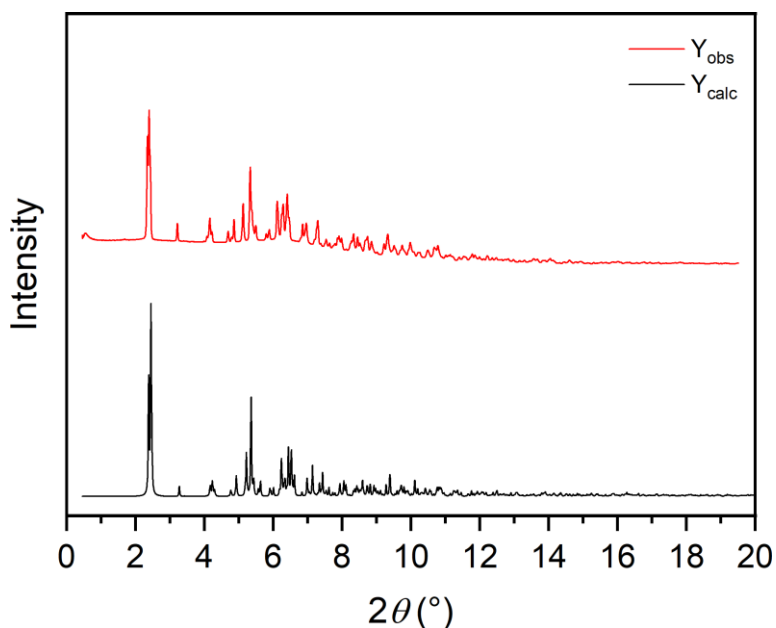
Figure S4. Comparison of powder x-ray diffraction pattern obtained for $K_2BC_4Ph_5$ (red trace) with a simulated pattern derived from CCDC:701219 (black trace).[55]

Figure S4.1. Unit Cell Parameters and Refinement Metrics for **1**·2THF.

Empirical formula	$C_{88}H_{90}B_2Dy_{0.97}KO_8$
Formula weight	1494.75
Temperature/K	100
Crystal system	triclinic
Space group	P-1
a/Å	12.547(5)
b/Å	15.210(6)
c/Å	20.620(8)
α/°	96.799(4)
β/°	100.948(4)
γ/°	101.827(4)
Volume/Å^3	3731(3)
Z	2
ρ_{calc}g/cm^3	1.331
μ/mm^{-1}	1.155
F(000)	1551.0
Crystal size/mm^3	$0.05 \times 0.05 \times 0.04$
Radiation	synchrotron ($\lambda = 0.7288$)
2Θ range for data collection/°	2.844 to 54.194
Index ranges	$-15 \leq h \leq 15, -19 \leq k \leq 18, -25 \leq l \leq 25$
Reflections collected	64045
Independent reflections	15231 [$R_{int} = 0.0656$, $R_{sigma} = 0.0580$]
Data/restraints/parameters	15231/235/1069
Goodness-of-fit on F^2	1.031
Final R indexes [I>=2σ (I)]	$R_1 = 0.0572$, w$R_2 = 0.1582$
Final R indexes [all data]	$R_1 = 0.0721$, w$R_2 = 0.1701$

Figure S4.2. Selected Distances and Angles for **1**·2THF.

Anion Index	Dy Site	Occupancy	Dy–centroid (Å)	centroid–Dy–centroid angle (°)
1	Dy1A	0.35523	2.3491(13) 2.2641(10)	155.99(13)
	Dy1B	0.12429	2.334(3) 2.275(2)	156.5(4)
2	Dy2A	0.46247	2.2118(8) 2.4187(8)	156.18(2)
	Dy2B	0.03418	2.392(6) 2.266(6)	153.2(3)
Average			2.33 ± 0.09	156 ± 1
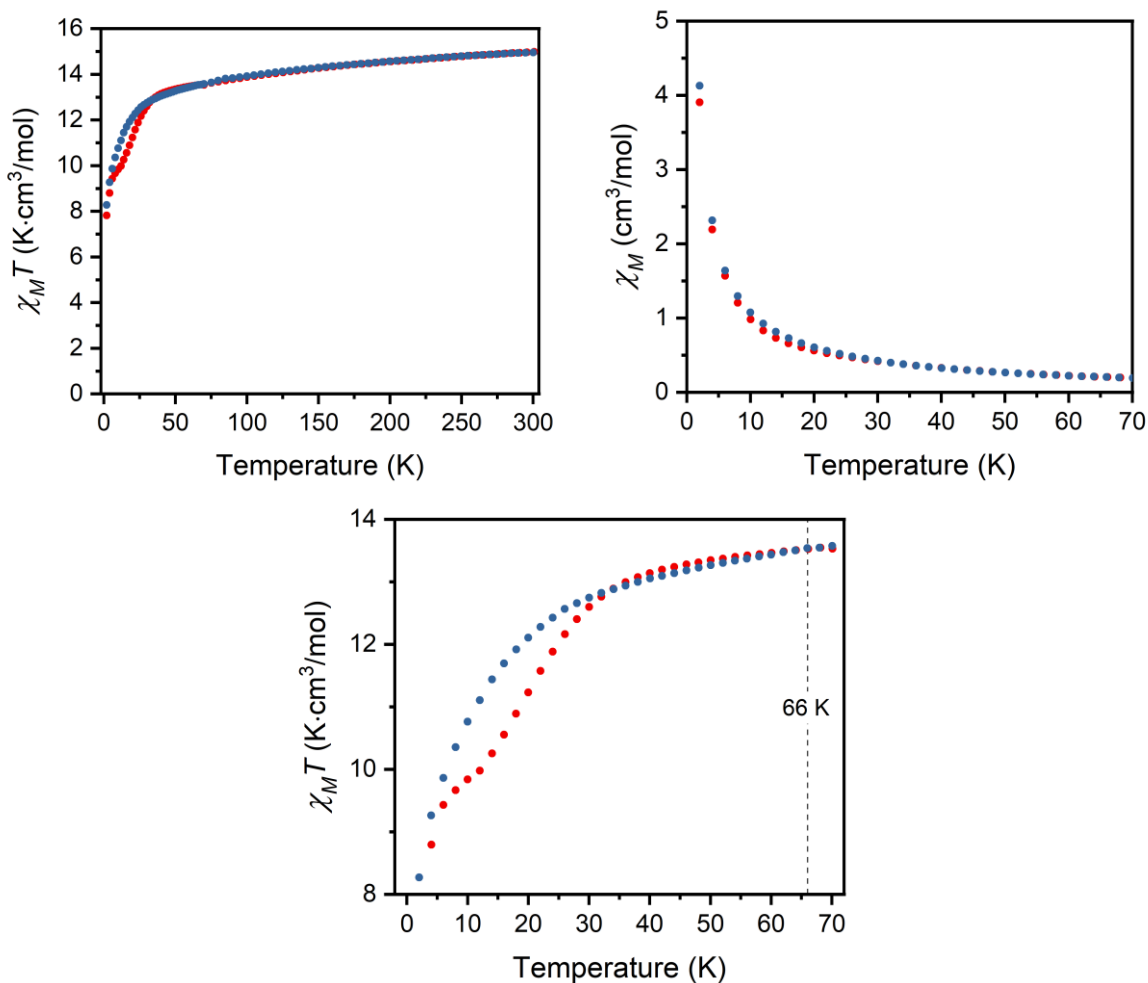
Figure S4.8. (Upper left) Temperature dependence of the molar magnetic susceptibility times temperature ($\chi_M T$) for a sample of one **1** cooled under zero dc field (red symbols) and under a field of 0.1 T (blue symbols). All data were collected under H_{dc} = 0.1 T. (Upper right) Temperature dependence of the molar magnetic susceptibility (χ_M) for a sample of one **1** cooled under zero dc field (red symbols) and under a field of 0.1 T (blue symbols). All data were collected under H_{dc} = 0.1 T. (Lower) Expanded view of the data in the upper plot from 2 to 70 K, showing T_{irrev} at 66 K.
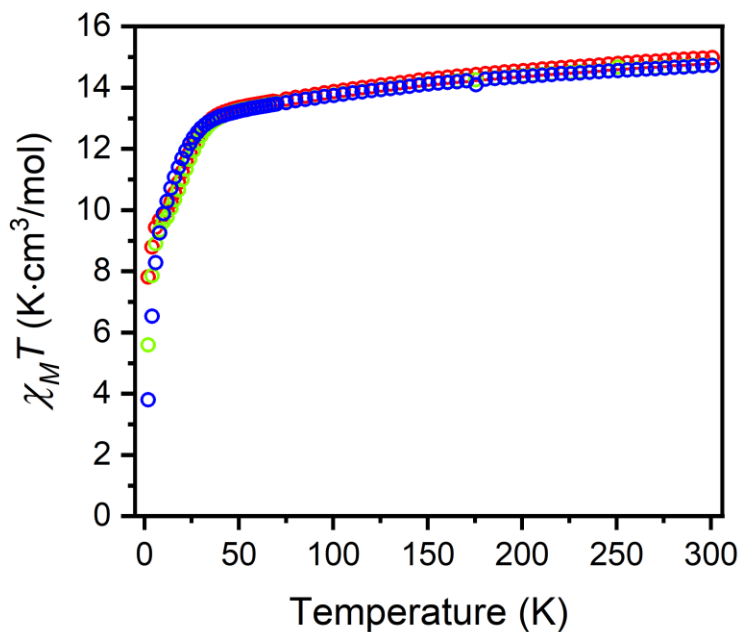
Figure S4.9. Temperature dependence of the molar magnetic susceptibility times temperature ($\chi_M T$) for a sample of one **1** cooled under zero dc field. Blue, green, and red symbols correspond to data collected under dc fields of 1, 0.5, and 0.1 T, respectively.
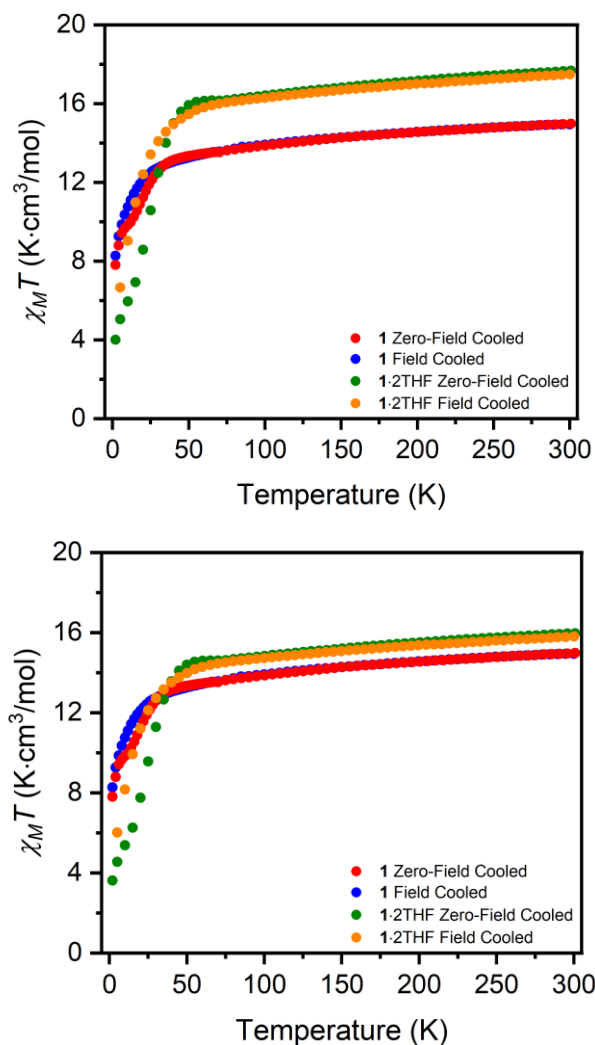
Figure S4.10. (Upper) Temperature dependence of the molar magnetic susceptibility times temperature ($\chi_M T$) for a sample of purported **1**·2THF cooled under zero dc field (green symbols) and under a field of 0.1 T (orange symbols). Data were worked up using the measured sample mass of 12.6 mg and using the molecular mass of 1498.9 g/mol for **1**·2THF. It is clear that the magnitude of the susceptibility is much higher than that measured for **1** at room temperature (red symbols represent zero-field cooled data and blue symbols represent field-cooled data, both measured under 0.1 T applied field) and much higher than predicted for free Dy^{3+}, 14.17 emu·K/mol, suggesting the molar mass used does not reflect the actual composition of the sample. (Lower) Adjusted temperature dependence of the molar magnetic susceptibility times temperature ($\chi_M T$) for the sample of purported **1**·2THF, where the sample molar mass was set to that of desolvated **1**, 1354.7 g/mol, which brings the magnitude of $\chi_M T$ at 300 K in into near agreement with that obtained for the fully desolvated sample **1**. This suggests that the sample of **1**·2THF used to prepare the second magnetic sample desolvates at least partially.

125
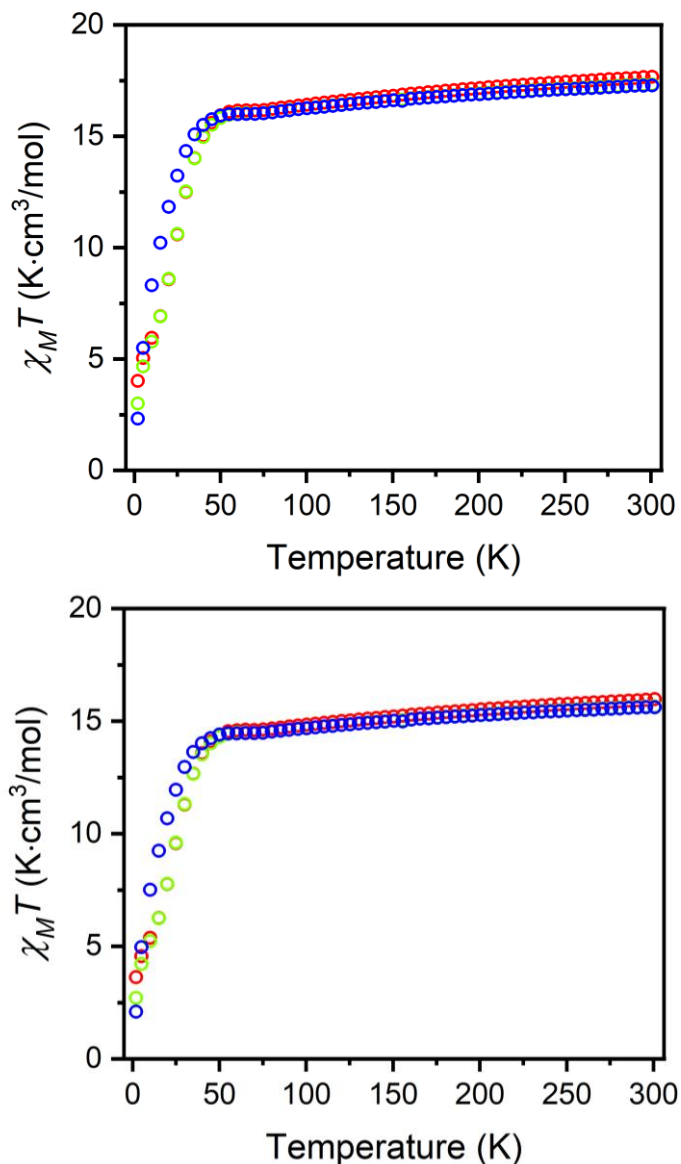
Figure S4.11. (Upper) Temperature dependence of the molar magnetic susceptibility times temperature ($\chi_M T$) for a sample of putative **1**·2THF cooled under zero dc field. Blue, green, and red symbols correspond to data collected under dc fields of 1, 0.5, and 0.1 T, respectively. Data were worked up using the measured sample mass of 12.6 mg and using the molecular mass of 1498.9 g/mol for **1**·2THF. It is clear that the magnitude of the susceptibility is much higher than that measured for **1** at room temperature (see Figure S4.9) and also much higher than predicted for free Dy^{3+} (14.17 emu·K/mol), indicating the molar mass used does not reflect the composition of the sample. (Lower) Adjustment of the data shown in the upper panel using a molar mass of 1354.7 g/mol, corresponding to desolvated **1**, brings the $\chi_M T$ magnitudes into near agreement with those collected for **1**, suggesting that the **1**·2THF used to prepare the second magnetic sample is at least partially desolvated.

Table S4.3. Tabulated Decay Fit Parameters for **1**. Estimated uncertainties in τ at the 1σ level were calculated with $\tau_{\pm} = \tau \exp\{\pm\frac{1.64\,\tan[\frac{\pi}{2}(1-\beta)]}{(1-\beta)^{0.141}}\}$ derived in Ref. 22 where τ and β are the fitted values from the stretched exponential function, and $\tau_{\pm}$ are the limits of the 1σ uncertainties.

T (K)	τ (s)	β	τ_{+}	τ_{-}
2	1277	0.774	1425	673
3	1086	0.710	1739	669
4	1093	0.711	1741	671
5	1094	0.712	1733	671
6	1079	0.716	1673	656
7	1046	0.713	1648	640
8	1024	0.726	1503	609
9	966	0.730	1387	569
10	926	0.741	1250	532
12	826	0.754	1036	460
14	729	0.760	883	399
16	647	0.757	797	357
18	583	0.754	731	324
20	526	0.747	686	298
22	480	0.739	655	277
24	443	0.733	625	259
28	383	0.731	547	225
32	338	0.733	477	198
36	297	0.738	408	172
40	244	0.760	296	134
44	244	0.760	296	134
48	227	0.778	247	118
52	201	0.776	222	105
56	185	0.813	162	86
60	157	0.791	158	79
64	131	0.862	80	50
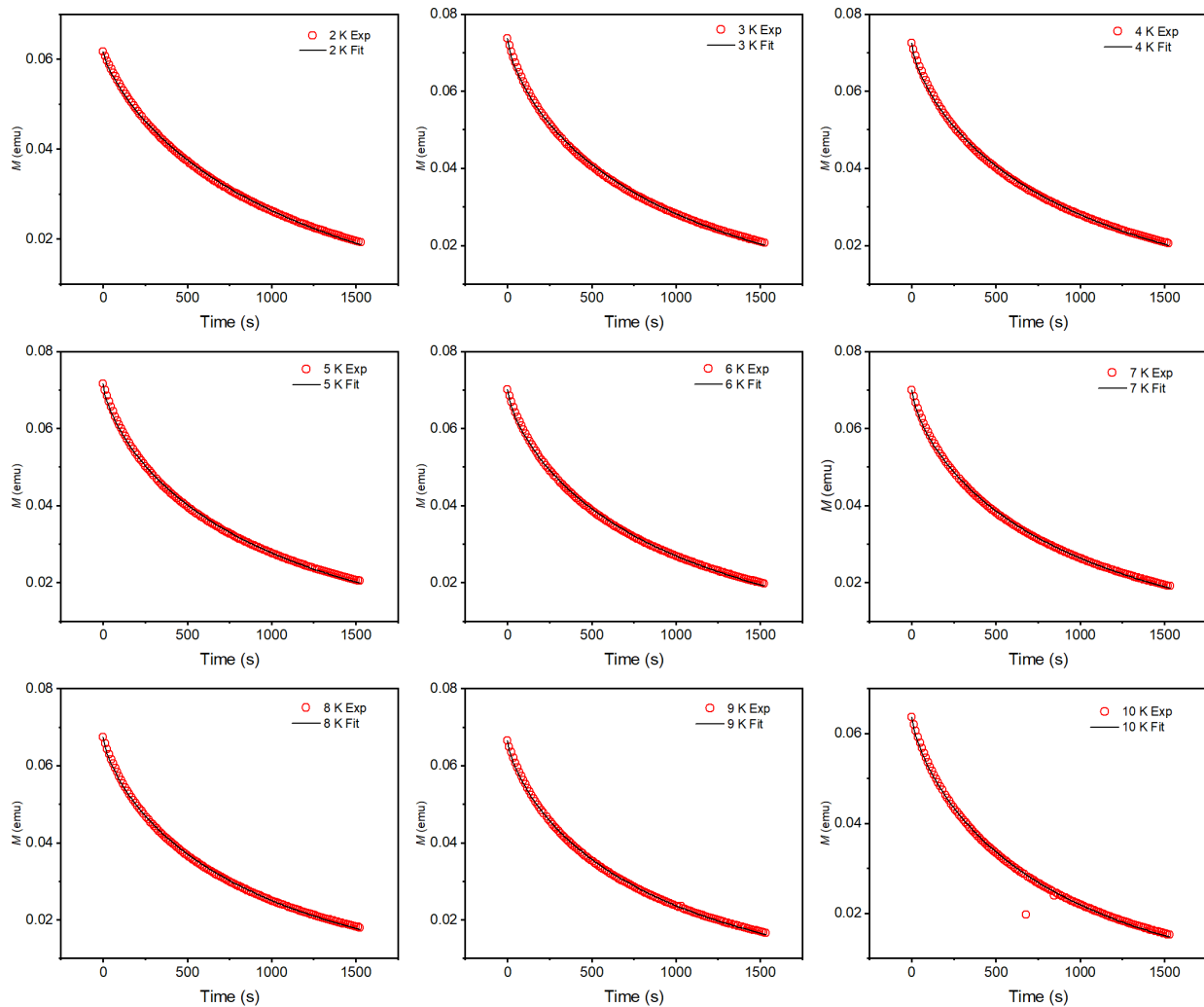
Figure S4.12. Normalized magnetization decay plots for **1** collected at the indicated temperatures. Circles indicate data points and black lines are fits using eq S1. The sample was initially magnetized under an applied magnetic field of 7 T for 5 min prior to data collection.
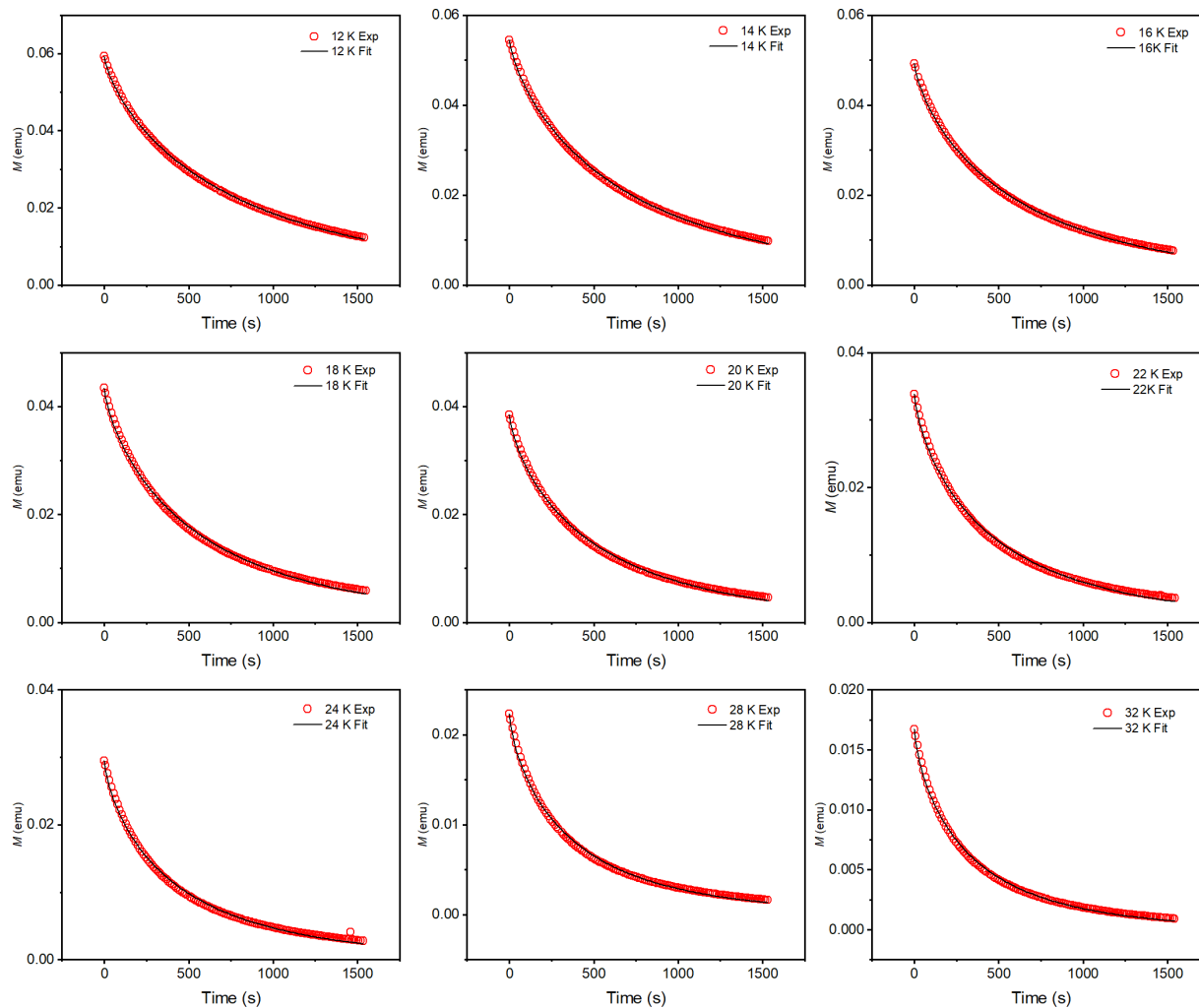
Figure S4.13. Normalized magnetization decay plots for **1** collected at the indicated temperatures. Circles indicate data points and black lines are fits using eq S1. The sample was initially magnetized under an applied magnetic field of 7 T for 5 min prior to data collection.
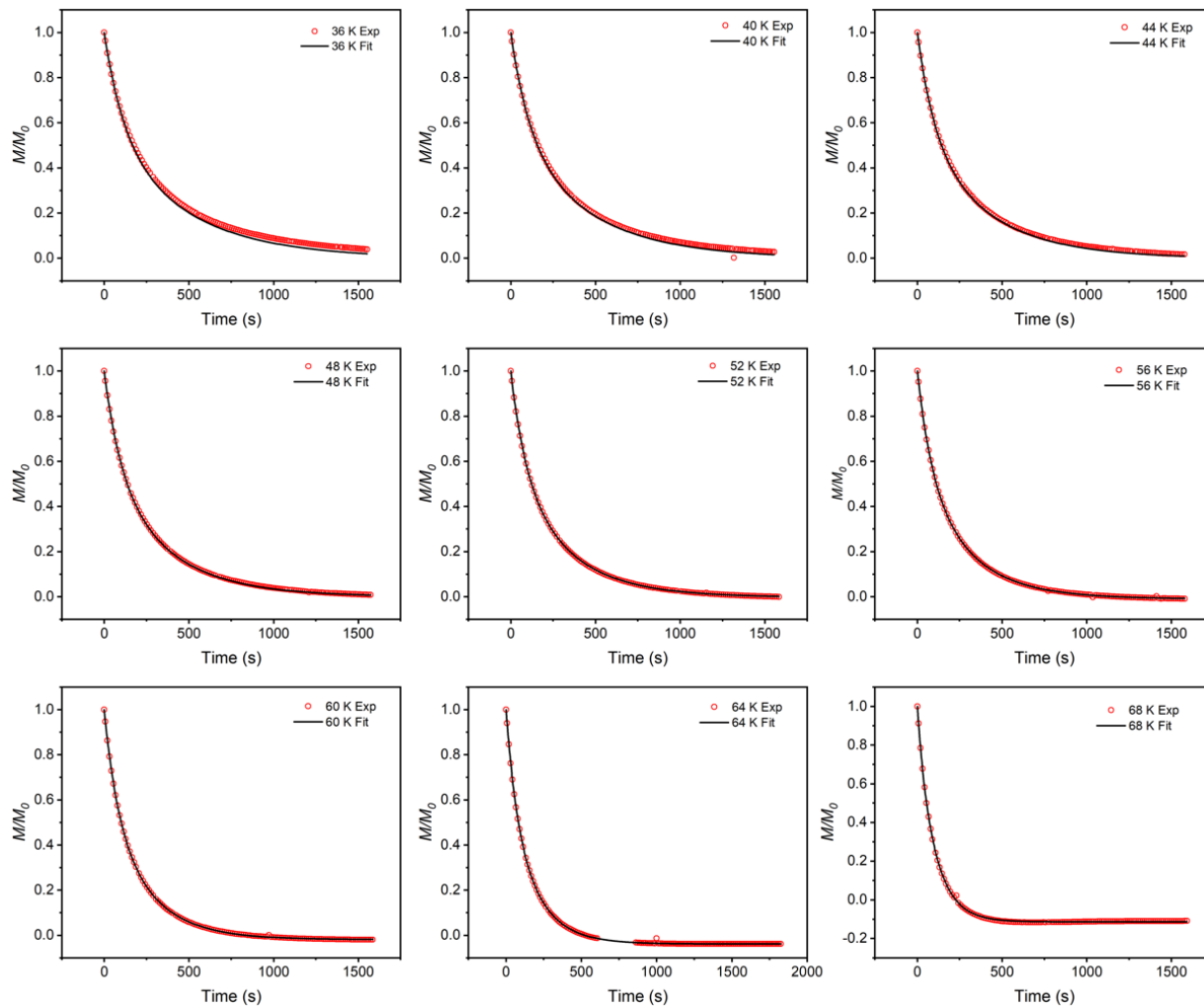
Figure S4.14: Normalized magnetization decay plots for **1** collected at the indicated temperatures. Circles indicate data points and black lines are fits using eq S1. The sample was initially magnetized under an applied magnetic field of 7 T for 5 min prior to data collection.

Table S4.4. Tabulated Decay Fit Parameters obtained for a magnetic sample prepared from crystals of **1**·2THF (see Section 1.6). Data are intended to verify reproducibility of data collected for **1** only. Estimated uncertainties in τ at the 1σ level were calculated with $\tau_{\pm} = \tau \exp\{\pm\frac{1.64 \ \tan[\frac{\pi}{2}(1-\beta)]}{(1-\beta)^{0.141}}\}$ derived in Ref. 22 where τ and β are the fitted values from the stretched exponential function, and $\tau_{\pm}$ are the limits of the 1σ uncertainties.

T (K)	τ (s)	β	τ₊	τ₋
2	1048	0.688	1884	674
4	988	0.694	1722	628
6	951	0.690	1691	609
8	944	0.698	1618	597
10	883	0.708	1430	546
12	823	0.752	1046	461
14	742	0.721	1119	446
16	693	0.727	1012	412
18	635	0.729	916	375
20	575	0.725	848	343
22	540	0.728	788	320
24	503	0.728	728	297
28	444	0.733	625	260
32	393	0.738	539	227
36	345	0.740	468	198
40	315	0.750	403	177
44	286	0.760	346	157
48	260	0.770	297	139
52	234	0.777	256	122
56	228	0.879	120	79
60	148	0.797	144	73
64	147	0.877	79	51
68	105	0.875	57	37
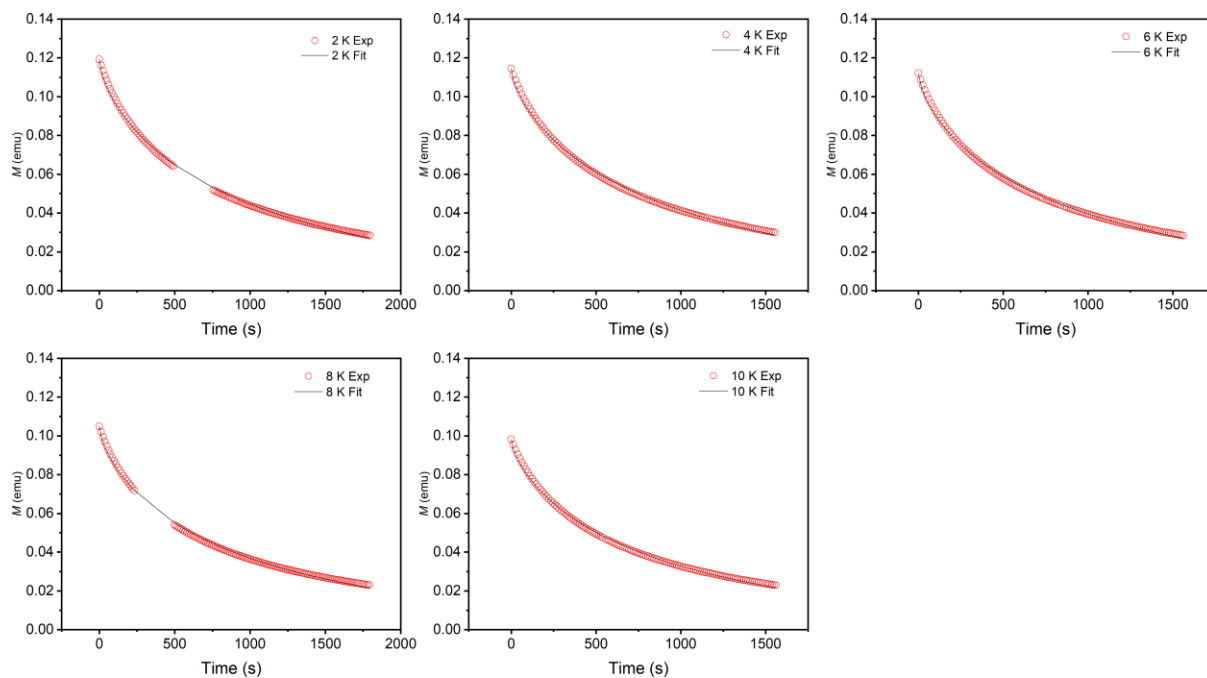
Figure S4.15. Normalized magnetization decay plots obtained for a magnetic sample prepared from crystals of **1**·2THF (see Section 1.6). Data are shown only to verify reproducibility of data collected for **1**, given the uncertainty in the solvation state of the compound. Circles indicate data points and black lines are fits using eq S1. The sample was initially magnetized under an applied magnetic field of 7 T for 5 min prior to data collection.
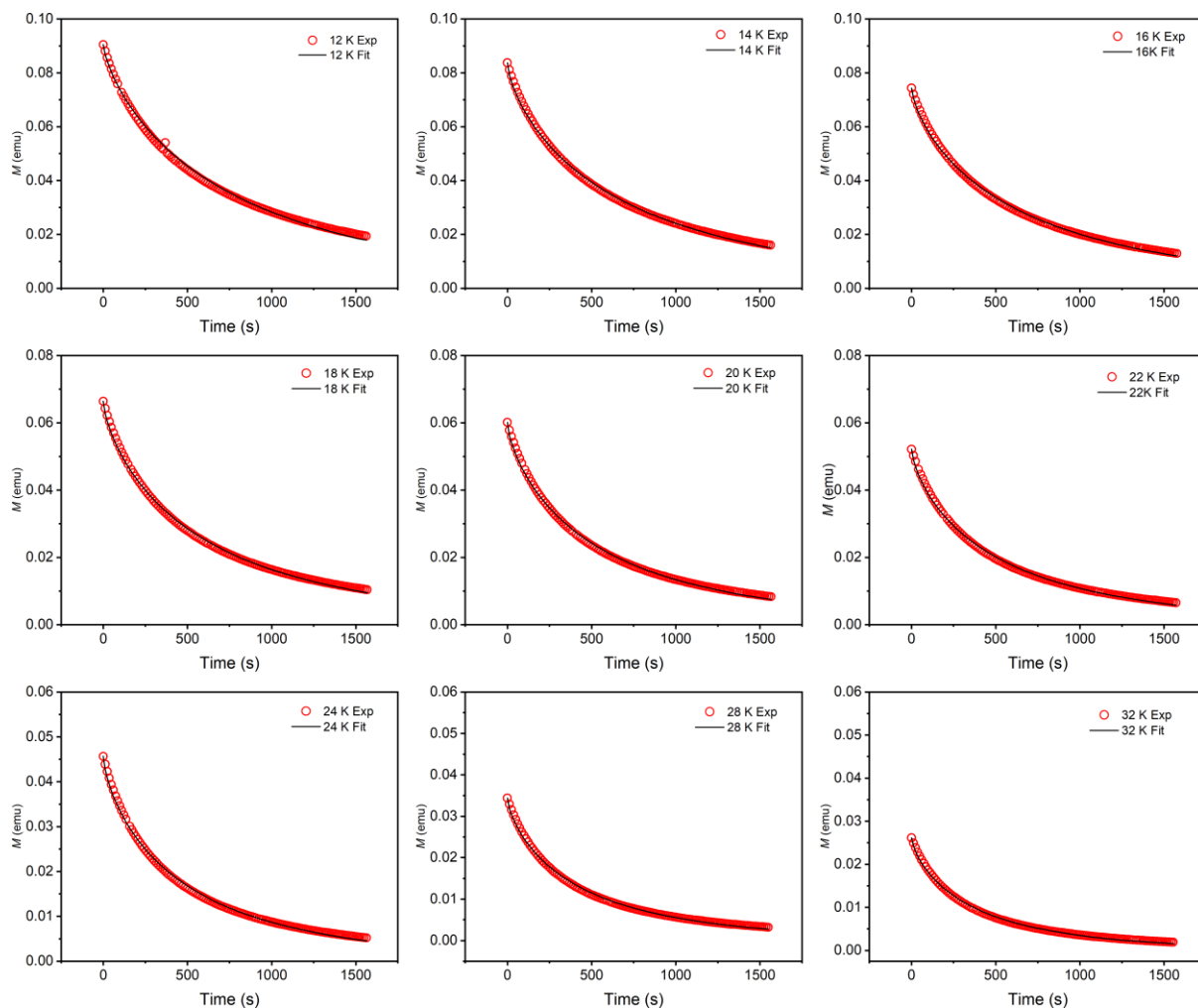
Figure S4.16. Normalized magnetization decay plots obtained for a magnetic sample prepared from **1**·2THF. Data are shown only to verify reproducibility of data collected for **1**, due to the uncertainty in the solvation state of the compound. Circles indicate data points and black lines are fits using eq S1. The sample was initially magnetized under an applied magnetic field of 7 T for 5 min prior to data collection.
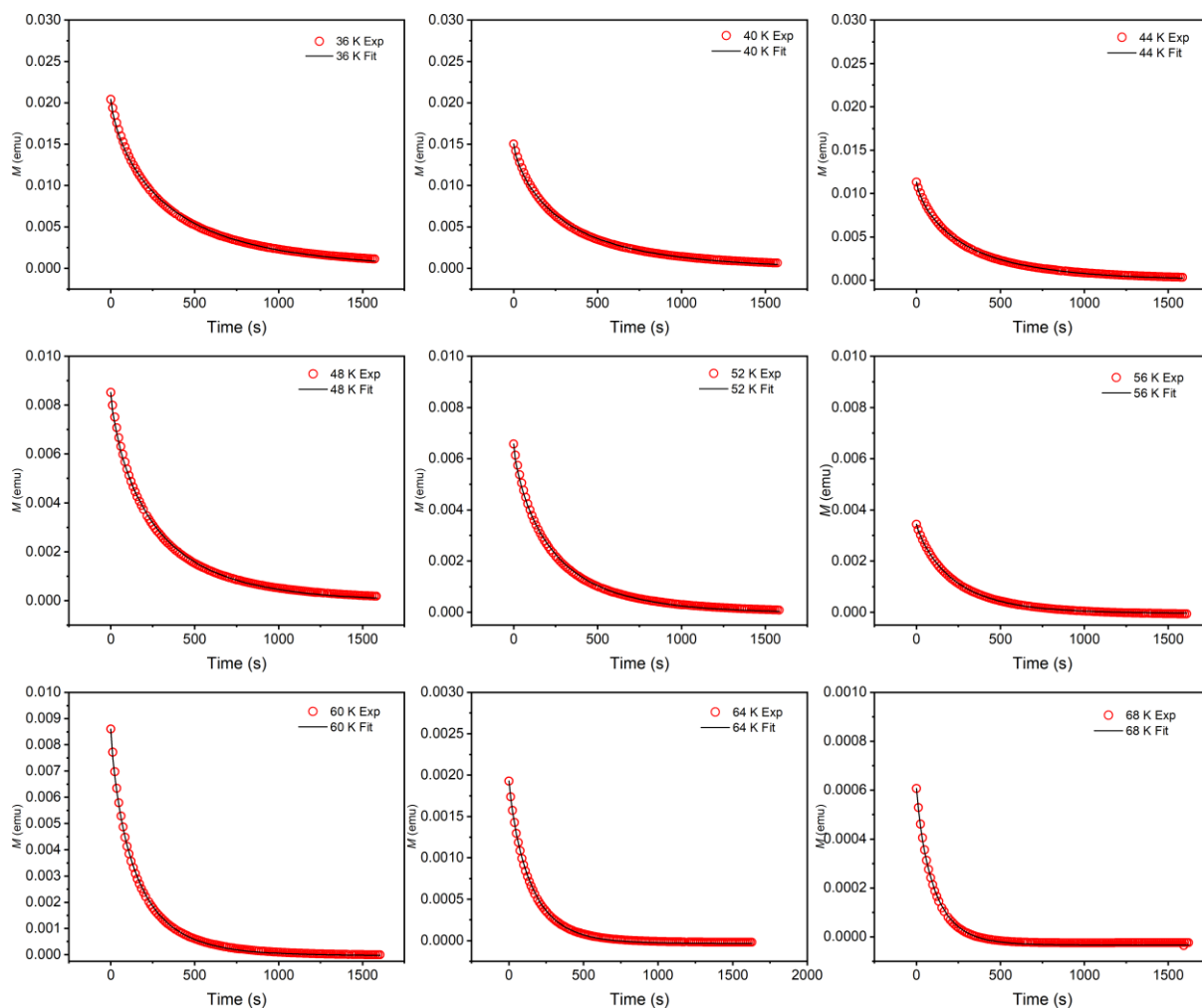
Figure S4.17. Normalized magnetization decay plots obtained for a magnetic sample prepared from **1**·2THF. Data are only intended to verify reproducibility of data collected for **1**, due to the uncertainty in the solvation state of the compound. Circles indicate data points and black lines are fits using eq S1. The sample was initially magnetized under an applied magnetic field of 7 T for 5 min prior to data collection.
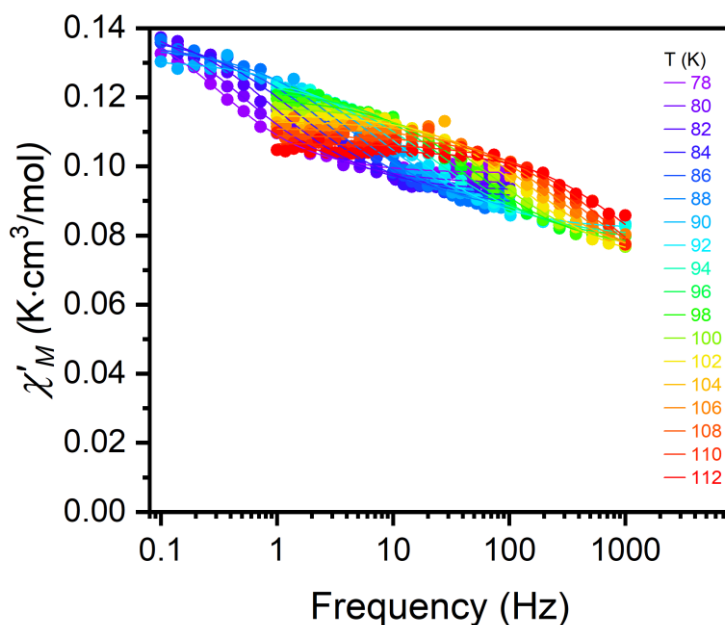
Figure S4.18. Molar in-phase ac magnetic susceptibility versus frequency data for **1**, collected under zero dc field. Symbols represent experimental data and lines are fits to the generalized Debye model (eqs S2 and S3). The susceptibility does not go to zero at the highest frequencies, suggesting that there is a second, faster relaxation process occurring outside of the measured frequency range.
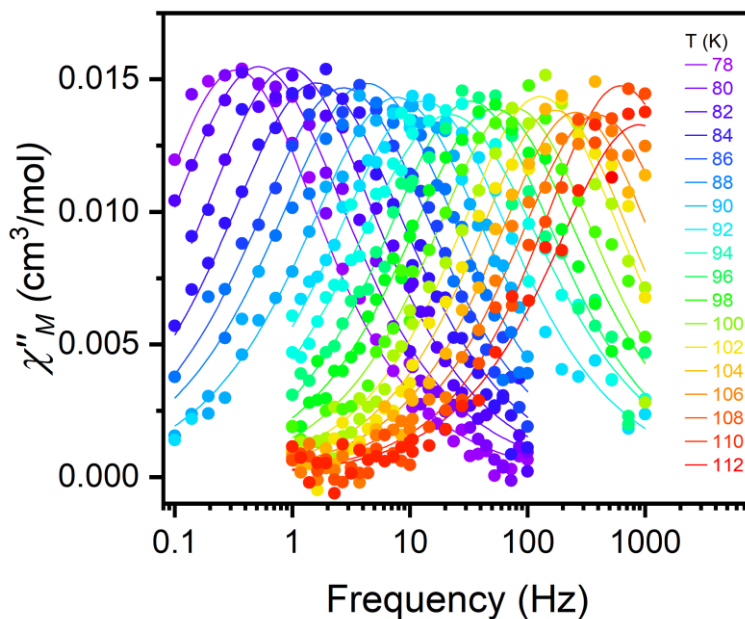
Figure S4.19. Molar out-of-phase ac magnetic susceptibility versus frequency data for **1**, collected under zero dc field. Symbols represent experimental data and lines are fits to the generalized Debye model (eqs S2 and S3).
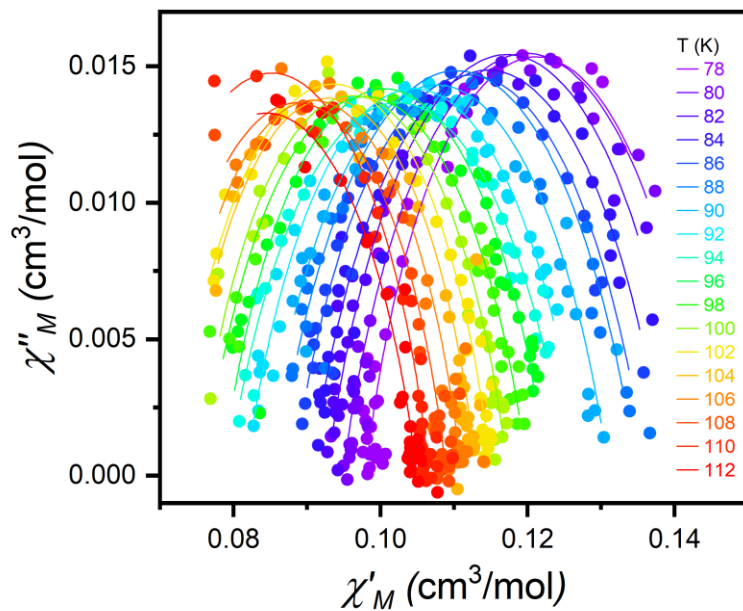
Figure S4.20. Cole-Cole plots for **1** generated from zero-field ac susceptibility data. Symbols represent experimental data and lines are fits to the generalized Debye model (eqs S2 and S3).

Table S4.5. Ac susceptibility fit parameters for **1**. All χ_S and χ values are reported in emu/mol.

T (K)	τ (s)	τ Error (s)	χ_S	χ_S Error	χ_T	χ_T Error	α	α error
78	0.48	0.03	0.0979	0.0002	0.144	0.001	0.26	0.02
80	0.31	0.02	0.0948	0.0003	0.145	0.001	0.29	0.02
82	0.171	0.008	0.0926	0.0003	0.1417	0.0009	0.29	0.02
84	0.099	0.004	0.0905	0.0004	0.1388	0.0007	0.30	0.02
86	0.058	0.002	0.0880	0.0004	0.1362	0.0007	0.30	0.02
88	0.037	0.002	0.0857	0.0007	0.1349	0.0007	0.31	0.02
90	0.0207	0.0008	0.0841	0.0006	0.1311	0.0005	0.30	0.02
92	0.0121	0.0003	0.0816	0.0003	0.1274	0.0005	0.29	0.01
94	0.0074	0.0003	0.0791	0.0005	0.1255	0.0005	0.32	0.02
96	0.0049	0.0002	0.0784	0.0005	0.1227	0.0004	0.27	0.01
98	0.0031	0.0001	0.0759	0.0005	0.1201	0.0003	0.28	0.01
100	0.0021	0.0001	0.0751	0.0007	0.1173	0.0003	0.26	0.02
102	0.0012	0.0000	0.0720	0.0006	0.1151	0.0002	0.25	0.01
104	0.00093	0.00005	0.073	0.001	0.1131	0.0003	0.24	0.02
106	0.00062	0.00005	0.071	0.001	0.1110	0.0003	0.24	0.03
108	0.00041	0.00003	0.068	0.002	0.1090	0.0003	0.25	0.02
110	0.00026	0.00003	0.064	0.003	0.1066	0.0003	0.23	0.03
112	0.00018	0.00003	0.064	0.003	0.1050	0.0002	0.27	0.03
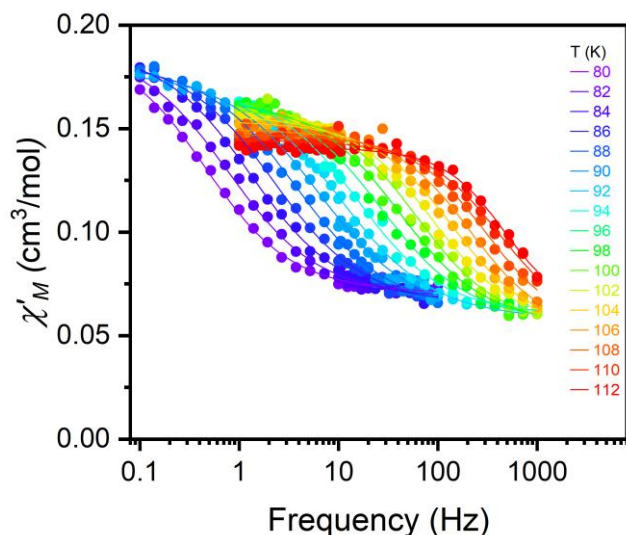
Figure S4.21. Molar in-phase ac magnetic susceptibility versus frequency data obtained under zero applied field for a magnetic sample prepared from **1**·2THF. Based on dc magnetic suscepti-bility measured for this sample (Figures S10 and S11), it is likely at least partially desolvated, and so data serve only to support reproducibility of data collected for **1**. Symbols represent experi-mental data and lines are fits to the generalized Debye model (eqs S2 and S3). Interestingly, the in-phase ac susceptibility for this sample approaches zero more closely than the same data for **1** (see Figure S4.18). This is the only readily apparent difference between the data obtained for the two samples.
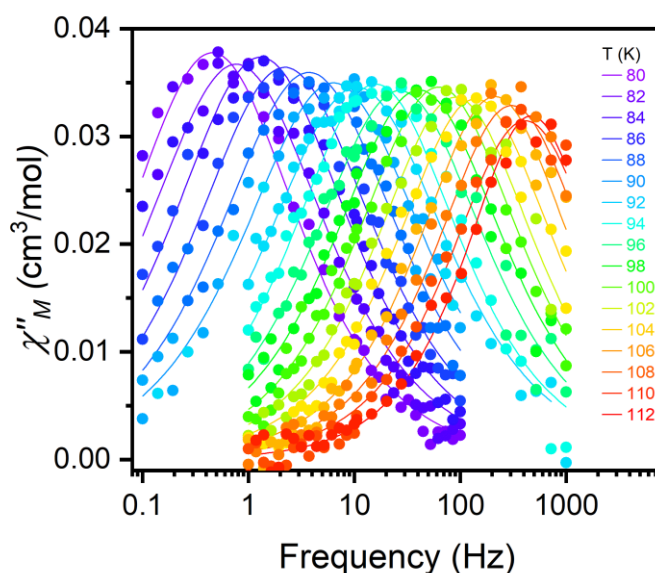
Figure S4.22. Molar out-of-phase ac magnetic susceptibility versus frequency data collected under zero applied field for a magnetic sample prepared from **1**·2THF. Based on dc magnetic suscepti-bility measured for this sample (Figures S10 and S11), it is likely partially desolvated, and so data serve only to support reproducibility of data collected for **1**. Symbols represent experimental data and lines are fits to the generalized Debye model (eqs S2 and S3).

138
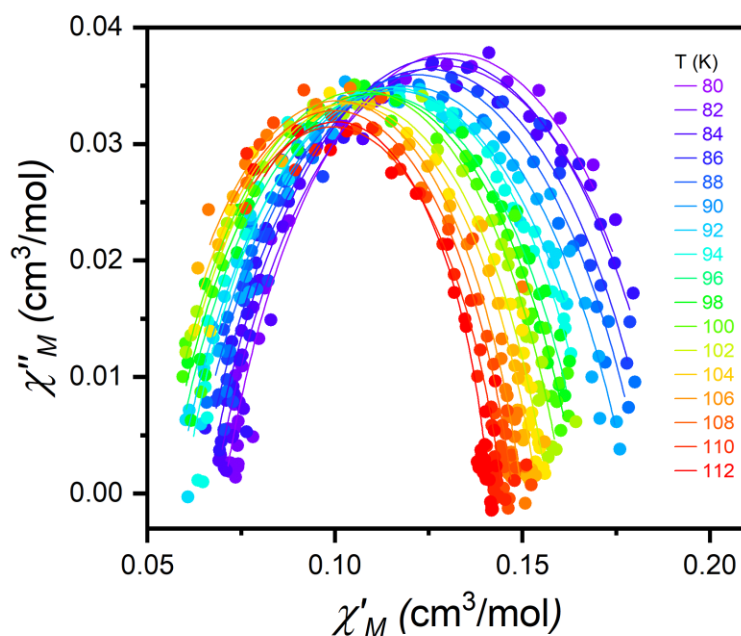
Figure S4.23. Cole-Cole plot of out-of-phase susceptibility versus in-phase susceptibility data collected under zero applied field for a magnetic sample prepared from **1**·2THF. Based on dc magnetic susceptibility measured for this sample (Figures S10 and S11), it is likely at least partially desolvated, and so data serve only to support reproducibility of data collected for **1**. Symbols represent experimental data and lines are fits to the generalized Debye model (eqs S2 and S3).

Table S4.6. Ac susceptibility fit parameters for a magnetic sample prepared from **1**·2THF, obtained from fits to data unadjusted for sample composition (see Figures S10, S11, and Section 1.6), which should affect only the magnitude of χ_S and χ_T (reported in emu/mol), and not the relaxation times or α values. These data are intended to verify reproducibility of data collected for **1**.

T (K)	τ (s)	τ Error (s)	χ_S	χ_S Error	χ_T	χ_T Error	α	α error
80	0.35	0.01	0.0702	0.0005	0.192	0.002	0.29	0.01
82	0.208	0.009	0.0676	0.0007	0.191	0.002	0.32	0.01
84	0.123	0.004	0.0658	0.0007	0.190	0.001	0.31	0.01
86	0.072	0.002	0.0638	0.0007	0.186	0.001	0.31	0.01
88	0.043	0.001	0.0614	0.0009	0.183	0.001	0.32	0.01
90	0.0252	0.0008	0.060	0.001	0.178	0.001	0.32	0.01
92	0.0151	0.0003	0.0575	0.0007	0.174	0.001	0.32	0.01
94	0.0100	0.0003	0.0596	0.0009	0.170	0.001	0.28	0.01
96	0.00597	0.0002	0.056	0.001	0.1672	0.0009	0.30	0.01
98	0.00391	0.0001	0.055	0.001	0.1647	0.0009	0.29	0.01
100	0.00256	0.00008	0.053	0.001	0.1609	0.0007	0.27	0.01
102	0.00178	0.00005	0.054	0.001	0.1567	0.0005	0.26	0.01
104	0.00115	0.00004	0.052	0.001	0.1539	0.0004	0.26	0.01
106	0.00075	0.00004	0.051	0.002	0.1498	0.0006	0.24	0.02
108	0.00052	0.00003	0.052	0.003	0.1474	0.0006	0.23	0.02
110	0.00039	0.00003	0.054	0.003	0.1446	0.0006	0.22	0.02
112	0.00034	0.00002	0.060	0.003	0.1410	0.0004	0.15	0.02

Table S4.7. Arrhenius fit parameters for a magnetic sample prepared from **1**·2THF, obtained from fits to data unadjusted for sample composition (see Figures S10, S11, and Section 1.6), which should affect only the magnitude of χ_S and χ_T (reported in emu/mol), and not the relaxation times or α values. These data are reported to verify reproducibility of data collected for **1**.

U_{eff} (cm^{1})	τ_0 (s)	C (s$^{-1}\cdot$K^n)	n	τ_{QTM} (s)
1600(100)	$10^{-12.6(8)}$	$10^{-5(2)}$	1(1)	$10^{3.1(3)}$
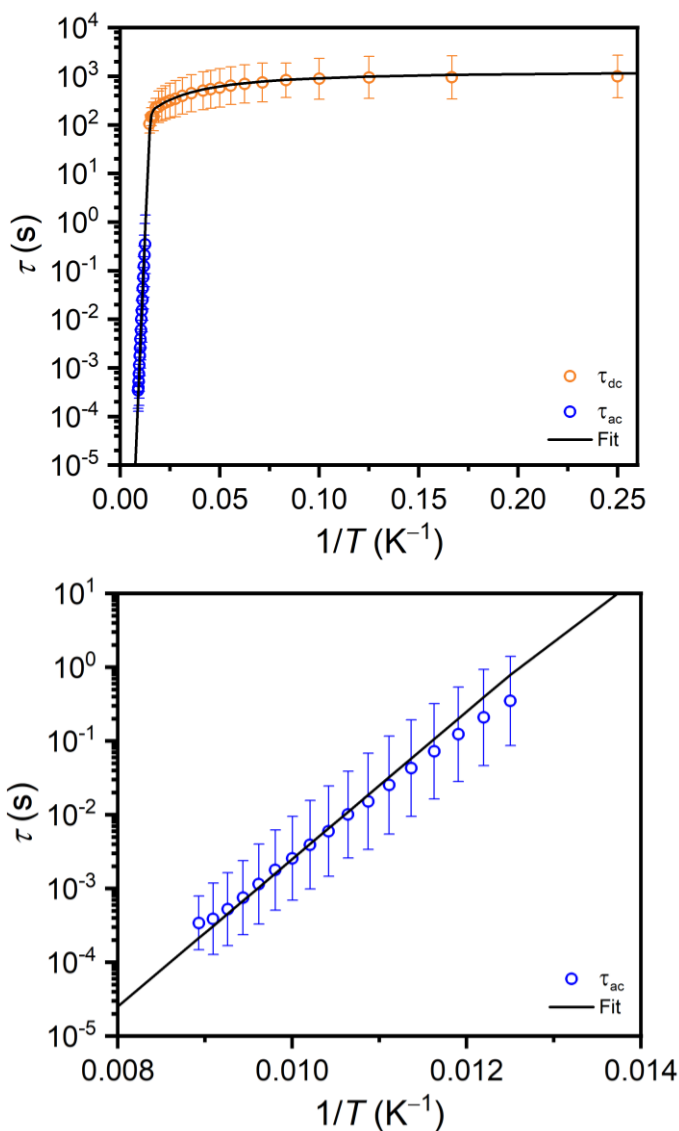
Figure S4.24. (Upper) Arrhenius plot of average relaxation times obtained for a magnetic sample prepared from **1**·2THF as described above (with 1σ uncertainties). These data are reported to verify reproducibility of data collected for **1**. Orange circles correspond to relaxation times from magnetization decay, blue circles correspond to relaxation times from ac susceptibility measurements. (Lower) Expanded view of the ac region in the upper plot. Fit curve generated using fitted parameters in Table S4.7 with Eq 1 from the main text.

Table S4.8. Cartesian coordinates of the PBE and PBE0 optimized structures of the [Dy(BC₄Ph₅)₂]⁻ anion in **1**·2THF.

	1-PBE			1-PBE0		
Dy	-0.34436	-0.23783	-0.02990	-0.33466	-0.19237	-0.04002
C	1.23979	2.41515	2.08639	1.28871	2.37535	2.08167
C	0.98129	-0.15792	2.21921	0.93754	-0.16858	2.21905
C	-2.89504	-0.93085	2.23033	-2.94438	-0.80955	2.20391
C	-0.09890	-1.11564	2.37760	-0.16704	-1.08519	2.35930
C	0.10150	-2.57534	2.43579	-0.01190	-2.54523	2.43087
B	-1.43299	-0.34462	2.34964	-1.46436	-0.27537	2.31912
C	0.43919	1.16771	2.06680	0.44706	1.16146	2.06255
C	-1.88190	2.31076	2.04499	-1.81743	2.38097	2.00313
C	-1.00896	1.11996	2.09665	-0.99203	1.16339	2.07026
C	-3.16676	-2.09991	1.48283	-3.25538	-1.96763	1.47631
H	-2.33838	-2.66684	1.04621	-2.45328	-2.56091	1.04395
C	2.22147	2.62558	3.07293	2.25213	2.55869	3.07616
H	2.41072	1.84283	3.80977	2.39838	1.78209	3.81858
C	1.00874	3.45137	1.16606	1.11346	3.39862	1.15077
H	0.24956	3.32345	0.39349	0.36787	3.29049	0.37205
C	1.73700	4.63862	1.20877	1.87975	4.55103	1.19216
H	1.53695	5.41189	0.46241	1.72306	5.31730	0.43909
C	2.72108	4.82395	2.18257	2.84451	4.71134	2.17608
H	3.30070	5.75022	2.21491	3.45268	5.61023	2.20835
C	2.95490	3.81107	3.11641	3.02311	3.70919	3.11954
H	3.71793	3.94277	3.88853	3.77161	3.82155	3.89838
C	-1.65924	3.43694	2.86510	-1.56065	3.49580	2.81049
H	-0.80904	3.43229	3.54972	-0.72080	3.46584	3.49555
C	-3.84396	3.46592	1.13736	-3.71701	3.58991	1.08036
H	-4.69335	3.45910	0.44856	-4.55686	3.60815	0.39183
C	-4.01515	-0.27945	2.79352	-4.02885	-0.11621	2.75936
H	-3.85717	0.62901	3.38041	-3.83692	0.78788	3.32896
C	-3.00521	2.35395	1.19435	-2.92391	2.45651	1.15041
H	-3.22827	1.49141	0.56189	-3.17131	1.60298	0.52750
C	-0.73396	-3.37976	3.24082	-0.87314	-3.30999	3.22840
H	-1.49413	-2.88888	3.85208	-1.62143	-2.79455	3.82067
C	-5.31429	-0.75299	2.60977	-5.33637	-0.54322	2.58831
H	-6.15449	-0.21862	3.06330	-6.14976	0.02243	3.03475
C	-3.59187	4.57839	1.94373	-3.43279	4.69086	1.87518
H	-4.24270	5.45545	1.89984	-4.04774	5.58399	1.82142
C	-4.46432	-2.57234	1.27650	-4.56101	-2.39459	1.28314
H	-4.62073	-3.46719	0.66721	-4.75094	-3.28521	0.69074

142

C	-2.49693	4.54996	2.81265	-2.35201	4.63054	2.74495
H	-2.28929	5.40812	3.45819	-2.11904	5.47977	3.38104
C	-5.54985	-1.89803	1.84090	-5.61253	-1.68153	1.84085
H	-6.56941	-2.26195	1.68691	-6.63772	-2.01021	1.69740
C	-0.61291	-4.76761	3.25370	-0.79222	-4.69166	3.25731
H	-1.28149	-5.35899	3.88599	-1.48000	-5.25325	3.88335
C	1.08102	-3.24270	1.66726	0.94800	-3.24139	1.68415
H	1.76257	-2.66428	1.03968	1.64560	-2.69217	1.06083
C	0.35079	-5.40707	2.46570	0.15561	-5.36162	2.49274
H	0.43984	-6.49641	2.47342	0.21376	-6.44553	2.51298
C	1.20073	-4.63159	1.67345	1.02858	-4.62404	1.70618
H	1.95935	-5.10060	1.04070	1.77512	-5.11775	1.09088
C	2.42309	-0.44830	2.38677	2.36306	-0.50374	2.39770
C	3.40010	0.09808	1.53542	3.35325	0.00286	1.55497
H	3.09291	0.73763	0.70709	3.07226	0.64223	0.72668
C	2.86215	-1.27451	3.43955	2.76385	-1.33014	3.45083
H	2.12239	-1.70486	4.11756	2.01039	-1.73131	4.11989
C	4.75493	-0.17175	1.71646	4.68935	-0.30560	1.74555
H	5.47816	0.26354	1.02178	5.42582	0.09967	1.05831
C	4.21754	-1.54861	3.62080	4.09996	-1.64325	3.64249
H	4.52905	-2.19802	4.44376	4.38370	-2.29270	4.46558
C	5.17329	-1.00241	2.75957	5.07126	-1.13551	2.79036
H	6.23451	-1.22413	2.89961	6.11706	-1.38701	2.93862
C	-1.15223	-2.43761	-2.29825	-1.19887	-2.40958	-2.29139
C	-0.89096	0.11602	-2.47329	-0.85124	0.11510	-2.47402
C	2.93424	0.98180	-2.02451	2.97716	0.86126	-2.00824
C	0.14519	1.10972	-2.28461	0.20696	1.07235	-2.29435
C	-0.06767	2.57082	-2.39519	0.04043	2.53342	-2.41671
B	1.48231	0.36571	-2.07213	1.50930	0.29357	-2.06918
C	-0.33618	-1.20862	-2.34504	-0.34486	-1.21147	-2.32814
C	1.98285	-2.29355	-2.03074	1.91842	-2.36839	-1.98435
C	1.08247	-1.12780	-2.05804	1.06256	-1.17619	-2.03568
C	3.23006	2.17691	-1.33660	3.29649	2.04755	-1.33750
H	2.43213	2.69738	-0.80362	2.51189	2.59669	-0.82899
C	-2.20841	-2.67150	-3.20383	-2.22688	-2.61060	-3.21945
H	-2.39299	-1.94512	-3.99765	-2.36301	-1.88656	-4.01524
C	-0.92739	-3.40830	-1.29825	-1.03623	-3.36963	-1.28602
H	-0.08875	-3.29686	-0.60579	-0.22153	-3.27933	-0.57374
C	-1.74018	-4.53580	-1.17901	-1.88383	-4.46191	-1.18469
H	-1.54068	-5.25012	-0.37605	-1.73333	-5.17252	-0.37781
C	-2.79368	-4.73622	-2.07183	-2.90868	-4.63312	-2.10176
H	-3.43439	-5.61701	-1.98298	-3.57589	-5.48603	-2.02703
C	-3.01400	-3.80128	-3.09050	-3.06761	-3.70494	-3.12477

H	-3.82771	-3.95463	-3.80460	-3.86012	-3.83455	-3.85585
C	1.83299	-3.37891	-2.92072	1.73822	-3.45256	-2.85246
H	1.01802	-3.35914	-3.64739	0.93437	-3.41689	-3.57980
C	3.93951	-3.43526	-1.10149	3.81449	-3.55228	-1.02929
H	4.75949	-3.43920	-0.37802	4.62344	-3.57276	-0.30484
C	4.00999	0.36354	-2.69643	4.03354	0.20217	-2.64898
H	3.82884	-0.56203	-3.24919	3.83166	-0.72006	-3.18530
C	3.06889	-2.34885	-1.13249	2.98665	-2.44491	-1.08339
H	3.22531	-1.51631	-0.44385	3.16425	-1.61267	-0.41141
C	0.78636	3.33728	-3.21305	0.91578	3.26050	-3.22998
H	1.57730	2.82426	-3.76361	1.68797	2.72192	-3.76817
C	5.30168	0.89312	-2.66655	5.33255	0.68756	-2.60746
H	6.11005	0.38038	-3.19675	6.12663	0.14498	-3.11361
C	3.76020	-4.51038	-1.97741	3.60668	-4.62634	-1.88474
H	4.43822	-5.36732	-1.95219	4.25095	-5.49914	-1.84195
C	4.51864	2.70923	-1.29032	4.59226	2.53598	-1.27910
H	4.70117	3.62563	-0.72141	4.79481	3.44838	-0.72508
C	2.70355	-4.46790	-2.89121	2.56544	-4.56295	-2.80037
H	2.55393	-5.29367	-3.59295	2.39360	-5.38835	-3.48568
C	5.56657	2.06685	-1.95554	5.62153	1.85542	-1.91506
H	6.57994	2.47694	-1.92103	6.63978	2.23151	-1.87164
C	0.65073	4.72204	-3.30913	0.82446	4.63897	-3.33683
H	1.33762	5.28603	-3.94653	1.52664	5.17283	-3.97083
C	-1.07140	3.26537	-1.69115	-0.93655	3.25797	-1.72630
H	-1.75445	2.71941	-1.03680	-1.63494	2.74217	-1.07554
C	-0.34626	5.38976	-2.59202	-0.14816	5.33794	-2.63445
H	-0.44551	6.47620	-2.66080	-0.21343	6.41895	-2.71186
C	-1.20959	4.64970	-1.78086	-1.03076	4.63627	-1.82617
H	-1.98680	5.14505	-1.19254	-1.78972	5.15674	-1.24960
C	-2.33907	0.42002	-2.51202	-2.28526	0.45907	-2.51167
C	-3.23516	-0.17796	-1.60066	-3.18662	-0.10650	-1.60180
H	-2.90738	-0.97799	-0.92645	-2.88155	-0.90935	-0.93244
C	-2.86390	1.38545	-3.39451	-2.78075	1.42808	-3.39052
H	-2.19206	1.86590	-4.10772	-2.10174	1.88495	-4.10124
C	-4.58183	0.18588	-1.54518	-4.51434	0.29150	-1.54347
H	-5.22928	-0.28921	-0.80404	-5.16742	-0.15965	-0.80302
C	-4.20986	1.73928	-3.35256	-4.10752	1.81597	-3.34655
H	-4.58820	2.49246	-4.04888	-4.46468	2.57198	-4.03935
C	-5.07530	1.15127	-2.42240	-4.98032	1.25909	-2.41763
H	-6.12762	1.44341	-2.38584	-6.01692	1.57845	-2.37953

Table S4.9. Normal mode frequencies (cm^{-1}) and transition intensities $(km\ mol^{-1})$ of the vibrational modes of **1-PBE**.

Mode	Frequency (cm^{-1})	Transition intensity $(km\ mol^{-1})$	Mode	Frequency (cm^{-1})	Transition intensity $(km\ mol^{-1})$	Mode	Frequency (cm^{-1})	Transition intensity $(km\ mol^{-1})$
1	13.618	0.751	120	725.549	10.232	239	1264.483	31.344
2	24.144	0.181	121	725.927	12.957	240	1278.342	2.231
3	25.629	0.166	122	730.005	16.494	241	1279.631	1.262
4	29.330	0.031	123	731.142	9.359	242	1280.357	1.520
5	29.541	0.164	124	746.077	2.942	243	1281.343	1.705
6	31.323	0.350	125	747.638	0.976	244	1282.650	2.246
7	32.207	0.197	126	751.443	5.788	245	1284.385	0.808
8	37.325	1.075	127	755.446	8.256	246	1286.306	5.757
9	40.000	0.801	128	759.224	12.752	247	1289.557	5.617
10	40.576	1.176	129	760.197	24.317	248	1293.258	2.459
11	42.904	1.357	130	761.569	14.778	249	1296.491	9.180
12	45.033	0.115	131	762.928	18.700	250	1307.327	2.021
13	49.650	0.021	132	778.276	17.171	251	1311.470	7.991
14	51.249	0.058	133	780.011	23.301	252	1324.172	1.543
15	52.928	0.549	134	826.261	0.700	253	1325.323	0.649
16	55.547	0.224	135	828.014	0.536	254	1328.122	0.227
17	56.164	0.350	136	829.832	0.850	255	1328.571	4.925
18	57.753	0.010	137	830.933	0.664	256	1329.157	5.228
19	60.000	0.217	138	831.904	0.789	257	1330.933	1.561
20	62.770	2.966	139	832.539	0.646	258	1331.833	0.207
21	75.173	0.335	140	833.176	0.544	259	1332.290	2.988
22	77.843	3.125	141	833.873	1.065	260	1334.900	0.545
23	79.870	0.176	142	836.468	0.369	261	1335.332	1.646
24	82.410	0.102	143	838.692	1.302	262	1343.561	9.792
25	84.512	0.101	144	880.094	2.824	263	1346.709	14.385
26	93.777	0.047	145	880.986	2.227	264	1351.649	10.198
27	96.056	0.238	146	886.322	4.584	265	1353.686	189.023
28	101.202	0.906	147	886.544	1.928	266	1370.348	30.682
29	105.743	3.118	148	886.989	0.363	267	1376.485	13.324
30	108.747	1.185	149	888.253	3.402	268	1411.427	3.812
31	114.694	1.047	150	888.613	5.644	269	1412.766	6.879
32	140.566	4.457	151	889.303	1.550	270	1423.416	0.599
33	140.978	0.297	152	891.434	0.814	271	1424.396	6.609
34	152.034	0.746	153	892.465	13.221	272	1424.562	2.366
35	162.174	2.063	154	893.099	14.736	273	1425.297	2.253
36	167.027	0.241	155	893.608	0.344	274	1426.720	7.706
37	172.612	3.808	156	909.188	0.260	275	1427.543	11.986
38	174.561	4.714	157	912.978	0.433	276	1428.029	10.611
39	198.271	11.290	158	926.218	0.751	277	1429.609	4.450

40	201.311	14.209	159	930.282	1.098	278	1465.407	9.074
41	202.163	1.890	160	932.572	0.941	279	1469.201	9.750
42	217.865	0.016	161	933.522	0.986	280	1469.711	11.964
43	218.835	0.113	162	935.692	1.043	281	1470.937	22.344
44	220.457	1.111	163	935.862	0.846	282	1471.710	77.459
45	221.847	0.538	164	937.332	0.862	283	1472.426	57.531
46	224.822	0.307	165	937.606	1.121	284	1473.737	91.297
47	227.713	0.631	166	940.099	0.453	285	1475.761	42.424
48	234.161	0.679	167	944.529	0.322	286	1477.648	38.960
49	235.436	0.213	168	945.164	1.071	287	1481.044	23.630
50	241.850	1.348	169	948.504	1.569	288	1552.529	0.664
51	243.669	0.134	170	950.709	0.757	289	1556.655	2.448
52	244.445	0.269	171	951.726	5.048	290	1557.115	0.508
53	247.050	0.063	172	953.566	0.431	291	1558.310	1.505
54	261.343	1.191	173	953.935	0.583	292	1558.754	3.839
55	263.608	1.202	174	954.490	3.434	293	1559.753	0.888
56	276.227	0.483	175	955.371	0.871	294	1560.578	1.744
57	278.477	0.264	176	957.630	0.736	295	1562.040	1.772
58	355.076	9.971	177	959.171	1.583	296	1564.199	1.766
59	365.273	22.381	178	984.101	0.124	297	1566.834	1.186
60	395.986	0.117	179	984.667	0.180	298	1579.083	13.012
61	399.250	0.104	180	985.268	0.578	299	1584.070	13.754
62	402.446	0.140	181	986.044	0.068	300	1585.138	8.283
63	403.533	2.313	182	986.535	2.352	301	1586.933	38.059
64	404.786	4.763	183	986.669	0.087	302	1586.981	68.397
65	405.531	1.566	184	988.261	0.048	303	1588.002	17.067
66	407.484	2.021	185	988.952	0.621	304	1588.387	103.618
67	408.360	0.452	186	989.217	0.017	305	1590.115	27.221
68	409.605	1.116	187	990.519	0.325	306	1591.301	12.777
69	410.949	1.600	188	1002.558	7.415	307	1593.460	21.853
70	411.265	1.949	189	1003.048	1.140	308	3034.419	7.807
71	412.464	1.710	190	1021.924	27.785	309	3057.728	2.073
72	416.541	8.649	191	1022.144	34.691	310	3057.906	5.214
73	422.326	4.398	192	1022.758	4.428	311	3063.702	0.990
74	477.813	0.028	193	1022.963	3.025	312	3064.275	4.892
75	478.912	0.035	194	1024.325	0.067	313	3065.232	2.341
76	494.081	0.477	195	1025.099	2.007	314	3066.054	4.902
77	497.087	0.212	196	1025.949	2.006	315	3066.783	2.897
78	502.614	1.097	197	1026.165	0.092	316	3067.286	3.224
79	508.426	2.481	198	1036.469	0.145	317	3068.146	1.566
80	521.968	9.151	199	1037.388	0.036	318	3070.075	14.139
81	524.080	1.117	200	1060.670	0.752	319	3070.409	3.324
82	529.163	4.472	201	1060.852	0.723	320	3074.130	4.442
83	531.745	6.109	202	1065.944	2.657	321	3074.556	11.718
84	539.841	21.055	203	1067.318	0.749	322	3075.668	15.785
85	542.496	6.294	204	1069.848	7.450	323	3076.005	14.223

86	545.458	15.032	205	1070.327	3.535	324	3076.468	6.894
87	550.024	5.174	206	1072.342	10.590	325	3077.519	12.601
88	606.455	1.922	207	1073.715	25.046	326	3077.949	8.426
89	606.815	0.233	208	1074.478	0.729	327	3081.037	23.003
90	607.233	0.957	209	1076.276	5.754	328	3081.231	10.344
91	608.079	0.552	210	1098.488	7.853	329	3083.522	33.033
92	609.111	2.723	211	1100.869	4.407	330	3086.936	15.071
93	610.420	0.087	212	1104.909	4.991	331	3087.342	43.515
94	611.519	0.006	213	1105.669	12.024	332	3087.882	17.512
95	612.047	0.192	214	1138.208	0.811	333	3088.594	12.090
96	612.853	1.847	215	1138.535	0.788	334	3089.483	33.262
97	613.216	1.112	216	1138.783	0.542	335	3090.000	35.757
98	622.085	0.452	217	1138.904	0.853	336	3091.482	40.811
99	623.845	0.037	218	1139.685	0.346	337	3091.597	23.043
100	635.246	3.258	219	1139.775	0.762	338	3094.339	23.564
101	637.118	2.027	220	1140.278	1.516	339	3094.667	41.969
102	637.772	0.482	221	1140.945	0.590	340	3095.132	26.182
103	652.345	0.843	222	1142.450	1.306	341	3096.411	24.776
104	654.602	2.325	223	1142.891	1.577	342	3097.406	11.217
105	657.581	7.041	224	1143.496	1.176	343	3098.354	13.090
106	660.088	11.161	225	1146.564	0.781	344	3099.540	20.124
107	661.177	29.563	226	1165.358	1.776	345	3099.660	12.657
108	662.271	12.116	227	1166.556	2.484	346	3102.065	19.953
109	685.747	0.389	228	1167.231	3.882	347	3103.213	8.115
110	692.063	28.988	229	1167.637	3.447	348	3103.624	21.328
111	692.455	24.343	230	1169.135	6.578	349	3103.982	2.233
112	692.609	4.437	231	1170.214	3.828	350	3104.295	12.589
113	693.379	48.600	232	1171.298	2.289	351	3105.557	13.737
114	694.914	30.030	233	1171.470	4.548	352	3106.204	19.140
115	696.087	18.681	234	1173.084	1.920	353	3106.258	13.772
116	696.193	36.071	235	1173.268	1.823	354	3106.449	9.044
117	697.145	93.803	236	1194.666	1.160	355	3111.286	10.084
118	698.820	27.503	237	1196.521	0.063	356	3112.441	2.285
119	700.787	74.588	238	1253.799	11.425	357	3112.753	3.589

Table S4.10. Normal mode frequencies (cm^{-1}) and transition intensities $(km\ mol^{-1})$ of the vibrational modes of **1-PBE0**.

Mode	Frequency (cm^{-1})	Transition intensity $(km\ mol^{-1})$	Mode	Frequency (cm^{-1})	Transition intensity $(km\ mol^{-1})$	Mode	Frequency (cm^{-1})	Transition intensity $(km\ mol^{-1})$
1	14.799	0.632	120	752.763	8.292	239	1309.753	31.275
2	24.451	0.195	121	753.874	13.140	240	1317.025	1.921
3	26.727	0.131	122	758.700	14.313	241	1319.293	0.358
4	29.744	0.017	123	760.119	6.973	242	1320.924	1.032
5	30.791	0.155	124	779.341	1.610	243	1321.696	0.677
6	32.698	0.642	125	781.117	1.975	244	1322.074	0.954
7	33.277	0.271	126	786.624	5.302	245	1325.410	5.876
8	37.204	0.974	127	789.315	25.620	246	1325.798	1.436
9	40.171	0.456	128	791.673	27.695	247	1328.862	3.796
10	41.996	2.292	129	792.966	8.405	248	1338.481	6.165
11	43.350	0.732	130	793.615	16.247	249	1343.749	24.558
12	45.666	0.167	131	794.920	25.940	250	1356.410	1.136
13	50.605	0.017	132	812.439	24.546	251	1356.973	0.487
14	52.912	0.035	133	814.033	29.536	252	1357.783	1.322
15	54.103	0.825	134	866.640	0.721	253	1358.860	0.486
16	56.823	0.202	135	868.118	0.960	254	1359.394	0.809
17	57.524	0.434	136	868.424	0.410	255	1359.715	1.146
18	59.524	0.003	137	871.133	0.391	256	1360.023	0.722
19	61.509	0.047	138	871.642	1.017	257	1361.358	0.967
20	64.116	3.730	139	872.037	0.431	258	1361.777	2.206
21	76.200	1.237	140	872.794	0.917	259	1363.148	1.169
22	77.962	3.645	141	874.367	0.795	260	1364.181	0.393
23	81.525	0.192	142	876.250	0.572	261	1365.626	4.794
24	84.327	0.189	143	878.971	1.197	262	1395.722	11.256
25	86.053	0.114	144	922.739	1.629	263	1401.778	10.878
26	96.419	0.028	145	924.603	0.426	264	1407.616	16.666
27	99.035	0.197	146	928.881	2.296	265	1409.778	186.686
28	103.980	0.917	147	929.511	3.124	266	1430.250	18.531
29	108.293	3.489	148	934.036	2.478	267	1437.265	6.183
30	112.483	1.225	149	934.405	0.908	268	1462.297	5.458
31	118.425	1.250	150	934.678	6.078	269	1463.530	9.229
32	145.154	2.641	151	937.255	7.118	270	1474.995	0.442
33	146.100	1.600	152	937.307	1.101	271	1476.010	8.546
34	159.155	0.609	153	938.158	2.157	272	1476.444	3.130
35	170.267	2.290	154	940.719	14.099	273	1477.127	1.259
36	175.444	0.247	155	941.404	15.678	274	1479.012	12.399
37	180.617	4.644	156	943.098	1.446	275	1480.024	16.682
38	182.922	3.354	157	946.564	0.499	276	1481.983	12.657
39	205.176	3.116	158	979.418	0.711	277	1483.556	4.295

40	208.353	5.054	159	984.400	1.112	278	1521.316	7.386
41	210.017	21.832	160	985.893	0.446	279	1524.610	2.784
42	225.392	0.054	161	986.210	1.703	280	1527.100	20.431
43	226.105	0.065	162	988.182	0.550	281	1528.588	20.349
44	229.044	1.180	163	988.312	0.938	282	1529.418	83.900
45	229.454	0.105	164	988.952	1.276	283	1529.953	32.323
46	233.492	0.621	165	991.085	0.581	284	1531.336	128.956
47	237.402	0.680	166	992.800	0.487	285	1533.477	80.374
48	242.324	0.787	167	996.729	1.502	286	1537.334	53.974
49	243.835	0.375	168	997.051	0.032	287	1540.997	27.730
50	251.162	1.494	169	1000.003	0.893	288	1622.215	0.664
51	253.442	0.264	170	1000.677	1.393	289	1626.019	0.321
52	254.838	0.177	171	1002.595	0.409	290	1627.168	2.987
53	257.766	0.031	172	1003.747	3.108	291	1628.678	1.913
54	270.616	1.473	173	1004.810	1.236	292	1629.703	0.459
55	272.595	1.067	174	1006.662	1.329	293	1630.290	6.006
56	285.644	0.542	175	1007.150	2.466	294	1630.677	0.993
57	288.275	0.336	176	1008.493	0.661	295	1631.341	1.824
58	371.503	10.786	177	1011.136	1.397	296	1634.917	1.644
59	382.066	27.552	178	1017.541	0.209	297	1637.165	1.166
60	413.451	0.096	179	1018.252	0.289	298	1650.519	10.543
61	416.751	0.180	180	1018.593	0.189	299	1654.897	8.858
62	419.308	0.801	181	1019.115	0.305	300	1655.894	14.399
63	420.266	4.423	182	1019.413	1.066	301	1658.012	72.058
64	421.155	4.309	183	1019.537	0.307	302	1658.345	51.699
65	422.028	1.129	184	1020.710	0.062	303	1659.000	87.514
66	424.833	2.313	185	1021.377	0.125	304	1659.267	30.427
67	425.699	0.153	186	1021.870	0.383	305	1661.605	30.068
68	426.736	0.833	187	1023.039	0.311	306	1662.762	14.183
69	427.618	1.898	188	1037.876	8.854	307	1665.181	21.211
70	428.694	0.217	189	1038.381	0.274	308	3127.429	9.023
71	430.164	1.073	190	1056.971	31.085	309	3146.623	1.369
72	434.203	9.088	191	1057.063	29.994	310	3146.863	4.523
73	440.506	4.707	192	1057.606	4.933	311	3152.736	3.405
74	497.130	0.013	193	1057.841	0.968	312	3152.908	0.858
75	498.423	0.087	194	1059.377	0.059	313	3153.638	1.864
76	514.691	0.450	195	1059.953	1.510	314	3154.355	4.172
77	517.902	0.200	196	1060.669	0.586	315	3155.069	2.575
78	523.230	0.934	197	1060.820	0.381	316	3155.822	2.419
79	529.861	3.014	198	1072.697	0.113	317	3156.591	1.106
80	541.575	9.237	199	1073.076	0.025	318	3158.973	2.509
81	543.148	0.888	200	1096.603	0.573	319	3159.541	12.806
82	547.923	4.214	201	1097.317	0.792	320	3162.654	3.765
83	550.542	5.423	202	1102.476	3.510	321	3163.834	10.959
84	561.664	25.259	203	1103.906	1.289	322	3164.676	14.580
85	564.832	6.792	204	1105.765	11.157	323	3165.315	16.414

86	567.653	13.154	205	1106.082	1.394	324	3166.076	5.706
87	573.763	4.864	206	1108.319	7.286	325	3166.603	7.144
88	625.838	1.923	207	1109.074	30.772	326	3166.786	11.985
89	625.972	0.076	208	1110.312	0.414	327	3170.011	24.485
90	626.435	0.852	209	1112.507	6.241	328	3170.137	5.118
91	627.475	0.400	210	1139.161	8.021	329	3173.055	31.106
92	628.343	2.476	211	1140.744	2.695	330	3176.260	15.200
93	629.681	0.048	212	1145.138	4.381	331	3176.830	33.146
94	630.820	0.007	213	1145.992	10.349	332	3177.272	10.851
95	631.311	0.149	214	1172.232	0.981	333	3177.613	50.332
96	632.065	1.738	215	1172.617	0.316	334	3178.266	9.319
97	632.395	1.063	216	1172.746	2.111	335	3179.999	47.683
98	642.346	0.403	217	1172.919	0.624	336	3180.843	13.041
99	643.607	0.078	218	1173.445	0.642	337	3181.349	38.895
100	657.187	0.089	219	1173.708	0.421	338	3183.381	16.532
101	658.221	0.782	220	1174.077	1.355	339	3183.526	38.325
102	661.975	4.090	221	1174.684	0.199	340	3184.684	23.599
103	674.226	0.564	222	1175.980	1.640	341	3186.434	18.748
104	675.632	1.771	223	1177.574	1.342	342	3187.514	8.500
105	684.401	7.181	224	1186.000	0.157	343	3187.862	7.695
106	685.739	6.412	225	1189.043	0.545	344	3188.697	11.221
107	686.368	35.036	226	1202.684	1.491	345	3189.776	17.700
108	691.231	22.945	227	1204.600	1.655	346	3190.917	16.870
109	718.641	0.560	228	1204.913	3.541	347	3192.983	12.272
110	721.057	15.238	229	1205.206	2.579	348	3193.033	14.347
111	722.494	37.005	230	1206.261	2.377	349	3194.627	0.902
112	722.640	24.623	231	1206.409	3.993	350	3194.943	18.073
113	723.433	35.087	232	1207.041	4.501	351	3195.044	16.729
114	724.886	29.536	233	1208.844	3.183	352	3195.087	2.699
115	725.698	14.398	234	1209.230	1.278	353	3195.349	7.917
116	726.292	21.199	235	1210.366	2.438	354	3195.614	6.377
117	727.170	108.415	236	1241.849	2.071	355	3200.355	8.611
118	729.204	35.840	237	1244.154	0.543	356	3201.792	1.415
119	730.527	102.514	238	1302.789	20.529	357	3203.881	2.959

Figure S4.25. Vibrational coupling strength $(S_j)^{19}$ of each vibrational mode of **1-PBE** in the range of 0 to 1700 cm^{-1}. Electronic energy states are shown in blue and transitions between states are given in orange.
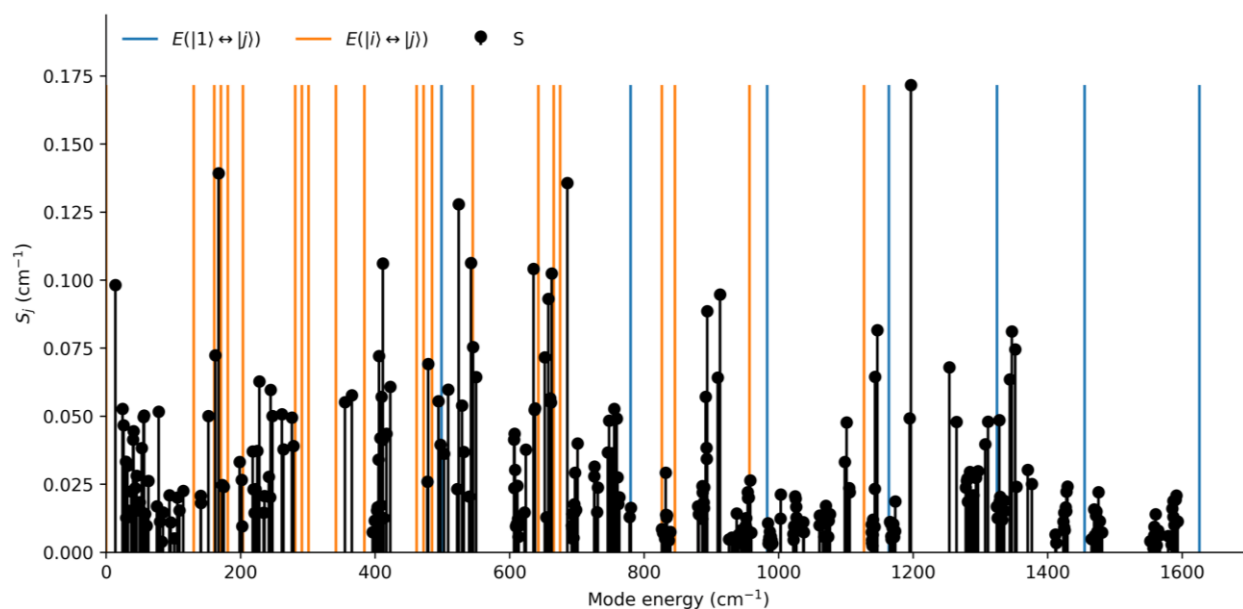

Figure S4.26. Vibrational coupling strength $(S_j)^{20}$ of each vibrational mode of **1-PBE0** in the range of 0 to 1700 cm^{-1}. Electronic energy states are shown in blue and transitions between states are given in orange.
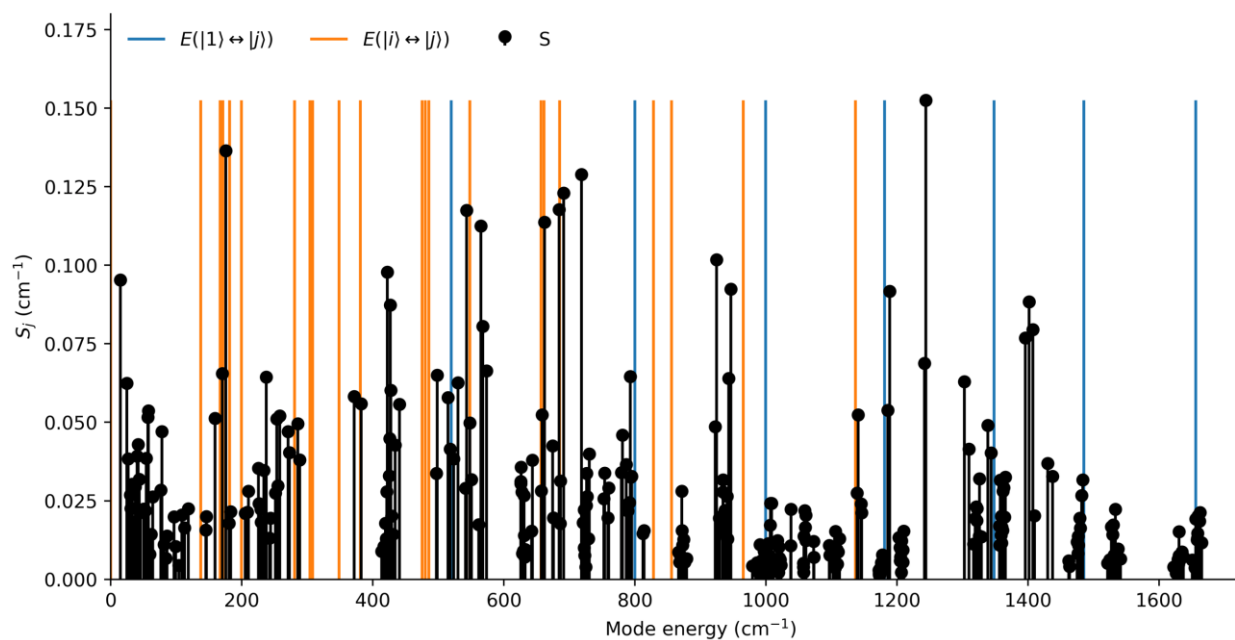
Table S4.11. Calculated electronic structure of one of the $[\text{Dy}(\text{BC}_4\text{Ph}_5)_2]^-$ anions in **1**·2THF.

Energy (cm^{-1})	CF Energy (cm^{-1})	g_x	g_y	g_z	θ (°)	Wavefunction	$<J_z>$
0.00	0.00	0.00	0.00	20.00	--	100% $|\pm15/2\rangle$	± 7.50
555.22	567.86	0.00	0.00	17.02	1.95	100% $|\pm13/2\rangle$	± 6.50
891.77	885.11	0.00	0.00	14.37	1.61	99% $|\pm11/2\rangle$	± 5.50
1111.88	1110.64	0.03	0.03	11.77	5.41	99% $|\pm9/2\rangle$	± 4.49
1300.73	1308.39	0.38	0.41	9.05	9.52	97% $|\pm7/2\rangle$ + 2% $|\pm3/2\rangle$	± 3.45
1476.28	1485.66	3.35	3.61	5.98	17.28	88% $|\pm5/2\rangle$ + 7% $|\pm1/2\rangle$ + 2% $|\mp3/2\rangle$	± 2.26
1624.30	1628.71	2.39	5.34	10.84	87.55	73% $|\pm3/2\rangle$ + 17% $|\mp1/2\rangle$ + 6% $|\mp5/2\rangle$	± 0.95
1790.59	1787.05	0.36	1.29	18.03	88.96	65% $|\pm1/2\rangle$ + 16% $|\mp3/2\rangle$ + 10% $|\mp1/2\rangle$	± 0.18

Table S4.12. Calculated electronic structure of one of the $[\text{Dy}(\text{BC}_4\text{Ph}_5)_2]^-$ anions in **1**·2THF using higher level methodology.

Energy (cm^{-1})	CF Energy (cm^{-1})	g_x	g_y	g_z	θ (°)	Wavefunction	$<J_z>$
0.00	0.00	0.00	0.00	19.90	--	100% $|\pm15/2\rangle$	± 7.50
542.59	550.73	0.00	0.00	16.99	2.03	100% $|\pm13/2\rangle$	± 6.50
860.06	855.64	0.00	0.00	14.35	1.24	99% $|\pm11/2\rangle$	± 5.50
1070.65	1070.05	0.03	0.03	11.76	5.67	99% $|\pm9/2\rangle$	± 4.49
1252.31	1257.28	0.41	0.44	9.04	9.52	96% $|\pm7/2\rangle$ + 2% $|\pm3/2\rangle$	± 3.44
1419.20	1425.18	3.45	3.73	5.96	17.59	87% $|\pm5/2\rangle$ + 8% $|\pm1/2\rangle$ + 2% $|\mp3/2\rangle$	± 2.25
1558.69	1561.53	2.37	5.23	10.93	87.59	72% $|\pm3/2\rangle$ + 17% $|\mp1/2\rangle$ + 6% $|\mp5/2\rangle$	± 0.94
1715.26	1712.98	0.35	1.22	18.00	88.93	64% $|\pm1/2\rangle$ + 16% $|\mp3/2\rangle$ + 10% $|\mp1/2\rangle$	± 0.18

Table S4.13. Electronic structure of **1-PBE**.

Energy (cm^{-1})	CF Energy (cm^{-1})	g_x	g_y	g_z	θ (°)	Wavefunction	$<J_z>$
0.00	0.00	0.00	0.00	20.00	--	100% $|\pm15/2\rangle$	± 7.50
488.59	498.50	0.00	0.00	17.06	1.94	100% $|\pm13/2\rangle$	± 6.50
784.44	779.74	0.00	0.00	14.42	1.01	99% $|\pm11/2\rangle$	± 5.50
984.25	982.90	0.02	0.02	11.80	5.04	99% $|\pm9/2\rangle$	± 4.50
1158.42	1163.86	0.13	0.15	9.05	8.87	97% $|\pm7/2\rangle$ + 2% $|\pm3/2\rangle$	± 3.45
1317.09	1324.68	3.66	4.13	5.91	22.98	86% $|\pm5/2\rangle$ + 9% $|\pm1/2\rangle$ + 2% $|\mp3/2\rangle$	± 2.21
1450.04	1454.95	2.15	5.36	11.36	89.89	70% $|\pm3/2\rangle$ + 19% $|\mp1/2\rangle$ + 8% $|\mp5/2\rangle$	± 0.84
1628.98	1625.53	0.24	0.76	18.36	89.65	66% $|\pm1/2\rangle$ + 20% $|\mp3/2\rangle$ + 5% $|\mp1/2\rangle$	± 0.10

Table S4.14. Electronic structure of **1-PBE** using higher level methodology.

Energy (cm⁻¹)	CF Energy (cm⁻¹)	g_x	g_y	g_z	θ (°)	Wavefunction	$<J_z>$
0.00	0.00	0.00	0.00	19.89	--	100% $\|\pm15/2\rangle$	± 7.50
475.46	481.82	0.00	0.00	17.03	1.99	100% $\|\pm13/2\rangle$	± 6.50
755.40	752.32	0.00	0.00	14.39	0.75	99% $\|\pm11/2\rangle$	± 5.50
946.94	946.17	0.02	0.02	11.78	5.29	99% $\|\pm9/2\rangle$	± 4.49
1114.46	1117.95	0.18	0.19	9.04	8.91	97% $\|\pm7/2\rangle$ + 2% $\|\pm3/2\rangle$	± 3.44
1265.34	1270.23	3.79	4.22	5.90	24.31	85% $\|\pm5/2\rangle$ + 10% $\|\pm1/2\rangle$ + 2% $\|\mp3/2\rangle$	± 2.20
1391.21	1394.44	2.11	5.21	11.44	89.88	70% $\|\pm3/2\rangle$ + 18% $\|\mp1/2\rangle$ + 8% $\|\mp5/2\rangle$	± 0.83
1559.99	1557.71	0.23	0.71	18.31	89.63	65% $\|\pm1/2\rangle$ + 20% $\|\mp3/2\rangle$ + 6% $\|\mp1/2\rangle$	± 0.10

Table S4.15. Electronic structure of **1-PBE0**.

Energy (cm⁻¹)	CF Energy (cm⁻¹)	g_x	g_y	g_z	θ (°)	Wavefunction	$<J_z>$
0.00	0.00	0.00	0.00	20.00	--	100% $\|\pm15/2\rangle$	± 7.50
508.38	519.61	0.00	0.00	17.05	2.07	100% $\|\pm13/2\rangle$	± 6.50
805.69	800.09	0.00	0.00	14.42	1.13	99% $\|\pm11/2\rangle$	± 5.50
1001.08	999.64	0.02	0.03	11.82	5.65	99% $\|\pm9/2\rangle$	± 4.49
1174.73	1181.03	0.10	0.14	9.07	9.40	97% $\|\pm7/2\rangle$ + 2% $\|\pm3/2\rangle$	± 3.45
1339.36	1347.96	3.46	3.91	5.93	19.90	87% $\|\pm5/2\rangle$ + 9% $\|\pm1/2\rangle$ + 2% $\|\mp3/2\rangle$	± 2.24
1480.04	1485.07	2.25	5.48	11.05	89.73	71% $\|\pm3/2\rangle$ + 18% $\|\mp1/2\rangle$ + 7% $\|\mp5/2\rangle$	± 0.88
1659.86	1656.15	0.28	0.94	18.22	89.83	69% $\|\pm1/2\rangle$ + 20% $\|\mp3/2\rangle$ + 3% $\|\mp1/2\rangle$	± 0.11

Table S4.16. Electronic structure of **1-PBE0** using higher level methodology.

| Energy (cm⁻¹)	CF Energy (cm⁻¹)	g_x	g_y	g_z	θ (°)	Wavefunction	$<J_z>$
0.00	0.00	0.00	0.00	19.90	--	100% $\|\pm15/2\rangle$	± 7.50
494.97	502.14	0.00	0.00	17.02	2.14	100% $\|\pm13/2\rangle$	± 6.50
775.54	771.88	0.00	0.00	14.39	0.83	99% $\|\pm11/2\rangle$	± 5.50
962.96	962.16	0.02	0.02	11.80	5.92	99% $\|\pm9/2\rangle$	± 4.49
1130.25	1134.28	0.14	0.17	9.06	9.46	97% $\|\pm7/2\rangle$ + 2% $\|\pm3/2\rangle$	± 3.44
1286.92	1292.43	3.58	4.01	5.92	20.89	86% $\|\pm5/2\rangle$ + 9% $\|\pm1/2\rangle$ + 2% $\|\mp3/2\rangle$	± 2.23
1419.87	1423.15	2.22	5.34	11.14	89.75	71% $\|\pm3/2\rangle$ + 18% $\|\mp1/2\rangle$ + 7% $\|\mp5/2\rangle$	± 0.87
1589.24	1586.81	0.27	0.88	18.18	89.82	68% $\|\pm1/2\rangle$ + 20% $\|\mp3/2\rangle$ + 4% $\|\mp1/2\rangle$	± 0.11
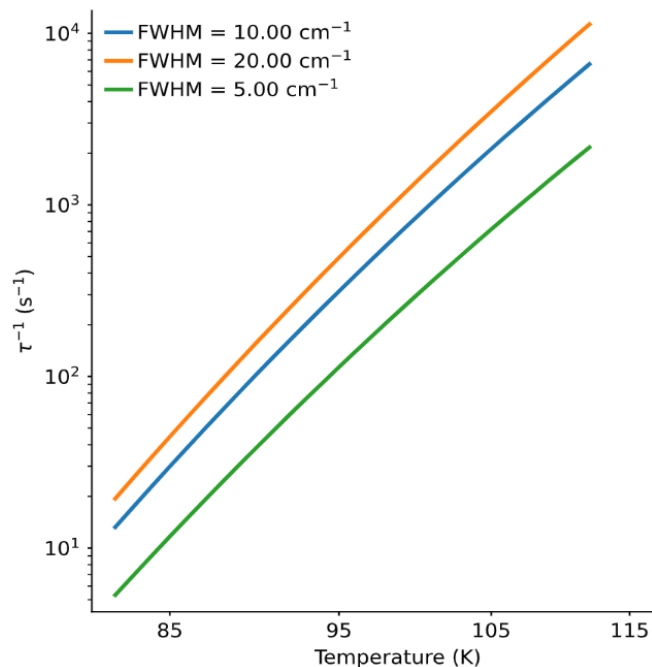
Figure S4.27. Calculated relaxation rates of **1-PBE** with fixed FWHM linewidths of 5 cm^{-1} (green), 10 cm^{-1} (blue) and 20 cm^{-1} (orange) in the temperature range of 82–112 K.
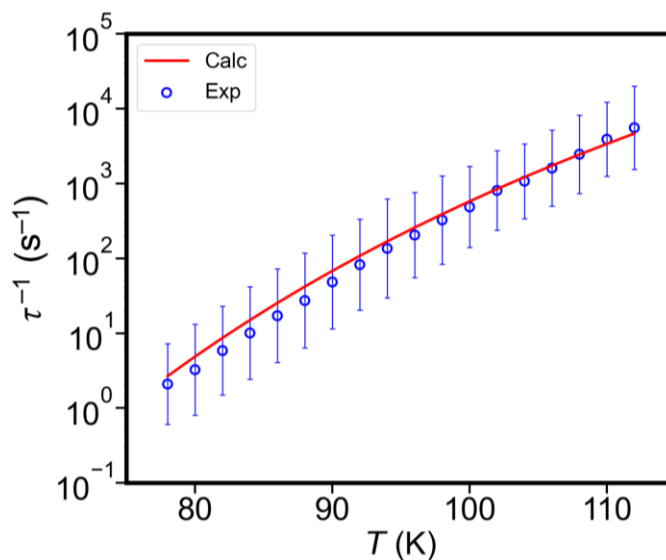

Figure S4.28. Temperature dependence of calculated relaxation rates for 1-PBE0 (red line, FWHM = 10 cm^{-1}) and experimental relaxation rates for **1** (blue symbols). Error bars are 1σ estimated standard deviations from the generalized Debye model.
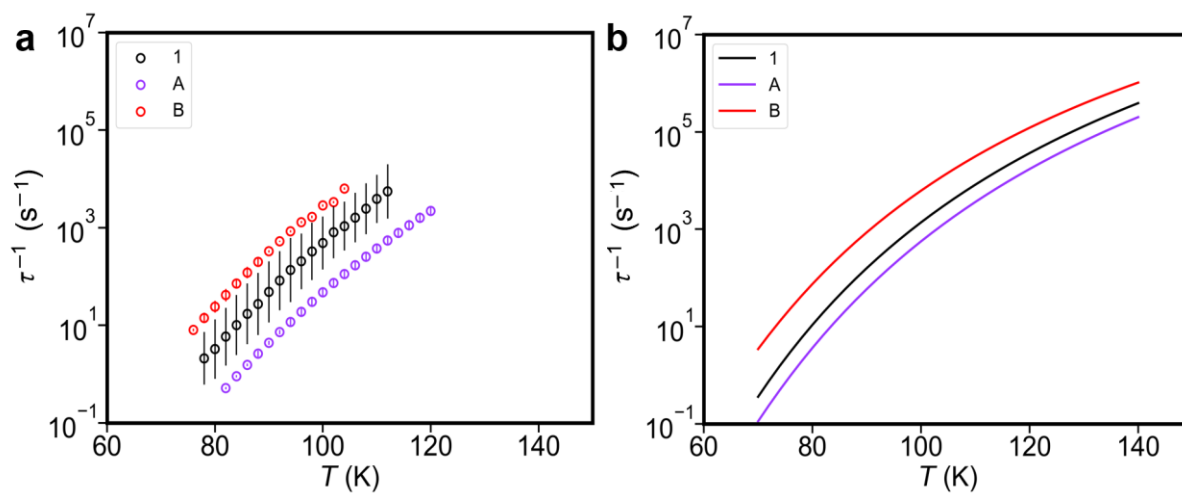
Figure S4.29. Temperature dependence of (a) experimental and (b) calculated relaxation rates for the **1-PBE** model (black), $[Dy(Cp^{iPr5})(Cp^{Me5})]^+$ (**A**; purple), and $[Dy(Cp^{iPr4})_2]^+$ (**B**; red). Calculations were all performed using a consistent methodology as for **1-PBE** with FWHM = 10 cm^{-1}.

Table S4.17. Mode-weighted comparison of **1-PBE** with $[Dy(Cp^{iPr5})(Cp^{Me5})]^{+}$ (**A**) performed at 100 K with FWHM = 10 cm^{-1}.

$\langle\bar{\bar{H}}_{SP}\rangle$	$\langle\bar{\bar{Q}}\rangle$	$\langle\bar{\bar{\rho}}\rangle$	$\langle\bar{\bar{n}}\rangle$	τ^{-1} (s^{-1})	$\tau^{-1}/\tau^{-1}{}_{1}$
A	**1-PBE**	**1-PBE**	**1-PBE**	3.91×10^{2}	0.45
1-PBE	**1-PBE**	**A**	**1-PBE**	8.49×10^{2}	0.98
1-PBE	**1-PBE**	**1-PBE**	**1-PBE**	8.64×10^{2}	1.00
1-PBE	**1-PBE**	**1-PBE**	**A**	8.81×10^{2}	1.02
1-PBE	**A**	**1-PBE**	**1-PBE**	1.22×10^{3}	1.41
$\langle\bar{\bar{H}}_{SP}\rangle$	$\langle\bar{\bar{Q}}\rangle$	$\langle\bar{\bar{\rho}}\rangle$	$\langle\bar{\bar{n}}\rangle$	τ^{-1} (s^{-1})	$\tau^{-1}/\tau^{-1}{}_{A}$
A	**A**	**1-PBE**	**A**	1.21×10^{2}	0.22
A	**A**	**A**	**1-PBE**	3.40×10^{2}	0.61
A	**A**	**A**	**A**	5.61×10^{2}	1.00
A	**1-PBE**	**A**	**A**	5.91×10^{2}	1.05
1-PBE	**A**	**A**	**A**	2.84×10^{3}	5.06

Table S4.18. Mode-weighted comparison of **1-PBE** with $[Dy(Cp^{iPr4})_{2}]^{+}$ (**B**), performed at 100 K with FWHM = 10 cm^{-1}.

$\langle\bar{\bar{H}}_{SP}\rangle$	$\langle\bar{\bar{Q}}\rangle$	$\langle\bar{\bar{\rho}}\rangle$	$\langle\bar{\bar{n}}\rangle$	τ^{-1} (s^{-1})	$\tau^{-1}/\tau^{-1}{}_{1}$
1-PBE	**1-PBE**	**1-PBE**	**B**	6.64×10^{2}	0.77
1-PBE	**1-PBE**	**1-PBE**	**1-PBE**	8.64×10^{2}	1.00
1-PBE	**1-PBE**	**B**	**1-PBE**	1.02×10^{3}	1.18
B	**1-PBE**	**1-PBE**	**1-PBE**	1.04×10^{3}	1.20
1-PBE	**B**	**1-PBE**	**1-PBE**	8.27×10^{3}	9.57
$\langle\bar{\bar{H}}_{SP}\rangle$	$\langle\bar{\bar{Q}}\rangle$	$\langle\bar{\bar{\rho}}\rangle$	$\langle\bar{\bar{n}}\rangle$	τ^{-1} (s^{-1})	$\tau^{-1}/\tau^{-1}{}_{B}$
B	**1-PBE**	**B**	**B**	4.16×10^{2}	0.07
B	**B**	**1-PBE**	**B**	3.04×10^{3}	0.49
B	**B**	**B**	**1-PBE**	4.70×10^{3}	0.76
B	**B**	**B**	**B**	6.17×10^{3}	1.00
1-PBE	**B**	**B**	**B**	1.90×10^{4}	3.08

Table S4.19. Calculated Löwdin charges for $[C_4BPh_5]^{2-}$, $[Cp^{iPr5}]^-$ and $[Cp^*]^-$ ligands.
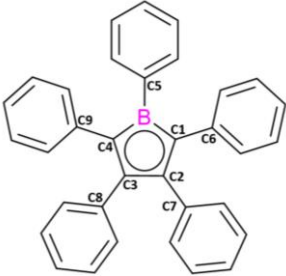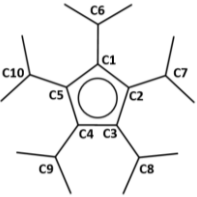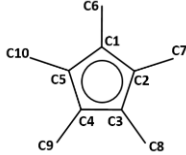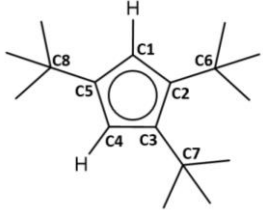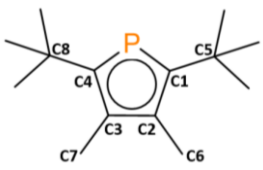
	$[C_4BPh_5]^{2-}$				$[Cp^{iPr5}]^-$				$[Cp^*]^-$		

Atom	Löwdin charge	Group	Löwdin charge	Atom	Löwdin charge	Group	Löwdin charge	Atom	Löwdin charge	Group	Löwdin charge
B	−0.37	Ph(C5)	−0.26	C1	−0.12	^iPr(C6)	−0.08	C1	−0.14	Me(C6)	−0.07
C1	−0.09	Ph(C6)	−0.28	C2	−0.12	^iPr(C7)	−0.08	C2	−0.13	Me(C7)	−0.06
C2	−0.08	Ph(C7)	−0.25	C3	−0.12	^iPr(C8)	−0.08	C3	−0.14	Me(C8)	−0.06
C3	−0.08	Ph(C8)	−0.21	C4	−0.12	^iPr(C9)	−0.08	C4	−0.13	Me(C9)	−0.07
C4	−0.09	Ph(C9)	−0.29	C5	−0.12	^iPr(C10)	−0.08	C5	−0.14	Me(C10)	−0.06
C$_4$B total	−0.71			C$_5$ total	−0.60			C$_5$ total	−0.68		

Table S4.20. Calculated Löwdin charges for $[Cp^{ttt}]^-$ and $[P(C^tBuCMe)_2]^-$ ligands.

	$[Cp^{ttt}]^-$				$[P(C^tBuMe)_2]^-$		

Atom	Löwdin charge	Group	Löwdin charge	Atom	Löwdin charge	Group	Löwdin charge
C1	−0.29	C6-^{t}Bu	−0.10	P	−0.09	C5-^{t}Bu	−0.07
C2	−0.12	C7-^{t}Bu	−0.10	C1	−0.24	C6-Me	−0.04
C3	−0.12	C8-^{t}Bu	−0.10	C2	−0.10	C7-Me	−0.04
C4	−0.28			C3	−0.10	C8-^{t}Bu	−0.07
C5	−0.11			C4	−0.24		
C$_5$ total	−0.90			C$_4$P total	−0.77		

Chapter 5: Lanthanide-Benzene Inverse Sandwich Series Stabilized by a δ-Bonding Interaction

McClain, K. R.[a]; Vincent, A. H.[b]; Rajabi, A.[c]; Furche, F.[c]; Harvey, B. G.[a]; Long, J. R. *In Preparation*. **2023**.

5.1: Introduction

Lanthanide-arene compounds are unusual compared to those of the transition metals.[1] The comparative scarcity of these compounds can be ascribed to the common $4f^n$ electron configuration of the most stable Ln^{3+} oxidation state. Elements with 4f valence electrons are distinct from transition metals in that their unpaired valence electrons are core-like, and so do not participate in the covalent interactions which are responsible for the existence of stable transition metal-arene compounds.[2]

The structurally characterized lanthanide-arene compounds in the literature can be broadly divided into two classes, those with formally neutral arenes and those with formally anionic arenes.[1] The first of the neutral arene adducts to be reported were the lanthanide haloaluminates, which feature neutral arenes in a weak induced dipole interaction with a central Ln^{3+} cation.[3] Low valent lanthanide arene compounds of the formula $Ln(1,3,5\text{-}tBu_3C_6H_3)_2$ (Ln = Y, Gd), which feature a formal Ln^0, have also been known since the late 1980s, however these compounds were necessarily synthesized via a challenging co-condensation of the corresponding metal vapor and 1,3,5-tris-tertbutylbenzene at 77 K.[4]

The first Ln-arene complex with an anionic benzene to be synthesized using a conventional solution based approach was the inverse sandwich compound $[Cp^{t\text{-}Bu2}_2La(\mu\text{-}\eta^6{:}\eta^6\text{-}C_6H_6)]^{1-}$.[5] Since this initial report, the number of structurally characterized inverse sandwich complexes with lanthanides bound to anionic arenes has expanded considerably. The series $[(Cp^{TMS}_2Ln)_2(\mu\text{-}\eta^6{:}\eta^6\text{-}C_6H_6)]^{2-}$ (Ln = La, Ce), formed via the reaction of in-situ generated $[K(2,2,2\text{-}Crypt)][(Cp^{TMS}_3Ln)(THF)]$ with benzene, exhibits the properties typical of inverse sandwich compounds with anionic benzene.[6] These compounds are frequently complex anions, with a distorted benzene subunit bridging two lanthanides. The coordination spheres of each lanthanide ion in these inverse sandwich compounds are filled out by bulky substituted cyclopentadienide anions on the periphery, resulting in an approximately trigonal ligand field. The bound benzene in $[(Cp^{TMS}_2Ln)_2(\mu\text{-}\eta^6{:}\eta^6\text{-}C_6H_6)]^{2-}$ (Ln = La, Ce) (Cp^{TMS} = trimethylsilylcyclopentadienide) is non-planar and asymmetric, with magnetic and spectroscopic properties consistent with Jahn-Teller distorted, closed shell $(C_6H_6)^{2-}$.[6] This Jahn-Teller distortion of the bound arene dianion is also typical for most lanthanide arene complexes of this type. The sole exceptions in the literature, namely $[Ln_2(BzN_6\text{-}Mes)]^{2-}$ (Ln = Y, Gd), leaned heavily on steric and entropic stabilization effects in order to enforce a planar arene geometry, which yielded a $S = 1$ benzene dianion.[7] A monoanionic benzene bridge has been observed in $[(Cp^{TMS2}_2La)_2(C_6H_6)]^-$ (Cp^{TMS2} = 1,3-(trimethylsilyl)cyclopentadienide) which also exhibits out of plane distortion consistent with the Jahn-Teller effect.[8]

---

[a] McClain, K. R. and Harvey, B. G carried out the synthesis and structure data collection for all compounds presented.

[b] Vincent, A. H. carried out the structural refinement, magnetic characterization, and spectroscopic characterization of all compounds presented.

[c] Rajabi, A. and Furche, F. carried out all of the DFT and TDDFT analysis presented in this chapter.

In addition to mono and dianionic arenes, formally tetra-anionic arene bridges have also been described in the literature. Representative of this group are compounds of the formula $[(NN^{TBS}Ln)_2(\mu\text{-biph})]^{2-}$ (Ln = Y, Gd, Dy), all three of which feature a bridging biphenyl tetra-anion.[9] As a result of the high nucleophilicity of the tetra-anionic biphenyl bridge, the metal arene distances for these compounds were somewhat shorter than those of previously reported dianionic arenes. The arene bridges in $[(NN^{TBS}Ln)_2(\mu\text{-biph})]^{2-}$ (Ln = Y, Gd, Dy) were also much more symmetric as the tetra-anion has an aromatic 4n+2 π-electron count and is therefore not impa.

Herein we report the synthesis and characterization of an unusual overall neutral series of lanthanide-benzene inverse sandwich compounds of the formula $(Cp^{iPr5}Ln)_2(\mu\text{-}\eta^6:\eta^6\text{-}C_6H_6)$ **1-Ln** (Ln = Y, Gd, Tb, Dy, Tm) (Cp^{iPr5} = pentaisopropylcyclopentadienyl) , all of which were found to feature a planar and highly symmetric (C_6H_6) bridging anion. Through characterization by single-crystal x-ray diffraction, magnetometry, UV/vis spectroscopy, and TD-DFT, the oxidation state configuration of all five compounds was determined to be ambiguous, best described as $Ln^{3+}\text{-}Bz^{4-}\text{-}Ln^{3+}$ with a high degree of metal-arene covalency. The planar geometry and unusual stability of the $(C_6H_6)^{4-}$ is demonstrated to be the result of an unusual δ-bonding interaction between the vacant d_{xy} and $d_{x^2-y^2}$ orbitals of the Ln^{3+} subunits and the π^* orbitals of $(C_6H_6)^{4-}$.

5.2: Results and Discussion

The synthetic route used to obtain each 1-Ln congener is pictured in Scheme 1. Treating a diethylether solution of the previously reported compound $(Cp^{iPr5}LnI)_2I_2$ (Ln = Y, Gd, Tb, Dy, Tm)[10] with excess benzene followed by KC_8, resulted in the precipitation of KI and the formation of 1-Ln over the course of four days. Following the removal of Et_2O and excess benzene under reduced pressure, the residues were extracted into n-hexane. After the KI was separated from the extract by filtration. The n-hexane extracts were concentrated under reduced pressure. Crystals suitable for diffraction analysis could be isolated via slow cooling of the corresponding n-hexane concentrate at $-35\,°C$. The thermal stability of **1-Ln** in solution is notable as concentrated n-hexane solutions could be boiled under ambient pressure without evident product decomposition.

Compounds **1-Ln** (Ln = Y, Gd, Tb, Dy, or Tm) were all found to be isostructural with one another (Figures S5.1-S5.5), crystallizing in P2/n with similar unit cell parameters (Table S5.1). The structure of **1-Gd** (Figure 5.1) is representative of the other congeners, with the metal centers related by a C_2 rotation axis which passes through the plane of the benzene ring. The bound benzene in all five structures exhibited in-plane rotational disorder.

The average benzene C-C bond lengths for all five **1-Ln** compounds were all found to be within error of one another, at 1.46(1) Å. Reported lanthanide bound η^6-arene C-C distances in the literature range from 1.223 to 1.517 Å. Short average C-C distances are characteristic of neutral bound arenes, whereas long C-C distances are indicative of anionic arenes which have formally populated π^* orbitals.[1] The C-C distances of the C_6H_6 fragment in each of the five 1-Ln congeners are all considerably longer than the average C-C distance of free benzene (1.388 Å), suggesting that the fragments are all anionic, with benzene π^* orbitals populated to some extent. The extent to which the π^* orbitals are populated is challenging to estimate using the C-C distances, given that there are no reported crystal structures containing a free benzene tetra-anion to make a direct comparison with. The best available example of an inverse sandwich compound with tetra-anionic benzene is with thorium, namely $[NN^{TBS}Th(THF)]_2(\mu\text{-}C_6H_6)$, which has an average benzene C-C

distance of 1.46 Å.[11] This structural observation is therefore consistent with three possible oxidation state assignments, namely Ln^{3+}-Bz^{4-}-Ln^{3+}, Ln^{2+}-Bz^{2-}-Ln^{2+}, and $Ln^{2.5+}$-Bz^{3-}-$Ln^{2.5+}$.
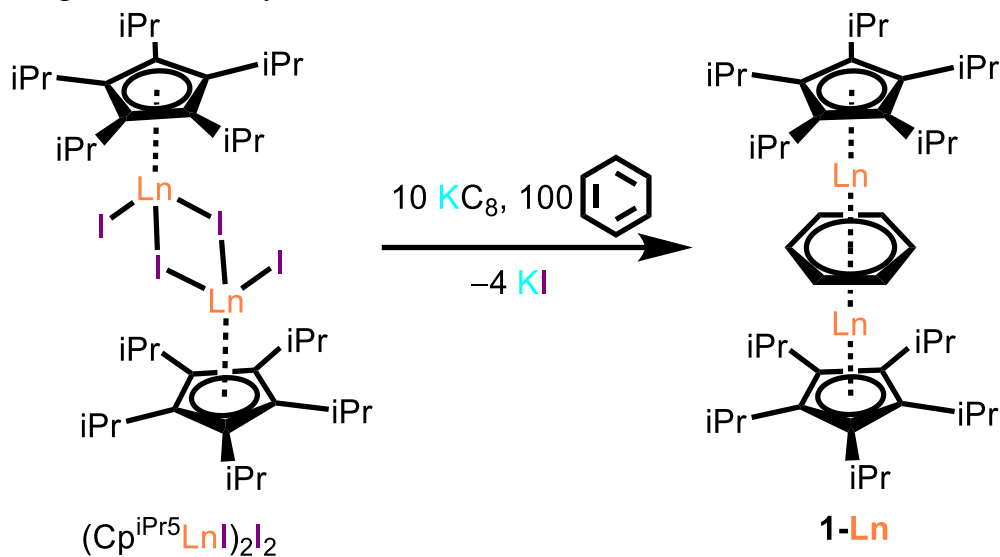
Scheme 5.1. Synthesis of **1-Ln** from $(Cp^{iPr5}LnI)_2I_2$ (Ln = Y, Gd, Tb, Dy, Tm)

We examined the sum of carbon-mean plane distances squared for each of the **1-Ln** structures, where the mean-plane is least-squares fit to the six benzene carbon atoms in each respective structure. A representative image of the mean plane calculated for **1-Gd** is pictured in Figure 1c. The sum of squared deviations can be taken as a quantitative measure of the relative out-of-plane distortion exhibited by the η^6-C_6H_6 fragment in each 1-Ln compound, as well as Ln-(η^6-Ar) complexes available in the Cambridge Structural Database (Tables S5.2-S5.7). The sum of squared deviation for **1-Y**, **1-Tb**, and **1-Dy** were found to be comparable to one another, with each having a sum of squared deviations on the order of 10^{-4}. **1-Gd** was found to have the most planar ring of the series, with a sum of squared deviations on the order of 10^{-5}. Conversely, **1-Tm** had the greatest amount of out-of-plane distortion, with a sum of squared deviations on the order of 10^{-3}. For reference, free benzene has a sum of squared deviations on the order of 10^{-4} whereas typical Jahn-Teller distorted $(C_6H_6)^{2-}$ is on the order of 10^{-1}.[12] The sum of squares for **1-Y**, **1-Gd**, **1-Tb**, and **1-Dy** sit close to or lower than their respective literature minima for η^6-arenes, indicating that the benzene ring is unusually planar in these four complexes, whereas the sum of squared deviations for **1-Tm** sits in the middle of the calculated literature range for Tm-η^6-Ar (Table S5.7). All of the **1-Ln** compounds had sum of squared deviations close to that of free benzene, indicating that the ring in all five congeners is approaching complete planarity. Interestingly, the sum-of-squared deviations for free benzene was found to exceed that of **1-Gd**, indicating that the benzene anion of **1-Gd** has no out-of-plane distortion whatsoever.

There are two unique benzene-metal distances in all five structures due to the in-plane rotational disorder of the ring. The average Ln-$Bz^{centroid}$ distances with parenthesized standard deviations in compounds **1-Y**, **1-Gd**, **1-Tb**, **1-Dy**, and **1-Tm** are 1.989(5), 2.038(7), 2.013(6), 1.99(1), and 1.9421(7) Å respectively. For compounds **1-Gd**, **1-Tb**, **1-Dy**, and **1-Tm**, the gradual decrease in metal-centroid distance mirrors the lanthanide contraction. The closest comparable Ln-$Ar^{centroid}$ distances were reported for the $(NN^{TBS}Ln)_2(\mu-(C_6H_5)_2)$ series of compounds, measured at 2.093,

2.113, and 2.054 Å for Ln = Y, Gd, and Dy respectively.[13] It is worth highlighting that the distance measured for compounds **1-Y**, **1-Gd**, and **1-Dy** are all considerably shorter, which indicates that the metal has an unusually strong interaction with the bridging benzene. Indeed, to our knowledge, the five 1-Ln compounds reported herein have the shortest metal-arene contacts to have been described in the CSD for their respective metal ions. The results of the Ln-Ar$_{centroid}$ literature survey are summarized in Table 5.1.
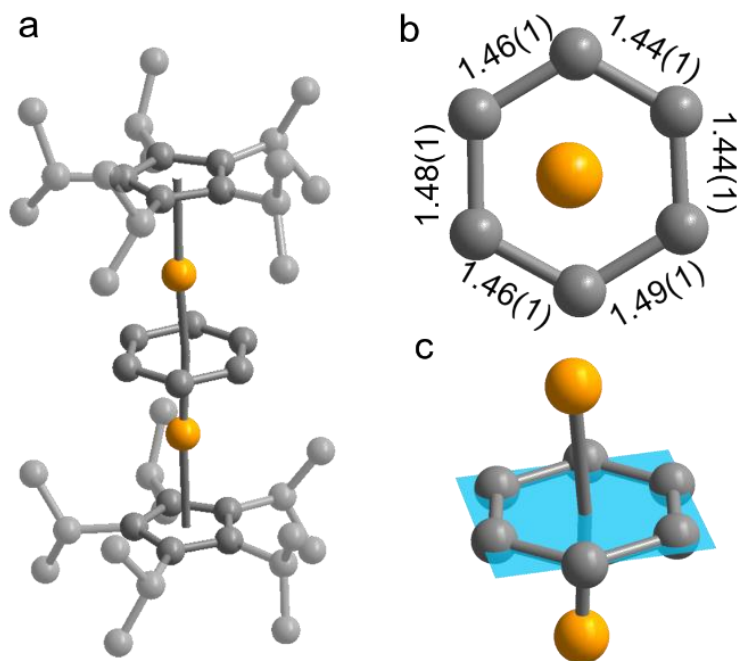

Figure 5.1. a) X-ray crystal structure of **1-Gd**. Minor rotationally disordered positions of the benzene ring and Cp^{iPr5} groups have been omitted for clarity. Hydrogen atom positions were also omitted for clarity. b) Top-down representation of **1-Gd**. Cp^{iPr5} groups were omitted for clarity. Rotationally disordered benzene position omitted for clarity. C-C distances are given in angstroms (Å). c) Inverse sandwich core of 1-Gd with least-squares fit plane. Gd, orange; C, gray.

The Ln-Cp^{iPr5} centroid distances of **1-Y**, **1-Gd**, **1-Tb**, **1-Dy**, and **1-Tm** are 2.3705(2), 2.4197(2), 2.3982(2), 2.3842(3), and 2.3272(1) Å respectively. These metal centroid distances closely mirror the lanthanide contraction and are consistent with the literature ranges for each respective metal. In previously reported Ln^{2+} and Ln^{3+} Cp^{iPr5} compounds, the Ln-Cp^{iPr5} centroid distances were found to be diagnostic of the metal oxidation state, with elongated Ln-Cp^{iPr5} distances indicative of Ln^{II} and formal d orbital occupation.[17,18] Y^{II}Cp$^{iPr5}_2$ has a reported Y-Cp^{iPr5} distance of 2.371(6) Å,[19] within error of compound **1-Y**, measured at 2.3705(2) Å. Cationic [Y^{III}Cp$^{iPr5}_2$]$^+$ has a much shorter distance of 2.331 Å. The same trend is observed for the remaining **1-Ln** congeners (Ln = Gd, Tb, Dy, and Tm), all of which were found to have Ln-Cp^{iPr5} centroid distances which approximately match those of the corresponding Ln^{II}Cp$^{iPr5}_2$ (Table 5.2). **1-Tm** stood out as an interesting exception to this trend, possessing a shorter metal centroid distance than that of Tm^{II}Cp$^{iPr5}_2$. We hypothesized this to be indicative of a change in ground state electron configuration from the 4f^{13} state typical of Tm^{2+}, as ions with 4f^{n}5d^1 ground state configurations have been

found to possess shorter metal Cp distances than those with a $4f^{n-1}$ ground state configuration.[18] As $[Tm^{III}Cp^{iPr5}_2]^+$ is unreported in literature, an additional comparison was drawn using the reported Ln-Cp* distances of Cp*LnCOT, all of which contain trivalent metal ions.[20–23] The Ln-Cp* centroid distances of Cp*LnCOT were all considerably shorter than those of $(Cp^{iPr5}Ln)_2(\mu\text{-}C_6H_6)$ (Ln = Y, Gd, Tb, Dy, or Tm), indicating that the Cp-metal distances of **1-Tm** are not consistent with either Tm^{III} or Tm^{II}. The closely matching Ln-Cp centroid distances of $Ln^{II}Cp^{iPr5}_2$ and **1-Ln** (Ln = Y, Gd, Tb, and Dy) however suggests that the cations of these species have non-zero 4d/5d-orbital occupation.

Table 5.1. Literature comparison of Ln-Ar$_{centroid}$ (Ln = Y, Gd, Tb, Dy, Tm) distances in Å

Ln	$[(NN^{TBS}Ln)_2(\mu\text{-}biph)]^-$ ref.[9,13]	$(Ar)Ln(AlCl_4)$ ref.[14,15,16]	$[Ln_2(BzN_6\text{-}Mes)]^{2-}$ ref.[7]	**1-Ln**
Y	2.093	----	2.283	1.989(5)
Gd	2.113	----	2.309	2.038(7)
Tb	----	2.488^a	----	2.013(6)
Dy	2.054	2.467^b	----	1.990(1)
Tm	----	2.463^b	----	1.9421(7)

^{a}Ar = C_6Me_6; ^{b}Ar = MeC_6H_5

Table 5.2. Literature comparison of Ln-Cp$_{centroid}$ (Ln = Y, Gd, Tb, Dy, Tm) distances in Å

Ln	$LnCp^{iPr5}_2$ ref[17,18]	$[LnCp^{iPr5}_2]^+$ ref[17]	Cp*LnCOT ref[20–23]	**1-Ln**
Y	2.371(6)	2.3307(1)	2.2954(3)	2.3705(2)
Gd	2.423(2)	----	2.3442(2)	2.4197(2)
Tb	2.4177(1)	2.325(2)	2.3326(2)	2.3982(2)
Dy	2.3848(1)	2.321(4)	2.3065(3)	2.3842(3)
Tm	2.449(3)	----	2.2438(3)	2.3272(1)

The absorption spectra of n-hexane solutions of **1-Ln** were collected from 300-800 nm in order to probe the HOMO-LUMO excitation and to inform our TDDFT studies. All five compounds have a strong band located between 320-350 nm (Figure 5.2). Compound **1-Y** was found to have the most intense band while compound **1-Dy** was found to have the weakest. Among the 4f-elements, a gradual decrease in band intensity was observed proceeding from **1-Gd** to **1-Dy**, however the band increases in intensity again with 1-Tm. The absorption maximum was found to shift upward in energy from **1-Gd** to **1-Tm**, proceeding from 350 to 320 nm. Strong visible absorption within this range in addition to the metal dependence of the band energy and intensity is most consistent with a LMCT from the central benzene anion π^* orbitals to an unoccupied MO of mainly 5d (4d in the case of **1-Y**) character centered on the lanthanide ions.
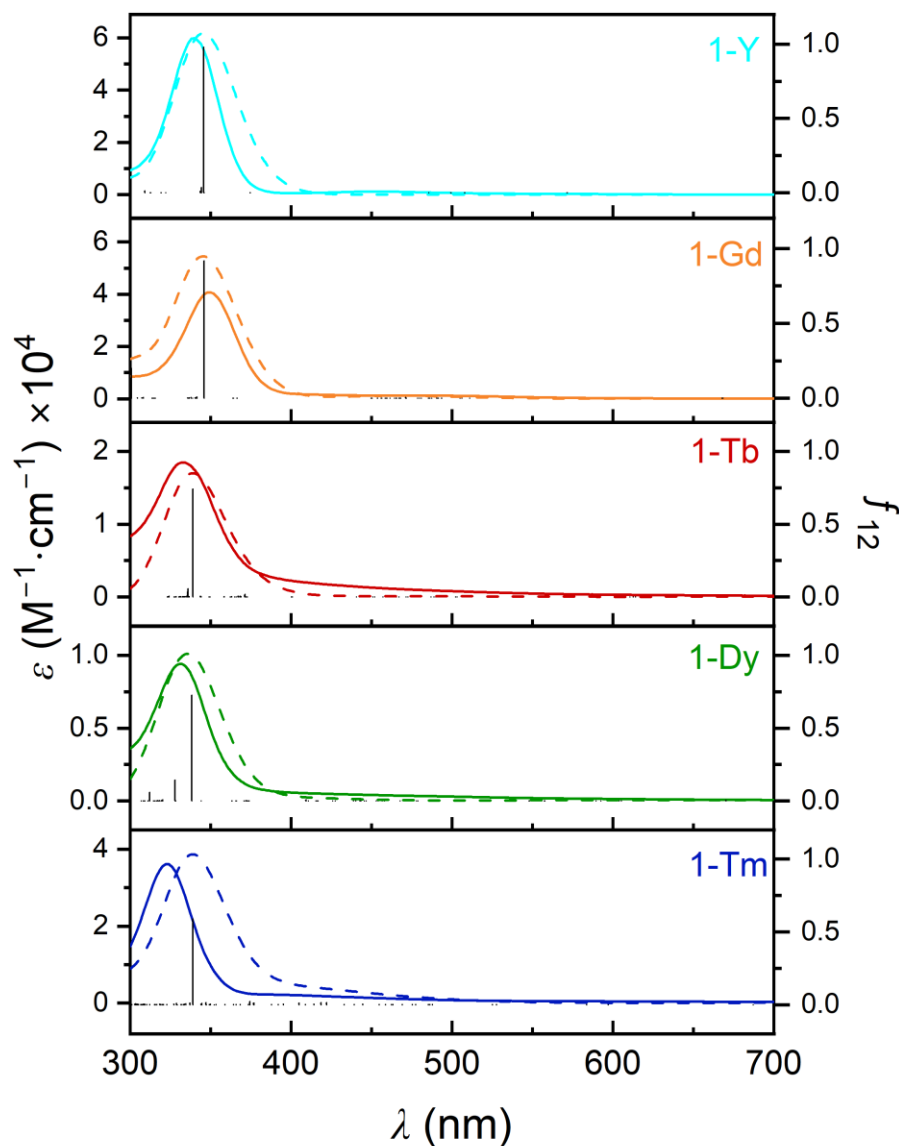
Figure 5.2. UV/visible spectra of n-hexane solutions of **1-Ln** (Ln = Y, Gd, Tb, Dy, Tm) compounds. Solid lines correspond to experimental ε values (left axis). Bar plots correspond to calculated oscillator strengths (right axis) for each transition obtained from TDDFT. Dashed lines correspond to calculated ε values derived from the transitions obtained from TDDFT. A gaussian spectral width of 0.2 eV was used. The calculated absorption spectrum of **1-Tb** was scaled by a factor of 0.33 while that of **1-Dy** was scaled by a factor of 0.20.

In order to probe the ground state configuration in compounds **1-Gd**, **1-Tb**, **1-Dy**, and **1-Tm**, dc magnetic susceptibility was measured as a function of temperature using SQUID magnetometry. Examining the temperature dependent susceptibility of **1-Gd** (Figure 4), the moment decreases monotonically with temperature, which indicates antiferromagnetic coupling. As Gd^{3+} has zero

orbital moment (L), the temperature dependence of the $\chi_M T$ profile could be fit in Phi[24] using a spin-only Hamiltonian (Equation 5.1). A fit consistent with two $S = 7/2$ Gd centers with an exchange coupling constant (J_{ex}) of $-2.94(2)$ cm^{-1} was obtained, indicating that the central benzene anion is closed shell. As the benzene dianion must be distorted in order to be $S = 0$, a tetra-anion is most consistent with this observation. Most J_{ex} values mediated by closed shell bridging ligands are <1 cm^{-1} in magnitude, meaning that the exchange observed for **1-Gd** is unusually strong.[25] The isothermal magnetization of **1-Gd** (Figure S5.10) is also consistent with strong antiferromagnetic exchange, as the magnetic moment remained unsaturated under a 7 T applied field at all measured temperatures. A 4f^7 valence electron configuration for each Gd is consistent with the observed temperature dependence of the magnetic susceptibility. The susceptibility profile and magnetization of **1-Gd** rules out a mixed-valent ground state configuration (Ln$^{2.5+}$ - Bz^{3-} - Ln$^{2.5+}$), as such a state would require both a higher room temperature $\chi_M T$ value as well as a temperature dependence indicative of a ferrimagnetic exchange coupled ground state, reminiscent that of the N$_2^{3-}$ radical bridged series of lanthanide compounds.[26] Additionally, such a ferrimagnetic ground state would likely exhibit magnetic saturation under modest applied fields; that **1-Gd** remains unsaturated at 7 T (Figure S5.7) further invalidates the Ln$^{2.5+}$ - Bz^{3-} - Ln$^{2.5+}$ assignment.
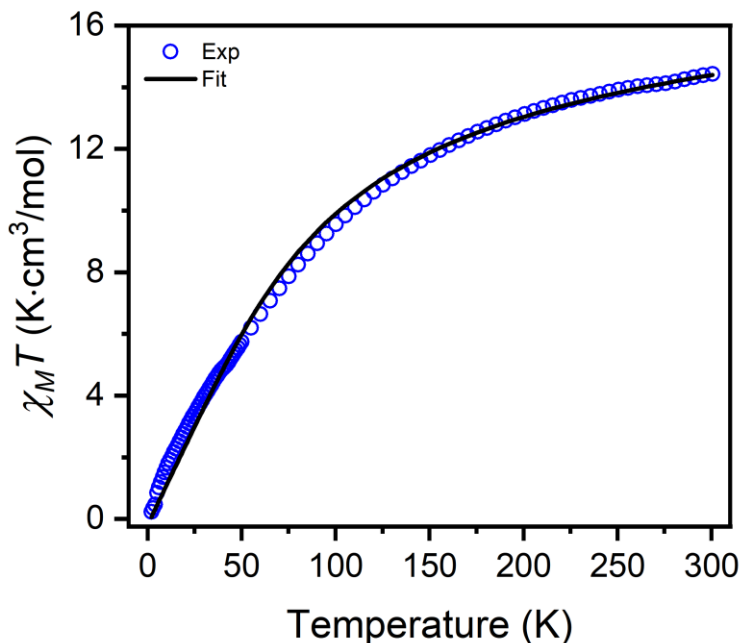

Figure 5.3. Molar susceptibility temperature product of **1-Gd** as a function of temperature under an applied field 0.5 T (blue circles). The black trace represents fit to spin-Hamiltonian given in equation 5.1 with two $S = 7/2$ Gd centers and $J_{ex} = -2.94(2)$ cm^{-1}. A temperature independent paramagnetism correction of 0.0028(1) K·cm^3/mol was applied during fitting.

$$\hat{H} = -2J_{ex}(\hat{S}_{Gd1} \cdot \hat{S}_{Gd2}) + \mu_B g(\hat{S}_{Gd1} + \hat{S}_{Gd2}) \cdot \vec{B} \qquad \text{(Equation 5.1)}$$

The magnetic susceptibilities of **1-Tb**, **1-Dy**, and **1-Tm** are characterized by the magnetic anisotropy of their respective lanthanide ions, though the monotonic increase in moment with

increasing temperature remains consistent throughout the series. The room temperature moment of **1-Tb** was found to be 21.3 ($K \cdot cm^3$/mol) which is consistent with two Tb ions with a $^7F_6$ ground state (Figure S5.9). Magnetic saturation could not be achieved under a 7 T field at low temperature (Figure S5.10), suggesting an antiferromagnetically coupled ground state similar to that observed in **1-Gd**.

Compound **1-Dy** deviates from **1-Gd** and **1-Tb** in its magnetic susceptibility, exhibiting divergence in the field-cooled/zero-field cooled susceptibility. The room temperature $\chi_M T$ value of 29.3 $K \cdot cm^3$/mol is consistent with two $^6H_{15/2}$ Dy ions coupled antiferromagnetically (Figure S5.13). Similar to 1-Tb, this ground state assignment is consistent with a $4f^n$ configuration Dy^{3+}. Within the $\chi_M T$ profile, a marked *decrease* in the $\chi_M T$ product is observed when $T > 44$ K (Figure S5.16). In most cases of superparamagnetic blocking, the zero-field cooled $\chi_M T$ product sharply *increases* as the value of $k_B T$ exceeds the activation threshold required for the blocked population to align with the applied field.[27] Slow magnetic relaxation for compound **1-Dy** was not observed. The divergence is hypothesized to be the result of a structural change which occurs below 44 K, however low temperature powder diffraction data was not obtained to validate this hypothesis. As was the case for **1-Gd** and **1-Tb**, the magnetic moment of **1-Dy** could not be saturated under a 7 T field, which further supports the assigned antiferromagnetically coupled ground state (Figure S5.14).

The room temperature $\chi_M T$ product of **1-Tm** was found to be 14.5 $K \cdot cm^3$/mol, consistent with two $4f^{12}$ Tm^{3+} ions (Figure S5.17). Like the other **1-Ln** congeners examined, this magnetic behavior is most consistent with Ln^{3+}- Bz^{4-} - Ln^{3+}. The $\chi_M T$ profile is consistent with the antiferromagnetic coupling observed in the other lanthanide congeners while the magnetization also does not saturate under high fields.

Computational studies were carried out using DFT to determine the ground state electronic structure of each **1-Ln** (Ln = Y, Gd, Tb, Dy, Tm) congener. For **1-Y**, several electronic occupations associated with $4d^1$ Y^{2+} and $4d^0$ Y^{3+} were investigated. Singlet and triplet benzene were also considered in assigning the overall number of unpaired electrons of the system. DFT calculations were carried out for singlet, triplet, and quintet states. The energy differences of the different spin states with respect to the ground state and the summary of the important structural parameters of the optimized structures are shown in Table S5.9. Table S5.11 shows the selected structural parameters of the ground state of **1-Y**. In the optimized ground state structure, the Y–Cp distance is 2.351 Å, which is similar to that of YCp^{iPr5}_2.[17,18] Moreover, there is a 0.08 Å elongation in the bridging benzene C–C distances, compared to those of free benzene, again mirroring the elongation observed in the crystal structure geometry. The benzene also remains planar in the 1-Y optimized geometry as the dihedral angles of the ring are near zero.

The two highest occupied molecular orbitals (HOMO and HOMO-1) of the **1-Y** singlet state structure (Figure S5.40) demonstrate notable mixing between the metal d-orbitals and the π^* orbitals of the C_6H_6 anion. Mulliken population analysis (MPA)[28] of HOMO and HOMO-1 indicate that the orbitals have 62% benzene π^* contribution, with 38% contribution from the $4d_{xy}$ and $4d_{x^2-y^2}$ of the Y ions (Table S5.10). The MO energies are also summarized in Table S5.10. HOMO and HOMO-1 closely resemble δ-symmetric orbitals, with two nodal planes perpendicular to the six-membered. δ-bonding type orbitals between metal and arene were the two HOMOs in all five 1-Ln congeners.

165

Natural population analysis (NPA)[29] revealed a d-orbital population of 1.121 ($n_{(d)}$=1.121) and a positive charge of 1.798 for each Y ion in the singlet ground state (Table S5.28). The spin state of the benzene in each of the three electron configurations is estimated by summing over the spin of each atom of the arene ring and is reported in Table S5.9. The other states were not pursued further as they were more than 1 eV higher in energy with respect to the ground state. By performing time-dependent DFT (TDDFT) calculations the UV-Vis spectrum of **1-Y** was simulated in Figure 5.2. The spectrum captures all the main transitions that are observed in the experimental spectrum shown in Figure 5.2. The summary of transitions is shown in Table S5.12. Transitions from HOMO and HOMO-1 to LUMO+2 and LUMO+3 constitute the intense band located at 345 nm. The very weak and broad absorption around 500 nm are transitions from HOMO and HOMO-1 to LUMO and LUMO+1.

Table 5.3: Spin state energies for **1-Gd**. Ne^- is the number of unpaired electrons defined for the complex. D_{C-C}^{avg} is the average C–C bond distance of benzene. D_{Gd-Bz} is the metal benzene centroid distance.

Ne^-	M_S	ΔE (eV)	D_{C-C}^{avg}(Å)	D_{Gd-Bz} (Å)	Bz Spin	$\langle S^2 \rangle$
18(a)	9	0	1.434	2.379	1.09	90.07
0(b)	0	0.26	1.435	2.380	0	9.03
16(c)	8	0.30	1.437	2.353	0.05	73.00
16(d)	8	0.47	1.436	2.377	1.10	73.05
14(e)	7	0.54	1.439	2.350	−1.31	58.0
14(f)	7	0.60	1.436	2.370	−0.25	58.01
0(g)	0	0.82	1.454	2.225	0	8.18
0(h)	0	--[a]	1.438	2.019	−0.14	7.09

[a] X2C SR all-electron energy value is not compared with ECP calculations as the computed energy minima systematically differ

(240β) HOMO   (240α) HOMO-1   (239β) HOMO-2   (239α) HOMO-3
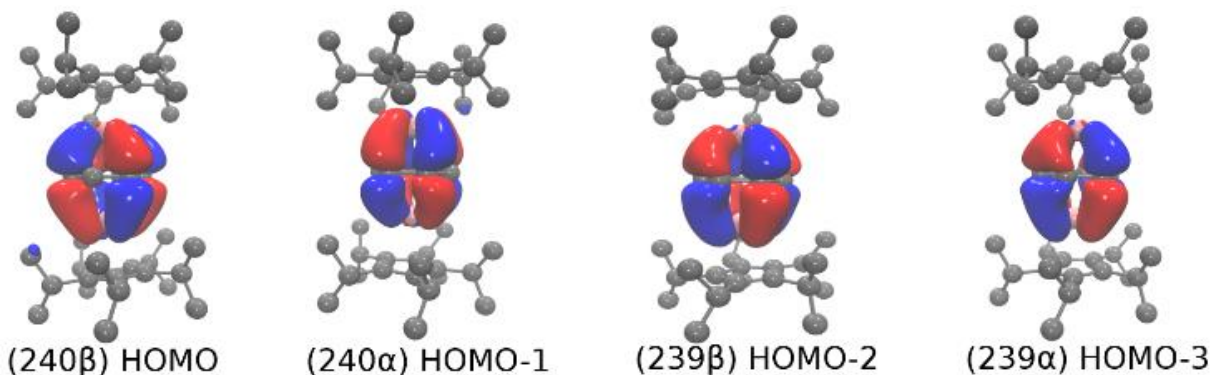
Figure 5.4. Highest occupied molecular orbitals of the **1-Gd** singlet ground state. Hydrogen atoms were omitted for clarity. A contour value of 0.03 was used in the orbital depictions.

The initial structures of **1-Gd** with the desired electronic occupations (with different numbers of unpaired electrons and HOMO-LUMO gaps) were optimized (Table 5.3). DFT calculations found an energy minimum corresponding to a singlet ground state 1-Gd(g). Although 1-Gd(g) state

is higher by 0.82 eV than the lowest-energy state 1-Gd(b), 1-Gd(g) has the structural parameters that better match the crystal structure data (Table S5.14). Furthermore, there is only an intense band in the higher energy region (300-400 nm) of the experimental spectrum of **1-Gd** complex which is only observed similarly in the simulated spectrum of singlet 1-Gd(g) state (S=0). The singlet state is in qualitative agreement with the spectrum obtained via experiment (Figure 5.2). The DFT results therefore suggest that the singlet state, in which the Gd ions are coupled antiferromagnetically, is the best model for the experimental 1-Gd complex in the ground state.

The selected metrical parameters for the ground state (1-Tb(c)) of the 1-Tb complex are given in Table S5.16. The Tb-Tb atom distance of 1-Tb(c) isomer is 4.048 Å, which is in excellent agreement with the crystallographic data for **1-Tb**. The benzene subunit remains planar in the optimized structure of singlet **1-Tb**. The frontier Kohn-Sham orbitals for this structure are displayed in Figure S5.43 and their energies can be found in Table S5.19. NPA is summarized in Table S5.28 and Table S5.29. The simulated UV-Vis spectrum of singlet **1-Tb** (Figure 5.2) illustrates a very strong transition at 344 nm which is from the HOMO orbitals to unoccupied molecular orbitals of Tb 5d parentage. The decomposition of LUMO+18 and LUMO+19 via the Mulliken population method demonstrates that these orbitals have 74% d character. A summary of notable excitations can be found in Table S5.17.

The Dy-Dy distance in the optimized singlet state, 1-Dy(c), is 4.034 Å, which is closest distance of all optimized **1-Dy** models to that observed in the crystal structure. Similar to 1-Gd(g) molecular complex here, benzene is somewhat distorted in the optimized geometry. The average C–C distance of the ring is 1.468 Å, which shows an elongation in C–C similar to all the other compounds described previously. The selected structural parameters of the **1-Dy** ground state are shown in Table S5.22, while orbital energies are given in Table S5.21. DFT indicates that the open-shell singlet structure is the ground state of **1-Dy**.

Finally, the Tm-Tm distance in the optimized singlet 1-Tm(c) is 3.946 Å, which is in good agreement with the observed crystal structure distance. The selected structural parameters of the optimized **1-Tm** ground state are given in Table S5.26, while orbital energies are given in Table S5.25. Similar to the other congeners, the average C-C distance in the optimized geometry is expanded from that of free benzene, suggesting occupation of the arene π* antibonding orbitals. The computational results suggest that **1-Tm** has an open shell singlet ground state, like the other three paramagnetic congeners.

To briefly recapitulate the experimental results, all five congeners of **1-Ln** were found to have elongated Ln–Cp^{iPr5} distances suggestive of d orbital occupation. The C_6H_6 structural parameters of all five compounds were consistent with a formally tetra-anionic benzene subunit The UV/vis spectra for each **1-Ln** congener were all dominated by an intense LMCT band centered around 350 nm. Finally, the room temperature $\chi_M T$ values of **1-Gd**, **1-Tb**, **1-Dy**, and **1-Tm** were all consistent with two 4f^n ions, indicating a Ln^{3+}–Bz^{4-}–Ln^{3+} oxidation state assignment.

The structure and accompanying orbital population analyses of the two highest occupied molecular orbitals for each **1-Ln** congener were critical in rationalizing their experimental properties. The computational results show that the frontier orbitals of the benzene tetra-anion, rather than being fully localized, are δ-bonding combinations of the 4d/5d orbitals of the two Ln ions and the π* orbitals of benzene. This bonding picture is true of all five **1-Ln** compounds. Furthermore, the TDDFT results show that the strong transitions between 300-400 nm are LMCTs from these

167

occupied δ-bonding orbitals to vacant metal d orbitals. In this covalent bonding picture, the magnetic properties of **1-Gd**, **1-Tb**, **1-Dy**, and **1-Tm** would present that of a $4f^n$ electron configuration at each metal ion, as the paired electrons in the two δ-type HOMOs cannot contribute to the observed magnetic susceptibility values. The unusually short Ln-Ar$_{centroid}$ distances as well as the elongated Ln-Cp^{iPr5}$_{centroid}$ distances we observed in all five 1-Ln compounds also arise readily in this covalent bonding picture. Formal population of δ-bonding combination would necessarily yield a short Ln-Bz distance and a long Ln-Cp^{iPr5} distance, as Ln-HOMOs are bonding with respect to the metals and benzene and are weakly antibonding with respect to the metals and Cp^{iPr5}. Finally, the benzene ring in this configuration would not be susceptible to the Jahn-Teller effect, given that its e_{2u} and e_{1g} sets are fully occupied. Given the present data ensemble and the DFT calculations performed on each compound in the **1-Ln** series, the best oxidation state assignment for all five compounds is Ln^{3+}–Bz^{4-}–Ln^{3+}, in which the bridging benzene tetra-anion is stabilized through its highly covalent interaction with the neighboring lanthanides.
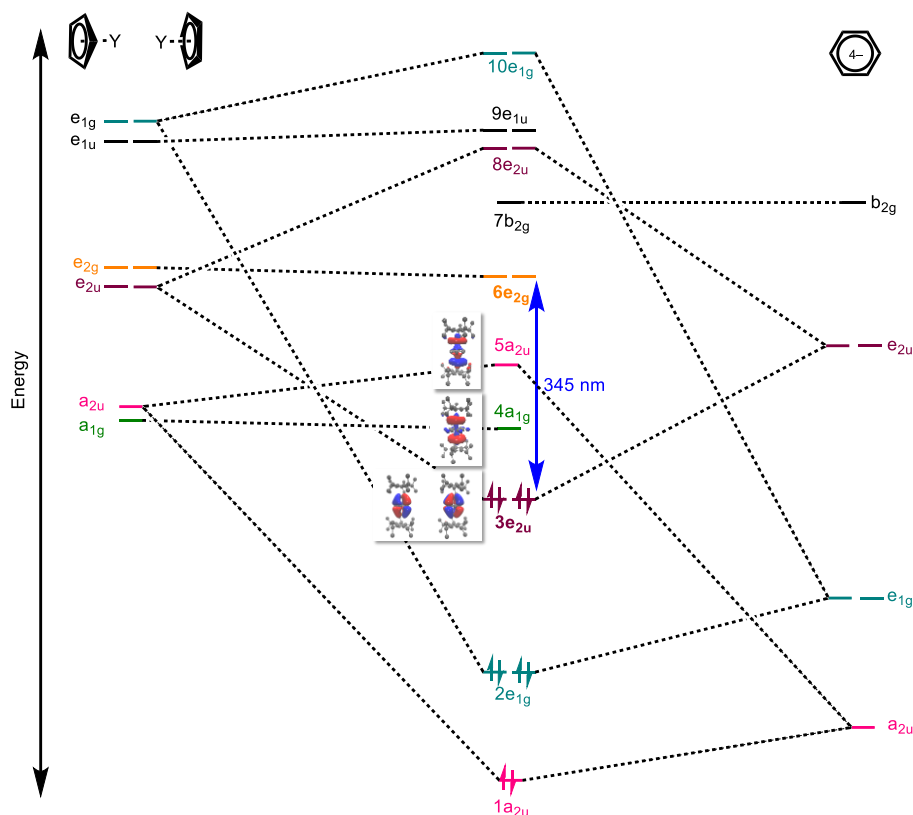

Figure 5.5. Qualitative interaction diagram for the **1-Y** metal-benzene interaction in D_{6h} point group symmetry. Cp groups were treated as single atom anions. The LMCT transition between $3e_{2u}$ and $6e_{2g}$ is labeled with a blue arrow. Surface plots of the HOMO ($3e_{2u}$) and two LUMOs ($4a_{1g}$ & $5a_{2u}$) are pictured. A contour value of 0.03 was used in the orbital depictions.

A qualitative MO diagram for **1-Y**, which is consistent with the aforementioned experimental and computational results, and which is generally representative of the series, is pictured in Figure 5.5. The diagram illustrates the interaction between the Y 4d orbital combinations and the benzene π system in D_{6h} point group symmetry. The terminal cyclopentadienyl groups are considered to be

mononuclear X-type ligands in this approximation. In this illustration, the frontier orbitals eluci-dated by the DFT calculations as well as the transition between the bonding ($3e_{2u}$) and non-bonding ($6e_{2g}$) d_{xy}, $d_{x^2-y^2}$ combinations are easily reproduced.

5.3: Conclusion and Outlook

To summarize, a new series of lanthanide-benzene inverse sandwich compounds of the for-mula $(Cp^{iPr5}Ln)_2(C_6H_6)$ **1-Ln** (Ln =Y, Gd, Tb, Dy, Tm) have been isolated in pure form and struc-turally characterized by Xray crystallography. The observed structural features along with the re-sults from magnetometry, UV/vis spectroscopy, and DFT calculations suggest that the compounds have a Ln^{3+}-Bz^{4-}-Ln^{3+} oxidation state configuration stabilized through an unusually covalent metal-arene δ-interaction. Moving forward, the isolability of compounds featuring alternative arene bridges (eg. toluene, fluorobenzene) as well as those of the early lanthanide ions (eg Ce^{3+}, Pr^{3+}, Nd^{3+}) should be explored. Additionally, the reactivity of the stabilized benzene tetra-anion in these compounds should also be examined. Given the benzene bridges high negative charge, it is likely to show high reactivity towards even weak electrophiles.

5.4 Experimental Methods

Synthesis of 1-Ln

Unless otherwise specified, all manipulations were performed using Schlenk or glovebox techniques under an atmosphere of purified argon with rigorous exclusion of water and oxygen. All solvents were purchased from Sigma-Aldrich as anhydrous grade in Sure/Seal™ bottles, purged for several hours with purified argon, and stored over activated 3 Å molecular sieves in an argon filled glovebox. Celite (AW Standard Super-Cel® NF) was purchased from Sigma-Aldrich and dried under vacuum at 150–200 °C overnight before being transferred to the glovebox. Potas-sium graphite (KC_8) was purchased from Strem and used as received or synthesized by the reaction of graphite with potassium at ~100 °C under argon. Anhydrous LnI_3 were purchased from Alfa Aesar as Ultra Dry™ grade reagents and used as received. The ligand salt $NaCp^{iPr5}$ was prepared using a previously published method.[30] The compounds $(Cp^{iPr5})_2Ln_2I_4$ (Ln = Y, Gd, Tb, Dy, Tm) were prepared using the previously reported procedure.[10] NMR spectra were recorded on a Bruker Avance 500 MHz spectrometer and internally referenced to the residual solvent signals. FT-IR spectra were recorded on a Perkin Elmer Avatar Spectrum 400 FTIR Spectrometer equipped with an attenuated total reflectance (ATR) attachment. UV-vis-NIR absorption spectra were collected with a CARY 5000 spectrophotometer interfaced with Varian WinUV software. Matrix Assisted Laser Desorption Ionization Time of Flight (MALDI-TOF) mass spectra were recorded on an Ap-plied Biosystems Voyager-DE PRO Workstation in positive ion mode. Samples were co-crystal-ized in an anthracene matrix on an AB SCIEX MALDI-TOF stainless steel sample plate. Spectra were averaged over 200 laser pulses with a low mass gate of 400 Dalton and a high mass gate of 1500 Dalton. Elemental analyses (C, H, N) were performed by the Microanalytical Facility at the University of California, Berkeley using a Perkin-Elmer 2400 Series II combustion analyzer. Mag-netic susceptibility measurements were collected using a Quantum Design MPMS-XL SQUID magnetometer.

Synthesis of [(Cp^{iPr5})Y]$_2$(μ-C$_6$H$_6$) (**1-Y**). Under argon, (Cp^{iPr5})$_2$Y$_2$I$_4$ (0.580 g / 0.469 mmol) and diethyl ether (40 mL) were combined in a 100 mL Schlenk flask with a glass-coated magnetic stirring bar and benzene (4.17 mL / 3.66 g / 46.9 mmol) was added via syringe to give a nearly colorless solution. Under vigorous stirring, KC$_8$ (0.634 g / 4.69 mmol) was added; a greenish color was observed in solution initially, which changed to brown within minutes. The reaction mixture was allowed to stir for 4 days at room temperature, then solvent was removed under vacuum. The dark solid residue was extracted by stirring with 100 mL of boiling n-hexane for 0.5 h, then filtered through a medium porosity fritted glass filter loaded with Celite and the filter pad extracted with additional boiling n-hexane (2 X 15 mL) to give a dark reddish-brown filtrate. This was concentrated to ~ 30 mL, heated to redissolve any precipitate, then transferred to a 40 mL vial, wrapped in Al foil and allowed to cool to room temperature overnight, then transferred to the freezer (−35 °C). Dark red prism crystals of 1-Y were isolated in multiple crops, washed with a small amount of cold (−35 °C) pentane and dried under vacuum. (0.135 g / 0.167 mmol / 36 % based on (Cp^{iPr5})$_2$Y$_2$I$_4$). MALDI ToF MS *m/z*: 807.02(1) ([M]$^+$). C$_{46}$H$_{76}$Y$_2$ (806.93): calcd (%) C 68.47, H 9.49; found (%) C 68.30, H 9.36.

Synthesis of [(Cp^{iPr5})Gd]$_2$(μ-C$_6$H$_6$) (**1-Gd**). Under argon, (Cp^{iPr5})$_2$Gd$_2$I$_4$ (0.540 g / 0.393 mmol) and diethyl ether (40 mL) were combined in a 100 mL Schlenk flask with a glass-coated magnetic stirring bar and benzene (3.49 mL / 3.07 g / 39.3 mmol) was added via syringe to give a light yellow solution. Under vigorous stirring, KC$_8$ (0.531 g / 3.93 mmol) was added; a blue color was observed in solution initially, which changed to reddish-brown within minutes. The reaction mixture was allowed to stir for 4 days at room temperature, then solvent was removed under vacuum. The dark solid residue was extracted by stirring with 100 mL of boiling n-hexane for 0.5 h, then filtered through a medium porosity fritted glass filter loaded with Celite and the filter pad extracted with additional boiling n-hexane (2 X 15 mL) to give a dark reddish-brown filtrate. This was concentrated to ~ 40 mL, heated to redissolve any precipitate, then transferred to 2 X 40 mL vials, wrapped in Al foil and allowed to cool to room temperature overnight, then transferred to the freezer (−35 °C). Dark reddish-brown prism crystals of 1-Gd were isolated in multiple crops, washed with a small amount of cold (−35 °C) pentane and dried under vacuum. (0.172 g / 0.182 mmol / 46 % based on (Cp^{iPr5})$_2$Gd$_2$I$_4$). MALDI ToF MS *m/z*: 942.510(3) ([M]$^+$). C$_{46}$H$_{76}$Gd$_2$ (943.61): calcd (%) C 58.55, H 8.12; found (%) C 58.18, H 8.00.

Synthesis of [(Cp^{iPr5})Tb]$_2$(μ-C$_6$H$_6$) (**1-Tb**). Under argon, (Cp^{iPr5})$_2$Tb$_2$I$_4$ (0.400 g / 0.291 mmol) and diethyl ether (40 mL) were combined in a 100 mL Schlenk flask with a glass-coated magnetic stirring bar and benzene (2.58 mL / 2.27 g / 29.1 mmol) was added via syringe to give a light yellow solution. Under vigorous stirring, KC$_8$ (0.393 g / 2.91 mmol) was added; a blue color was observed in solution initially, which changed to reddish-brown within minutes. The reaction mixture was allowed to stir for 4 days at room temperature, then solvent was removed under vacuum. The dark solid residue was extracted by stirring with 100 mL of boiling n-hexane for 0.5 h, then filtered through a medium porosity fritted glass filter loaded with Celite and the filter pad extracted with additional boiling n-hexane (2 X 15 mL) to give a dark reddish-brown filtrate. This was concentrated to ~ 8 mL, heated to redissolve any precipitate, then transferred to a 40 mL vial, wrapped in Al foil and allowed to cool to room temperature overnight, then transferred to the freezer (−35 °C). Dark reddish-brown prism crystals of **1-Tb** were isolated in multiple crops, washed with a small amount of cold (−35 °C) pentane and dried under vacuum. (0.075 g / 0.079 mmol / 27 %

based on $(Cp^{iPr5})_2Tb_2I_4)$. MALDI ToF MS *m/z*: 946.218(7) ([M]$^+$). $C_{46}H_{76}Tb_2$ (946.96): calcd (%) C 58.34, H 8.09; found (%) C 58.68, H 7.85.

Synthesis of $[(Cp^{iPr5})Dy]_2(\mu\text{-}C_6H_6)$ (**1-Dy**). Under argon, $(Cp^{iPr5})_2Dy_2I_4$ (0.420 g / 0.304 mmol) and diethyl ether (40 mL) were combined in a 100 mL Schlenk flask with a glass-coated magnetic stirring bar and benzene (2.70 mL / 2.37 g / 30.3 mmol) was added via syringe to give a light yellow solution. Under vigorous stirring, KC_8 (0.410 g / 3.03 mmol) was added; a blue color was observed in solution initially, which changed to reddish-brown within minutes. The reaction mixture was allowed to stir for 4 days at room temperature, then solvent was removed under vacuum. The dark solid residue was extracted by stirring with 100 mL of boiling n-hexane for 0.5 h, then filtered through a medium porosity fritted glass filter loaded with Celite and the filter pad extracted with additional boiling n-hexane (2 X 15 mL) to give a dark reddish-brown filtrate. This was concentrated to ~ 20 mL, heated to redissolve any precipitate, then transferred to a 40 mL vial, wrapped in Al foil and allowed to cool to room temperature overnight, then transferred to the freezer (−35 °C). Dark reddish-brown prism crystals of **1-Dy** were isolated in multiple crops, washed with a small amount of cold (−35 °C) pentane and dried under vacuum. (0.132 g / 0.138 mmol / 45 % based on $(Cp^{iPr5})_2Dy_2I_4$). MALDI ToF MS *m/z*: 953.88(1) ([M]$^+$). $C_{46}H_{76}Dy_2$ (954.11): calcd (%) C 57.91, H 8.03; found (%) C 57.58, H 7.68.

Synthesis of $[(Cp^{iPr5})Tm]_2(\mu\text{-}C_6H_6)$ (**1-Tm**). Under argon, $(Cp^{iPr5})_2Tm_2I_4$ (0.500 g / 0.358 mmol) and diethyl ether (40 mL) were combined in a 100 mL Schlenk flask with a glass-coated magnetic stirring bar and benzene (3.18 mL / 2.80 g / 35.8 mmol) was added via syringe to give a yellow-orange solution. Under vigorous stirring, KC_8 (0.484 g / 3.58 mmol) was added and the reaction mixture was allowed to stir for 4 days at room temperature, then solvent was removed under vacuum. The dark solid residue was extracted by stirring with 100 mL of boiling n-hexane for 0.5 h, then filtered through a medium porosity fritted glass filter loaded with Celite and the filter pad extracted with additional boiling n-hexane (2 X 15 mL) to give a dark reddish-brown filtrate. This was concentrated to ~ 20 mL, heated to redissolve any precipitate, then transferred to a 40 mL vial, wrapped in Al foil and allowed to cool to room temperature overnight, then transferred to the freezer (−35 °C). Dark brown prism crystals of **1-Tm** were isolated in multiple crops, washed with a small amount of cold (−35 °C) pentane and dried under vacuum. (0.156 g / 0.161 mmol / 45 % based on $(Cp^{iPr5})_2Tm_2I_4$). $C_{46}H_{76}Tm_2$ (966.98): calcd (%) C 57.14, H 7.92; found (%) C 57.20, H 7.83.

NMR Spectroscopy

^{89}Y NMR spectrum of **1-Y** was collected at 9.4 T under ambient temperature at the UC Davis NMR facility on their Avance 400 MHz instrument. Sample was dissolved in C_6D_6 and sealed inside of a J. Young NMR tube beneath an atmosphere of argon prior to measurement. C_6D_6 (99.8%) was purchased from Sigma-Adrich, saturated with argon using three freeze-pump-thaw cycles, and dried for 72 hours over 3 Å molecular sieves prior to use.

X-ray Crystallography Data Collection and Refinement Details

Samples were coated with Parabar oil and mounted on a MiTeGen polyimide loop prior to measurment. X-ray intensity data were measured using a Bruker SMART Apex II diffractometer outfitted with a PHOTON II CPAD detector. Data collection was performed at 100 K under the N_2 stream of an Oxford Cryosystems cryostream with MoKα radiation (graphite monochrometer). The frames were integrated, and scaling was performed using APEX3 software, including a multi-scan absorption correction. Crystal structure models were obtained using intrinsic phasing method as implemented in ShelXT.[31] The structural models were refined with least-squares fitting as implemented in ShelXL.[32] Olex2 was used as a graphical frontend throughout the refinement process.[33]

CheckCIF A & B Level Alerts

1-Y:
PLAT215_ALERT_3_B Disordered C11   has ADP max/min Ratio .....   4.7 Note
   C11 is one of the rotationally disordered carbon atoms of the benzene ring. The large ADP max/min ratio is a product of the incomplete modeling of the rotational disorder combined with the equivalent occupancies given to each of the disordered components. A simplified model with equivalent chemical occupancies for each disordered benzene position was used to overcome refinement instability which was observed when the chemical occupancy values were floating.

1-Gd:
PLAT934_ALERT_3_B Number of (Iobs-Icalc)/Sigma(W) > 10 Outliers ..   2 Check

1-Tb:
PLAT934_ALERT_3_B Number of (Iobs-Icalc)/Sigma(W) > 10 Outliers ..   2 Check

1-Dy:
PLAT215_ALERT_3_B Disordered C4   has ADP max/min Ratio .....   4.2 Note

   C4 is one of the rotationally disordered carbon atoms of the benzene ring. The large ADP max/min ratio is a product of the incomplete modeling of the rotational disorder combined with the equivalent occupancies given to each of the disordered components. A simplified model with equivalent chemical occupancies for each disordered benzene position was used to overcome refinement instability which was observed when the chemical occupancy values were floating.

PLAT934_ALERT_3_B Number of (Iobs-Icalc)/Sigma(W) > 10 Outliers ..   2 Check

SQUID Magnetometry

All magnetic measurements were carried out on a Quantum Design MPMS-XL SQUID magnetometer. Crystalline samples were dried under vacuum, mechanically ground, loaded into a

quartz tube (inner diameter 5 mm outer diameter 7 mm), covered with a solid layer of eicosane, and flame sealed under vacuum. The eicosane was subsequently melted at 40 °C in order to restrain the sample (prevent crystallite torquing) and to improve thermal conductivity between the sample and the environment. Diamagnetic corrections were calculated using Pascal's constants[34], and were applied to all reported magnetic susceptibility values unless otherwise noted. Material quantities: **1-Gd**, 31.6 mg sample with 61.0 mg of eicosane. **1-Tb**, 8.6 mg sample with 30.2 mg eicosane. **1-Dy**, 12.8 mg sample with 48.2 mg eicosane. **1-Tm**, 29.2 mg sample with 86.3 mg eicosane.

5.5. Computational Methods

In order to determine the ground state and optimized structures of $(Cp^{iPr5}Ln)_2(\mu\text{-}\eta^6\text{:}\eta^6\text{-}C_6H_6)$ complexes (Ln = Y, Gd, Tb, Dy, Tm), density functional theory (DFT) calculations were initially conducted in the gas phase. Geometry optimizations were performed on structures obtained from single X-ray diffraction data, using C_1 symmetry. The TPSSh hybrid meta- Generalized Gradient Approximation (meta-GGA) density functional[35], including Grimme's D3 dispersion correction[36] with a Becke-Johnson damping function, and the Resolution of Identity (RI-*J*) approximation[37], were employed. The practicality of the TPSSh hybrid functional for lanthanide complexes, particularly those with small HOMO-LUMO gaps, has been demonstrated in previous studies.[38] For C and H atoms, the double-ζ split valence basis set with polarization functions (def2-SVP)[39] was used, while the triple-ζ basis set with polarization functions (def2-TZVP)[40] was employed for the metallic atoms. Stuttgart-Cologne scalar-relativistic small core effective core potentials (ECPs)[41] were also included for these metallic atoms. A lanthanide molecular complex can exhibit degeneracy in its various 4f configurations due to the contracted nature of the 4f orbitals. Therefore, small core ECPs were utilized to explicitly treat 4f electrons, as opposed to 4f-in-core ECP calculations, which are necessary to determine the appropriate 4f configuration for lanthanide complexes with near-degenerate f-occupations. The convergence tolerances for geometry and electron density were set to 10^{-4} a.u. and 10^{-7}, respectively. Quadrature grids of size 4[42] were employed for numerical integration. The optimized structures were confirmed as minima on their respective ground-state potential energy surfaces through harmonic vibrational analysis.[43]

All spin multiplicities corresponding to M^{2+}/Bz^{2-} and M^{3+}/Bz^{4-} in **1-Ln** complexes were explored. Electronic configurations, including $4f^{n+1}$ and $4f^n$, indicative of the oxidation states of the metals, as well as unconventional configurations involving d orbitals, were assessed. Achieving self-consistent field (SCF) convergence for many of these electronic occupations was extremely challenging. Nevertheless, Fermi smearing, in conjunction with SCF damping and level shifting, was employed to attain specific electronic configurations. These techniques have proven effective for other open-shell lanthanide complexes[44] with shallow potential energy surfaces in facilitating SCF convergence. Fermi smearing with the following settings was employed to obtain the specific electronic occupations of the valence shell including $4f^{n+1}$ and $4f^n5d^1$ for the lanthanide complexes. The initial temperature was set between 2000-3000 K, and the final temperature to be between 50-150 K with an annealing factor of 0.85 to ensure the desired electronic configuration. The occupation numbers were fixed during Fermi smearing to achieve the specified spin state. Ground-state optimization was then carried out for all the possible electronic configurations describing different spin states (various numbers of unpaired electrons) for each complex.

All-electron calculations using the scalar-relativistic exact two-component (X2C-SR) DFT optimizations[45,46] were further performed on the ECP-optimized lanthanide compounds in their singlet state. The diagonal local approximation to the unitary decoupling transformation (DLU) was employed.[47,48] Segmented-contracted x2c-type basis sets,[49] including x2c- TZVPall-2c for metals and x2c-SVPall-2c for nonmetallic atoms, were used. Additionally, the finite nucleus model was utilized.[50] The same functional and dispersion correction choices from the ECP computations were employed in the X2C computations. Grids with an increased number of radial points (gridsize 5a) were used.[49]

The solvation effects of hexane on the lanthanide complexes were accounted for using the conductor-like screening implicit solvation model (COSMO),[51] with a dielectric constant of $E = 1.887$ and an index of refraction $n = 1.3727$. The structures obtained with COSMO were confirmed to be local minima through vibrational analysis. Time-dependent density functional theory (TDDFT)[38] computations with the nonorthonormal Krylov sub-space method,[52] were carried out to simulate the UV-Vis spectrum and investigate the nature of transitions. These computations involved 180-200 vertical excitations on the optimized structures in the liquid phase, using the same functional and choice of basis sets as previously described. Electronic absorption spectra were computed using a Gaussian spectral line shape with a width of 0.2 eV, centered on the oscillator energy.

All calculations were performed using the TURBOMOLE quantum chemistry package.[53] For the visualization of the orbitals, the VMD program with a contour value of 0.03 was used.[54]

5.6: Acknowledgments

5.7: References and Footnotes

(1)   Bochkarev, M. N. Synthesis, Arrangement, and Reactivity of Arene−Lanthanide Compounds. *Chem. Rev.* **2002**, *102* (6), 2089–2118. DOI: 10.1021/cr010329i.
(2)   Cotton, S. *Lanthanide and Actinide Chemistry*; John Wiley & Sons, 2013.
(3)   Fan, B.; Shen, Q.; Lin, Y. Synthesis and Structure of H6-Benzenelanthanoidtris(Aluminum Tetrachlorides) (Ln = La, Nd, Sm). *J. Organomet. Chem.* **1989**, *377* (1), 51–58. DOI: 10.1016/0022-328X(89)80050-6.
(4)   Brennan, J. G.; Cloke, F. G. N.; Sameh, A. A.; Zalkin, A. Synthesis of Bis(η-1,3,5-Tri-t-Butylbenzene) Sandwich Complexes of Yttrium(0) and Gadolinium(0); the X-Ray Crystal Structure of the First Authentic Lanthanide(0) Complex, [Gd(η-But3C6H3)2]. *J. Chem. Soc. Chem. Commun.* **1987**, No. 21, 1668–1669. DOI: 10.1039/C39870001668.
(5)   Cassani, M. C.; Duncalf, D. J.; Lappert, M. F. The First Example of a Crystalline Subvalent Organolanthanum Complex: [K([18]Crown-6)- (H2-C6H6)2][(LaCptt2)2(μ-H6:H6-C6H6)]•2C6H6 (Cptt = H5-C5H3But2-1,3). *J. Am. Chem. Soc.* **1998**, *120* (49), 12958–12959. DOI: 10.1021/ja980377t.

(6)   Fieser, M. E.; Ferrier, M. G.; Su, J.; Batista, E.; Cary, S. K.; Engle, J. W.; Evans, W. J.; Lezama Pacheco, J. S.; Kozimor, S. A.; Olson, A. C.; Ryan, A. J.; Stein, B. W.; Wagner, G. L.; Woen, D. H.; Vitova, T.; Yang, P. Evaluating the Electronic Structure of Formal Ln ^{II} Ions in Ln ^{II} (C $_5$ H $_4$ SiMe $_3$) $_3$ $^{1-}$ Using XANES Spectroscopy and DFT Calculations. *Chem. Sci.* **2017**, *8* (9), 6076–6091. DOI: 10.1039/C7SC00825B.

(7)   Gould, C. A.; Marbey, J.; Vieru, V.; Marchiori, D. A.; David Britt, R.; Chibotaru, L. F.; Hill, S.; Long, J. R. Isolation of a Triplet Benzene Dianion. *Nat. Chem.* **2021**, *13* (10), 1001–1005. DOI: 10.1038/s41557-021-00737-8.

(8)   Palumbo, C. T.; Darago, L. E.; Dumas, M. T.; Ziller, J. W.; Long, J. R.; Evans, W. J. Structure, Magnetism, and Multi-Electron Reduction Reactivity of the Inverse Sandwich Reduced Arene La2+ Complex [{[C5H3(SiMe3)2]2La}2(μ-H6:H6-C6H6)]1–. *Organometallics* **2018**, *37* (19), 3322–3331. DOI: 10.1021/acs.organomet.8b00523.

(9)   Huang, W.; Le Roy, J. J.; Khan, S. I.; Ungur, L.; Murugesu, M.; Diaconescu, P. L. Tetraanionic Biphenyl Lanthanide Complexes as Single-Molecule Magnets. *Inorg. Chem.* **2015**, *54* (5), 2374–2382. DOI: 10.1021/ic5029788.

(10) Gould, C. A.; McClain, K. R.; Reta, D.; Kragskow, J. G. C.; Marchiori, D. A.; Lachman, E.; Choi, E.-S.; Analytis, J. G.; Britt, R. D.; Chilton, N. F.; Harvey, B. G.; Long, J. R. Ultrahard Magnetism from Mixed-Valence Dilanthanide Complexes with Metal-Metal Bonding. *Science* **2022**, *375* (6577), 198–202. DOI: 10.1126/science.abl5470.

(11) Yu, C.; Liang, J.; Deng, C.; Lefèvre, G.; Cantat, T.; Diaconescu, P. L.; Huang, W. Arene-Bridged Dithorium Complexes: Inverse Sandwiches Supported by a δ Bonding Interaction. *J. Am. Chem. Soc.* **2020**, *142* (51), 21292–21297. DOI: 10.1021/jacs.0c11215.

(12) Gentner, T. X.; Rösch, B.; Ballmann, G.; Langer, J.; Elsen, H.; Harder, S. Low Valent Magnesium Chemistry with a Super Bulky β-Diketiminate Ligand. *Angew. Chem. Int. Ed.* **2019**, *58* (2), 607–611. DOI: 10.1002/anie.201812051.

(13) Huang, W.; Dulong, F.; Wu, T.; Khan, S. I.; Miller, J. T.; Cantat, T.; Diaconescu, P. L. A Six-Carbon 10π-Electron Aromatic System Supported by Group 3 Metals. *Nat. Commun.* **2013**, *4* (1), 1448. DOI: 10.1038/ncomms2473.

(14) Fagin, A. A.; Bochkarev, M. N.; Kozimor, S. A.; Ziller, J. W.; Evans, W. J. Comparative Reductive Reactivity of SmI2 with TmI2 in the Synthesis of Lanthanide Arene Complexes. *Z. Für Anorg. Allg. Chem.* **2005**, *631* (13–14), 2848–2853. DOI: 10.1002/zaac.200500173.

(15) Liu, S.-S.; Yan, B.; Meng, Z.-S.; Gao, C.; Wang, B.-W.; Gao, S. Two Half-Sandwich Organometallic Single-Ion Magnets with Toluene Coordinated to the Dy(III) Ion: The [(C7H8)Dy(AlCl4)3] and [(C7H8)Dy(AlBr4)3] Complexes. *Inorg. Chem. Commun.* **2017**, *86*, 312–314. DOI: 10.1016/j.inoche.2017.05.006.

(16) Liu, S.-S.; Ziller, J. W.; Zhang, Y.-Q.; Wang, B.-W.; Evans, W. J.; Gao, S. A Half-Sandwich Organometallic Single-Ion Magnet with Hexamethylbenzene Coordinated to the Dy(III) Ion. *Chem. Commun.* **2014**, *50* (77), 11418–11420. DOI: 10.1039/C4CC04262J.

(17) Gould, C. A.; McClain, K. R.; Yu, J. M.; Groshens, T. J.; Furche, F.; Harvey, B. G.; Long, J. R. Synthesis and Magnetism of Neutral, Linear Metallocene Complexes of Terbium(II) and Dysprosium(II). *J. Am. Chem. Soc.* **2019**, *141* (33), 12967–12973. DOI: 10.1021/jacs.9b05816.

(18) McClain, K. R.; Gould, C. A.; Marchiori, D. A.; Kwon, H.; Nguyen, T. T.; Rosenkoetter, K. E.; Kuzmina, D.; Tuna, F.; Britt, R. D.; Long, J. R.; Harvey, B. G. Divalent Lanthanide Metallocene Complexes with a Linear Coordination Geometry and Pronounced 6s–5d Orbital Mixing. *J. Am. Chem. Soc.* **2022**, *144* (48), 22193–22201. DOI: 10.1021/jacs.2c09880.

175

(19) McClain, K. R.; Gould, C. A.; Chakarawet, K.; Teat, S. J.; Groshens, T. J.; Long, J. R.; Harvey, B. G. High-Temperature Magnetic Blocking and Magneto-Structural Correlations in a Series of Dysprosium(Iii) Metallocenium Single-Molecule Magnets. *Chem. Sci.* **2018**, *9* (45), 8492–8503. DOI: 10.1039/c8sc03907k.

(20) Evans, W. J.; Johnston, M. A.; Clark, R. D.; Ziller, J. W. Variability of (Ring Centroid)–Ln–(Ring Centroid) Angles in the Mixed Ligand C5Me5/C8H8 Complexes (C5Me5)Ln(C8H8) and [(C5Me5)Yb(THF)](μ-H8:η8-C8H8)[Yb(C5Me5)]. *J. Chem. Soc. Dalton Trans.* **2000**, No. 10, 1609–1612. DOI: 10.1039/A908412F.

(21) Evans, W. J.; Davis, B. L.; Champagne, T. M.; Ziller, J. W. C–H Bond Activation through Steric Crowding of Normally Inert Ligands in the Sterically Crowded Gadolinium and Yttrium (C5Me5)3M Complexes. *Proc. Natl. Acad. Sci.* **2006**, *103* (34), 12678–12683. DOI: 10.1073/pnas.0602672103.

(22) Jiang, S.-D.; Liu, S.-S.; Zhou, L.-N.; Wang, B.-W.; Wang, Z.-M.; Gao, S. Series of Lanthanide Organometallic Single-Ion Magnets. *Inorg. Chem.* **2012**, *51* (5), 3079–3087. DOI: 10.1021/ic202511n.

(23) Evans, W. J.; Schmiege, B. M.; Lorenz, S. E.; Miller, K. A.; Champagne, T. M.; Ziller, J. W.; DiPasquale, A. G.; Rheingold, A. L. Reductive Reactivity of the Organolanthanide Hydrides, [(C5Me5)2LnH]x, Leads to Ansa-Allyl Cyclopentadienyl (H5-C5Me4CH2−C5Me4CH2-H3)2- and Trianionic Cyclooctatetraenyl (C8H7)3- Ligands. *J. Am. Chem. Soc.* **2008**, *130* (26), 8555–8563. DOI: 10.1021/ja8011726.

(24) Chilton, N. F.; Anderson, R. P.; Turner, L. D.; Soncini, A.; Murray, K. S. PHI: A Powerful New Program for the Analysis of Anisotropic Monomeric and Exchange-Coupled Polynuclear d- and f-Block Complexes. *J. Comput. Chem.* **2013**, *34* (13), 1164–1175. DOI: 10.1002/jcc.23234.

(25) Demir, S.; Jeon, I.-R.; Long, J. R.; Harris, T. D. Radical Ligand-Containing Single-Molecule Magnets. *Coord. Chem. Rev.* **2015**, *289–290*, 149–176. DOI: 10.1016/j.ccr.2014.10.012.

(26) Demir, S.; Gonzalez, M. I.; Darago, L. E.; Evans, W. J.; Long, J. R. Giant Coercivity and High Magnetic Blocking Temperatures for N2 3− Radical-Bridged Dilanthanide Complexes upon Ligand Dissociation. *Nat. Commun.* **2017**, *8* (1), 2144. DOI: 10.1038/s41467-017-01553-w.

(27) Hansen, M. F.; Mørup, S. Estimation of Blocking Temperatures from ZFC/FC Curves. *J. Magn. Magn. Mater.* **1999**, *203* (1), 214–216. DOI: 10.1016/S0304-8853(99)00238-3.

(28) Mulliken, R. S. Electronic Population Analysis on LCAO–MO Molecular Wave Functions. I. *J. Chem. Phys.* **1955**, *23* (10), 1833–1840. DOI: 10.1063/1.1740588.

(29) Reed, A. E.; Weinstock, R. B.; Weinhold, F. Natural Population Analysis. *J. Chem. Phys.* **1985**, *83* (2), 735–746. DOI: 10.1063/1.449486.

(30) Dezember, T.; Sitzmann, H. Die Fulven-Route Zum Pentaisopropylcyclopentadienid / The Fulvene Route to Pentaisopropylcyclopentadienide. *Z. Für Naturforschung B* **1997**, *52* (8), 911–918. DOI: 10.1515/znb-1997-0805.

(31) Sheldrick, G. M. SHELXT – Integrated Space-Group and Crystal-Structure Determination. *Acta Crystallogr. Sect. Found. Adv.* **2015**, *71* (1), 3–8. DOI: 10.1107/S2053273314026370.

(32) Müller, P.; Herbst-Irmer, R.; Spek, A. L.; Schneider, T. R.; Sawaya, M. R. *Crystal Structure Refinement: A Crystallographer's Guide to SHELXL*; Oxford University Press, 2006. DOI: 10.1093/acprof:oso/9780198570769.001.0001.

(33) Dolomanov, O. V.; Bourhis, L. J.; Gildea, R. J.; Howard, J. a. K.; Puschmann, H. OLEX2: A Complete Structure Solution, Refinement and Analysis Program. *J. Appl. Crystallogr.* **2009**, *42* (2), 339–341. DOI: 10.1107/S0021889808042726.

(34) Bain, G. A.; Berry, J. F. Diamagnetic Corrections and Pascal's Constants. *J. Chem. Educ.* **2008**, *85* (4), 532. DOI: 10.1021/ed085p532.

(35) Staroverov, V. N.; Scuseria, G. E.; Tao, J.; Perdew, J. P. Comparative Assessment of a New Nonempirical Density Functional: Molecules and Hydrogen-Bonded Complexes. *J. Chem. Phys.* **2003**, *119* (23), 12129–12137. DOI: 10.1063/1.1626543.

(36) Grimme, S.; Antony, J.; Ehrlich, S.; Krieg, H. A Consistent and Accurate Ab Initio Parametrization of Density Functional Dispersion Correction (DFT-D) for the 94 Elements H-Pu. *J. Chem. Phys.* **2010**, *132* (15), 154104.

(37) Eichkorn, K.; Treutler, O.; Öhm, H.; Häser, M.; Ahlrichs, R. Auxiliary Basis Sets to Approximate Coulomb Potentials. *Chem. Phys. Lett.* **1995**, *240* (4), 283–290. DOI: 10.1016/0009-2614(95)00621-A.

(38) Bauernschmitt, R.; Ahlrichs, R. Treatment of Electronic Excitations within the Adiabatic Approximation of Time Dependent Density Functional Theory. *Chem. Phys. Lett.* **1996**, *256* (4), 454–464. DOI: 10.1016/0009-2614(96)00440-X.

(39) Weigend, F.; Ahlrichs, R. Balanced Basis Sets of Split Valence, Triple Zeta Valence and Quadruple Zeta Valence Quality for H to Rn: Design and Assessment of Accuracy. *Phys Chem Chem Phys* **2005**, *7* (18), 3297–3305. DOI: 10.1039/B508541A.

(40) Gulde, R.; Pollak, P.; Weigend, F. Error-Balanced Segmented Contracted Basis Sets of Double-ζ to Quadruple-ζ Valence Quality for the Lanthanides. *J. Chem. Theory Comput.* **2012**, *8* (11), 4062–4068. DOI: 10.1021/ct300302u.

(41) Dolg, M.; Stoll, H.; Preuss, H. Energy-Adjusted Abinitio Pseudopotentials for the Rare Earth Elements. *J. Chem. Phys.* **1989**, *90* (3), 1730–1734.

(42) Treutler, O.; Ahlrichs, R. Efficient Molecular Numerical Integration Schemes. *J. Chem. Phys.* **1995**, *102* (1), 346–354. DOI: 10.1063/1.469408.

(43) Deglmann, P.; May, K.; Furche, F.; Ahlrichs, R. Nuclear Second Analytical Derivative Calculations Using Auxiliary Basis Set Expansions. *Chem. Phys. Lett.* **2004**, *384* (1), 103–107. DOI: 10.1016/j.cplett.2003.11.080.

(44) Rajabi, A.; Grotjahn, R.; Rappoport, D.; Furche, F. A DFT Perspective on Organometallic Lanthanide Chemistry. *Dalton Trans.* **2024**. DOI: 10.1039/D3DT03221C.

(45) Peng, D.; Middendorf, N.; Weigend, F.; Reiher, M. An Efficient Implementation of Two-Component Relativistic Exact-Decoupling Methods for Large Molecules. *J. Chem. Phys.* **2013**, *138* (18), 184105. DOI: 10.1063/1.4803693.

(46) Franzke, Y. J.; Middendorf, N.; Weigend, F. Efficient Implementation of One- and Two-Component Analytical Energy Gradients in Exact Two-Component Theory. *J. Chem. Phys.* **2018**, *148* (10), 104110. DOI: 10.1063/1.5022153.

(47) Franzke, Y. J.; Weigend, F. NMR Shielding Tensors and Chemical Shifts in Scalar-Relativistic Local Exact Two-Component Theory. *J. Chem. Theory Comput.* **2019**, *15* (2), 1028–1043.

(48) Peng, D.; Reiher, M. Local Relativistic Exact Decoupling. *J. Chem. Phys.* **2012**, *136* (24).

(49) Pollak, P.; Weigend, F. Segmented Contracted Error-Consistent Basis Sets of Double-and Triple-ζ Valence Quality for One-and Two-Component Relativistic All-Electron Calculations. *J. Chem. Theory Comput.* **2017**, *13* (8), 3696–3705.

(50) Visscher, L.; Dyall, K. G. DIRAC–FOCK ATOMIC ELECTRONIC STRUCTURE CAL-CULATIONS USING DIFFERENT NUCLEAR CHARGE DISTRIBUTIONS. *At. Data Nucl. Data Tables* **1997**, *67* (2), 207–224. DOI: 10.1006/adnd.1997.0751.

(51) Klamt, A.; Schüürmann, G. COSMO: A New Approach to Dielectric Screening in Solvents with Explicit Expressions for the Screening Energy and Its Gradient. *J. Chem. Soc. Perkin Trans. 2* **1993**, No. 5, 799–805. DOI: 10.1039/P29930000799.

(52) Furche, F.; Krull, B. T.; Nguyen, B. D.; Kwon, J. Accelerating Molecular Property Calculations with Nonorthonormal Krylov Space Methods. *J. Chem. Phys.* **2016**, *144* (17), 174105. DOI: 10.1063/1.4947245.

(53) Kaupp, A. M. K.; Khani, S. K.; Müller, T.; Mack, F.; Nguyen, B. D.; Parker, S. M.; Perlt, E.; Rappoport, D.; Reiter, K.; Roy, S. TURBOMOLE: Modular Program Suite for Ab Initio Quantum-Chemical and Condensed-Matter Simulations. **2020**.

(54) Humphrey, W.; Dalke, A.; Schulten, K. VMD: Visual Molecular Dynamics. *J. Mol. Graph.* **1996**, *14* (1), 33–38. DOI: 10.1016/0263-7855(96)00018-5.

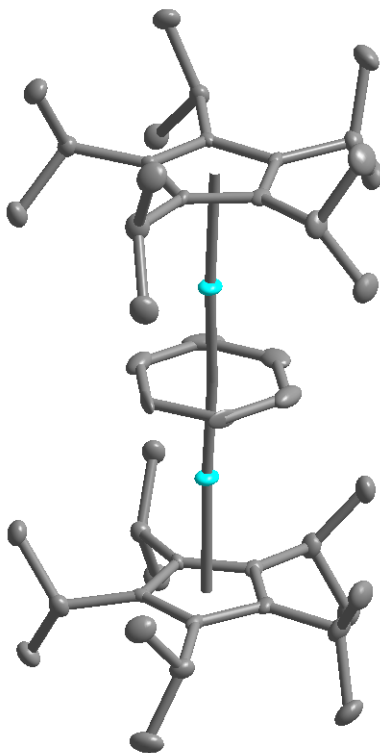**5.8: Supplementary Information**

Figure S5.1. Crystal structure of **1-Y**. Y, Cyan; C, gray. Ellipsoids are drawn at 50% probability. Hydrogen atom and minor disorder positions have been omitted for clarity.

Figure S5.2. Crystal structure of **1-Gd**. Gd, orange; C, gray. Ellipsoids are drawn at 50% probability. Hydrogen atom and minor disorder positions have been omitted for clarity

Figure S5.3. Crystal structure of **1-Tb**. Tb, red; C, gray. Ellipsoids are drawn at 50% probability. Hydrogen atom and minor disorder positions have been omitted for clarity
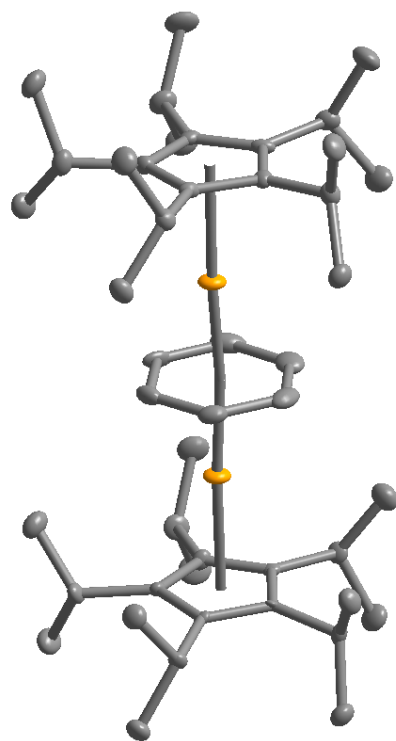
Figure S5.4. Crystal structure of **1-Dy**. Dy, green; C, gray. Ellipsoids are drawn at 50% probability. Hydrogen atom and minor disorder positions have been omitted for clarity
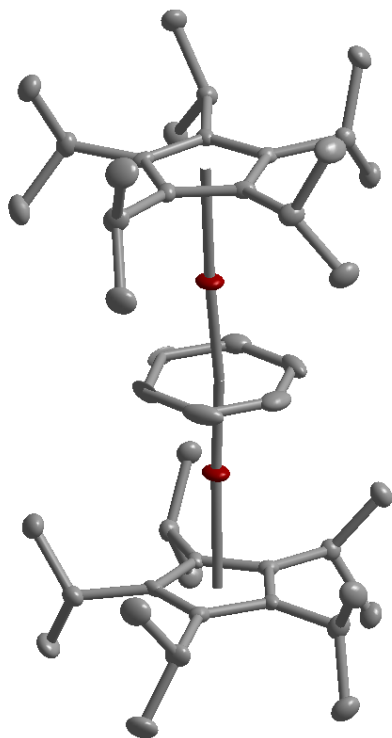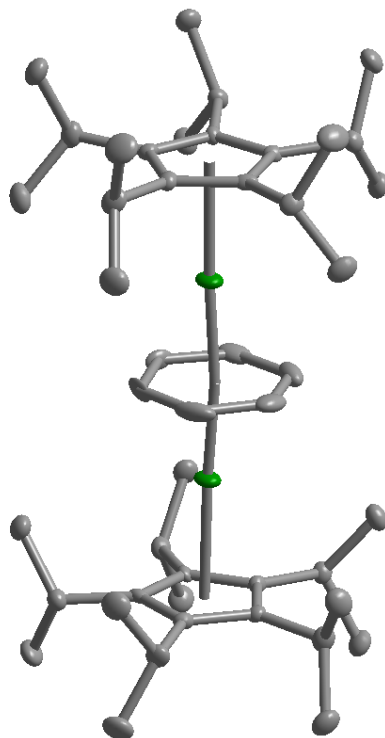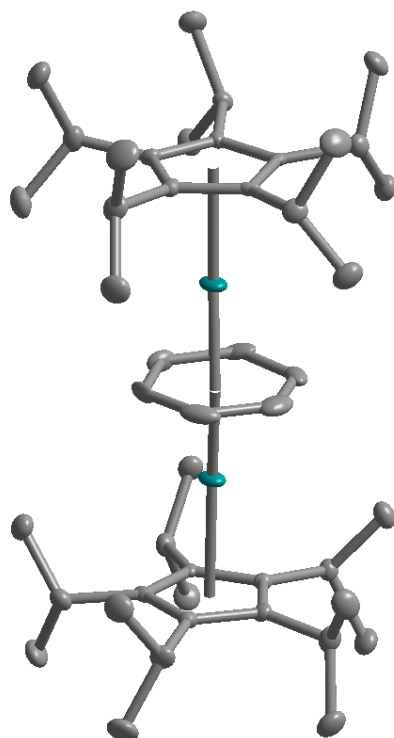
Figure S5.5. Crystal structure of **1-Tm**. Tm, blue; C, gray. Ellipsoids are drawn at 50% probability. Hydrogen atom and minor disorder positions have been omitted for clarity

Table S5.1. Unit Cell Metrics and Refinement Parameters for compounds 1-**Ln** (Ln = Y, Gd, Tb, Dy, Tm)

Compound	1-Y	1-Gd	1-Tb	1-Dy	1-Tm
Empirical formula	$C_{46}H_{70}Y_2$	$C_{46}H_{70}Gd_2$	$C_{46}H_{70}Tb_2$	$C_{46}H_{70}Dy_2$	$C_{46}H_{70}Tm_2$
Formula weight	800.84	937.52	940.86	948.02	960.88
Temperature/K	100	100	100	100	100
Crystal system	monoclinic	monoclinic	monoclinic	monoclinic	monoclinic
Space group	P2/n	P2/n	P2/n	P2/n	P2/n
a/Å	15.3920(9)	15.5090(5)	15.4480(5)	15.4016(13)	15.2497(3)
b/Å	9.8462(5)	9.8117(3)	9.8220(3)	9.8337(8)	9.8545(2)
c/Å	16.2170(9)	16.2094(5)	16.1975(6)	16.2056(14)	16.1989(3)
α/°	90	90	90	90	90
β/°	116.440(2)	116.8010(10)	116.5860(10)	116.477(2)	116.1200(10)
γ/°	90	90	90	90	90
Volume/Å^3	2200.7(2)	2201.61(12)	2197.79(13)	2197.0(3)	2185.73(8)
Z	2	2	2	2	2
ρ_{calc}g/cm^3	1.209	1.414	1.422	1.433	1.46
μ/mm^{-1}	2.651	3.013	3.219	3.402	4.06
F(000)	848	948	952	956	968
Crystal size/mm^3	0.363 × 0.199 × 0.128	0.194 × 0.171 × 0.104	0.178 × 0.155 × 0.138	0.17 × 0.139 × 0.099	0.265 × 0.154 × 0.144
Radiation	MoKα (λ = 0.71073)	MoKα (λ = 0.71073)	MoKα (λ = 0.71073)	MoKα (λ = 0.71073)	MoKα (λ = 0.71073)
2Θ range for data collection/°	4.136 to 50.7	4.152 to 50.7	4.146 to 50.692	4.142 to 50.694	4.134 to 50.698
Index ranges	-18 ≤ h ≤ 18, -11 ≤ k ≤ 11, -19 ≤ l ≤ 19	-18 ≤ h ≤ 18, -11 ≤ k ≤ 11, -19 ≤ l ≤ 19	-18 ≤ h ≤ 18, -11 ≤ k ≤ 11, -19 ≤ l ≤ 19	-18 ≤ h ≤ 18, -11 ≤ k ≤ 11, -19 ≤ l ≤ 19	-18 ≤ h ≤ 18, -11 ≤ k ≤ 11, -19 ≤ l ≤ 19
Reflections collected	69663	68433	26352	26268	58766
Independent reflections	4020 [R_{int} = 0.0556, R_{sigma} = 0.0217]	4034 [R_{int} = 0.0482, R_{sigma} = 0.0171]	4018 [R_{int} = 0.0184, R_{sigma} = 0.0118]	4016 [R_{int} = 0.0227, R_{sigma} = 0.0137]	3988 [R_{int} = 0.0247, R_{sigma} = 0.0103]
Data/restraints/parameters	4020/98/345	4034/122/345	401/86/345	4016/102/345	3988/86/345
Goodness-of-fit on F^2	1.096	1.129	1.105	1.105	1.152
Final R indexes [I>=2σ (I)]	R_1 = 0.0224, wR_2 = 0.0551	R_1 = 0.0165, wR_2 = 0.0396	R_1 = 0.0121, wR_2 = 0.0329	R_1 = 0.0130, wR_2 = 0.0335	R_1 = 0.0112, wR_2 = 0.0292
Final R indexes [all data]	R_1 = 0.0275, wR_2 = 0.0574	R_1 = 0.0195, wR_2 = 0.0409	R_1 = 0.0130, wR_2 = 0.0334	R_1 = 0.0140, wR_2 = 0.0340	R_1 = 0.0133, wR_2 = 0.0310
Largest diff. peak/hole / e Å^{-3}	0.39/-0.22	0.54/-0.50	0.43/-0.25	0.41/-0.38	0.37/-0.41

Table S5.2. Arene carbon-Mean Plane Distances (displacement vector normal to plane) for all Y-$(\eta^6\text{-Ar})$ containing compounds in CSD with calculated sum of squares. (Ar = carbon six membered ring). Mean plane was calculated in Mercury using the six ring carbon positions. η^6-bound tetra-phenylborates were excluded from the analysis

CSD CODE	D_1 (Å)	D_2 (Å)	D_3 (Å)	D_4 (Å)	D_5 (Å)	D_6 (Å)	$\sum_{i=1}^{6} D_i^2$
CUKLOL	0.089	0.1	0.196	0.101	0.089	0.182	0.126167
EZIBUN*	0	0	0	0	0	0	0
GIRHUN	0.019	0.039	0.042	0.024	0.004	0.001	0.0215
ICAWOC	0.001	0.003	0.013	0.019	0.014	0.004	0.009
ICELEL	0.001	0.003	0	0.004	0.006	0.004	0.003
KUGLUV	0.005	0.003	0.002	0.005	0.002	0.003	0.003333
KUGLUV	0.003	0.005	0.01	0.007	0	0.005	0.005
MALXAY	0.009	0	0.011	0.014	0.004	0.007	0.0075
MUXDUH	0.035	0.026	0.004	0.009	0.001	0.023	0.016333
NIVNEL	0.044	0.013	0.041	0.065	0.034	0.021	0.036333
NIVNIP	0.003	0.028	0.032	0.006	0.025	0.029	0.0205
ODEYEB	0.032	0.019	0.022	0.05	0.036	0.004	0.027167
TOPFOT	0.015	0.057	0.052	0.003	0.038	0.032	0.032833
TOPFOT	0.029	0.002	0.013	0	0.029	0.042	0.019167
XEKRIP	0.024	0.02	0.047	0.029	0.017	0.043	0.03
YEMWOE	0	0.075	0.073	0	0.073	0.075	0.049333
YEMWUK	0	0.063	0.062	0	0.062	0.063	0.041667
YEMXUL	0	0.082	0.081	0	0.081	0.082	0.054333
EZICEY	0.007	0.012	0.014	0.005	0.024	0.024	0.014333
Average Sum of Squared Deviations*							0.012

*EZIBUN excluded from literature average as six membered ring appears to have been fixed to a plane during structure refinement

Table S5.3. Arene carbon-mean plane distances (displacement vector normal to plane) for all Gd-(η^6-Ar) containing compounds in CSD with calculated sum of squares. (Ar = carbon six membered ring). Mean plane was calculated in Mercury using the six ring carbon positions. η^6-bound tetra-phenylborates were excluded from the analysis

CSD CODE	DIST1 (Å)	DIST2 (Å)	DIST3 (Å)	DIST4 (Å)	DIST5 (Å)	DIST6 (Å)	$\sum_{i=1}^{6} D_i^2$
QATNAE	0.001	0.009	0.018	0.017	0.007	0.002	0.000748
QATNAE	0.02	0.012	0.004	0.012	0.003	0.013	0.000882
QATNUY	0.019	0.022	0.017	0.007	0.003	0.009	0.001273
FOGJEQ	0.005	0.018	0.019	0.003	0.027	0.027	0.002177
POXMEW	0	0.064	0.062	0	0.062	0.064	0.01588
POXMOG	0.074	0.071	0.006	0.081	0.077	0.001	0.023044
YEHLAB	0.019	0.035	0.035	0.019	0.003	0.003	0.00319
YEHLIJ	0.025	0.025	0.025	0.025	0.025	0.025	0.00375
YILSOB*	0	0	0	0	0	0	0
EZICAU	0.001	0.002	0.005	0.007	0.007	0.003	0.000137
EZICIC	0.013	0.011	0	0.009	0.007	0.004	0.000436
Average Sum of Squared Deviations*							0.00515

*YILSOB excluded from literature average as six membered ring appears to have been fixed to a plane during structure refinement

Table S5.4. Arene carbon-mean plane distances (displacement vector normal to plane) for all Tb-$(\eta^6$-Ar) containing compounds in CSD with calculated sum of squares. (Ar = carbon six membered ring). Mean plane was calculated in Mercury using the six ring carbon positions. η^6-bound tetraphenylborates were excluded from the analysis

CSD CODE	DIST1 (Å)	DIST2 (Å)	DIST3 (Å)	DIST4 (Å)	DIST5 (Å)	DIST6 (Å)	$\sum_{i=1}^{6} D_i^2$
QOPZEC	0.007	0.02	0.014	0.004	0.017	0.012	0.001094
Average Sum of Squares*							0.001094

Table S5.5. Arene carbon-mean plane distances (displacement vector normal to plane) for all Dy-(η^6-Ar) containing compounds in CSD with calculated sum of squares. (Ar = carbon six membered ring). Mean plane was calculated in Mercury using the six ring carbon positions. η^6-bound tetra-phenylborates were excluded from the analysis

CSD CODE	D_1 (Å)	D_2 (Å)	D_3 (Å)	D_4 (Å)	D_5 (Å)	D_6 (Å)	$\sum_{i=1}^{6} D_i^2$
JIZVIA	0.014	0.011	0.002	0.012	0.009	0.004	0.000562
JIZVIA	0.025	0.01	0.013	0.021	0.007	0.017	0.001673
JIZVIA	0.032	0.021	0.01	0.031	0.019	0.013	0.003056
JIZVIA	0.033	0.016	0.014	0.028	0.011	0.019	0.002807
BEWWOP	0.231	0.112	0.128	0.241	0.116	0.116	0.167282
DUXGUB	0.017	0.01	0.025	0.013	0.014	0.03	0.002279
HATPAW	0.003	0.003	0.004	0.01	0.01	0.003	0.000243
HATPEA	0.024	0.027	0.011	0.007	0.01	0.006	0.001611
LOKQAE	0.005	0.008	0.011	0	0.013	0.016	0.000635
MUXFAP	0.038	0.029	0.004	0.012	0.002	0.023	0.002978
POXMAS	0	0.074	0.072	0	0.072	0.074	0.02132
POXMIA	0	0.083	0.082	0	0.082	0.083	0.027226
QOPZIG	0.005	0.017	0.013	0.002	0.014	0.01	0.000783
WAQYUJ	0.007	0.014	0.005	0.01	0.018	0.008	0.000758
YEHDEX	0.024	0.024	0.024	0.024	0.024	0.024	0.003456
YEHKUU	0.018	0.033	0.034	0.021	0.006	0.005	0.003071
YEHMAC	0.005	0.002	0.012	0.033	0.041	0.027	0.003672
Average Sum of Squared Deviations*							0.014318

Table S5.6. Arene carbon-mean plane distances (displacement vector normal to plane) for all Tm-$(\eta^6\text{-Ar})$ containing compounds in CSD with calculated sum of squares. (Ar = carbon six membered ring). Mean plane was calculated in Mercury using the six ring carbon positions. η^6-bound tetraphenylborates were excluded from the analysis

CSD CODE	D_1 (Å)	D_2 (Å)	D_3 (Å)	D_4 (Å)	D_5 (Å)	D_6 (Å)	$\sum_{i=1}^{6} D_i^2$
FUQFIH	0.004	0.003	0	0.002	0.001	0.002	0.000034
MAWXAK	0.002	0.002	0.01	0.018	0.018	0.01	0.000856
RIRQOY	0.062	0.178	0.102	0.095	0.204	0.123	0.111702
SALJAR	0.005	0.001	0.007	0.009	0.004	0.003	0.000181
Average Sum of Squared Deviations*							0.028193

Table S5.7. Arene carbon–mean plane distances (displacement vector normal to plane) for 1-Ln with calculated sum of squares. (Ar = carbon six membered ring). Mean plane was calculated in Mercury using the six ring carbon positions. Literature ranges from Tables S5.2 – S5.6 are included for comparison.

Compound	D_1 (Å)	D_2 (Å)	D_3 (Å)	D_4 (Å)	D_5 (Å)	D_6 (Å)	$\sum_{i=1}^{6} D_i^2$	Lit. Range of $\sum_{i=1}^{6} D_i^2$
1-Y	0.003	0.003	0.008	0.008	0.002	0.003	1.59×10^{-4}	$1.70\times10^{-5} - 1.08\times10^{-1}$
1-Gd	0.005	0.0008	0.0023	0.0017	0.0044	0.0011	5.44×10^{-5}	$1.37\times10^{-4} - 2.30\times10^{-2}$
1-Tb*	0.005	0.004	0.008	0.005	0.004	0.009	2.27×10^{-4}	$0 - 1.09\times10^{-3}$
1-Dy	0.009	0.005	0.001	0.002	0.002	0.007	1.64×10^{-4}	$2.43\times10^{-4} - 1.67\times10^{-1}$
1-Tm	0.022	0.017	0.001	0.012	0.007	0.01	1.07×10^{-3}	$3.40\times10^{-5} - 1.11\times10^{-1}$

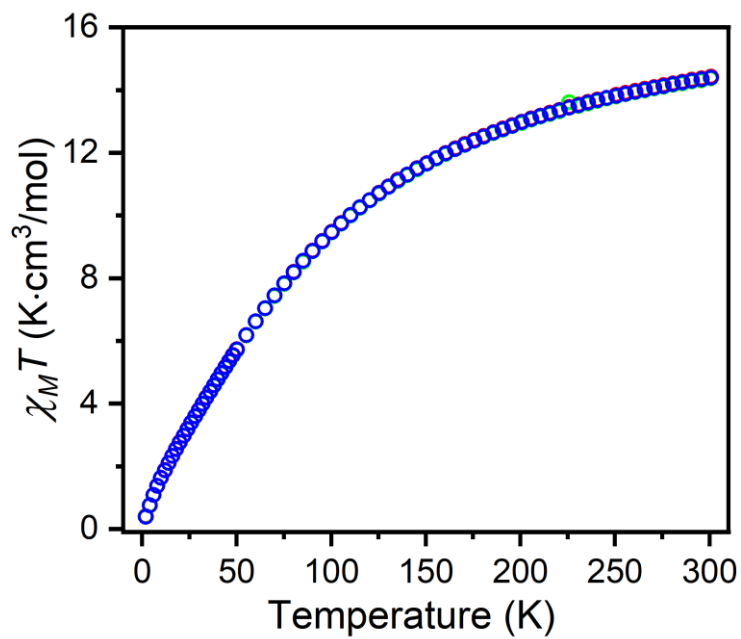*Lit. Range minimum arbitrarily set to zero as the CSD contained one Tb-η^6-Ar structure

Figure S5.6. Variable field dc magnetic susceptibility of **1-Gd** measured under 0.1 T (red), 0.5 T (green) and 1 T (blue) applied fields.
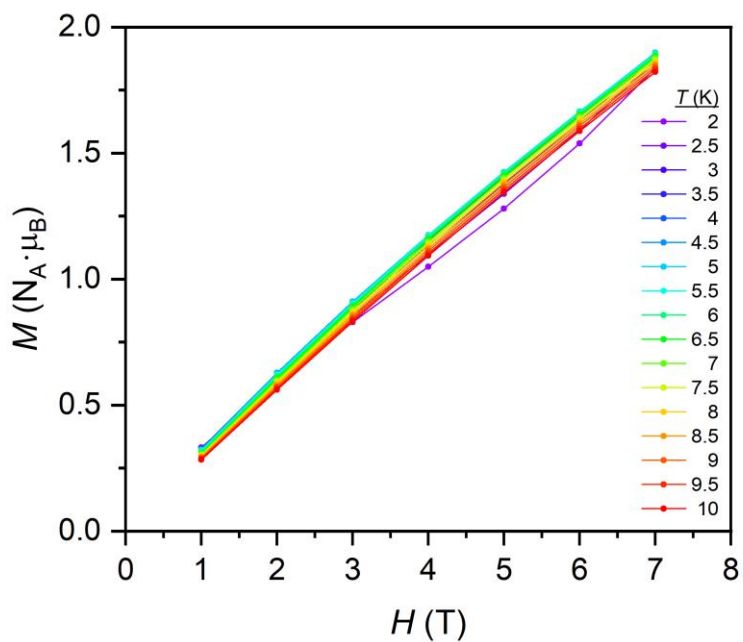
Figure S5.7. Isothermal Magnetization of **1-Gd** measured from 2-10 K. Solid lines are guides for the eye
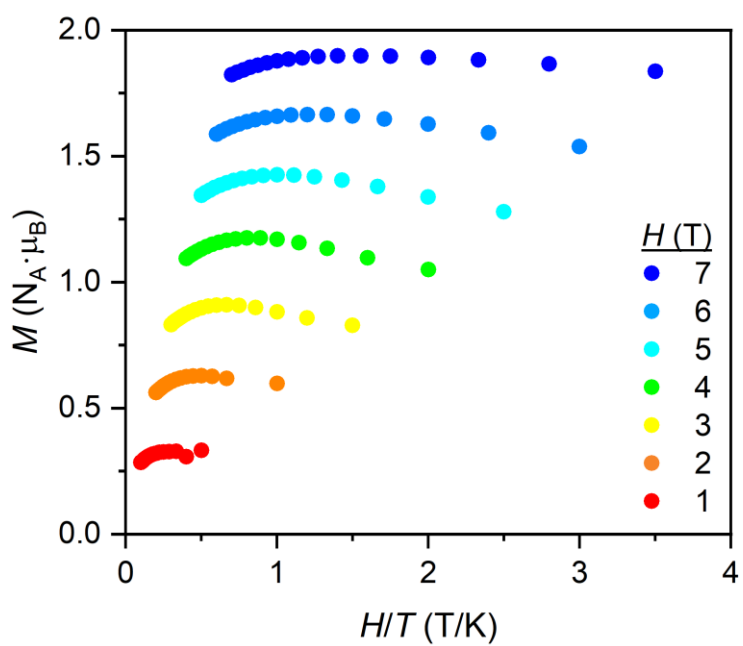

Figure S5.8. Reduced magnetization data of **1-Gd** measured under 1-7 T applied fields
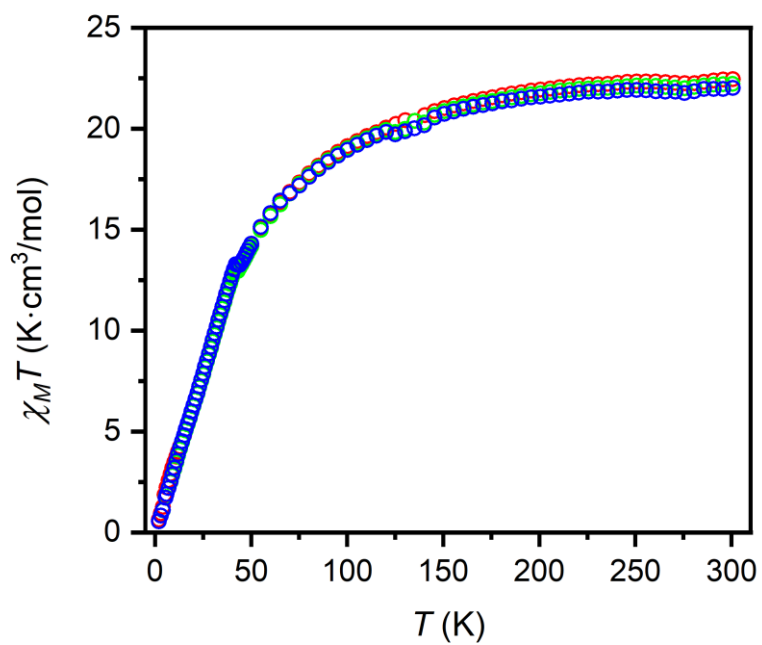
Figure S5.9. Variable field dc magnetic susceptibility of **1-Tb** measured under 0.1 T (red), 0.5 T (green) and 1 T (blue) applied fields.
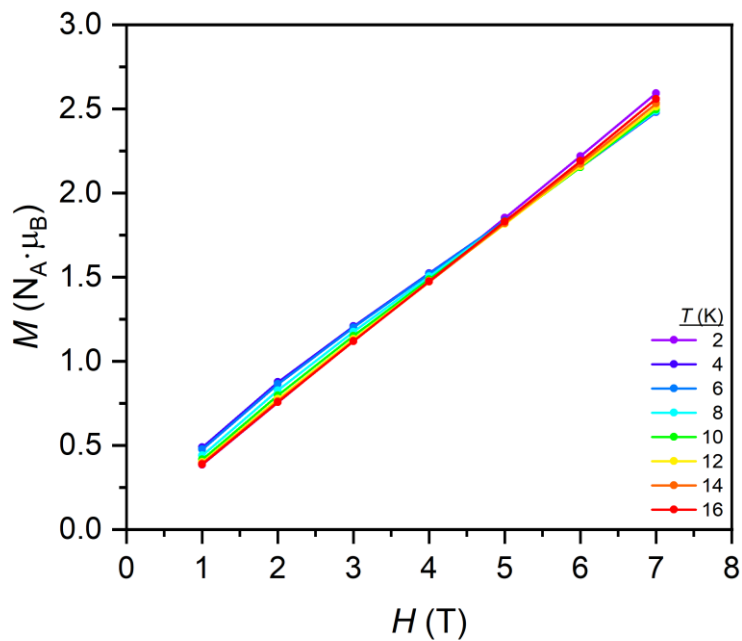
Figure S5.10. Isothermal magnetization of **1-Tb** measured from 2-16 K. Solid lines are guides for the eye.
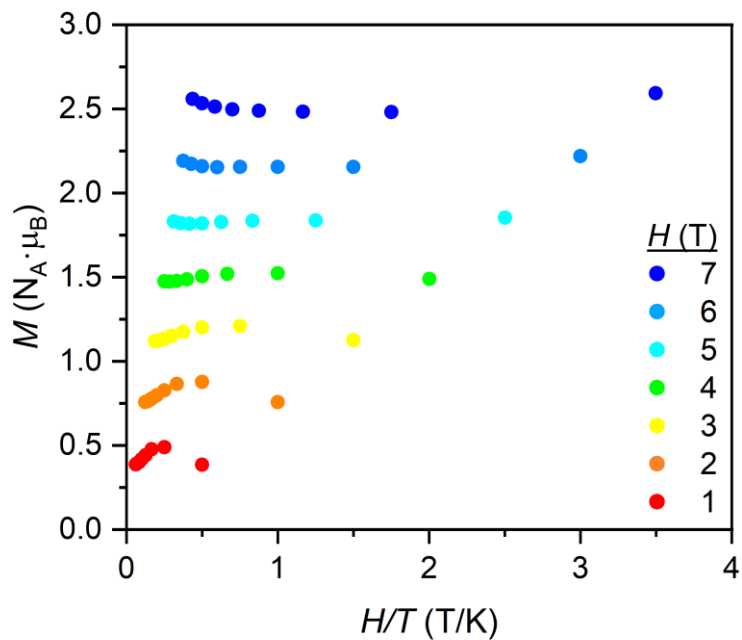

Figure S5.11. Reduced magnetization of **1-Tb** measured under 1-7 T applied fields
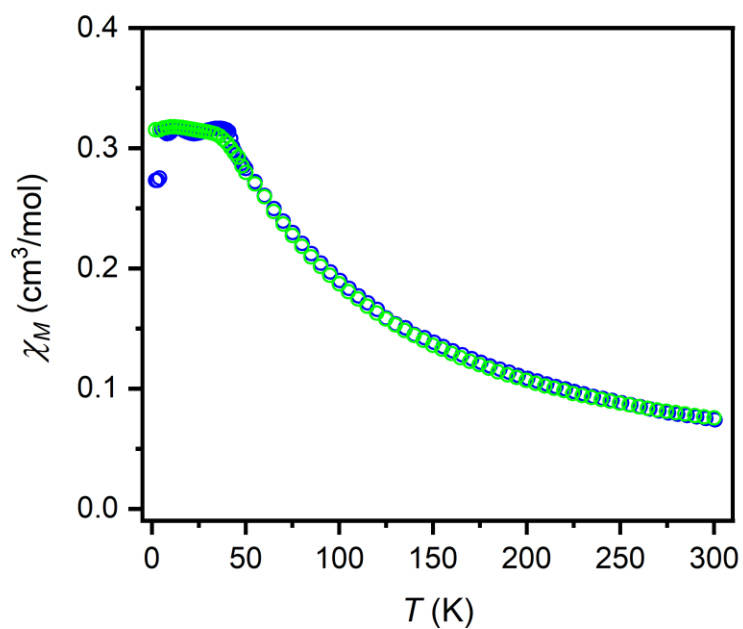
Figure S5.12. Field cooled (green circles) and zero-field cooled (blue circles) susceptibility of **1-Tb** measured under 0.5 T applied field
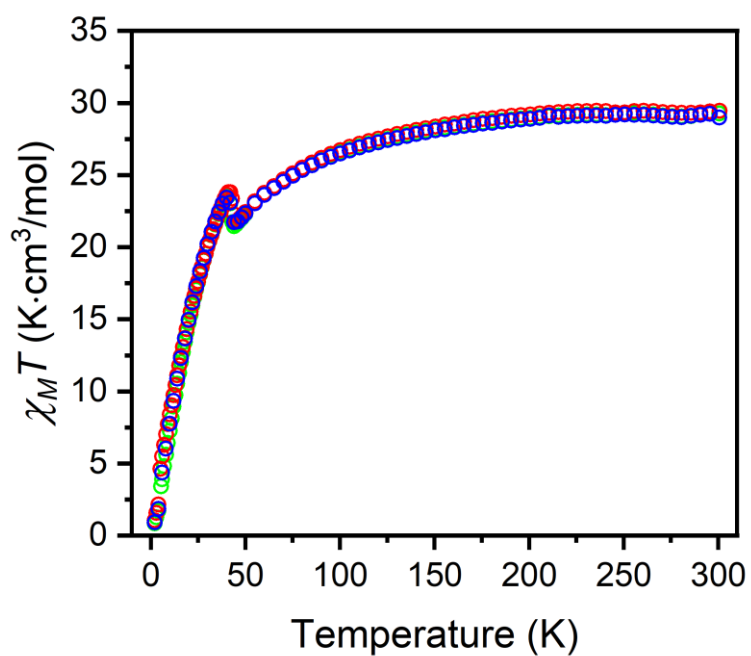

Figure S5.13. Variable field dc magnetic susceptibility of **1-Dy** measured under 0.1 T (red), 0.5 T (green) and 1 T (blue) applied fields.
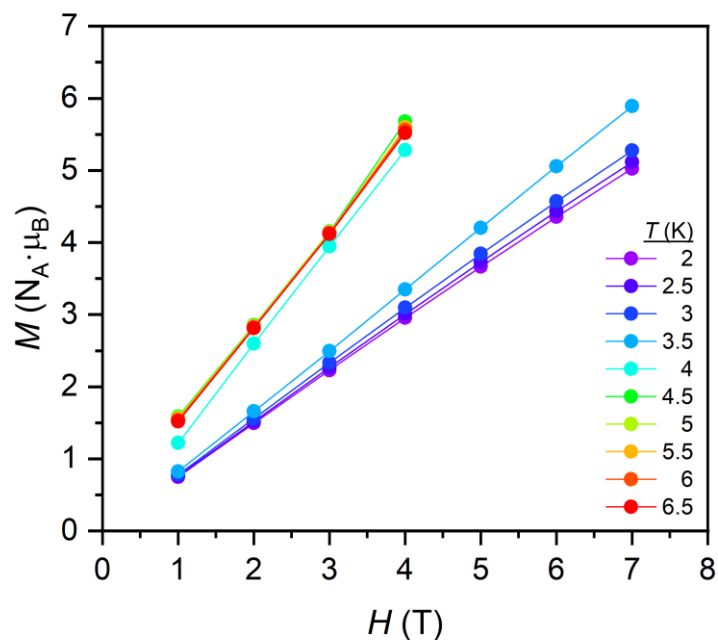
Figure S5.14. Isothermal Magnetization of **1-Dy**. Solid lines are guides for the eye. From 4 K onward, the magnetization was saturating SQUID detector at fields beyond 4 T.

Figure S5.15. Reduced magnetization of **1-Dy** measured under 1-7 T applied fields

196

Figure S5.16. Field cooled (green circles) and zero-field cooled (blue circles) susceptibility of **1-Dy** measured under 0.5 T applied field
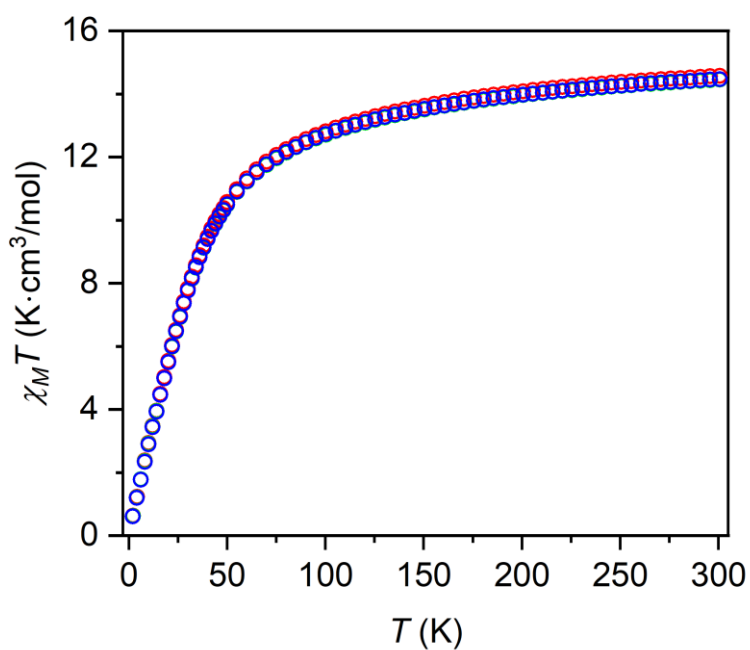
Figure S5.17. Variable field dc magnetic susceptibility of **1-Tm** measured under 0.1 T (red), 0.5 T (green) and 1 T (blue) applied fields.
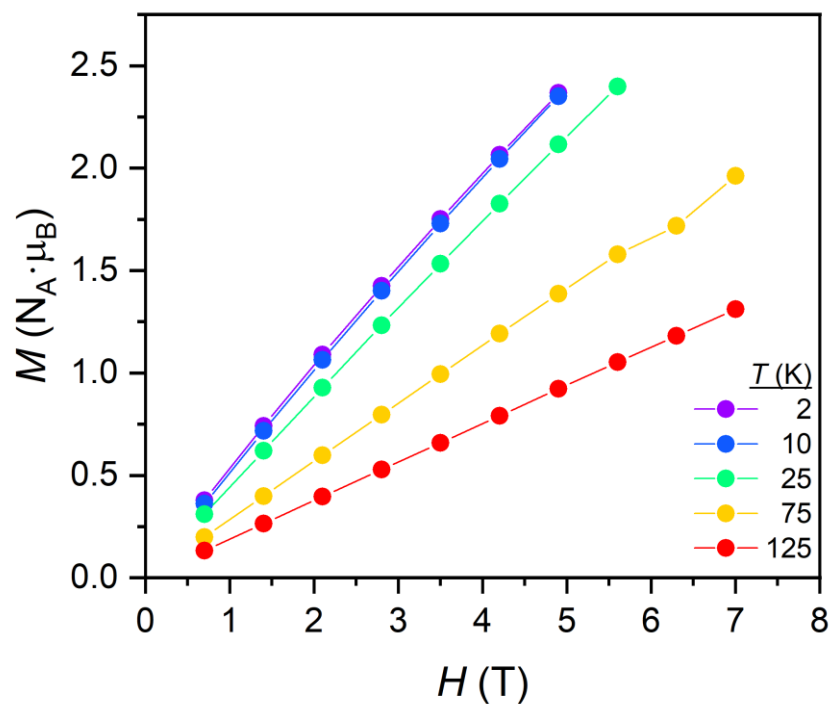
Figure S5.18. Isothermal Magnetization of **1-Tm**. Solid lines are guides for the eye. From 4 K onward, the magnetization was saturating SQUID detector at fields beyond 4 T.
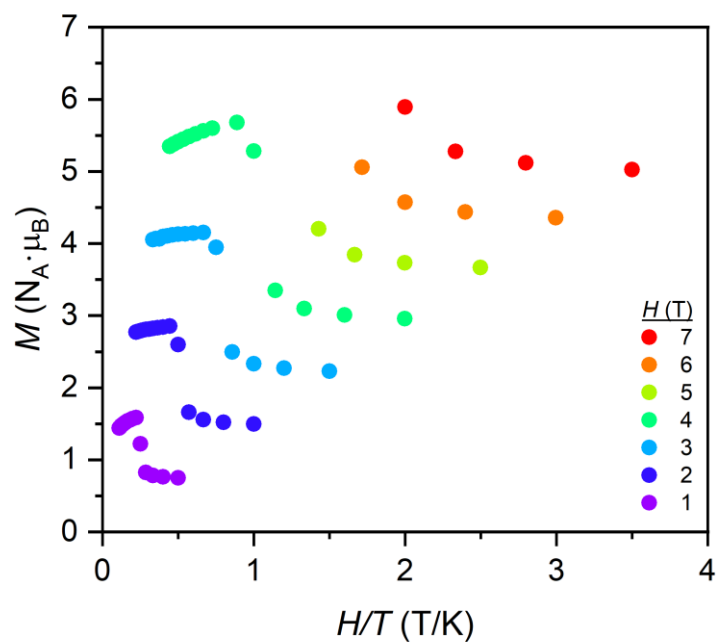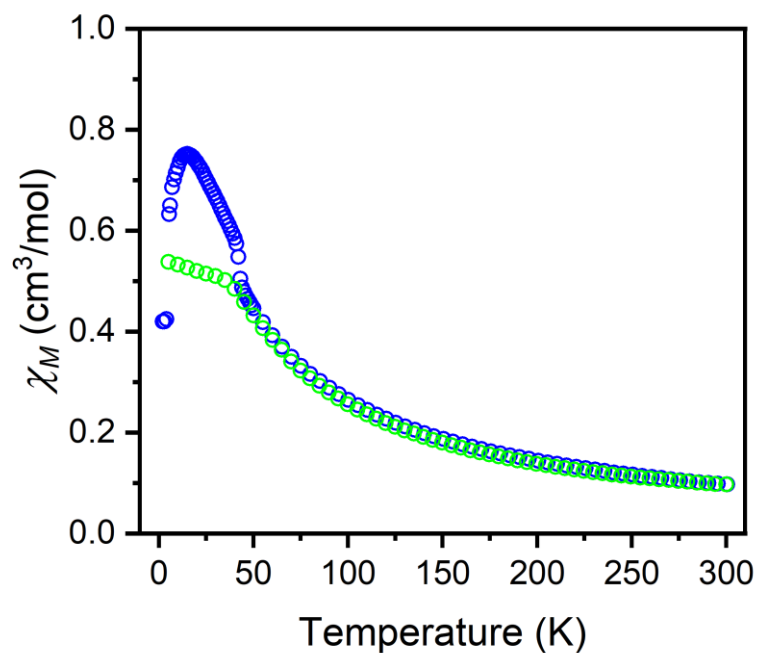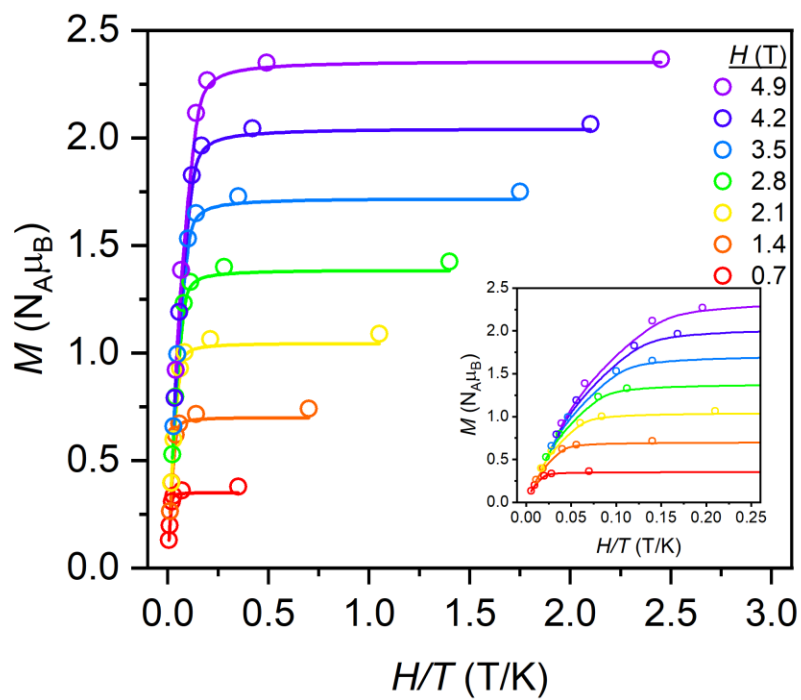

Figure S5.19. Reduced magnetization of **1-Tm** measured under 0.7-4.9 T applied fields. Solid lines are guides for the eye
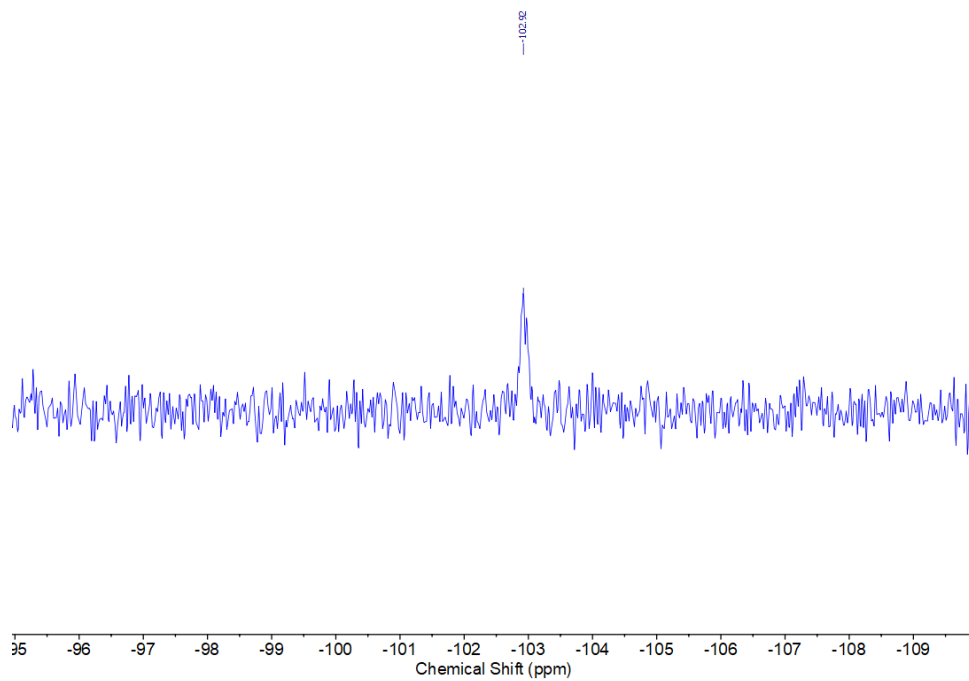
Figure S5.20. ^{89}Y NMR Spectrum of **1-Y** at 25 MHz in C_6D_6
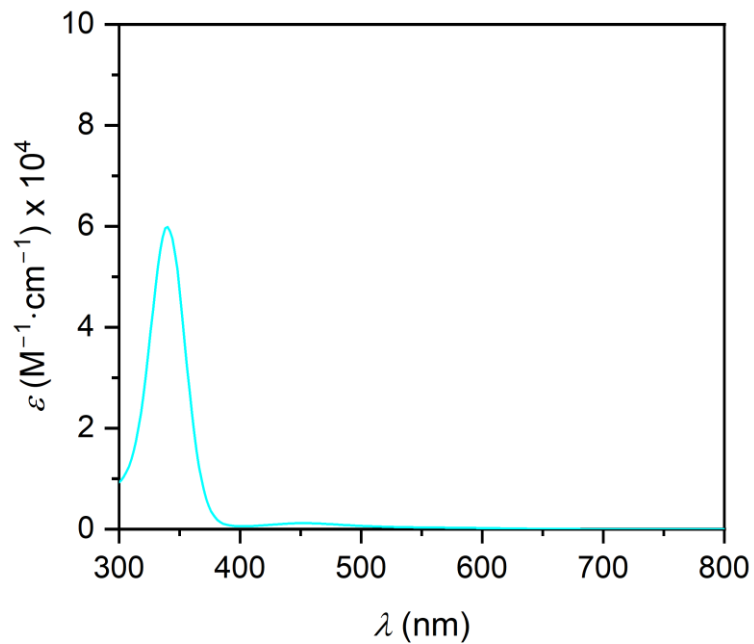
Figure S5.21. UV/Vis spectrum of **1-Y** in n-hexane solution.
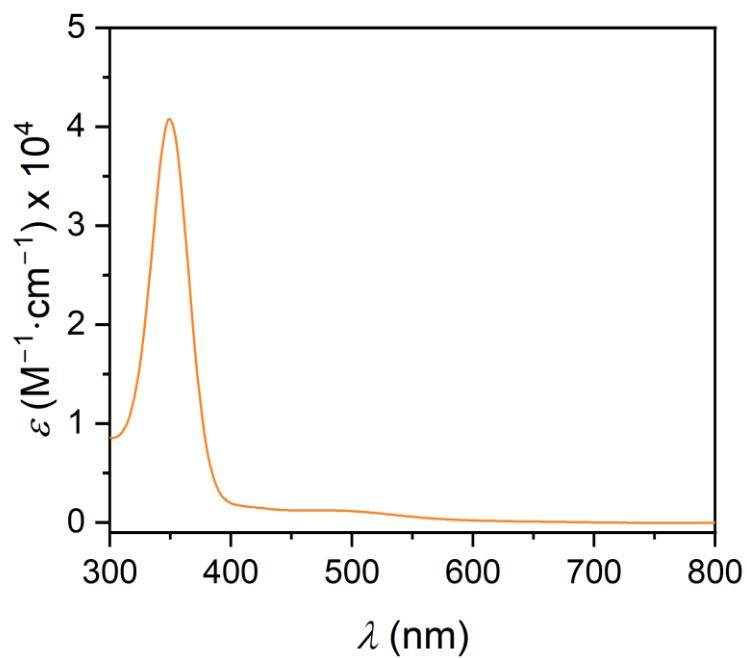
Figure S5.22. UV/vis spectrum of **1-Gd** in n-hexane solution.
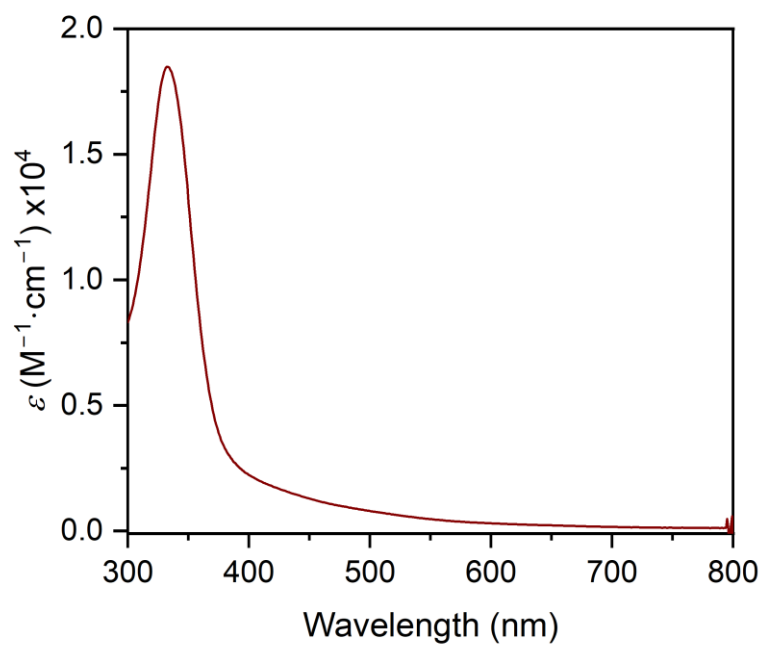
Figure S5.23. UV/vis Spectrum of **1-Tb** in n-hexane solution.
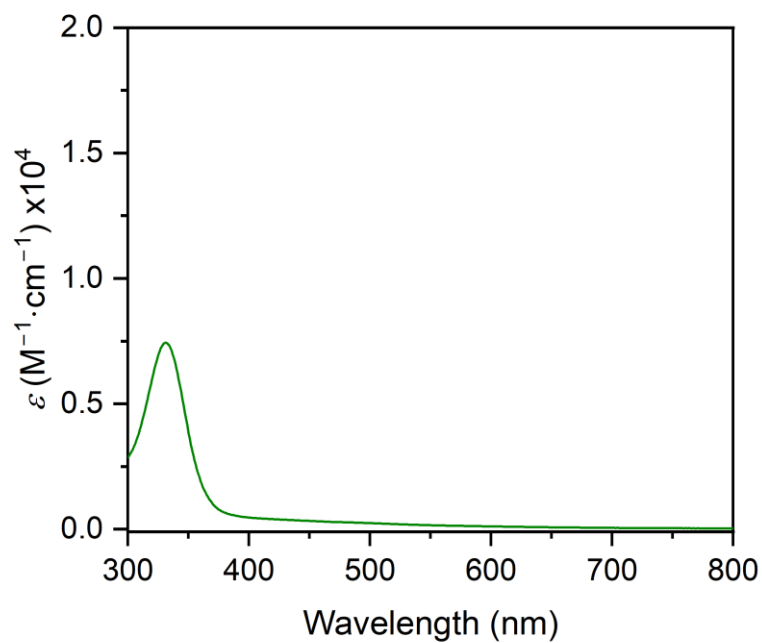
Figure S5.24. UV/vis spectrum of **1-Dy** in n-hexane solution.
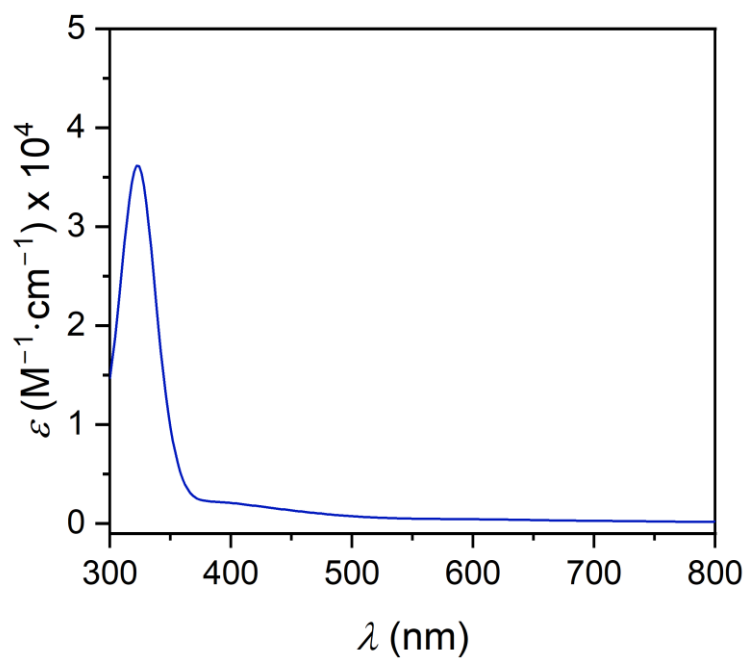
Figure S5.25. UV/vis spectrum of **1-Tm** in n-hexane solution.
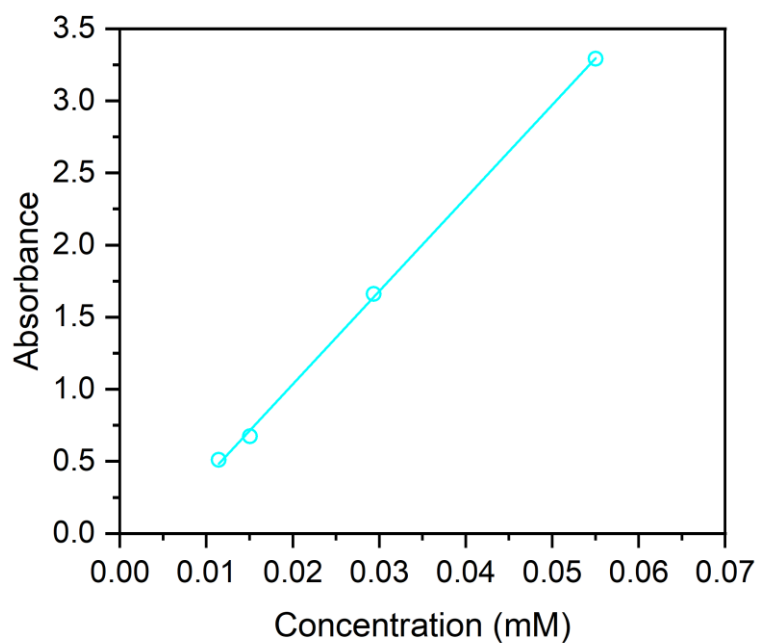
Figure S5.26. Beer's law plot of **1-Y**. Circles correspond to absorption maxima, line corresponds to fit to: $A=\varepsilon lM+b$. $\varepsilon = 64500$ (600) $M^{-1}\cdot cm^{-1}$, $b = -0.25$
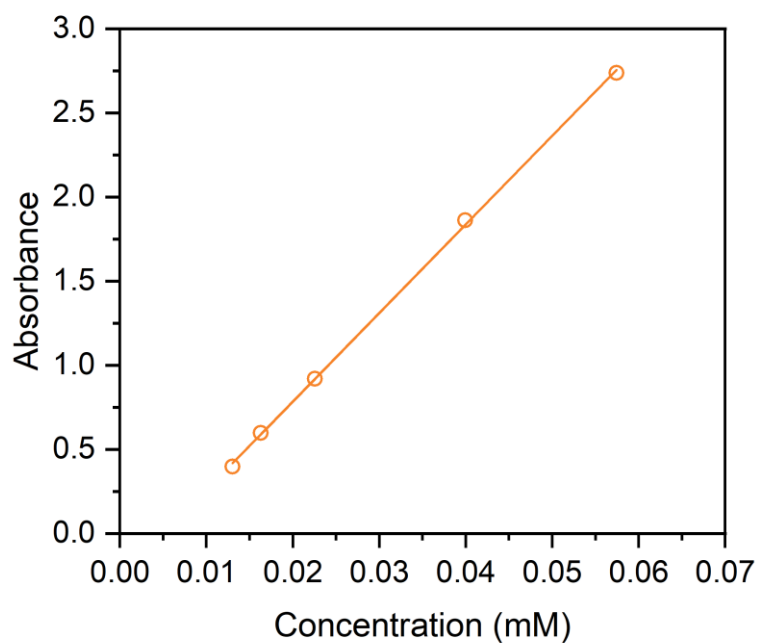
Figure S5.27. Beer's law plot of **1-Gd**. Circles correspond to absorption maxima, line corresponds to fit to: $A=\varepsilon lM+b$. $\varepsilon = 52700$(600) $M^{-1}\cdot cm^{-1}$, $b = -0.26$
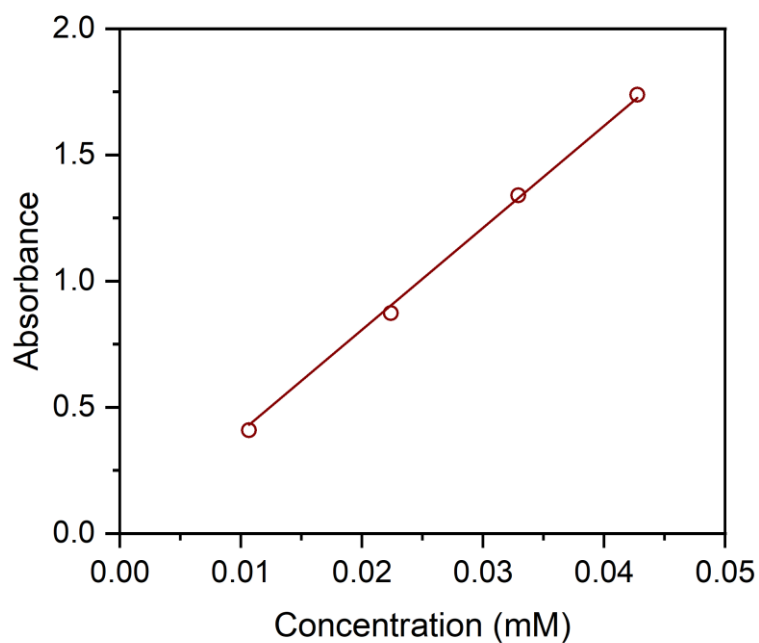
Figure S5.28. Beer's law plot of **1-Tb**. Circles correspond to absorption maxima, line corresponds to fit to: $A=\varepsilon lM+b$. $\varepsilon = 40400$ (400) $M^{-1}\cdot cm^{-1}$, $b = 0$
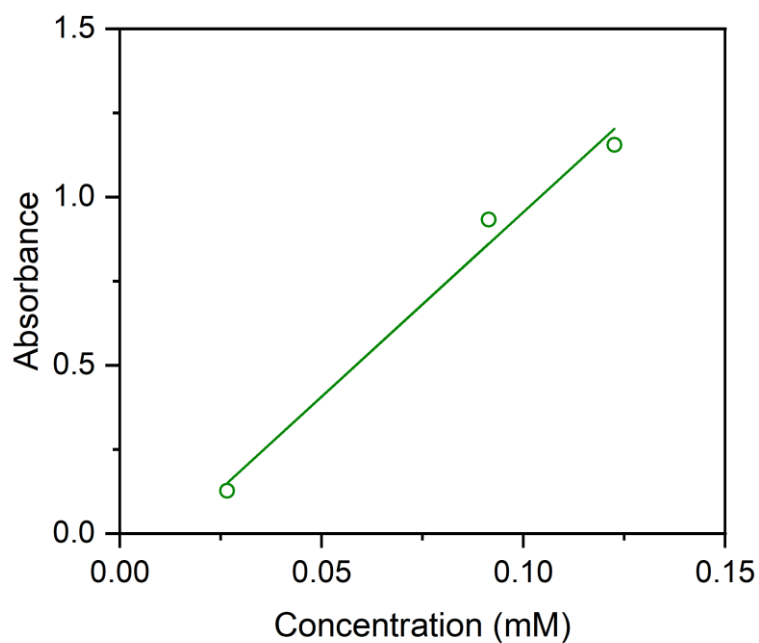
Figure S5.29. Beer's law plot of **1-Dy**. Circles correspond to absorption maxima, line corresponds to fit to: $A=\varepsilon lM+b$. $\varepsilon = 11000(1300)$ $M^{-1}\cdot cm^{-1}$, $b = -0.14$
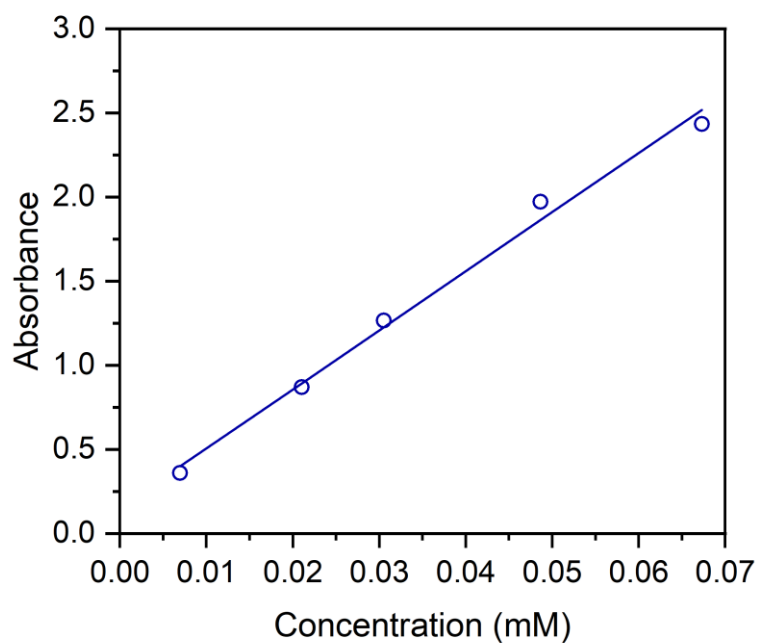
Figure S5.30. Beer's law plot of **1-Tm**. Circles correspond to absorption maxima, line corresponds to fit to: $A=\varepsilon l M+b$. $\varepsilon = 35000(1800)$ $M^{-1} \cdot cm^{-1}$, $b = 0.15$

Table S5.8. Beer's law fit summary for compounds 1-5 with parenthesized uncertainties

Compound	ε ($M^{-1} \cdot cm^{-1}$)	λ (nm)
1-Y	64500(600)	340
1-Gd	52700(600)	350
1-Tb	40400(400)	332
1-Dy	11000(1300)	331
1-Tm	35000(1800)	320
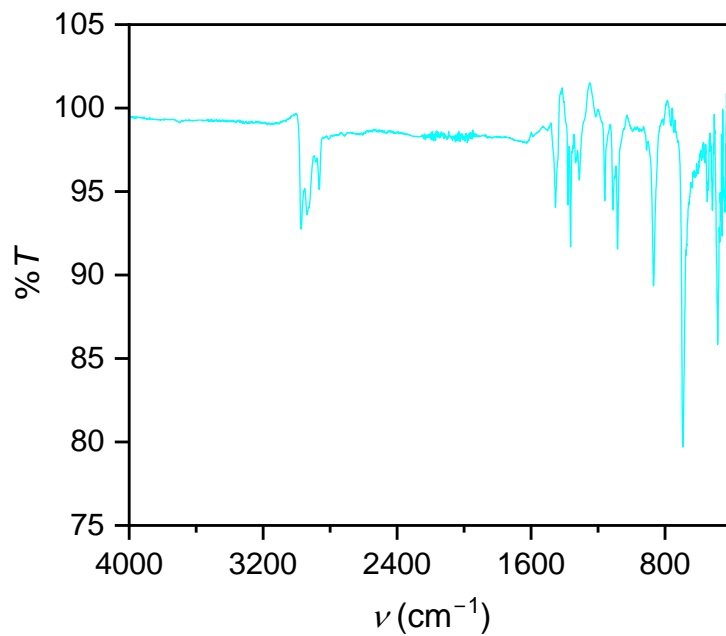
Figure S5.31. Fourier-transform infrared spectrum of **1-Y**
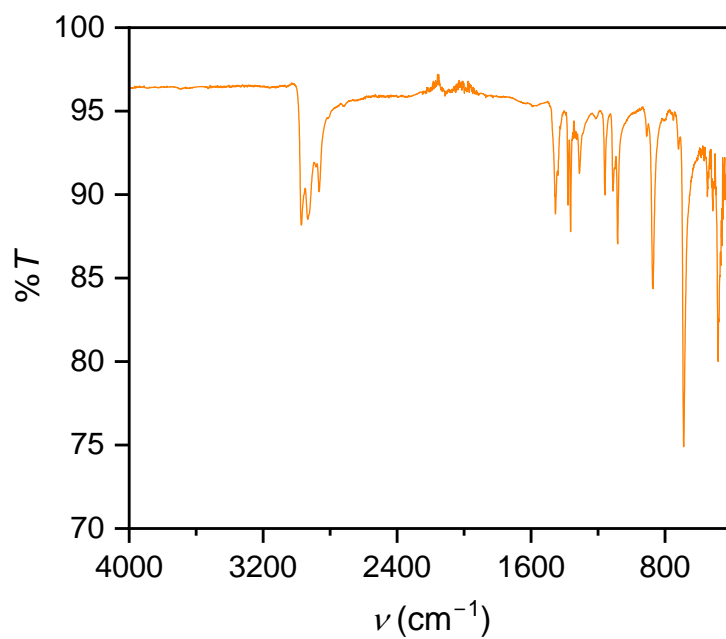
Figure S5.32. Fourier Transform Infrared Spectrum of **1-Gd**
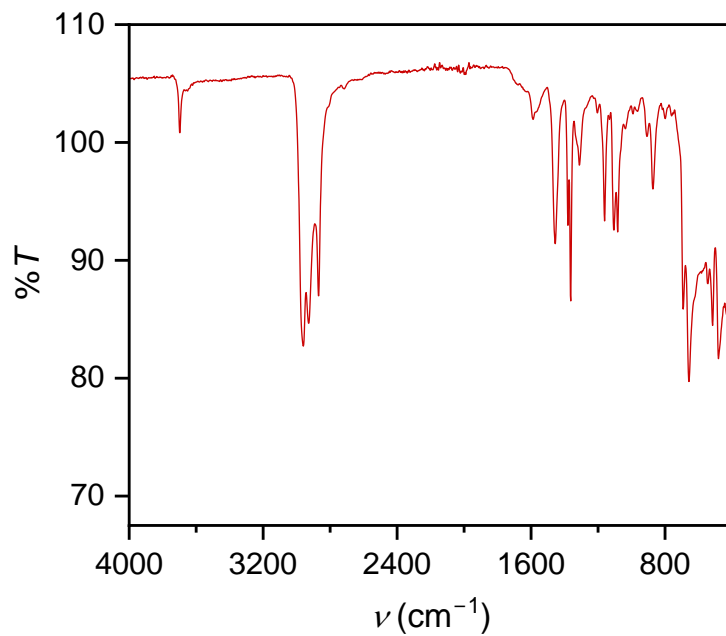
Figure S5.33 Fourier-Transform Infrared Spectrum of **1-Tb**
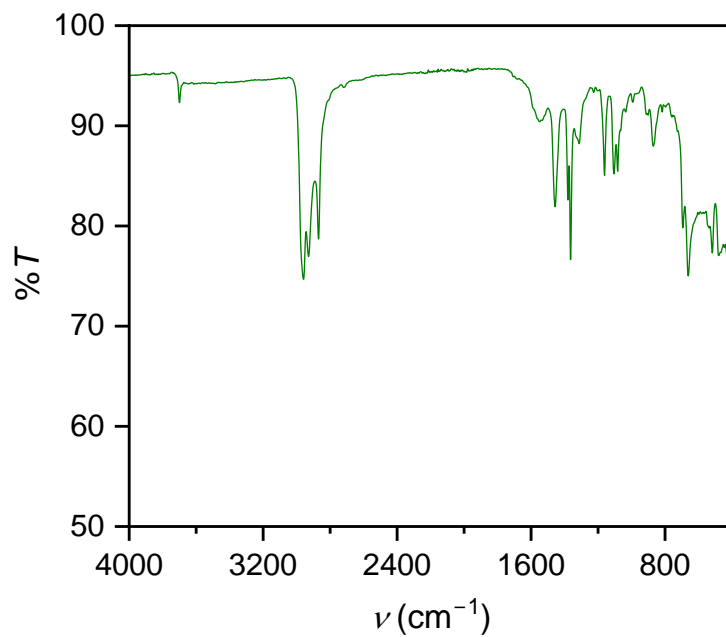
Figure S5.34 Fourier-Transform Infrared Spectrum of **1-Dy**
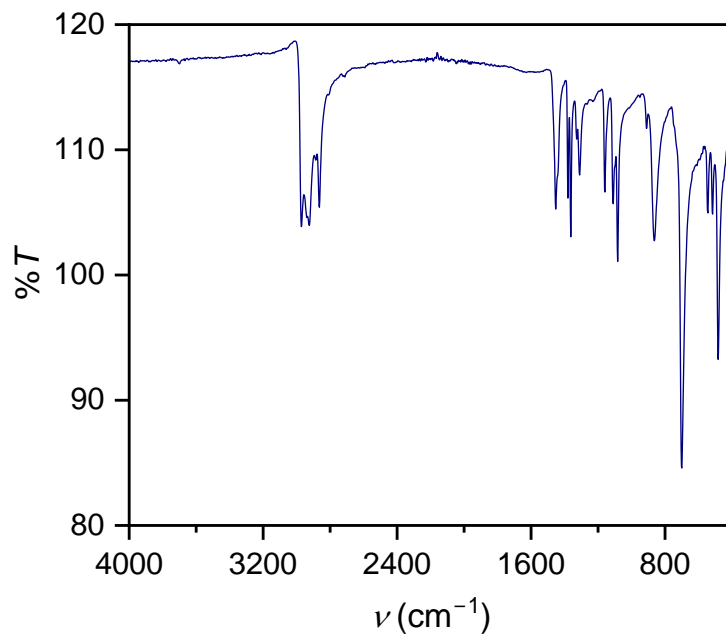
Figure S5.35. Fourier-Transform Infrared Spectrum of **1-Tm**
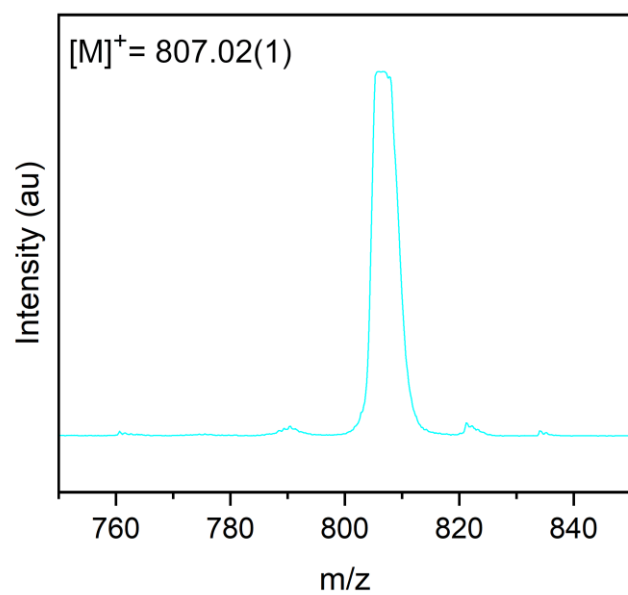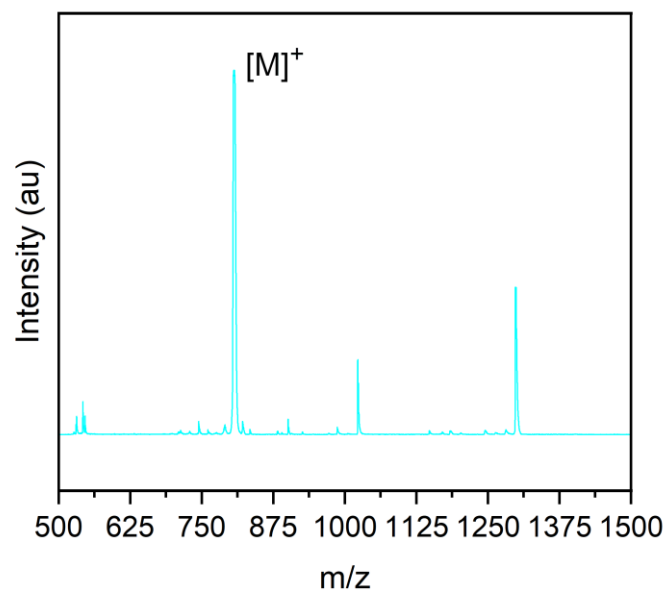
Figure S5.36. Matrix assisted laser desorption ionization mass spectrum of **1-Y**
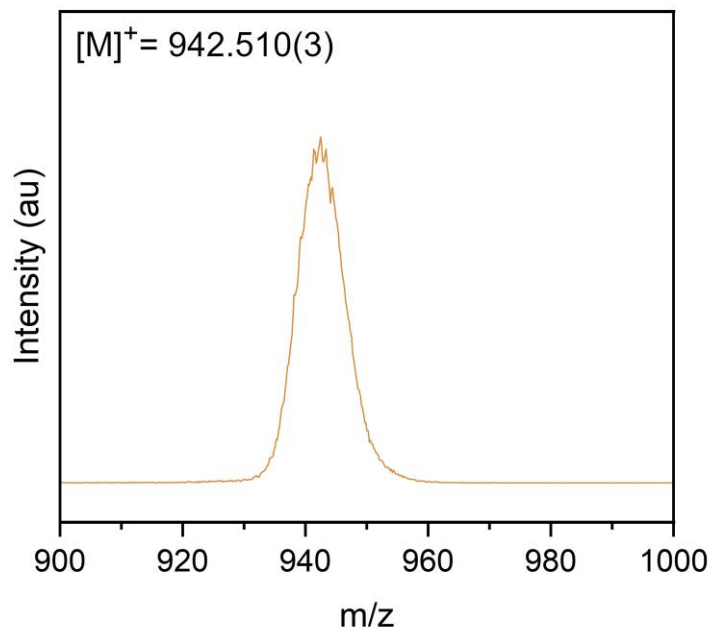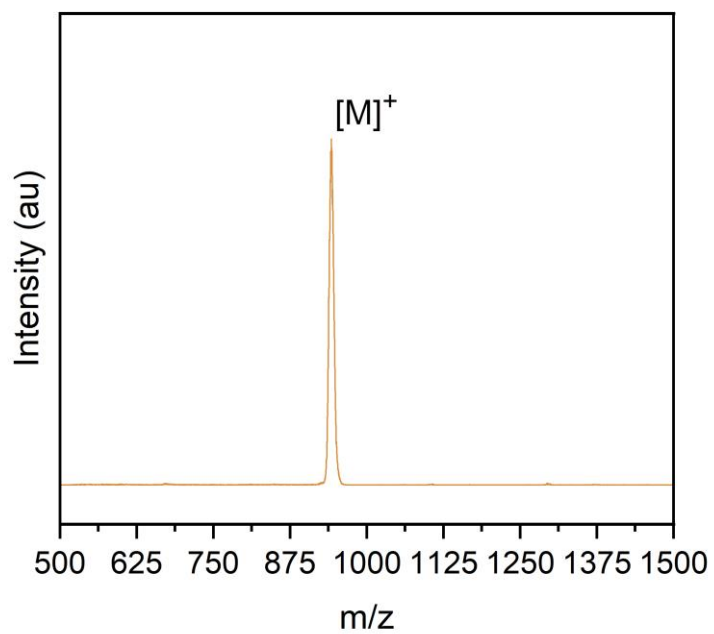
Figure S5.37. Matrix assisted laser desorption ionization mass spectrum of **1-Gd**
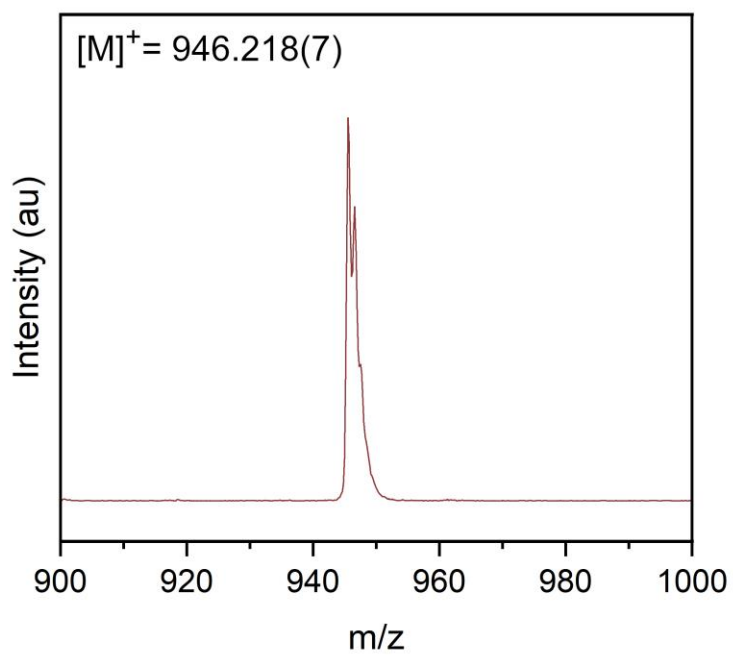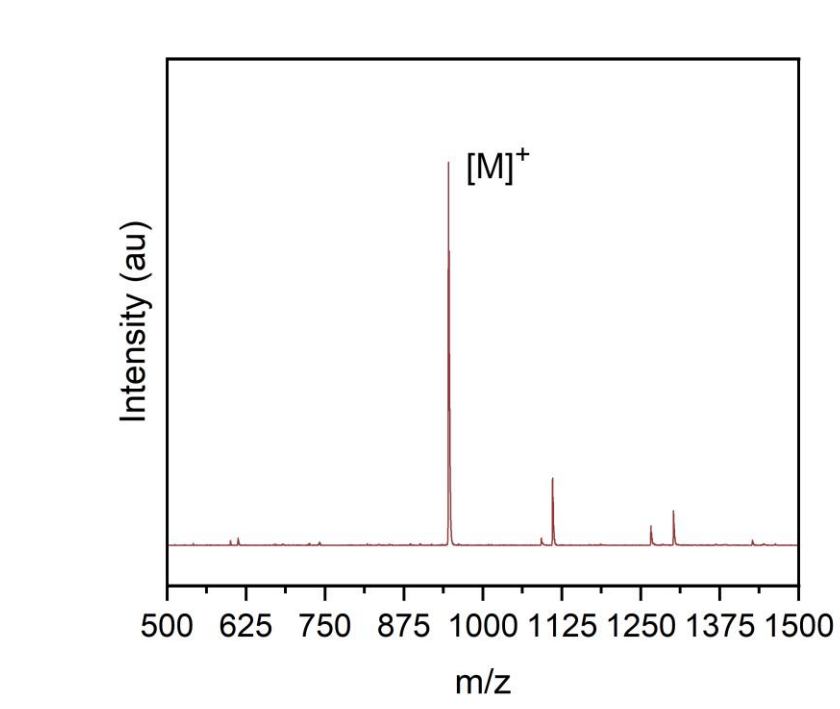
Figure S5.38 Matrix assisted laser desorption ionization mass spectrum of **1-Tb**
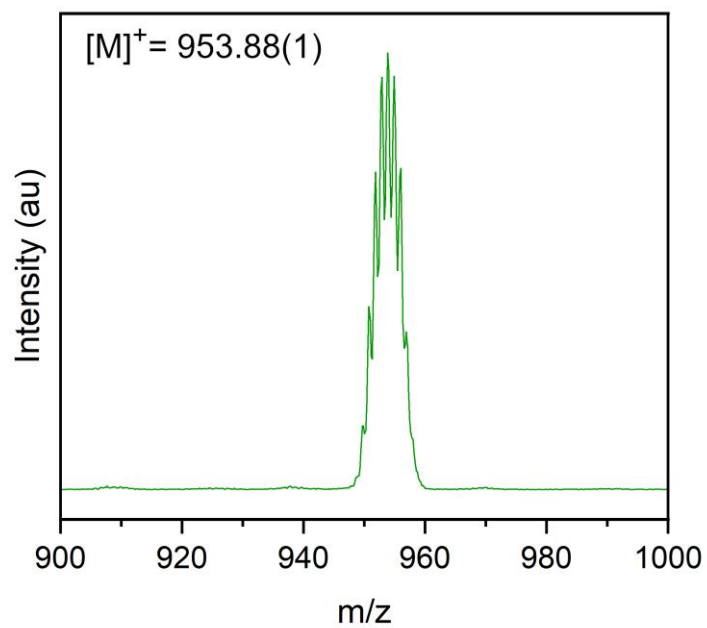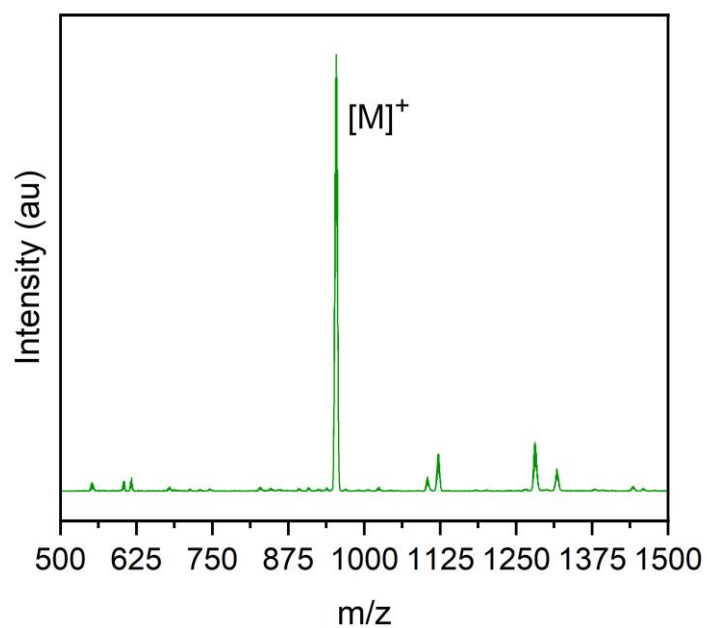
Figure S5.39 Matrix assisted laser desorption ionization mass spectrum of **1-Dy**

Table S5.9: Spin state energies for **1-Y**. Ne^- is the number of unpaired electrons defined for the complex. D_{C-C}^{avg} is the average C–C bond distance of benzene.

n_e*	Ms	ΔE (eV)	D_{C-C}^{avg} (Å)	Y–Bz(Å)	cp1–Bz–cp2	Y–cp(Å)	Bz spin	$\langle S^2 \rangle$
0 (a)	0	0	1.472	1.982	174.3	2.351	0	0
2 (b)	1	1.56	1.455	2.112	170.2	2.329	0.60	2.01
4 (c)	2	2.69	1.437	2.250	174.8	2.333	1.16	6.01
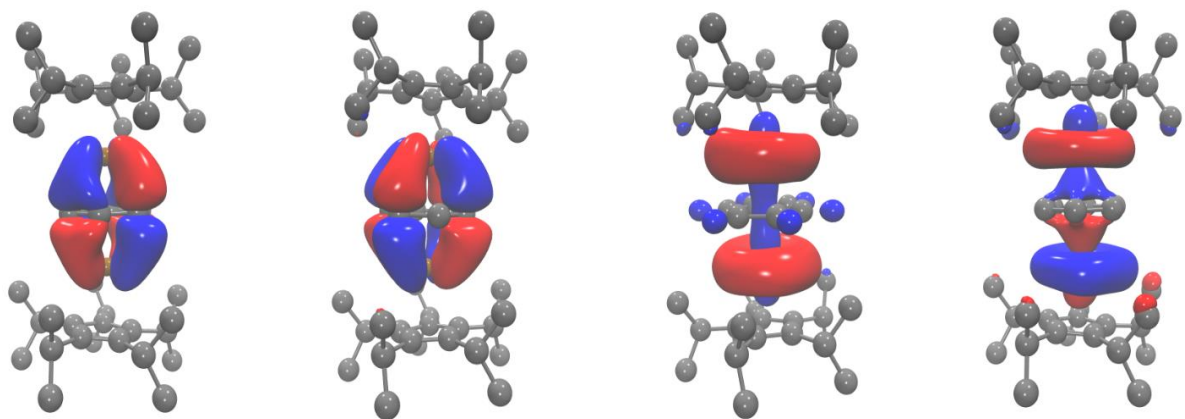
(186α) HOMO-1   (187α) HOMO   (188α) LUMO   (189α) LUMO+1

Figure S5.40: Highest occupied molecular orbitals of the 1-Y singlet ground state. Hydrogen atoms were omitted for clarity. A contour value of 0.03 was used in the orbital depictions

Table S5.10: Molecular orbital energies and Mulliken population analysis (MPA) of **1-Y** singlet complex. The % metal character identifies the overall metal contribution from both Y centers combined to the molecular orbital, the %d character identifies how much of the total orbital originates directly from the metal d orbitals. The % Bz character shows the overall contribution of the six carbons of the bridged benzene.

	Orbital	Energy (eV)	% Metal Character	% d Character	% Bz character
LUMO+6	194α, α	+0.516	0	0	0
LUMO+5	193α, α	+0.515	0	0	0
LUMO+4	192α, α	+0.264	0	0	0
LUMO+3	191α, α	−0.309	73.2	72.8	2.2
LUMO+2	190α, α	−0.318	71.6	71.2	3.1
LUMO+1	189α, α	−0.466	94.1	85.3	5.9
LUMO	188α, α	−0.762	83.2	49.4	6.5
HOMO	187α, α	−3.414	37.8	36.4	62.1
HOMO-1	186α, α	−3.415	37.6	36.1	62.0
HOMO-2	185α, α	−5.116	8.2	3.1	2.7
HOMO-3	184α, α	−5.116	8.2	3.2	2.6

Table S5.11: Selected bond distances (Å) and angles (deg) for optimized geometry of **1-Y**.[b] and [c] are dihedral angles.

	$(Cp^{iPr5} Y)_2(Bz)$		
Y(1) · · · Y(2)	3.963		
Y(1) − Cnt(Cp1)	2.352	Y(2) − Cnt(Cp2)	2.352
Y(1) − C(3)	2.644	Y(2) − C(14)	2.644
Y(1) − C(4)	2.661	Y(2) − C(15)	2.662
Y(1) − C(5)	2.634	Y(2) − C(16)	2.634
Y(1) − C(6)	2.661	Y(2) − C(17)	2.662
Y(1) − C(7)	2.644	Y(2) − C(18)	2.645
Y(1) − Cnt(Bz)	1.982	Y(2) − Cnt(Bz)	1.982
Y(1) − C(8)	2.492	Y(2) − C(8)	2.470
Y(1) − C(9)	2.477	Y(2) − C(9)	2.458
Y(1) − C(10)	2.471	Y(2) − C(10)	2.491
Y(1) − C(11)	2.454	Y(2) − C(11)	2.458
Y(1) − C(12)	2.459	Y(2) − C(12)	2.478
Y(1) − C(13)	2.458	Y(2) − C(13)	2.454
Y(1) − (Cnt)(Bz) − Y(2)	178.5	C(8) − C(9)	1.468
Cnt(Cp1) − Y(1) − Cnt(Bz)	174.8	C(8) − C(10)	1.470
Cnt(Cp2) − Y(2) − Cnt(Bz)	174.6	C(10) − C(12)	1.470
Cnt(Cp1) − Cnt(Bz) − Cnt(Cp2)	174.3	C(12) − C(13)	1.474
C(8)–C(9)-C(11)-C(13)[b]	−0.8	C(13) − C(11)	1.476
C(8)-C(10)-C(12)-C(13)[c]	−0.6	C(11) − C(9)	1.474

Table S5.12: Electronic excitation summary for **1-Y**. All excitations computed are single excitations involving alpha spin to alpha spin transitions. Oscillator strengths are reported in the length gauge. Only the dominant contributions to the overall excitation are reported.

Wavelength (nm)	Oscillator Strength	Dominant contributions	
		Occupied Virtual	% weight
571	0.00008	$187\alpha188\alpha$	98.7
571	0.00008	$186\alpha188\alpha$	98.7
508	0.0004	$186\alpha189\alpha$	92.4
507	0.0004	$187\alpha189\alpha$	91.9
499	0.00006	$186\alpha190\alpha$	49.4
		$187\alpha191\alpha$	49.4
485	0.00006	$186\alpha191\alpha$	57.6
		$187\alpha190\alpha$	40.3
374	0.0001	$187\alpha192\alpha$	99.3
374	0.0001	$186\alpha192\alpha$	99.3
345	0.0002	$187\alpha193\alpha$	28.7
		$186\alpha193\alpha$	24.4
345	1.0	$187\alpha191\alpha$	43.0
		$186\alpha190\alpha$	42.4
344	0.03	$187\alpha193\alpha$	52.9
		$187\alpha194\alpha$	42.4
344	0.0007	$186\alpha193\alpha$	39.4
		$187\alpha194\alpha$	27.4
343	0.01	$186\alpha194\alpha$	61.6
		$186\alpha193\alpha$	35.7
322	0.0008	$186\alpha195\alpha$	75.9
		$187\alpha196\alpha$	23.4
319	0.0004	$187\alpha195\alpha$	53.4
		$186\alpha196\alpha$	45.1
312	0.00001	$185\alpha188\alpha$	89.3
309	0.01	$182\alpha188\alpha$	80.7
309	0.01	$183\alpha188\alpha$	81.0

Table S5.13: Spin state energies for **1-Gd**. Ne^- is the number of unpaired electrons defined for the complex. D_{C-C}^{avg} is the average C–C bond distance of benzene.

n_e*	Ms	ΔE (eV)	D_{C-C}^{avg} (Å)	Gd–Bz (Å)	cp1–Bz–cp2	Gd–cp(Å)	Bz spin	$<S^2>$
18 (a)	9	0	1.434	2.379	169.3	2.413	1.09	90.07
0 (b)	0	0.26	1.435	2.380	165.0	2.419	0	9.03
16 (c)	8	0.30	1.437	2.353	170.3	2.415	0.05	73.00
16 (d)	8	0.47	1.436	2.377	166.5	2.417	1.10	73.05
14 (e)	7	0.54	1.439	2.350	162.7	2.424	−1.31	58.0
14 (f)	7	0.60	1.436	2.370	165.6	2.419	−0.25	58.01
0 (g)	0	0.82	1.454	2.225	176.3	2.418	0	8.18
0 (h)	0	_**	1.468	2.019	175.5	2.395	-0.14	7.09

(240β) HOMO   **(240α) HOMO-1**   **(239β) HOMO-2**   **(239α) HOMO-3**

(241α) LUMO   **(241β) LUMO+1**   **(242β) LUMO+2**   **(242α) LUMO+3**

Figure S5.41: Highest occupied molecular orbitals of the **1-Gd** singlet ground state. Hydrogen atoms were omitted for clarity. A contour value of 0.03 was used in the orbital depictions

Figure S5.42: Calculated UV-Vis spectral comparison for **1-Gd**. Experimental (connected blue dots) and simulated (solid lines) spectra of all **1-Gd** calculated states with various number of unpaired electrons. A Gaussian spectral lineshape with the width of 0.2 eV was used.

Table S5.14: Selected bond distances (Å) and angles (deg) for 1-Gd(g).[b] and [c] are dihedral angles.

	(Cp^{iPr5}Gd)$_2$(Bz)		
Gd(1) · · · Gd(2)	4.038		
Gd(1) − Cnt(Cp1)	2.019	Gd(2) − Cnt(Cp2)	2.019
Gd(1) − C(3)	2.669	Gd(2) − C(14)	2.673
Gd(1) − C(4)	2.691	Gd(2) − C(15)	2.697
Gd(1) − C(5)	2.706	Gd(2) − C(16)	2.706
Gd(1) − C(6)	2.694	Gd(2) − C(17)	2.687
Gd(1) − C(7)	2.670	Gd(2) − C(18)	2.668
Gd(1) − Cnt(Bz)	2.225	Gd(2) − Cnt(Bz)	2.224
Gd(1) − C(8)	2.488	Gd(2) − C(8)	2.514
Gd(1) − C(9)	2.487	Gd(2) − C(9)	2.495
Gd(1) − C(10)	2.498	Gd(2) − C(10)	2.487
Gd(1) − C(11)	2.515	Gd(2) − C(11)	2.487
Gd(1) − C(12)	2.503	Gd(2) − C(12)	2.486
Gd(1) − C(13)	2.485	Gd(2) − C(13)	2.507
Gd(1) − (Cnt)(Bz) − Gd(2)	178.8	C(8) − C(9)	1.466
Cnt(Cp1) − Gd(1) − Cnt(Bz)	174.1	C(8) − C(10)	1.469
Cnt(Cp2) − Gd(2) − Cnt(Bz)	174.2	C(10) − C(12)	1.472
Cnt(Cp1) − Cnt(Bz) − Cnt(Cp2)	175.5	C(12) − C(13)	1.470
C(8)-C(9)-C(11)-C(13)[b]	−0.8	C(13) − C(11)	1.466
C(8)-C(10)-C(12)-C(13)[c]	−0.6	C(11) − C(9)	1.464

Table S5.15: Molecular orbital energies and Mulliken population analysis (MPA) of 1-Gd singlet complex. The % metal character identifies the overall metal contribution from both Gd centers combined to the molecular orbital, the %d character identifies how much of the total orbital originates directly from the metal d orbitals. The % Bz character shows the overall contribution of the six carbons of the bridged benzene.

	Orbital	Energy (eV)	% Metal Character	% d Character	% Bz character
LUMO+11	246β, α	−0.261	79.8	66.0	3.2
LUMO+9	245β, α	−0.268	76.2	66.6	4.3
LUMO+3	242α, α	−0.353	88	7	0
LUMO+2	242β, α	−0.356	89	7	0
LUMO+1	241β, α	−0.896	100	66.9	0
LUMO	241α, α	−0.897	100	70	0
HOMO	240β, α	−3.457	39.2	35.1	60.8
HOMO-1	240α, α	−3.457	39.3	35.2	60.7
HOMO-2	239β, α	−3.467	39.6	35.7	60.4
HOMO-3	239α, α	−3.467	39.6	35.7	60.4

Table S5.16. Spin state energies for **1-Tb**. Ne^- is the number of unpaired electrons defined for the complex. $D_{\text{C-C}}^{\text{avg}}$ is the average C–C bond distance of benzene.

n_e*	Ms	ΔE (eV)	$D_{\text{C-C}}^{\text{avg}}$ (Å)	Tb–Bz(Å)	cp1–Bz–cp2	Tb–cp(Å)	Bz spin	$\langle S^2 \rangle$
16 (a)	8	0	1.454	2.062	174.8	2.371	-0.22	72.11
14 (b)	7	0.03	1.461	2.038	172.5	2.376	-0.26	56.85
0 (c)	0	0.10	1.465	2.019	171.0	2.379	0	7.60
0 (d)	0	-**	1.469	1.993	170.9	2.381	-0.14	6.05
12 (e)	6	1.07	1.449	2.184	175.8	2.394	−0.78	43.87
10 (f)	5	1.27	1.454	2.153	177.3	2.395	−0.84	32.86
10 (g)	5	4.49	1.441	2.339	172.0	2.404	−1.20	33.00

(241β) HOMO (241α) HOMO-1 (240α) HOMO-2 (240β) HOMO-3

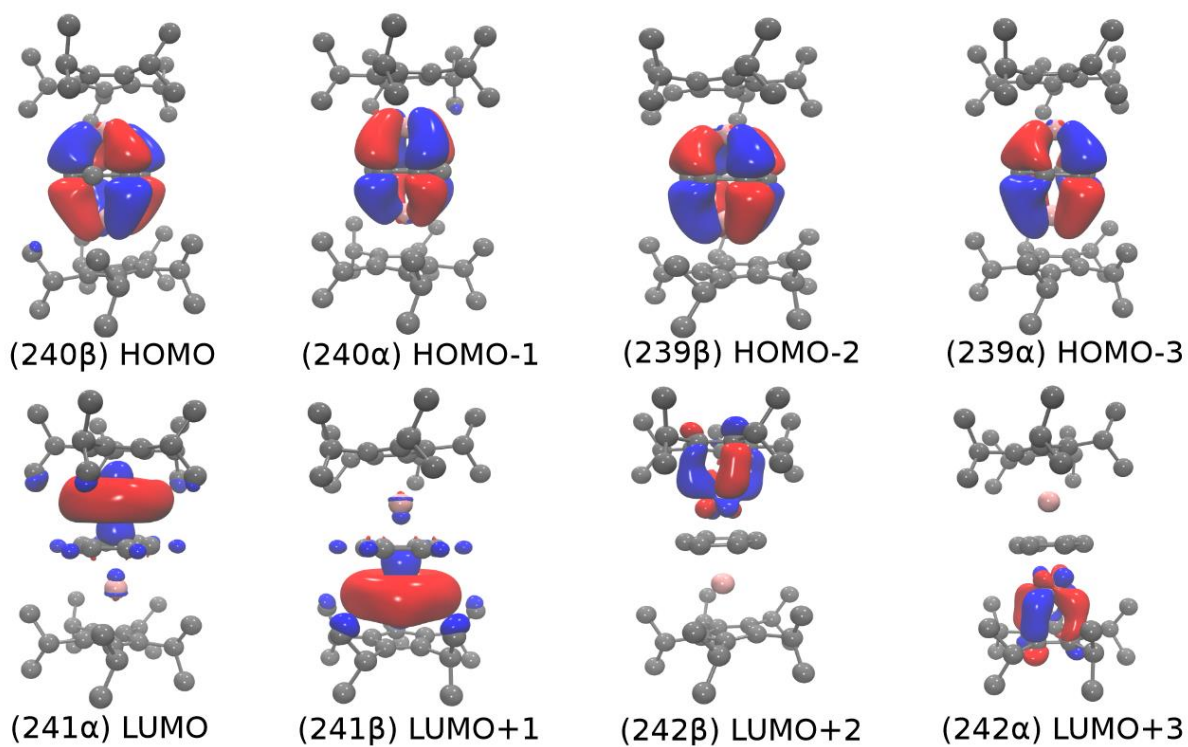(242β) LUMO (242α) LUMO+1 (243α) LUMO+2 (243β) LUMO+3
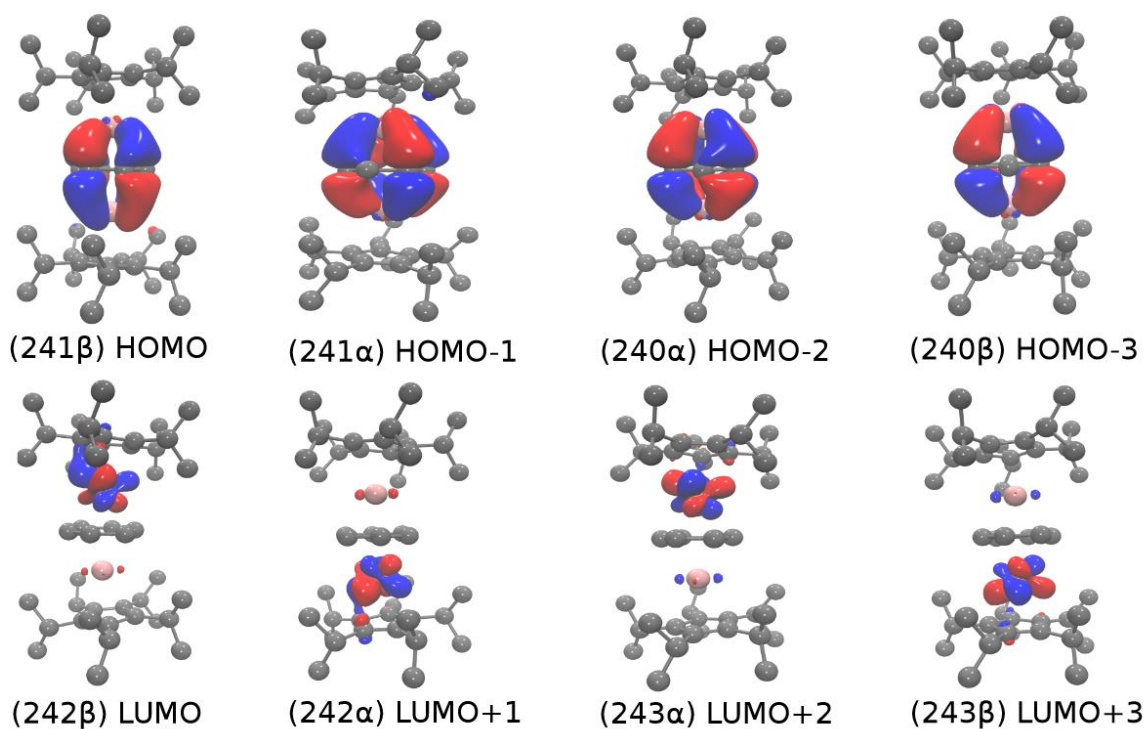
Figure S5.43: Highest occupied molecular orbitals of the **1-Tb** singlet ground state. Hydrogen atoms were omitted for clarity. A contour value of 0.03 was used in the orbital depictions
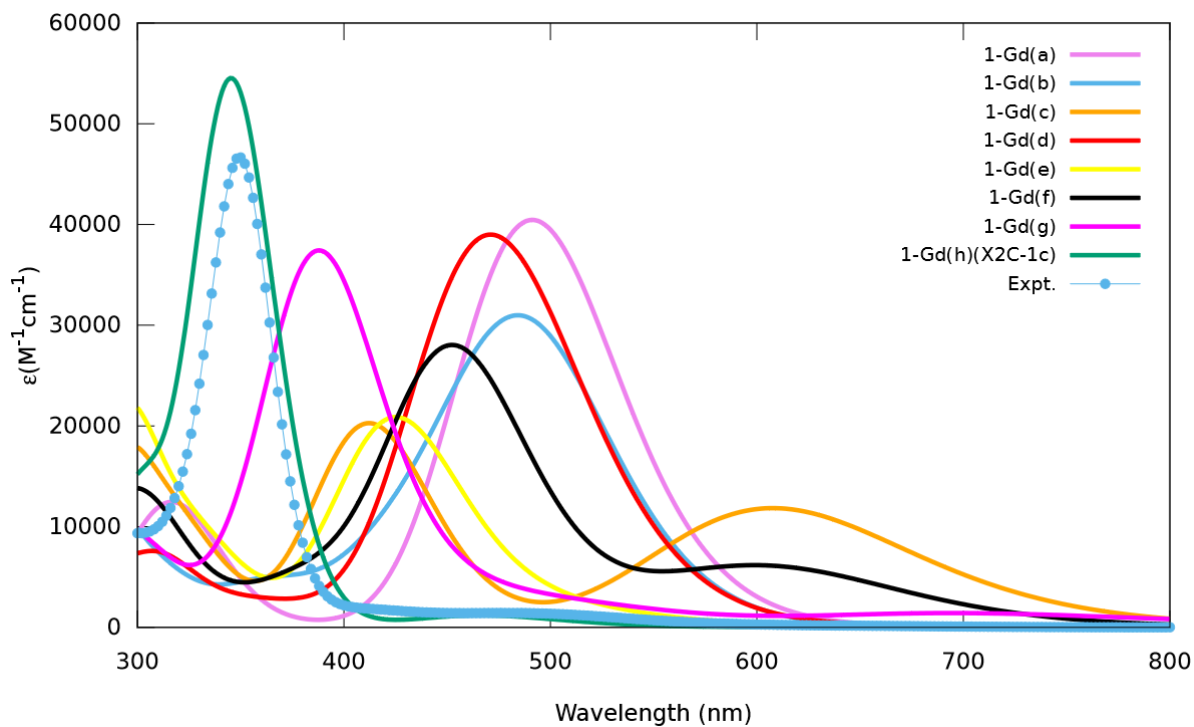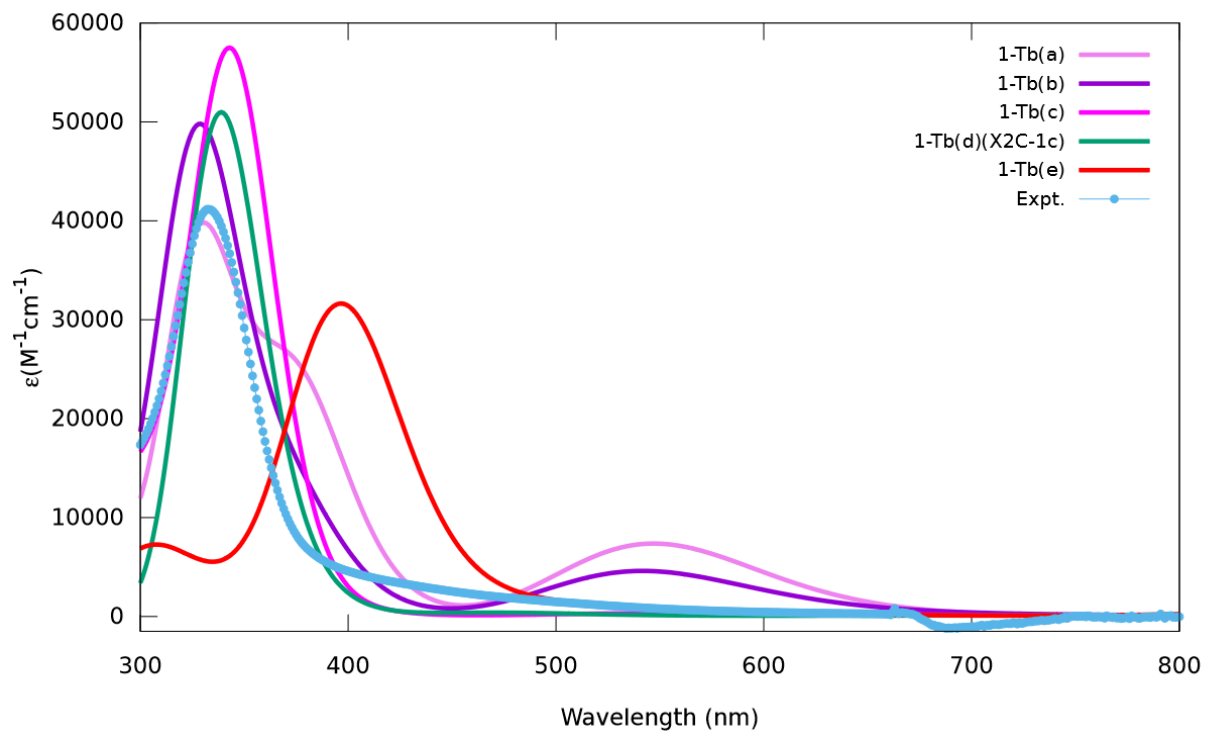
Figure S5.44: Calculated UV-Vis spectral comparison for **1-Tb**. Experimental (connected blue dots) and simulated (solid lines) spectra of all **1-Tb** calculated states with various number of unpaired electrons. A Gaussian spectral lineshape with the width of 0.2 eV was used.

Table S5.17. Electronic excitation summary for **1-Tb**. All excitations computed are single excitations involving alpha spin to alpha spin transitions. Oscillator strengths are reported in the length gauge. Only the dominant contributions to the overall excitation are reported.

Wavelength (nm)	Oscillator Strength	Dominant contributions		
		Occupied	Virtual	% weight
727	0.0006	240α	244α	51.6
		240β	244β	40.5
614	0.0002	241β	245β	35.8
		241α	245α	32.9
506	0.0006	241α	246α	70.1
		241β	246β	22.4
477	0.0009	240β	248β	34.3
		240β	249β	16.2
452	0.0009	241α	249α	36.9
		241β	248β	23.2
371	0.02	235β	242β	40.2
		237β	242β	35.9
339	0.7	241α	251α	12.7
		241β	251β	11.7
		240α	248α	11.5
		240β	250β	5.6
331	0.002	240β	253β	45.2
		241α	254α	43.6

Table S5.18: Selected bond distances (Å) and angles (deg) for **1-Tb**. [b] and [c] are dihedral angles.

	$(Cp^{iPr_5} Tb)_2(Bz)$		
Tb(1) · · · Tb(2)	3.986		
Tb(1) − Cnt(Cp1)	2.381	Tb(2) − Cnt(Cp2)	2.281
Tb(1) − C(3)	2.679	Tb(2) − C(14)	2.672
Tb(1) − C(4)	2.694	Tb(2) − C(15)	2.656
Tb(1) − C(5)	2.682	Tb(2) − C(16)	2.665
Tb(1) − C(6)	2.660	Tb(2) − C(17)	2.688
Tb(1) − C(7)	2.657	Tb(2) − C(18)	2.693
Tb(1) − Cnt(Bz)	1.993	Tb(2) − Cnt(Bz)	1.993
Tb(1) − C(8)	2.477	Tb(2) − C(8)	2.500
Tb(1) − C(9)	2.507	Tb(2) − C(9)	2.483
Tb(1) − C(10)	2.471	Tb(2) − C(10)	2.494
Tb(1) − C(11)	2.477	Tb(2) − C(11)	2.450
Tb(1) − C(12)	2.442	Tb(2) − C(12)	2.469
Tb(1) − C(13)	2.481	Tb(2) − C(13)	2.456
Tb(1) − (Cnt)(Bz) − Tb(2)	177.9	C(8) − C(9)	1.464
Cnt(Cp1) − Tb(1) − Cnt(Bz)	173.7	C(8) − C(10)	1.464
Cnt(Cp2) − Tb(2) − Cnt(Bz)	173.4	C(10) − C(12)	1.467
Cnt(Cp1) − Cnt(Bz) − Cnt(Cp2)	170.9	C(12) − C(13)	1.473
C(8)-C(9)-C(11)-C(13)[b]	4.2	C(13) − C(11)	1.474
C(8)-C(10)-C(12)-C(13)[c]	-4.1	C(11) − C(9)	1.469

Table S5.19: Molecular orbital energies and Mulliken population analysis (MPA) of **1-Tb** singlet complex. The % metal character identifies the overall metal contribution from both Tb centers combined to the molecular orbital, the %d character identifies how much of the total orbital originates directly from the metal d orbitals. The % Bz character shows the overall contribution of the six carbons of the bridged benzene.

	Orbital	Energy (eV)	% Metal Character	% d Character	% Bz character
LUMO+19	251α, α	−0.125	80.0	54.9	1.4
LUMO+17	250β, α	−0.163	90.0	40.9	0
LUMO+13	248α, α	−0.211	82.8	64.0	2.7
LUMO+3	243β, α	−1.120	100	5.6	0
LUMO+2	243α, α	−1.127	98.9	5.6	0
LUMO+1	242α, α	−1.133	97.6	5.4	0
LUMO	242β, α	−1.139	97.6	5.4	0
HOMO	241β, α	−3.486	38.7	32.0	61.3
HOMO-1	241α, α	−3.489	39.3	32.3	60.7
HOMO-2	240α, α	−3.499	39.0	32.7	61.0
HOMO-3	240β, α	−3.503	39.6	33.1	60.4

Table S5.20: Spin state energies for **1-Dy**. Ne^- is the number of unpaired electrons defined for the complex. $D_{C\text{-}C}{}^{avg}$ is the average C–C bond distance of benzene. $D_{Gd\text{-}Bz}$ is the metal benzene centroid distance

n_e	Ms	ΔE (eV)	C–C^d (Å)	Dy–Bz (Å)	cp1–Bz–cp2	Dy–cp (Å)	Bz spin	$\langle S^2 \rangle$
12 (a)	6	0	1.453	2.140	196.9	2.386	0.45	42.78
12 (b)	6	0.03	1.441	2.272	178.3	2.393	-0.16	43.02
0 (c)	0	0.07	1.469	2.017	164.8	2.374	0	6.32
0 (d)	0	-**	1.467	1.982	172.8	2.368	-0.09	5.00
10 (e)	5	0.15	1.442	2.258	174.7	2.396	−0.40	32.00
8 (f)	4	0.27	1.440	2.318	173.1	2.388	−1.40	23.00
0 (g)	0	0.30	1.451	2.184	171.0	2.384	−0.67	6.73
14 (h)	7	1.28	1.436	2.269	167.9	2.382	1.00	56.60

(242α) HOMO   (242β) HOMO-1   (241β) HOMO-2   (241α) HOMO-3

(243β) LUMO   (243α) LUMO+1   (244α) LUMO+2   (244β) LUMO+3
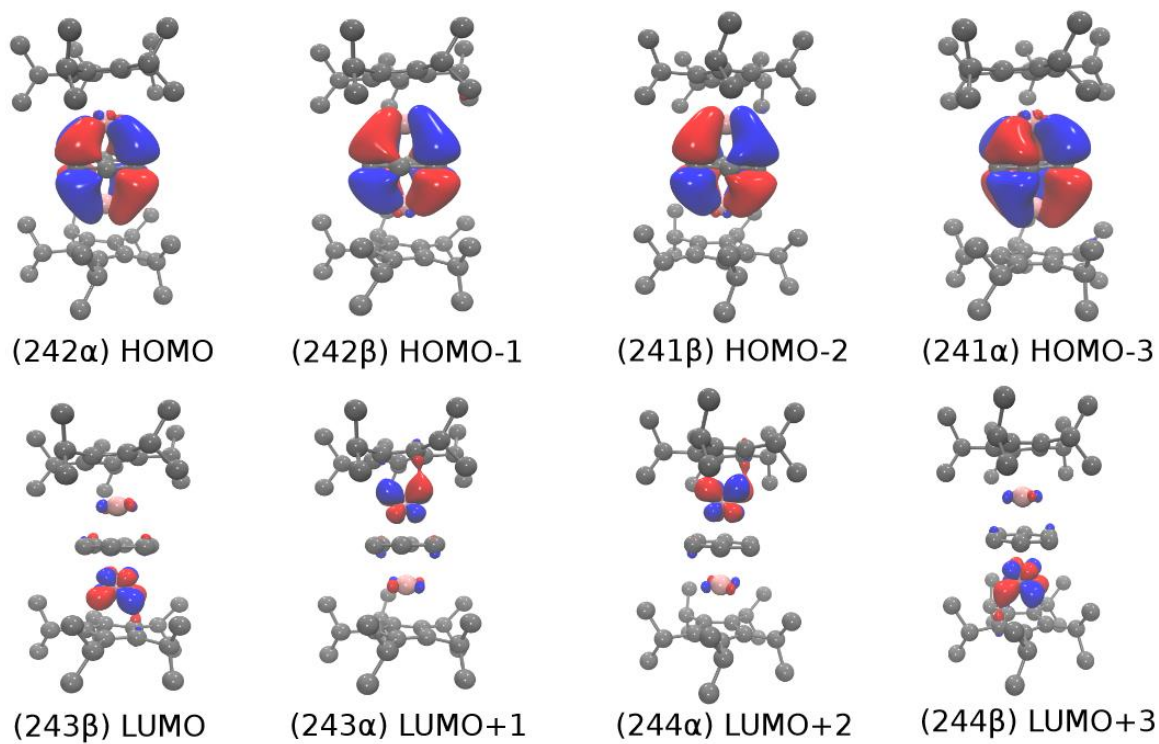
Figure S5.45: Highest occupied molecular orbitals of the **1-Dy** singlet ground state. Hydrogen atoms were omitted for clarity. A contour value of 0.03 was used in the orbital depictions
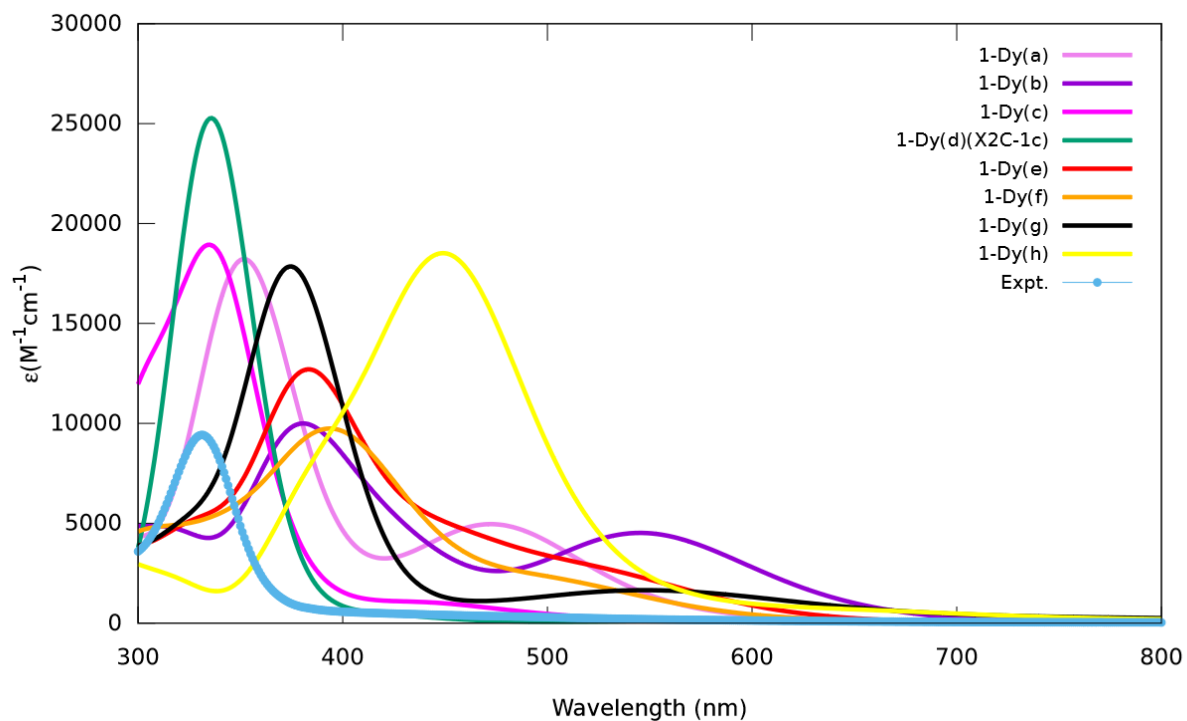
Figure S5.46: Calculated UV-Vis spectral comparison for **1-Dy**. Experimental (connected blue dots) and simulated (solid lines) spectra of all **1-Dy** calculated states with various number of unpaired electrons. A Gaussian spectral lineshape with the width of 0.2 eV was used.

Table S5.21: Molecular orbital energies and Mulliken population analysis (MPA) of **1-Dy** singlet complex. The % metal character identifies the overall metal contribution from both Dy centers combined to the molecular orbital, the %d character identifies how much of the total orbital originates directly from the metal d orbitals. The % Bz character shows the overall contribution of the six carbons of the bridged benzene.

	Orbital	Energy (eV)	% Metal Character	% d Character	% Bz character
LUMO+15	250β, α	−0.035	69.8	67.0	0
LUMO+14	250α, α	−0.035	70.8	68.0	0
LUMO+13	249α, α	−0.076	70.1	69.0	0
LUMO+12	249β, α	−0.076	70.2	70.3	0
LUMO+3	244β, α	−1.497	98.8	7.0	0
LUMO+2	244α, α	−1.498	98.7	7.0	0
LUMO+1	243α, α	−1.510	98.8	7.2	0
LUMO	243β, α	−1.512	98.7	7.2	0
HOMO	242α, α	−3.459	40.2	29.3	59.8
HOMO-1	242β, α	−3.459	39.6	28.8	58.5
HOMO-2	241β, α	−3.466	39.4	29.2	60.6
HOMO-3	241α, α	−3.466	39.5	29.1	60.5

Table S5.22: Selected bond distances (Å) and Angles (deg) for **1-Dy** [b] and [c] are dihedral angles.

	$(Cp^{iPr_5} Dy)_2(Bz)$		
Dy(1) $\cdots$ Dy(2)	3.963		
Dy(1) − Cnt(Cp1)	2.368	Dy(2) − Cnt(Cp2)	2.368
Dy(1) − C(3)	2.646	Dy(2) − C(14)	2.679
Dy(1) − C(4)	2.656	Dy(2) − C(15)	2.673
Dy(1) − C(5)	2.676	Dy(2) − C(16)	2.654
Dy(1) − C(6)	2.678	Dy(2) − C(17)	2.648
Dy(1) − C(7)	2.660	Dy(2) − C(18)	2.663
Dy(1) − Cnt(Bz)	1.982	Dy(2) − Cnt(Bz)	1.982
Dy(1) − C(8)	2.479	Dy(2) − C(8)	2.483
Dy(1) − C(9)	2.464	Dy(2) − C(9)	2.473
Dy(1) − C(10)	2.463	Dy(2) − C(10)	2.474
Dy(1) − C(11)	2.455	Dy(2) − C(11)	2.451
Dy(1) − C(12)	2.465	Dy(2) − C(12)	2.461
Dy(1) − C(13)	2.448	Dy(2) − C(13)	2.452
Dy(1) − (Cnt)(Bz) − Dy(2)	178.2	C(8) − C(9)	1.464
Cnt(Cp1) − Dy(1) − Cnt(Bz)	174.4	C(8) − C(10)	1.463
Cnt(Cp2) − Dy(2) − Cnt(Bz)	174.6	C(10) − C(12)	1.466
Cnt(Cp1) − Cnt(Bz) − Cnt(Cp2)	172.8	C(12) − C(13)	1.470
C(8)-C(9)-C(11)-C(13)[b]	−0.8	C(13) − C(11)	1.472
C(8)-C(10)-C(12)-C(13)[c]	−0.3	C(11) − C(9)	1.468

Table S5.23: Electronic excitation summary for **1-Dy**. All excitations computed are single excitations involving alpha spin to alpha spin transitions. Oscillator strengths are reported in the length gauge. Only the dominant contributions to the overall excitation are reported.

Wavelength (nm)	Oscillator Strength	Dominant contributions		
		Occupied	Virtual	% weight
670	0.005	241β	244β	23.1
		241α	244α	22.7
		242β	243β	22.1
555	0.001	242α	246α	27.5
		241α	247α	17.7
		241β	246β	15.0
439	0.0008	241α	249α	22.5
		241β	249β	22.5
		242α	250α	18.3
409	0.007	236α	244α	19.1
		236β	244β	12.0
		238α	244α	10.4
		239α	243α	8.6
372	0.001	237α	244α	26.5
		237β	244β	17.3
		239α	244α	15.7
338	0.7	242α	250α	17.5
		242β	250β	17.5
		241β	249β	16.5
		241α	249α	16.5

Table S5.24: Spin state energies for **1-Tm**. Ne^- is the number of unpaired electrons defined for the complex. D_{C-C}^{avg} is the average C–C bond distance of benzene. D_{Gd-Bz} is the metal benzene centroid distance

n_e	Ms	ΔE (eV)	C–C^d (Å)	Tm1–Bz (Å)	Tm2–Bz (Å)	cp1–Bz–cp2	Tm–Cp (Å)	Bz spin	$\langle S^2 \rangle$
4 (a)	2	0	1.464	1.998	1.997	168.8	2.326	0.37	6.01
2 (b)	1	0.37	1.457	2.066	2.068	170.1	2.327	-0.46	3.02
0 (c)	0	0.74	1.450	2.123	2.124	169.9	2.324	-1.1	2.02
0 (d)	0	_**	1.467	1.982	1.982	172.8	2.368	-0.09	5.00

(247α) HOMO   (246α) HOMO-1   (243β) HOMO-2   (242β) HOMO-3

(244β) LUMO   (245β) LUMO+1   (246β) LUMO+2   (247β) LUMO+3
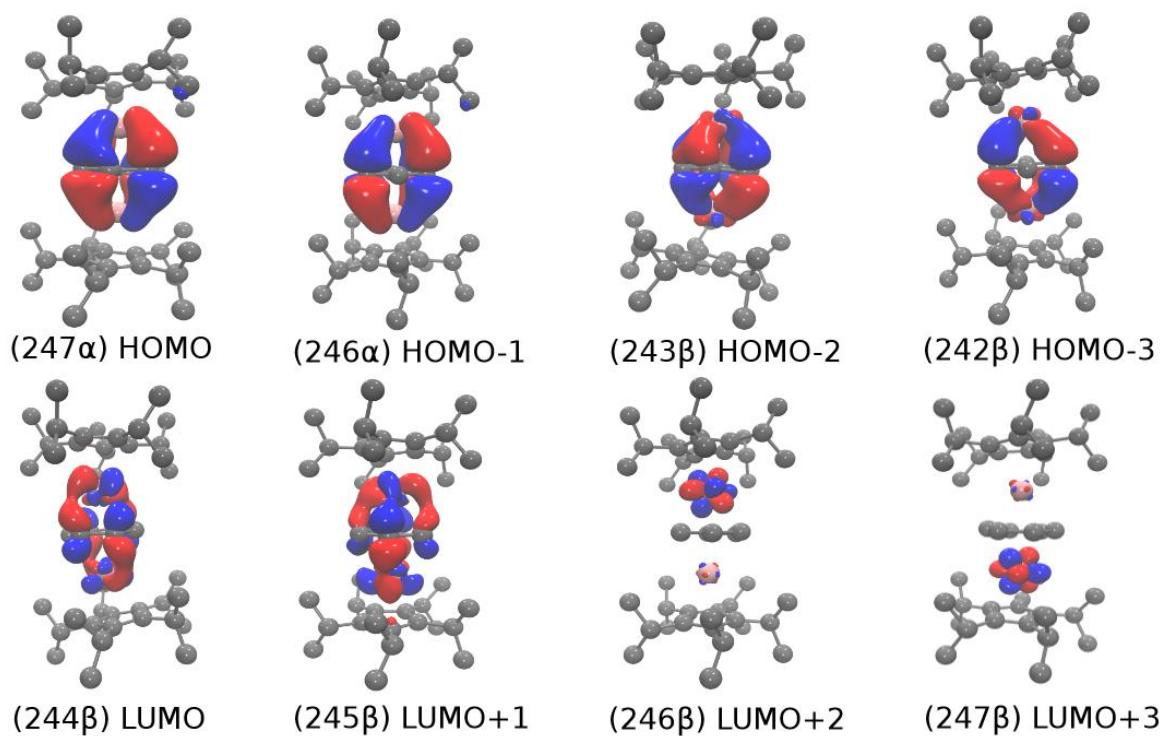
Figure S5.47: Highest occupied molecular orbitals of the **1-Tm** singlet ground state. Hydrogen atoms were omitted for clarity. A contour value of 0.03 was used in the orbital depictions

Figure S5.48: Calculated UV-Vis spectral comparison for **1-Dy**. Experimental (connected blue dots) and simulated (solid lines) spectra of all **1-Dy** calculated states with various numbers of unpaired electrons. A Gaussian spectral lineshape with the width of 0.2 eV was used.

Table S5.25: Molecular orbital energies and Mulliken population analysis (MPA) of **1-Tm** quintet complex. The % metal character identifies the overall metal contribution from both Tm centers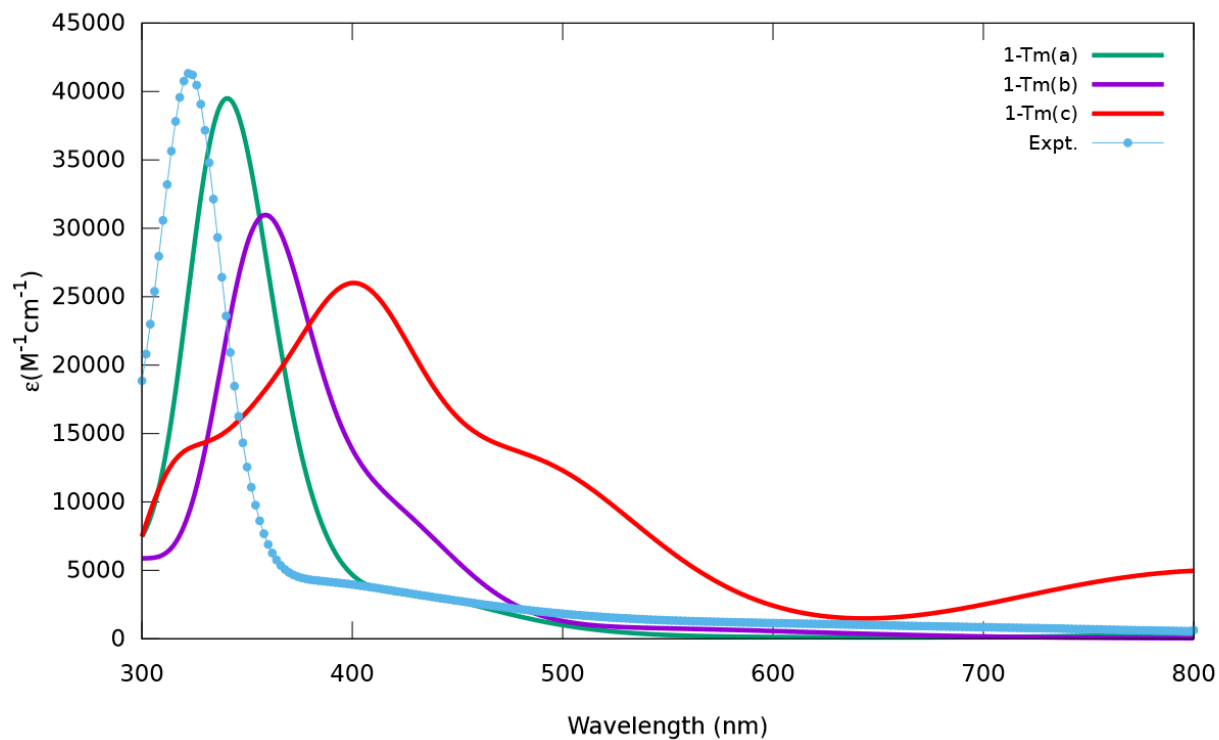 combined to the molecular orbital, the %d character identifies how much of the total orbital originates directly from the metal d orbitals. The % Bz character shows the overall contribution of the six carbons of the bridged benzene.

	Orbital	Energy (eV)	% Metal Character	% d Character	% Bz character
LUMO+13	252β, α	+0.288	61.6	60.3	0
LUMO+12	251β, α	+0.254	91.8	68.0	0
LUMO+10	250β, α	+0.209	64.5	60.9	35.5
LUMO+9	251α, α	+0.105	65.1	64.1	0
LUMO+8	250α, α	+0.029	67.8	66.4	0
LUMO+6	249α, α	−0.216	95.2	90.3	0
LUMO+5	248β, α	−0.473	100	42.8	0
LUMO+3	247β, α	−1.133	100	00.0	0
LUMO+2	246β, α	−1.158	100	00.3	0
LUMO+1	245β, α	−1.986	73.9	16.3	25.0
LUMO	244β, α	−2.051	76.9	15.0	23.1
HOMO	247α, α	−3.321	31.7	29.3	68.3
HOMO-1	246α, α	−3.348	32.3	29.9	67.7
HOMO-2	243β, α	−3.402	57.8	15.4	42.2
HOMO-3	242β, α	−3.429	59.2	14.3	40.8
HOMO-5	240β, α	−4.597	81.4	0.9	18.6
HOMO-6	239β, α	−4.730	79.4	1.1	20.6
HOMO-7	238β, α	−4.769	79.5	1.4	20.5
HOMO-12	237β, α	−5.113	40.3	4.1	58.6
HOMO-13	236β, α	−5.150	43.6	3.8	55.3
HOMO-14	235β, α	−5.180	40.0	4.0	60.0
HOMO-15	234β, α	−5.190	35.9	4.8	64.1
HOMO-16	233β, α	−5.400	97.6	0.1	2.4
HOMO-21	228β, α	−5.960	100	0.4	0

Table S5.26: Selected bond distances (Å) and Angles (deg) for 1-Tm optimized geometry.[b] and [c] are dihedral angles.

	(Cp^{iPr5}Tm)$_2$(Bz)		
Tm(1) · · · Tm(2)	3.946		
Tm(1) − Cnt(Cp1)	2.318	Tm(2) − Cnt(Cp2)	2.318
Tm(1) − C(3)	2.630	Tm(2) − C(14)	2.639
Tm(1) − C(4)	2.581	Tm(2) − C(15)	2.662
Tm(1) − C(5)	2.585	Tm(2) − C(16)	2.626
Tm(1) − C(6)	2.636	Tm(2) − C(17)	2.580
Tm(1) − C(7)	2.664	Tm(2) − C(18)	2.588
Tm(1) − Cnt(Bz)	1.973	Tm(2) − Cnt(Bz)	1.974
Tm(1) − C(8)	2.478	Tm(2) − C(8)	2.480
Tm(1) − C(9)	2.525	Tm(2) − C(9)	2.415
Tm(1) − C(10)	2.413	Tm(2) − C(10)	2.522
Tm(1) − C(11)	2.410	Tm(2) − C(11)	2.486
Tm(1) − C(12)	2.486	Tm(2) − C(12)	2.406
Tm(1) − C(13)	2.434	Tm(2) − C(13)	2.437
Tm(1) − (Cnt)(Bz) − Tm(2)	177.8	C(8) − C(9)	1.462
Cnt(Cp1) − Tm(1) − Cnt(Bz)	166.7	C(8) − C(10)	1.463
Cnt(Cp2) − Tm(2) − Cnt(Bz)	167.0	C(10) − C(12)	1.470
Cnt(Cp1) − Cnt(Bz) − Cnt(Cp2)	165.9	C(12) − C(13)	1.468
C(8)-C(9)-C(11)-C(13)[b]	10.4	C(13) − C(11)	1.468
C(8)-C(10)-C(12)-C(13)[c]	10.6	C(11) − C(9)	1.470

Table S5.27: Electronic excitation summary for **1-Tm**. All excitations computed are single excitations involving alpha spin to alpha spin transitions. Oscillator strengths are reported in the length gauge. Only the dominant contributions to the overall excitation are reported.

Wavelength (nm)	Oscillator Strength	Dominant contributions	
		Occupied Virtual	% weight
751	0.0002	228β244β	28.1
		228β246β	23.7
657	0.0003	242β247β	58.0
581	0.0005	240β245β	61.4
493	0.001	247α249α	85.9
474	0.003	237β245β	32.6
		237β244β	31.6
446	0.004	247α250α	67.7
431	0.03	247α251α	42.7
		243β250β	23.4
405	0.01	242β252β	41.9
		243β250β	39.9
376	0.0002	243β251β	85.0
367	0.07	235β246β	39.1
		236β246β	13.5
		238β246β	13.2
363	0.02	234β247β	38.8
		239β247β	9.5
		237β247β	8.8
342	0.05	246α254α	86.5
340	0.2	243β253β	53.2
		246α254α	7.8
339	0.3	243β253β	41.9
		242β252β	9.6
		247α251α	8.4
336	0.04	242β253β	91.5
308	0.006	237β248β	31.0
		233β248β	28.6

Table S5.28. Atomic populations analysis from NPA (total density) for indicated **1-Ln** ground states

State	atom	charge	n(s)	n(p)	n(d)	n(f)
1-Y(a)	Y(1)	1.798	2.068	6.007	1.121	0
1-Y(a)	Y(2)	1.797	2.068	6.007	1.122	0
1-Gd(h)	Gd(1)	1.738	10.063	24.002	21.113	7.084
1-Gd(h)	Gd(2)	1.737	10.063	24.002	21.113	7.084
1-Tb(d)	Tb(1)	1.699	10.064	24.002	21.101	8.132
1-Tb(d)	Tb(2)	1.699	10.064	24.002	21.102	8.132
1-Dy(d)	Dy(1)	1.719	10.063	24.005	21.004	9.209
1-Dy(d)	Dy(2)	1.719	10.063	24.005	21.003	9.209
1-Tm(a)	Tm(1)	1.679	10.065	24.005	20.845	12.404
1-Tm(a)	Tm(2)	1.678	10.065	24.005	20.842	12.408

Table S5.29. Atomic populations analysis from NPA (spin density) for indicated 1-Ln ground states

State	atom	charge	n(s)	n(p)	n(d)	n(f)
1-Gd(h)	Gd(1)	7.319	0.023	0.084	0.329	6.883
1-Gd(h)	Gd(2)	-7.146	-0.006	-0.036	-0.237	-6.867
1-Tb(d)	Tb(1)	6.169	0.018	+0.069	0.240	5.842
1-Tb(d)	Tb(2)	-6.005	-0.005	-0.028	-0.148	-5.825
1-Dy(d)	Dy(1)	-4.877	-0.004	-0.025	-0.104	-4.743
1-Dy(d)	Dy(2)	4.991	0.014	0.050	0.156	4.771
1-Tm(a)	Tm(1)	1.812	0.004	0.014	0.213	1.580
1-Tm(a)	Tm(2)	1.807	0.005	0.015	0.212	1.576

Chapter 6: Closing Remarks

6.1. Introduction

In these concluding remarks, the work presented in the preceding chapters will be situated with current contemporary literature. Each section will begin with a brief review of the main results from each effort, followed by a perspective on how to best build on the results shared here to achieve new milestones in the field.

6.2. Exchange Coupled Single Molecule Magnets and their Future Prospects

In chapter 2, a new series of tetrathiotungstate compounds of the formula $[(Cp*_2Ln)_2(\mu\text{-}WS_4)]^-$ (Ln = Y, Gd, Tb, Dy) was synthesized and characterized. While the bridging tetrathiotungstate trianion was found to participate in appreciable magnetic exchange with the bound lanthanide ions, the geometry of the bridge precluded the formation of a giant-spin ground state. As a result, $[(Cp*_2Tb)_2(\mu\text{-}WS_4)]^-$ and $[(Cp*_2Dy)_2(\mu\text{-}WS_4)]^-$ exhibited fast magnetic relaxation at low temperatures. This shortcoming motivated efforts to identify a square planar metalloligand bridge, which was expected to yield magnetic anisotropy in the coupled ground state. Chapter 3 describes the efforts at obtaining the aforementioned compounds bridged by a square planar metalloligand. The complex anion of the formula $[Co(pdt)_2]^{2-}$ was found to be stable upon coordination to $(Cp*_2Ln)^+$, forming $(Cp*_2Ln)_2(\mu\text{-}Co(pdt)_2)$ (Ln = Y, Gd, Dy; pdt^{2-} = 1,2-diphenylethenedithiolate). The longer relaxation times of $(Cp*_2Dy)_2(\mu\text{-}Co(pdt)_2)$ over those of $[(Cp*_2Dy)_2(\mu\text{-}WS_4)]^-$ vindicated this approach, showing that the magnetic anisotropy of the coupled ground state is impacted by the bridge geometry. Additionally, the coordination of $[Co(pdt)_2]^{2-}$ to the lanthanide ions facilitated a post-synthetic reduction of the bridge to the trianion. While these compounds exhibited an undesirable D_{2d} bridge geometry, they stand as a rare example of an $S = 1$ bridge engaging in appreciable magnetic exchange with gadolinium.

While Chapters 2 and 3 present several new molecular complexes as well as new metalloligands, the magnetic properties of the compounds are worse than the most recent exchange based single molecule magnets that have emerged in the literature (i.e. $(Cp^{iPr5}Dy)_2I_3$ and $Dy_2@C_{80}$).[1,2] While the neutral compound $(Cp*_2Dy)_2(\mu\text{-}Co(pdt)_2)$ may be a reasonable candidate for surface deposition and electrical actuation at low temperature, future efforts in this domain will likely focus on enumerating the number of lanthanide compounds which exhibit direct double-exchange through an itinerant electron rather than exchange mediated by a bridge. The reason for this is that bridge mediated coupling will always be weak compared to direct metal-to-metal double exchange, as the singly occupied molecular orbital will always be bridge-centered rather than lanthanide-centered as a result of the low electronegativity of the lanthanides.

The inherent shortcomings that bridged compounds suffer from can be overcome with additional work, however. If a bridge with numerous unpaired electrons can be shown to simultaneously engage in appreciable ferromagnetic exchange ($J \sim 10 - 20$ cm^{-1}) with bound lanthanides while also promoting a strongly anisotropic coupled ground state, that compound is likely to exhibit properties competitive with those of $(Cp^{iPr5}Dy)_2I_3$. Weak exchange coupling can be overcome additively, as additional bridge spins yield additional stabilization of the coupled ground state over that of comparable systems restricted to $S = 1/2$. This effect is illustrated quantitatively in Figure 6.1 for a bridge-coupled system. Given that transition metal and f-element complexes are routinely capable of supporting multiple unpaired electrons, it seems reasonable to assume that, if such an

exchange-based system is ever realized, it will almost certainly include a high-spin metalloligand bridge.
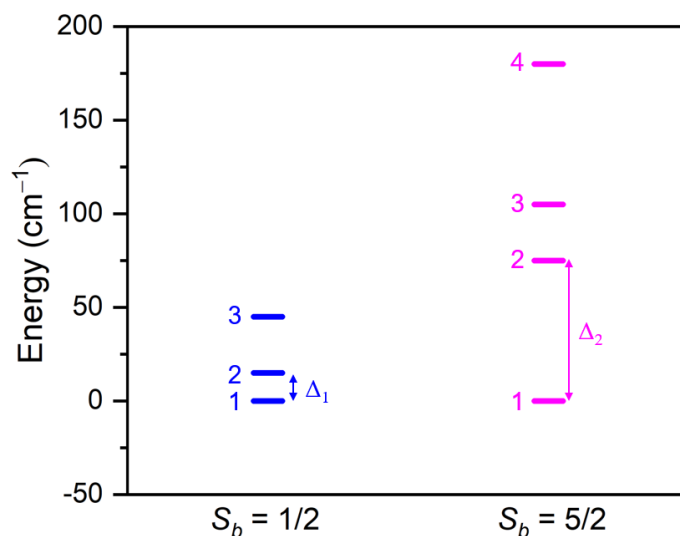

Figure 6.1: Quantitative comparison of the eigenvalues for a bridged coupling scheme, with Hamiltonian given in Equation 6.1. Both schemes involve two $S = 1/2$ centers, S_1 and S_2, interacting with a central bridging spin, S_b, with an exchange coupling constant $J_{ex} = +15$ cm^{-1}. For the blue eigenvalues, $S_b = 1/2$. For the magenta eigenvalues, $S_b = 5/2$. The energy separating the coupled ground state from the first excited state in each coupling scheme is indicated by Δ, where $\Delta_1 = 15$ cm^{-1}, $\Delta_2 = 75$ cm^{-1}. Though the exchange coupling strength remains equivalent, the coupled ground state becomes more well isolated as the value of S_b increases, with the general relationship $\Delta = 2J_{ex}S_B$. Eigenvalues plotted were obtained using Phi.[3]

$$\hat{H} = -2J_{ex}\hat{S}_b(\hat{S}_1 + \hat{S}_2)$$

Equation 6.1

6.3. Future Prospects of Borolide Based Single Molecule Magnets

Chapter 4 described the synthesis and characterization of a new dysprosium bis-borolide single molecule magnet. The pentaphenylborolide dianion is isoelectronic to the pentaphenylcyclopentadienide monoanion, while being significantly more nucleophilic. It was hoped that this would result in a higher strength axial crystal field than that which was observed for previously described dysprosocenium cations. A complex of the formula $[Dy(BC_4Ph_5)_2]^-$ was successfully synthesized and characterized, which was found to have a large U_{eff} value of 1500(100) cm^{-1}. This barrier and the other figures of merit for the aforementioned anion were found to be comparable to the best reported dysprosocenium derivative, with a high blocking temperature of 65 K.

The borolide dianion is an attractive alternative to Cp^{iPr5} in the design of single-molecule magnets moving forward. The borolide system is simple to derivatize and should present a much stronger ligand field to a bound lanthanide assuming an all alkyl substituted version of the dianion can be successfully realized. Alkyl groups should minimize the inductive withdrawal of the peripheral substituents on the 5-membered ring dianion, which will result in higher U_{eff} and T_B values

compared to those found in this work. Realizing alkyl substituted lanthanide borolides therefore seems to be the best way forward from the results presented here.

Additionally, there are several high anisotropy heteroleptic targets enabled by the borolide dianion. For example, one might obtain a compound of the formula $IDy(BC_4Mes_5)$ from the reaction of the pentamesitylborolide salt (Figure 6.2) $K_2BC_4Mes_5$ and DyI_3, as the steric bulk of the mesityl groups would prevent the formation of the otherwise preferred bis-borolide sandwich compound. Assuming that the mesityl groups are sufficiently large to block all but a single axial coordination site on the lanthanide, this heteroleptic compound should be an excellent precursor to a number of high anisotropy targets, as ligands would necessarily bind axially as illustrated in Figure 6.3. The iodide should be readily displaced by an alkoxide or a terminal fluoride, both of which may improve the U_{eff} and T_B values of the final targets over those exhibited by either the bis-borolides or the reported dysprosocenium cations.[4,5]
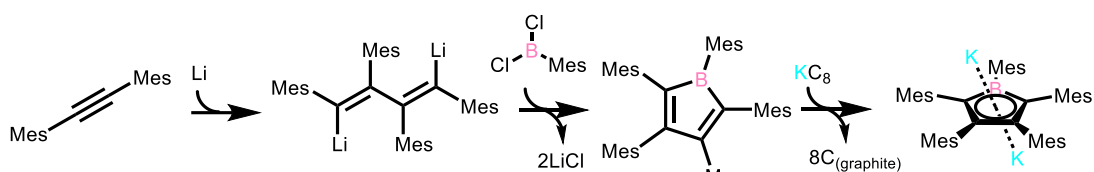

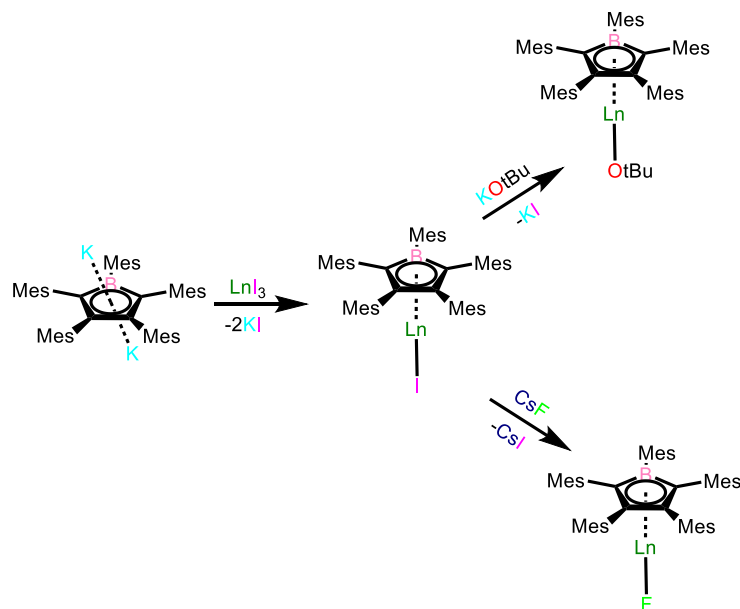**Figure 6.2**. Possible synthetic route to potassium pentamesitylborolide

Figure 6.3. Potential synthetic routes to high anisotropy heteroleptic lanthanide borolides

6.4. Realizing Inverse Sandwich Compounds with Slow Relaxation

Chapter 5 described the preparation and characterization of unusual benzene bridged lanthanide compounds of the formula $(Cp^{iPr5}Ln)_2(\mu\text{-}C_6H_6)$ (Ln = Y, Gd, Tb, Dy, Tm). The benzene in all five of these compounds was found to be a closed-shell benzene tetra-anion stabilized in a highly covalent interaction with the 5d orbitals of the bound lanthanides (4d for Y). DFT calculations showed that covalent interaction to be a δ-bonding interaction between the orbitals of d_{xy}, $d_{x^2-y^2}$ parentage and the π system of the benzene bridge.

245

Though these compounds themselves did not exhibit single molecule magnetism, it is likely that post synthetic oxidation of these, and similar derived compounds may yield stable radical bridged compounds with superlative properties. The frontier orbitals of the arene bridge have been shown to engage in considerable overlap with the adjacent lanthanide ions. Should the radical monocation or monoanion of $(Cp^{iPr5}Gd)_2(\mu\text{-}C_6H_6)$ exhibit similar behavior, the strength of the exchange interaction between the lanthanide and the ligand radical should be substantial. Though the impact of the arene bridge on the magnetic anisotropy of the spin-ground state is unclear, the coupled ground state would likely be well stabilized in the monocation or monoanion, given the strength of the exchange observed in previous arene bridged lanthanide compounds.[6] Additionally, the methods demonstrated in the synthesis of the $(Cp^{iPr5}Ln)_2(\mu\text{-}C_6H_6)$ series could also be conceivably applied in appending $(Cp^{iPr5}Ln)$ to the surface of graphene nanostructures or fullerenes, which may prove useful in fabricating novel devices with surface bound single ion magnets.[7]

6.5. References and Footnotes

(1) Gould, C. A.; McClain, K. R.; Reta, D.; Kragskow, J. G. C.; Marchiori, D. A.; Lachman, E.; Choi, E.-S.; Analytis, J. G.; Britt, R. D.; Chilton, N. F.; Harvey, B. G.; Long, J. R. Ultrahard Magnetism from Mixed-Valence Dilanthanide Complexes with Metal-Metal Bonding. *Science* **2022**, *375* (6577), 198–202. DOI: 10.1126/science.abl5470.

(2) Liu, F.; Krylov, D. S.; Spree, L.; Avdoshenko, S. M.; Samoylova, N. A.; Rosenkranz, M.; Kostanyan, A.; Greber, T.; Wolter, A. U. B.; Büchner, B.; Popov, A. A. Single Molecule Magnet with an Unpaired Electron Trapped between Two Lanthanide Ions inside a Fullerene. *Nat. Commun.* **2017**, *8* (1), 16098. DOI: 10.1038/ncomms16098.

(3) Chilton, N. F.; Anderson, R. P.; Turner, L. D.; Soncini, A.; Murray, K. S. PHI: A Powerful New Program for the Analysis of Anisotropic Monomeric and Exchange-Coupled Polynuclear d- and f-Block Complexes. *J. Comput. Chem.* **2013**, *34* (13), 1164–1175. DOI: 10.1002/jcc.23234.

(4) Norel, L.; Darago, L. E.; Guennic, B. L.; Chakarawet, K.; Gonzalez, M. I.; Olshansky, J. H.; Rigaut, S.; Long, J. R. A Terminal Fluoride Ligand Generates Axial Magnetic Anisotropy in Dysprosium Complexes. *Angew. Chem. - Int. Ed.* **2018**, *57* (7), 1933–1938. DOI: 10.1002/anie.201712139.

(5) Ding, Y. S.; Chilton, N. F.; Winpenny, R. E. P.; Zheng, Y. Z. On Approaching the Limit of Molecular Magnetic Anisotropy: A Near-Perfect Pentagonal Bipyramidal Dysprosium(III) Single-Molecule Magnet. *Angew. Chem. - Int. Ed.* **2016**, *55* (52), 16071–16074. DOI: 10.1002/anie.201609685.

(6) Gould, C. A.; Marbey, J.; Vieru, V.; Marchiori, D. A.; David Britt, R.; Chibotaru, L. F.; Hill, S.; Long, J. R. Isolation of a Triplet Benzene Dianion. *Nat. Chem.* **2021**, *13* (10), 1001–1005. DOI: 10.1038/s41557-021-00737-8.

(7) Candini, A.; Klyatskaya, S.; Ruben, M.; Wernsdorfer, W.; Affronte, M. Graphene Spintronic Devices with Molecular Nanomagnets. *Nano Lett.* **2011**, *11* (7), 2634–2639. DOI: 10.1021/nl2006142.